ENGINEERING

POLYMERIC DRUG DELIVERY VEHICLES

FOR ENHANCED TISSUE TARGETING

by
Jayoung Kim

A thesis submitted to Johns Hopkins University in conformity with the requirements for the degree of Doctor of Philosophy

Baltimore, Maryland
April 2018

Abstract

Development of therapeutic drugs, including small molecules, peptides, proteins, and nucleic acids, is centered upon their function through novel molecular targets or enhanced efficacy in comparison to existing drugs. However, one of the major limitations these drugs often suffer from is low drug concentration at the target site due to fast clearance post administration, which leads to overdosing and frequent dosings that can have further complications such as safety and patient compliance. Hence, there has been a strong effort during the past few decades in the field of biomaterials to develop drug delivery vehicles that enhance the localization of drugs at the site of disease while minimizing side effects. In particular, polymeric nanoparticles and microparticles have been utilized as platform technologies to protect, carry, and release the drug cargo in controlled fashion.

This thesis presents multiple approaches to engineering polymeric nanoparticles and microparticles based on different targeting modalities with the goal of maximizing the bioavailability of the drug in cancer and ocular disease applications. Two types of polymers, poly(beta-amino ester) (PBAE) and poly(lactic-co-glycolic acid) (PLGA), were utilized to optimize the delivery of a small molecule, peptides, and plasmid DNA. To maximize the delivered dose of the drug cargo of interest, physical size and shape modifications of nanoparticles were investigated for passive targeting. In particular, poly(ethylene glycol)-modified PBAE polymer was used to formulate pDNA-carrying polyplex and small molecule-carrying micelles for enhanced diffusion by size and prolonged circulation by shape, respectively. Next, biochemical modifications of polymers were explored for active targeting of nanoparticles to target tissue. Specifically, polymer structure-dependent tissue targeting was investigated with PBAE-pDNA polyplex nanoparticles, and active tumor targeting with

integrin-binding peptide-coated PLGA nanoparticles were studied. Finally, optimization of PBAE nano- and PLGA microparticles delivering nucleic acids and therapeutic peptide, respectively, were studied to enhance patient compliance and long-term therapeutic efficacy following two different local delivery routes to ocular spaces. Taken together, the findings from these polymeric nano- and microparticles with different targeting modalities show their clinical potential as efficient drug delivery systems.

Thesis Committee

Jordan J. Green, Ph.D. (*Advisor, reader*)

Associate Professor, Department of Biomedical Engineering,

Johns Hopkins University School of Medicine

Aleksander S. Popel, Ph.D. (*Thesis Committee Chair, reader*)

Professor, Department of Biomedical Engineering,

Johns Hopkins University School of Medicine

Honggang Cui, Ph.D.

Associate Professor, Department of Chemical & Biomolecular Engineering,

Johns Hopkins University School of Engineering

Alfredo Quiñones-Hinojosa, M.D.

Professor, Department of Neurological Surgery,

Mayo Clinic Jacksonville

Acknowledgements

Many people have had both direct and indirect impact on my professional and personal journey through Ph.D. program ending with this thesis. I would like to express my utmost gratitude to all of them.

First and foremost, I would like to sincerely thank Dr. Jordan J. Green, my mentor and advisor, for his insightful guidance in and out of the lab. I was able to survive through struggles and succeed in Ph.D. study owing to his encouragement and faith. His showing of patience, passion and kindness taught me what it takes to be an able mentor. I am grateful to Dr. Green for the overwhelming opportunity he provided that became a solid starting ground for my exciting career as an engineer.

I would also like to thank the professors and collaborators at the Johns Hopkins University, the Wilmer Eye Institute, and Mayo Clinic Jacksonville – Drs. Aleksander Popel, Honggang Cui, Peter Campochiaro, Niranjan Pandey, Alfredo Quiñones-Hinojosa, Hugo Guerrero-Cazares, Greg Semanza, Justin Sacks, Betty Tyler, Hai-Quan Mao, Warren Grayson, Jennifer Elisseeff, Esak Lee, Adam Mirando, Hojjat Bazzazi, Raquel Lima e Silva, Jikui Shen, Kun Ding, Young Lee, Alejandro Ruiz-Valls, Sagar Shah, Paula Schiapparelli, Noah Gorelick, Debangshu Samanta, Deepa Bhat, and Rawan Al-kharboosh, Carla Vazquez Ramos, John Choi, Michelle Seu, Yong Ren – for their support. Their excellence in research and teaching was the driving force in opening my eyes to the field of biomaterials / tissue engineering and in continuing my future post-doctoral research. I especially thank Drs. Popel, Cui, and Quiñones for taking their precious time to review my thesis.

I will not be able to forget my labmates - Nupura Bhise, Joel Sunshine, Ron Shmueli, Stephany Tzeng, Corey Bishop, Kristen Kozielski, Randall Meyer, David Wilson, Yuan Rui,

Camila Zamboni, Maziar Mohammadi, Hannah Vaughan, Elana Ben-Akiva, Kelly Rhodes, and Johan Karlsson – who definitely contributed much to make the Green Lab the best lab. I especially extend my gratitude to Ron Shmueli, who as my first graduate student mentor in the lab, had taught me everything that needs to be of a biomedical researcher. I also would like to thank the undergraduate and high-school students – Yechan Kang, James Shamul, Ben Lee, and Alyssa Shin – for their hard work in supporting my research and the joy they bring to the lab.

I have been extremely privileged to have many supporting friends within Baltimore as well as afar, who provided the fun and encouragement in every step along the way. They have been always there to celebrate and console at times of both joy and sadness. Thank you for your everlasting friendship Jungsoo, Ethan, Jiwoong, JongSoo, Halim, Sungho, Jiho, Shoumyo, Sungwon, Jun-Ha, Jace, Yoonmin, Kiani, AFIOS members, Kyung Seok, and TK.

Most importantly, I express my heartfelt gratitude to my wife and my (extended) family. I was very fortunate to meet the love of my life during my study in Baltimore. Seungmin, I always pray that we have a fantastic life ahead of us that is filled with love, happiness, and blessing. Thank you for being here by my side throughout the journey. Also, I could not have come this far without the support from such loving parents, sister, brother-in-law, nephew, parents-in-law, and sister-in-law. Your relentless support for my life, study and career was, is and will always be appreciated.

Last but not least, I would like to thank the Samsung Scholarship for their external funding toward my study. Both financial support and academic / personal mentorship made my dream of graduate education a reality. I will not forget the mission I bear to become a global leader that follows your vision.

To God and my family,

I can do all this through him, who gives me strength (Philippians 4:13)

Table of Contents

List of tables

List of figures

Chapter 1

Introduction to the thesis

1.1 Significance of drug delivery systems

With the advancement of scientific tools and a better understanding of pathological targets, an increasing number of novel drugs is being investigated at the research and pre-clinical stages. These drugs often show therapeutic efficiency in pre-clinical disease models, but still suffer from high attrition rate going through clinical trials[1]. Clinical translation of these drugs is often limited due to two major reasons: aqueous solubility and poor pharmacokinetics profile. More than 40% of the drug candidates are considered to be non-soluble in aqueous solution[2] and need to be modified to become water-soluble and thus biocompatible. For example, conjugation of hydrophilic molecule poly(ethylene glycol) to drugs led to many FDA-approved products[3], while particle systems encapsulating smaller drug cargos are also widely explored[4]. Moreover, low bioavailability of the drugs at the target site can result from degradation, non-specific absorption or lack of specific absorption, and elimination through the mononuclear phagocytic system or kidney secretion[5,6]. Insufficient pharmacokinetic properties are exacerbated in the presence of mucosal layer, as in the case with oral delivery or topical ocular delivery (eye drop)[7,8]. In order to overcome such drawbacks, there has been recent effort to adapt an *in silico* method to systematically design drug that would have advantageous physicochemical properties in their native form[9]. Drug delivery systems, such as particles, hydrogels, or other depot systems, are also a very active field of research that aims

to increase bioavailability of the cargo drug through protection, targeted delivery, and/or spatiotemporally controlled release. In particular, this thesis will focus on polymeric nanoparticles and microparticles as drug delivery vehicles.

1.2 Biological barriers to successful drug delivery

While drug delivery systems are aimed to enhance a drug's bioavailability at the target site, they must overcome the same biological barriers as naked drugs would face in order to reach the site of action. The barriers can vary depending on the route of administration, the target organ or disease, and the mode of drug's action. For local injection, drug delivery particles need to be administered to an accurate position and either efficiently diffuse throughout the affected disease area or form a stable depot for sustained release. In systemic injection, the vehicles must evade clearance by body's immune system, in particular monocytes and macrophages, extravasate around the target organ, and diffuse throughout the affected disease area[10,11]. The particles' role may extend at the cellular level with the drug's mechanism of action. For exogenous DNA or molecules that function within the nucleus, the particles must facilitate cellular endocytosis, endosomal escape, and nuclear transport. Nuclear transport is not necessary for drugs whose action is in the cytoplasm, such as siRNA. For drugs that can either penetrate the cell membrane well or induce downstream effect by binding to cell membrane proteins, then the particles must be able to release the cargo in the extracellular space. Each of these barriers has resulted in investigation of diverse methods for modifying nanoparticles and microparticles to optimize bioavailability.

1.3 Approaches to modifying polymeric nanoparticles and microparticles for tissue targeting

While efficiently targeting the diseased tissue remains one of the biggest challenges of drug delivery, many targeting modalities are being explored to enhance specific tissue accumulation. In particular, polymeric nanoparticles and microparticles are extensively investigated because they are composed of synthetic polymers that can be modified or tuned in various ways to enable different designs with unique physical and chemical properties[12]. Targeting methods can be broadly categorized into three groups: passive targeting, active targeting, and local delivery (physical targeting).

Passive targeting involves increasing the chance of particle accumulation at the target tissue by prolonging systemic circulation time[13]. In cancer, the hypothesis that small particles of less than 200 nm can extravasate to the tumor tissue through leaky vasculature around the tumor, known as the enhanced permeability and retention effect, led to strategies such as surface coating with poly(ethylene glycol) to produce small, stable nanoparticles[14]. Other ways to increase blood half-life include increasing aspect ratio of particles to evade phagocytosis[15], surface decorating with self-recognition CD47 peptide[16], or more recently red blood cell (RBC) membrane coating or RBC hitchhiking[17,18].

Active targeting is mediated by specific receptor-ligand interaction. A widely utilized method is to conjugate ligands to the surface of nanoparticles that will specifically bind to receptors that are only present or overexpressed on the target cell(s). For example, cyclic RGD and folate have been used to home to tumor endothelium and tissue via integrin and folic receptor binding, respectively[19,20]. Transferrin is another molecule that has also been studied to bind to their respective receptors on endothelial cells in brain vasculature to mediate

transcytosis[21]. Moreover, there have been a number of studies that showed the ability of polymer's chemical structure to direct tissue targeting[22,23]. Namely, Jeong et al. showed that different molecular weights of polyethylenimine result in varying biodistribution profiles[22].

Lastly, many drug delivery systems are physically targeted to the disease tissue by local or direct injection into the site of interest. Although this method may guarantee the highest drug concentration where needed, it often necessitates an invasive operation that can minimize patient compliance and/or require more sophisticated drug design to satisfy the clinical requirement of the local environment. The wafer-type design of Gliadel® is well-suited as it is placed in the cavity that is created from surgical resection of a brain tumor[24]. For ocular application, microneedles have been developed to inject therapeutics into the artificially created suprachoroidal space, along with an excipient to facilitate the spread of the fluid following the injection[25].

1.4 Specific aims

In this thesis work, six different tissue targeting modalities are reported using polymeric nanoparticles and microparticles. The thesis begins with passive targeting of nanoparticles by control of physical size (chapter 2) and shape (chapter 3), followed by active targeting with polymer's structure (chapter 4) and non-canonical peptide (chapter 5), and concludes with the discussion of two local delivery routes in ocular application, suprachoroidal (chapter 6) and intravitreal (chapter 7).

Aim 1. Develop poly(ethylene glycol)-coated poly(beta-amino ester)-based nanoparticles for passive targeting to tumor

1.1 Small, stable poly(beta-amino ester) nanoparticles for gene delivery

1.2 Filamentous-shaped poly(beta-amino ester) micelles for small molecule delivery

Aim 2. Investigate biomaterial- and ligand-mediated active targeting of polymeric nanoparticles

2.1 Biodistribution of poly(beta-amino ester)-DNA nanoparticles via polymer structure-dependent targeting

2.2 Pharmacokinetics of poly(lactic-co-glycolic acid)-poly(ethylene glycol) nanoparticles surface-coated with integrin-targeted biomimetic peptide

Aim 3. Optimize polymeric nano- and microparticles as local drug delivery vehicles for ocular applications

3.1 Suprachoroidal delivery of plasmid DNA using poly(beta-amino ester) nanoparticles

3.2 Intravitreal delivery of poly(lactic-co-glycolic acid) microparticles containing anti-angiogenic peptide

1.5 References

(1) Ku, M. S.; Dulin, W., A biopharmaceutical classification-based right-first-time formulation approach to reduce human pharmacokinetic variability and project cycle time from first-in-human to clinical proof-of-concept. *Pharm Dev Technol* **2012,** 17, (3), 285-302.

(2) Savjani, K. T.; Gajjar, A. K.; Savjani, J. K., Drug solubility: Importance and enhancement techniques. *ISRN Pharm* **2012,** 2012, 195727.

(3) Turecek, P. L.; Bossard, M. J.; Schoetens, F.; Ivens, I. A., Pegylation of biopharmaceuticals: A review of chemistry and nonclinical safety information of approved drugs. *J Pharm Sci* **2016,** 105, (2), 460-475.

(4) Kalepu, S.; Nekkanti, V., Insoluble drug delivery strategies: Review of recent advances and business prospects. *Acta Pharm Sin B* **2015,** 5, (5), 442-53.

(5) Zelikin, A. N.; Ehrhardt, C.; Healy, A. M., Materials and methods for delivery of biological drugs. *Nat Chem* **2016,** 8, (11), 997-1007.

(6) Eddershaw, P. J.; Beresford, A. P.; Bayliss, M. K., Adme/pk as part of a rational approach to drug discovery. *Drug Discov Today* **2000,** 5, (9), 409-414.

(7) Benedetti, M. S.; Whomsley, R.; Poggesi, I.; Cawello, W.; Mathy, F. X.; Delporte, M. L.; Papeleu, P.; Watelet, J. B., Drug metabolism and pharmacokinetics. *Drug Metab Rev* **2009,** 41, (3), 344-90.

(8) Joseph, R. R.; Venkatraman, S. S., Drug delivery to the eye: What benefits do nanocarriers offer? *Nanomedicine (Lond)* **2017,** 12, (6), 683-702.

(9) Sager, J. E.; Yu, J.; Ragueneau-Majlessi, I.; Isoherranen, N., Physiologically based pharmacokinetic (pbpk) modeling and simulation approaches: A systematic review of published models, applications, and model verification. *Drug Metab Dispos* **2015,** 43, (11), 1823-37.

(10) Blanco, E.; Shen, H.; Ferrari, M., Principles of nanoparticle design for overcoming biological barriers to drug delivery. *Nat Biotechnol* **2015,** 33, (9), 941-51.

(11) Mitragotri, S.; Burke, P. A.; Langer, R., Overcoming the challenges in administering biopharmaceuticals: Formulation and delivery strategies. *Nat Rev Drug Discov* **2014,** 13, (9), 655-72.

(12) Kim, J.; Wilson, D. R.; Zamboni, C. G.; Green, J. J., Targeted polymeric nanoparticles for cancer gene therapy. *J Drug Target* **2015,** 23, (7-8), 627-41.

(13) Petros, R. A.; DeSimone, J. M., Strategies in the design of nanoparticles for therapeutic applications. *Nat Rev Drug Discov* **2010,** 9, (8), 615-27.

(14) Harris, J. M.; Martin, N. E.; Modi, M., Pegylation: A novel process for modifying pharmacokinetics. *Clin Pharmacokinet* **2001,** 40, (7), 539-51.

(15) Champion, J. A.; Mitragotri, S., Role of target geometry in phagocytosis. *Proc Natl Acad Sci U S A* **2006,** 103, (13), 4930-4.

(16) Rodriguez, P. L.; Harada, T.; Christian, D. A.; Pantano, D. A.; Tsai, R. K.; Discher, D. E., Minimal "self" peptides that inhibit phagocytic clearance and enhance delivery of nanoparticles. *Science* **2013,** 339, (6122), 971-5.

(17) Anselmo, A. C.; Gupta, V.; Zern, B. J.; Pan, D.; Zakrewsky, M.; Muzykantov, V.; Mitragotri, S., Delivering nanoparticles to lungs while avoiding liver and spleen through adsorption on red blood cells. *ACS Nano* **2013,** 7, (12), 11129-37.

(18) Hu, C. M.; Zhang, L.; Aryal, S.; Cheung, C.; Fang, R. H.; Zhang, L., Erythrocyte membrane-camouflaged polymeric nanoparticles as a biomimetic delivery platform. *Proc Natl Acad Sci U S A* **2011,** 108, (27), 10980-5.

(19) Miura, Y.; Takenaka, T.; Toh, K.; Wu, S.; Nishihara, H.; Kano, M. R.; Ino, Y.; Nomoto, T.; Matsumoto, Y.; Koyama, H.; Cabral, H.; Nishiyama, N.; Kataoka, K., Cyclic rgd-linked polymeric micelles for targeted delivery of platinum anticancer drugs to glioblastoma through the blood-brain tumor barrier. *ACS Nano* **2013,** 7, (10), 8583-92.

(20) Wang, J.; Liu, W.; Tu, Q.; Wang, J.; Song, N.; Zhang, Y.; Nie, N.; Wang, J., Folate-decorated hybrid polymeric nanoparticles for chemically and physically combined paclitaxel loading and targeted delivery. *Biomacromolecules* **2011,** 12, (1), 228-34.

(21) Wiley, D. T.; Webster, P.; Gale, A.; Davis, M. E., Transcytosis and brain uptake of transferrin-containing nanoparticles by tuning avidity to transferrin receptor. *Proc Natl Acad Sci U S A* **2013,** 110, (21), 8662-7.

(22) Jeong, G. J.; Byun, H. M.; Kim, J. M.; Yoon, H.; Choi, H. G.; Kim, W. K.; Kim, S. J.; Oh, Y. K., Biodistribution and tissue expression kinetics of plasmid DNA complexed with polyethylenimines of different molecular weight and structure. *J Control Release* **2007,** 118, (1), 118-25.

(23) Poon, Z.; Lee, J. B.; Morton, S. W.; Hammond, P. T., Controlling in vivo stability and biodistribution in electrostatically assembled nanoparticles for systemic delivery. *Nano Lett* **2011,** 11, (5), 2096-103.

(24) Perry, J.; Chambers, A.; Spithoff, K.; Laperriere, N., Gliadel wafers in the treatment of malignant glioma: A systematic review. *Curr Oncol* **2007,** 14, (5), 189-94.

(25) Kim, Y. C.; Oh, K. H.; Edelhauser, H. F.; Prausnitz, M. R., Formulation to target delivery to the ciliary body and choroid via the suprachoroidal space of the eye using microneedles. *Eur J Pharm Biopharm* **2015,** 95, (Pt B), 398-406.

Chapter 2

Synthesis and application of poly(ethylene glycol)-co-poly(β-amino ester) copolymers for cancer gene therapy

2.1 Introduction

Small cell lung cancer (SCLC) is a neuroendocrine subtype of lung cancer that accounts for 15% of all lung cancer cases.[1] SCLC is initially sensitive to chemotherapy and radiation, most often involving a combination of cisplatin-etoposide chemotherapy with chest radiation, prophylactic cranial irradiation, or hyperfractionated thoracic radiation.[2] Glioblastoma (GBM) is the most common form of brain tumor in adults that accounts for more than 10000 deaths in the United States in spite of tumor resection, chemotherapy, and radiation.[3,4] It has also been reported recently that GBM tumor mass consists of fully differentiated cancer cells and brain tumor initiating cells (BTIC), which possess stem-like properties and can be insensitive to chemotherapeutic drugs, hence responsible for recurrence.[5] However, SCLC and GBM still have one of the highest fatality rates among cancers due to its high recurrence and metastasis.[6,7] New therapies are needed to improve the survival of patients with these tumors.

Gene therapy is a promising technology due to its tremendous potential as a selective and potent therapeutic for genetic diseases including cancer. Many approaches to DNA-based

---

Parts of this chapter were originally published in and modified from Kim J, Kang Y, Tzeng SY, Green JJ. "Synthesis and application of poly(ethylene glycol)-co-poly(beta-amino ester) copolymers for small cell lung cancer gene therapy," *Acta Biomaterialia*, 2016, 41:293-301.

therapeutics have been identified and validated, such as tumor suppressor genes including TNF-related apoptosis-inducing ligand (TRAIL) and p53.[8,9] Another method is suicidal gene therapy, which induces apoptosis of tumor cells by delivering exogenous DNA, such as that encoding Herpes simplex virus thymidine kinase (HSV-tk) that converts prodrugs *in situ* to an active form.[10]

There has been parallel effort to develop efficient, safe, and stable gene delivery vectors. Although viral vectors have the advantage of high transduction efficacy, limitations in cargo capacity, difficulty of production, and safety concerns due to immunogenic and mutagenic factors have led to the emergence of non-viral approaches as alternatives.[11,12] Poly(β-amino ester)s (PBAEs), a class of biodegradable cationic polymers, have been shown to exhibit low levels of toxicity and high rates of both DNA and siRNA transfection in various types of cells.[13-17]. These cationic polymers are able to bind with negatively charged nucleotides and form polyplexes by electrostatic interactions. Previous studies have shown that the biophysical properties of these PBAE polyplexes allow them to overcome critical barriers to gene delivery at the cellular level, including cellular uptake and endosomal escape via pH buffering.[18,19] However, there has been limited effort to modify PBAE polyplexes to promote biological stability at the systemic and tissue levels, which is a critical property to facilitate efficient *in vivo* utilization and crossing of extracellular barriers.[20-22] Poly(ethylene glycol) (PEG), a water-soluble molecule with low toxicity, is widely used with a variety of biomaterials to minimize unwanted interactions with biomolecules. Its neutral and hydrophilic structure not only reduces surface charge of particles but also provides steric hindrance to reduce non-specific adsorption and aggregation. These properties have been

shown to significantly enhance stability and increase half-life of biologics and particles in systemic circulation.[23,24]

PEGylation has the potential to reduce non-specific interactions between polyplexes and biological molecules and off-target cells. However, PEGylating polyplexes also generally has a negative effect on cellular uptake and transfection to target cells, which has been referred to as the "PEG dilemma."[25] Due to the shielding of positive surface charge by neutral PEG molecules, polyplexes are not only preventing non-specific protein adsorption but also become less associated with the plasma membrane of target cells. Decreased polyplex-cell interaction has been correlated to reduced cellular uptake and transfection.[26,27]

The present study introduces a synthesis method to conjugate PEG to PBAE polymers and a combinatorial method was used to formulate polyplexes from a blend of PEGylated PBAEs (PEG-PBAEs) and end-capped PBAEs (ePBAEs) developed in our lab[16] in order to overcome the PEG dilemma. The resulting PEG-PBAE polyplexes maintain particle stability and efficacy over time, diffuse through brain tumor mass *in vivo*, successfully transfect SCLC, BTIC375 and GBM1A cells *in vitro*, and deliver suicidal gene HSV-tk *in vitro* to activate ganciclovir to kill SCLC cells.

2.2 Methods

Materials

1,4-butanediol diacrylate (B4), 4-amino-1-pentanol (S4), 5-amino-1-pentanol (S5), 1-(3-aminopropyl)-4-methylpiperazine (E7) (Alfa Aesar), 1,5-pentanediol diacrylate (B5) (Monomer Polymer & Dajac Labs), 2-methylpentane-1,5-diamine (E4) (TCI America), 2-(3-

aminopropylamino)ethanol (E6) (Fluka), poly(ethylene glycol) methyl ether thiol (800 Da), branched 25 kDa poly(ethylenimine) (PEI) (Sigma-Aldrich), α-Mercaptoethyl-ω-methoxy polyoxyethylene (5000 Da) (NOF America Corporation), and cell culture media components were purchased and used as received. pEGFP-N1 (EGFP) DNA (purchased from Elim Biopharmaceuticals and amplified by Aldevron, Fargo, ND), ganciclovir (Invivogen, San Diego, CA), Label IT-Tracker Cy3 kit (Mirus Bio LLC), and CellTiter 96 AQueous One MTS assay (Promega, Fitchburg, WI) were obtained from commercial vendors and used per manufacturer's instructions. HSV-tk gene was cloned into the pcDNA3.1 vector (Life Technologies) and amplified (Aldevron, Fargo, ND).

Polymer synthesis and characterization

ePBAEs and PEG-PBAEs were synthesized in a two-step reaction using small commercially-available molecules as described in **Figure 2.1**. As an example, acrylate-terminated base polymer poly(1,4-butanediol diacrylate-*co*-4-amino-1-butanol) (B4S4) was first synthesized by mixing a backbone monomer (B4) and a side-chain monomer (S4) at 1.2:1 or 1.05:1 B4:S4 monomer molar ratios in DMSO as a 500 mg/mL solution and stirring at 90 °C for 24 h. The base polymer was purified in cold diethyl ether, dried under vacuum with desiccant for 24 h, and the molecular weight and chemical structure of the base polymer were confirmed by Bruker Avance III 500 MHz NMR spectrometer in $CDCl_3$. Base polymers were end-capped with a small molecule (E4, E6, or E7) by dissolving base polymer and end-capping molecule at 1:30 M ratio in THF as a 100 mg/mL solution and shaking the mixture at room temperature for 3 h. Final ePBAE polymers were purified in cold diethyl ether, dried

under vacuum with desiccant for 24 h, confirmed with ^{1}H NMR for complete conjugation, and then stored with desiccant at −20 °C as 100 mg/mL solutions in DMSO.

Amine-catalyzed, thiol-ene Michael addition reaction was used to conjugate PEG to the base polymer B4S4.[28] Briefly, B4S4, methoxy PEG-thiol, and E7 molecules were mixed at 1:2.5:0.2 M ratios as a 100 mg/mL solution in DMSO and stirred at room temperature for 24 h at 1000 rpm. Final block copolymers were precipitated in diethyl ether at room temperature without centrifugation, confirmed with ^{1}H NMR for complete conjugation, and stored with desiccant at −20 °C as 100 mg/mL solutions in DMSO. The nomenclature of different PEG-PBAEs used in this study is listed in **Table 2.1**.

Particle formulation and characterization

PBAE polyplexes were made at 60 and 75 w/w mass ratios of ePBAE to DNA in 25 mM sodium acetate buffer (pH = 5). For example, diluted polymer solution at 3.6 mg/mL was mixed into diluted DNA solution at 0.06 mg/mL at equal volume to form 60 w/w polyplexes, and the mixture was incubated for 10 min to allow complexation. 75 w/w was tested to check for cytotoxicity of ePBAE at higher polymer concentration.

PEG-PBAE polyplexes were made at 30, 60, 90 w/w ratios of total polymer to DNA in 25 mM sodium acetate buffer (pH = 5). Polymer used to condense DNA was a mixture of ePBAE and PEG-PBAE at three different mass ratios of 1:2, 1:1, and 2:1. For example, 50 μg of ePBAE 447 and 100 μg of PEG-PBAE 5k-4k were diluted to 3.6 mg/mL total polymer concentration with 25 mM sodium acetate buffer (pH = 5), and the polymer solution was mixed with diluted DNA solution at 0.06 mg/mL at equal volume to form polyplexes

with 447:5k-4k 1:2 w/w and polymer:DNA 60 w/w ratios. These polyplexes were incubated for 10 min to allow complexation.

The polyplex size was determined by nanoparticle tracking analysis (NTA) using Nanosight NS500 (Malvern Instruments, 532 nm laser) and dynamic light scattering (DLS) using Malvern Zetasizer Nano ZS (Malvern Instruments, detection angle 173°, 633 nm laser). The polyplexes prepared at DNA concentration of 0.1 mg/mL were diluted 1000-fold and 2-fold into 25 mM sodium acetate buffer or 2× PBS to a total volume of 400 μL for Nanosight and Zetasizer, respectively. To determine polyplexes' stability over time, cuvettes with the polyplex solution were stored in dark at room temperature until specific time points, then the polyplex size was re-measured following a brief resuspension. The polyplexes were diluted in artificial cerebrospinal fluid (ACSF) in order to determine the particle stability over time by Zetasizer for application in therapy against glioblastoma. Only number-weighted measurements with particle concentrations above 15 particles/frame by NTA and intensity-weighted Z-average measurements passing the quality control expert advice criteria by DLS are reported. Zeta potential was determined using Malvern a Zetasizer Nano ZS (Malvern Instruments) with samples prepared at DNA concentration of 0.03 mg/mL diluted 2-fold into 25 mM sodium acetate buffer (pH = 5.0) for a total volume of 800 μL. The mean and standard deviation were calculated.

Cell culture

H446 small cell lung cancer cells (ATCC) were cultured at 37 °C and 5% CO_2 in ATCC-modified RPMI 1640 media (Life Technologies A10491-01), supplemented with 10% FBS

and 1% penicillin/streptomycin. IMR-90 human lung fibroblast cells (ATCC) were cultured at 37 °C and 5% CO_2 in Eagle's minimum essential media (Cellgro 10-009-CV), supplemented with 10% FBS. BTIC375 brain tumor initiating cells and GBM1A glioblastoma cells (Quinones lab) were cultured at 37 °C and 5% CO_2 in DMEM/ F-12 (1:1) (Cellgro 10-009-CV) with 1X B-27 supplement, 1% antibiotic-antimycotic (Invitrogen), 20 ng/mL basic fibroblast growth factor (bFGF), and 20 ng/mL epidermal growth factor (EGF).

DNA delivery assays

Polyplex delivery. Cells were plated at a density of 15,000 cells/well (100 μL/well) in 96-well tissue culture plates and were incubated for 24 h. For BTIC375 and GBM1A, 96-well plates were incubated with laminin (5 μg/mL) for 2 h prior to cell seeding. pEGFP labeled with Cy3 per manufacturer's instructions (Label IT Tracker kit) and unlabeled pEGFP were used for uptake and transfection experiments, respectively. Polyplexes were prepared as described above to a final DNA concentration of 0.03 mg/mL. Then, 20 μL of polyplexes was added to 100 μL of serum-containing medium in each well. For PEI polyplexes, pEGFP-Cy3 diluted into 150 mM NaCl to 60 μg/mL was mixed with equal volume of PEI diluted into 150 mM NaCl to 120 μg/mL (2 w/w) from a stock solution of 1 mg/mL in dH_2O. PEI polyplexes were also incubated for 10 min to complex, and 20 μL of polyplex solution was added to 100 μL of medium in each well. For uptake experiments, cells were incubated with polyplexes for 4 h for H446 and 2 h for BTIC375/GBM1A, washed twice with heparin-containing PBS (50 μg/mL), and prepared for flow cytometry. For transfection experiments, cells were incubated with polyplexes for 4 h for H446 and 2 h for BTIC375/GBM1A, washed

twice with heparin-containing PBS, and incubated with 100 μL fresh media for an additional 48 h, and analyzed qualitatively with fluorescent microscope and quantitatively with FACS analysis.

Cell viability. Cells were treated following the same protocol as transfection. Following 4 h (H446) or 2 h (BTIC375, GBM1A) of incubation with polyplexes, cells were washed twice with heparin-containing PBS, added with 100 μL of fresh media, and incubated for an additional 24 h at 37 °C. 20 μL of CellTiter 96 AqueousOne MTS reagent were added per well, cells were incubated with reagent at 37 °C, and absorbance was measured at 490 nm using a Synergy 2 plate reader (Biotek) every 30 min until the highest absorbance signal reached 1.2. Absorbance signal was normalized to that of untreated cells after subtracting the background signal. All conditions were prepared in quadruplicates.

Flow cytometry. To prepare for flow cytometry (Accuri C6 with HyperCyt high-throughput adaptor), cells were detached using 30 μL of 0.05% trypsin, resuspended with 170 μL of FACS buffer (PBS containing 2% v/v FBS), transferred to a round-bottom 96-well plate and centrifuged at 800 rpm at 4 °C for 5 min. 170 μL of supernatant was removed, and the remaining 30 μL was triturated to resuspend the cells. Propidium iodide (PI) (Invitrogen, Carlsbad, CA) was added to FACS buffer at 1:200 to detect cells in the process of apoptosis for transfection assay.

For uptake, % positive is the percentage of total cells that are Cy3+ as measured by two-dimensional gating of FL1 vs. FL2 using FlowJo 7.6.5 software. For transfection, % positive is the percentage of total cells that are EGFP+ as measured by sequential two-dimensional gating of PI- by FSC-H vs. FL2 and EGFP+ by FL1 vs. FL2. At least 500 cell counts were analyzed for each measurement. All conditions were prepared in quadruplicates.

Delivery of pHSV-tk and ganciclovir

Cells were treated following the same protocol as transfection using pHSV-tk DNA. Following 4 h (H446) or 2 h (BTIC375, GBM1A) of incubation with polyplexes, cells were washed twice with heparin-containing PBS and incubated with 100 μL of fresh media for 24 h at 37°C. The media was then replaced with fresh media containing 10 or 20 μg/mL of ganciclovir. Following additional 48 h incubation at 37°C, the media was replaced with fresh media containing 10 or 20 μg/mL of ganciclovir. Cell death was measured 24 h after the second ganciclovir treatment with CellTiter 96 AQueous CellTiter reagent as described above. All conditions were prepared in quadruplicates. Stock ganciclovir solution at 5 mg/mL was prepared by dissolving it in 2% 1 M NaOH, and then neutralizing the pH with 1% 1 M HCl, 40% dH_2O, and 57% 1X PBS by volume.

In vivo *nanoparticle diffusion in orthotopic glioblastoma xenograft*

Athymic nude male mice were anesthesized and stereotatically injected with 5 x 10^5 primary human brain tumor initiating cells (BTIC375) at 8 weeks old. After a 4-week period for tumor formation, polyplexes carrying Cy5-labeled (Label IT Tracker kit, Mirus Bio) pEGFP DNA (4 μL, 0.7 μg DNA) were stereotatically injected at the site of tumor. Polyplexes were either non-PEGylated polyplex composed of 447 30 w/w or PEG-PBAE polyplex composed of 447 and 0.8k-13k 1:2 45 w/w that were lyophilized with 30 mg/mL sucrose, stored at -20 C, and resuspended in water. After 24 h, mice were sacrificed and

perfused and fixed with 1X PBS and 10% formalin to remove the brain. Harvested brains were stored overnight in 10% formalin, transferred to 30% sucrose for 24 h, embedded in optimal cutting temperature (OCT) compound, and cryo-sectioned in 10-μm slices. Slices were imaged by fluorescence microscopy to observe particle spread (Cy5) using an Axio Observer A1.

Statistics

All statistical analysis was performed with GraphPad Prism 5 software package. One-way ANOVA with post-hoc Dunnett test was used to test statistical significance of multiple conditions against the control group ($p < 0.05$). A Student's *t*-test was used to test statistical significance of cell death from the same HSV-tk and ganciclovir treatment between H446 and IMR-90 cells ($p < 0.01$).

2.3 Results

Synthesis and characterization of PBAE and PEG-PBAE polymer

We first sought to synthesize and confirm the molecular weight as well as the completion of synthesis of ePBAEs and PEG-PBAEs. Both types of PBAEs share the same base polymer, with the molecular weight controlled by the molar ratio of backbone (B) to side-chain (S) monomers in the Step 1 reaction (**Figure 2.1**). Two molar ratios, 1.2:1 and 1.05:1, as well as two (B) and (S) monomer types each were used to synthesize four different

acrylate-terminated base polymers with molecular weight distribution as shown in **Figure 2.2**; the closer the monomer ratio is to unity, the greater the degree of polymerization.
A total of 9 ePBAEs were synthesized with three base polymers, B4S4, B4S5, and B5S5 of approximately 10 kDa, and three end-capping (E) molecules, E4, E6, and E7, by Step 2A end-capping reaction (**Figure 2.1**). Similar molecular weights were selected for each polymer structure. An example of an ePBAE nomenclature is 457, which is base polymer B4S5 end-capped with E7. A total of 4 PEG-PBAEs were synthesized with two base polymers (B4S4 at 4 and 13 kDa), and two methoxy PEG-thiol molecules (0.8 and 5 kDa). E7 was selected as the amine catalyst in this Step 2B PEGylation reaction because of its use in our lab for end-capping of PBAEs and its non-toxicity in our studies.[4] A trace amount of E7 (5% mol) was used to ensure PEGylation occurred and not E7-endcapping.

Because end-capping reactions involve a nucleophilic addition to acrylates, the completion of end-capping can be confirmed using ^{1}H NMR. Once the diacrylates on the base polymer (**Figure 2.3A/B**) reacted with (E) molecules to yield ePBAE or with methoxy PEG-thiol molecules to yield PEG-PBAE (**Figure 2.3C**), the signature peaks for protons on acrylates disappeared, verifying that every base polymer in the reaction was completely end-capped.

Preparation and characterization of PEG-PBAE polyplexes

Polyplexes are formulated via electrostatic interaction between cationic polymer and negatively charged DNA. Thus, N/P ratio, the ratio of amines in the polymer (N, positively charged) to phosphates in the DNA (P, negatively charged), is an important parameter for

polyplex formulation. N/P ratio can also be converted to the total or the effective weight-to-weight ratio (w/w) between the polymer and the DNA, or vice versa, as long as the amine density and molecular weight are known. The total polymer:DNA w/w ratios that were used are converted to the effective PBAE:DNA w/w ratios and N/P ratios in **Table 2.2**. For PEG-PBAE polyplexes, ePBAE was also blended in with PEG-PBAE, and their weight to weight ratio was added as another parameter.

Polyplex stability over time was investigated with both nanoparticle tracking analysis (NTA) and dynamic light scattering (DLS) by measuring the increase in particle size over 24 h. While NTA directly measures the number-averaged hydrodynamic diameter, DLS reports an intensity-weighted average that is skewed towards larger or aggregated particles.[29,30] Polyplex formulations that yielded significant aggregation or decomplexation as indicated by low particle concentration on NTA or large particle size over the detection limit on DLS were eliminated from further consideration as candidate gene delivery formulations (**Figure 2.4A**). PBAE polyplex size of 447 60 w/w was similar to that reported in previous literature.[31] Four formulation conditions, indicated by red arrows, showed an initial particle size of 90–110 nm and minimal aggregation over time by NTA in 25 mM sodium acetate buffer. These small polyplex formulations were ePBAE blended with 5k-4k 1:2 30 w/w, 5k-4k 1:1 30 w/w, 5k-13k 1:2 30 w/w, and 5k-13k 1:1 30 w/w, and they were selected for subsequent transfection evaluation. A similar trend was observed when PEG-PBAE polyplexes are formulated with another ePBAE, 457 (**Figure 2.5**). While polyplexes with PEG-PBAE polymer synthesized from 4 kDa PBAE base polymer significantly aggregated over time in PBS, polyplexes with PEG-PBAE polymer synthesized from 13 kDa PBAE base polymer remained nanosized (~300 nm) after 24 h incubation in PBS. All four formulations

showed a slight decrease in surface charge to +7 mV in NaAc, although not statistically significant, in comparison to 447 60 w/w PBAE polyplexes (**Figure 2.4B**). When the PEG-PBAE polyplexes was sized in artificial cerebrospinal fluid (ACSF), formulations of 447 ePBAE blended with 0.8k-6k at 2:1, 1:1, and 1:2 30 w/w showed an extended period of stability between 2 h and 5 h in comparison to 447 60 w/w alone or blended with other PEG-PBAE polymer (**Figure 2.6**). Maintaining small size until 5 h can be critical, as the polyplexes may still diffuse through the tumor tissue during the first hours post-injection. Beyond that, the polyplexes may disintegrate due to polymer degradation or be cleared out of the tissue through the body's natural mechanism.

High-throughput evaluation of uptake, transfection and cytotoxicity

High-throughput evaluation was sequentially performed at two levels to select the most optimized polyplex formulation based on uptake and transfection of polyplexes in H446, BTIC375, and GBM1A cells. For SCLC, PBAE polyplexes formed with 9 different ePBAEs were initially tested to select the best ePBAE polymer that would be blended with PEG-PBAE polymers in the subsequent screening. As shown in **Figure 2.7B**, ePBAEs with more hydrophobic base polymer generally formed polyplexes with higher cytotoxicity to H446 cells, evidenced by B5S5 polyplexes leaving no viable cells 48 h after transfection. Higher H446 cellular uptake of ePBAE polyplexes with B4S5 base polymer did not result in a higher transfection rate than those with B4S4 base polymer, possibly due to different endocytosis pathways or rate-limiting downstream steps (**Figure 2.7A/C, 2.8**).[18] Top performing ePBAEs 444, 446, 447, and 457 with cell viability over 80% and transfection

efficacies of 60–75% were blended into four selected PEG-PBAE polyplex formulations for subsequent evaluation.

As anticipated due to the shielding properties of PEG, the H446 cellular uptake and transfection efficacy of PEG-PBAE polyplexes significantly decreased in comparison to unPEGylated PBAE polyplexes (**Figure 2.9A/C, 2.8**). Among PEG-PBAE polyplexes, formulation with 5k-4k polymer generally resulted in higher uptake efficacy than that with 5k-13k polymer, which is consistent with the enhanced particle stability of 5k-13k polyplexes (**Figure 2.4A/B**), potentially from greater PEG shielding, limiting the polyplexes' interaction with the cell membrane. However, transfection efficacies of PEG-PBAE polyplexes formed with 5k-4k and 5k-13k polymer at 1:1 30 w/w condition were similar, indicating polyplexes with 5k-13k polymer more efficiently deliver the DNA cargo to the nucleus to be transcribed following endocytosis. Also, PEG-PBAE polyplexes blended with 457 ePBAE resulted in the highest SCLC uptake and transfection overall, which is comparable to the results from PBAE polyplex screening. This may be due to hydrophobicity of 457 that allows for stronger condensation and more stable particles. Specifically, PEG-PBAE polyplex formed from 457 blended with 5k-13k at 1:1 30 w/w condition was internalized in 30% of H446 cells, and transfected 40%. The higher measured transfection rate compared to the measured uptake rate is likely due to the lower sensitivity of measuring successful cellular uptake compared to successful gene expression (expressed plasmid leads to an amplified GFP florescence signal compared to the fluorescence signal from the labeled plasmid itself). This formulation also showed second highest geometric mean GFP fluorescence intensity, which is an indicator of the amount of protein expressed by the transgene per cell (**Figure 2.10**).

For BTIC375 and GBM1A, five ePBAEs were tested (**Figure 2.11A/B, 2.12A/B**) for the initial screen to select the best transfecting polymer. Interestingly, more hydrophobic ePBAEs with B4S5 base polymer and with E7 or E3 end-groups showed lowest cell viability in both BTIC375 and GBM1A. However, 447 and 457 gave the highest transfection efficacy, in terms of both % of cells and geometric mean fluorescence, again in both cell types. Based on the result with H446 that blending of PEG-PBAE to ePBAE can reduce cytotoxicity, we selected 447 and 457 for subsequent PEG-PBAE polyplex screening despite ePBAE's toxicity due to the high transfection efficacy. As shown in **Figure 2.11C-E**, we observed tolerable cell viability in a few formulations with BTIC375, including 447 blended with 0.8k-13k 1:2 45 w/w or with 0.8k-4k 1:2 90 w/w. These formulations also resulted in 70-80% transfection efficacy, which is comparable to that of 447 ePBAE alone. Surprisingly, there was a decrease in cell viability for GBM1A with some formulations of PEG-PBAE polyplex, such as 2k-5k 2:1 60 w/w and 90 w/w (**Figure 2.12C**). Polyplexes composed of 447 blended with 0.8k-5k PEG-PBAE polymers did not cause cytotoxicity, and 447 + 0.8k-5k 2:1 60 w/w formulation showed transfection efficacy of approximately 27% (**Figure 2.12D**). It is important to note that two distinct PEG-PBAE polyplexes had optimal cell viability and transfection for each of the cell types that are present in glioblastoma tissue. This suggests that the ideal therapeutic approach could be a combination of the two polyplexes to attack both fully differentiated and stem-like brain tumor cells.

Therapeutic activity against small cell lung cancer with PEG-PBAE/pHSV-tk polyplexes and ganciclovir

Ganciclovir is a widely investigated prodrug of interest for suicide gene therapy for different types of cancer.[4,32,33] The nontoxic ganciclovir prodrug is phosphorylated into ganciclovir triphosphate by the HSV-tk gene product, which then disrupts DNA replication and causes cell death.[34,35] We examined PEG-PBAE polyplexes as a functional vehicle for small cell lung cancer gene therapy by delivering PEG-PBAE/pHSV-tk polyplexes followed by ganciclovir treatment. The optimal PEG-PBAE polyplex formulation 457 + 5k-13k 1:1 30 w/w was chosen and was compared to 457 60 w/w PBAE polyplexes for transfection of both H446 human small cell lung cancer cells and IMR-90 human lung fibroblasts as a healthy control cell type. PBAE and PEG-PBAE polyplexes were able to kill 60% and 35% of cancer cells, respectively (**Figure 2.13A**). Interestingly, the level of cell death induced by two types of polyplexes correlated closely with their EGFP transfection efficacies of 73% and 43% (**Figure 2.7A and 2.9A**), but not with their EGFP geometric mean intensities of 170,000 and 4000 RFUs (**Figure 2.10**). The expression of HSV-tk, followed by treatment with ganciclovir, is expected to cause death of the transfected cell. A twofold increase of the ganciclovir dosage had negligible effect on cell death, demonstrating that the exogenous gene expression of HSV-tk was the limiting factor determining cell killing.

The same PEG-PBAE and PBAE polyplexes showed different outcomes with IMR-90 human lung fibroblasts. First, polyplexes formed with 457 ePBAE complexed with pEGFP at 60 w/w had significant inherent cytotoxicity of 50% (**Figure 2.13B**). This demonstrates the potential fragility of healthy human cells and the need for biocompatible, non-cytotoxic formulations. This concern with potential PBAE polyplex cytotoxicity is resolved when 457 ePBAE is blended with 5k-13k at 1:1 ratio, as evidenced by near 100% viability from pEGFP as well as pHSV-tk + 0 μg/mL ganciclovir controls. This reduced

cytotoxicity is likely due to a combination of less 457 ePBAE being used to form PEG-PBAE polyplexes in comparison to non-PEGylated PBAE polyplexes of the same total w/w and due to PEG molecules shielding potentially unfavorable interaction between surface-exposed positively charged 457 and cellular components. In addition, the same PEG-PBAE/HSV-tk DNA polyplexes + ganciclovir system is more specific in promoting killing of human lung cancer H446 cells than healthy human lung IMR-90 fibroblasts with statistical significance ($p < 0.01$); 35% of H446 cells and 15% of IMR-90 cells are killed at the 10 μg/mL ganciclovir dosage. Overall, these results show the potential of stable and effective PEG-PBAE polyplexes for lung cancer gene therapy.

Brain tumor tissue penetration following local injection in vivo

We next investigated the ability of PEG-PBAE polyplexes to diffuse through the dense tumor tissue following injection, which would allow greater affected (transfected) area and effective inhibition of tumor growth or even recession. The presence of PEG on the surface of nanoparticles enhances diffusivity because it allows neutral surface with steric hindrance to prevent particle aggregation as well as non-specific adsorption of serum proteins. As a preliminary study, Cy5-labeled PEG-PBAE polyplex composed of 447 and 0.8k-13k 1:2 45 w/w was injected directly into the orthotopic BTIC375 tumor in the brain and the spread was imaged on histological sections. As shown by the representative image in **Figure 2.14**, PEG-PBAE polyplexes were able to diffuse further from the injection site over 24 h period than 447 30 w/w PBAE polyplexes. This demonstrates the utility of safe PEG-PBAE polyplexes to penetrate and target wider area of diseased tissue.

2.4 Discussion

Nanoparticles, including polyplexes that are formed by electrostatic interaction between cationic polymer and negatively charged nucleic acids, that are intended to be used for systemic administration, need to overcome challenges of destabilization in physiological saline, adsorption of serum proteins, and aggregation post-administration, which all can lead to rapid clearance from the blood. Furthermore, colloidal stability at sub-400 nm diameter is critical for nanoparticles in cancer therapy to utilize passive targeting to tumors and their leaky vasculature via the enhanced permeation and retention (EPR) effect.[25,36] In addition, these nanoparticles must be able to enter and diffuse into the tumor tissue to effectively target greater number of cancer cells. A new copolymer synthesized by conjugating the hydrophilic molecule PEG to selected PBAE base polymers provided steric hindrance to the resulting PEG-PBAE polyplexes that minimized particle aggregation and maintained an effective size for the EPR effect and enhanced diffusivity.

When formulating both PBAE and PEG-PBAE polyplexes, the N/P ratios used are relatively high in comparison to polyplexes of different polymers, such as PEI (**Table 2.2**). Non-degradable PEI, with its high charge density, becomes cytotoxic at higher N/P ratios unless it is modified with degradable moieties.[37,38] Two features of the PBAE chemical structure allows for polyplexes with much higher N/P ratios. Firstly, PBAE has repeated ester bonds along its backbone and hence is hydrolytically degradable into small bioeliminable units and thus much higher w/w ratios can be utilized.[19] Secondly, most of PBAEs' positive charge is from tertiary amines, some of which are not protonated in the physiological range of pH 5.1–7.4.[19] Thus, N/P ratio is a function of pH and not the necessarily the same as the

ratio of positive charges to negative charges within the polyplexes. This pH dependence of the PBAE polyplexes' charge is an important feature as it provides pH buffering capacity, protecting DNA in endosomes and promoting endosomal escape consistent with the proton sponge hypothesis, enabling successful transfection.[39]

PEG-PBAE polyplexes have ePBAE blended in at different mass ratios of ePBAE to PEG-PBAE. Although PEG-PBAE polymer has tertiary amines along the backbone that can be protonated and associate with the DNA, the end-group structure of ePBAE has been implicated to serve important and complimentary functions. For example, different end-groups were found to regulate specific uptake mechanisms and downstream steps leading to successful transfection.[18,19] PEGylating polyplexes of various polymers has been shown to affect cellular uptake and intracellular trafficking significantly,[40] often reducing cellular uptake and gene delivery efficacy *in vitro*. While residual positive charge on the surface can contribute to particle-cell interaction, the presence and exposure of select ePBAE in PEG-PBAE polyplexes can promote cellular uptake via specific pathways that leads to greater transfection.

457 ePBAE, which was selected from high-throughput screening of H446 SCLC cells to be blended into PEG-PBAE polyplexes, yielded results that were in agreement to previous literature, which showed high *in vivo* efficacy of 457 PBAE polyplexes in a subcutaneous H446 xenograft mice model.[41] Interestingly, the PEG-PBAE polyplexes used against H446 small cell lung cancer cells were able to kill cancer cells more than IMR-90 lung fibroblasts through HSV-tk/ganciclovir treatment. This cancer cell selectivity in efficacy is possibly due to a higher doubling rate of cancer cells than fibroblasts, since ganciclovir phosphorylated by HSV-tk kills cells by disrupting DNA replication in actively dividing cells.[34] However,

another potential explanation is cancer specificity of the ePBAE polymer. Our group has previously shown that specific ePBAE structure (including the (3-Aminopropyl)-4-methylpiperazine (E7) end-group) leads to increased transfection in various tumor cells in comparison to the healthy cells in the same tissue [3,42] including glioblastoma. This is also in concert with our finding that 447 ePBAE has the highest transfection efficacy amongst ePBAEs tested against BTIC375 and GBM1As. Intriguingly, this ePBAE polyplex cancer cell transfection specificity with E7 is evident in corresponding tumor and non-tumor primary cell samples that show the same cell doubling time and have the same percentage of polyplex cellular uptake.[3]

Since the current PEG-PBAE polyplexes do not have an active targeting functionality, further modification for cancer targeting, such as conjugation of a targeting ligand to the polymer and/or insertion of a cancer-specific promoter in the plasmid DNA, can further enhance their therapeutic efficiency in cancer therapy.[43] This work demonstrates an important step in the design of non-viral vectors that utilize the PBAE platform. Through the synthesis of new PEGylated PBAE polymers and new PEG-PBAE/ePBAE formulations via combinatorial approach, stability was enhanced and non-specific cytotoxicity was prevented. Our PEG-PBAE polyplexes are anticipated to show enhanced *in vivo* functional efficacy due to two main effects: bioavailability and cellular transfection. PEGylation of PBAE polyplexes may enhance diffusion in the tissue, as shown through our *in vivo* finding, and pharmacokinetics in the systemic circulation. Also, a blend of best performing ePBAE in PEG-PBAE polyplex may also allow for cell specificity, efficient cellular uptake, and transfection, thereby overcoming the “PEG dilemma.”

2.5 Conclusion

PBAEs are a class of cationic polymers that has been shown to transfect a wide range of cell types with high efficiency. In an effort to make more stable PBAE polyplexes, we synthesized PEG-PBAEs using thiol-ene Michael addition reaction and fabricated new polyplexes with blends of PEG-PBAEs and ePBAEs. After selecting the best performing ePBAEs through screening against cytotoxicity and transfection in small cell lung cancer cells (H446) and glioblastoma cells (BTIC375 and GBM1A), PEG-PBAE polyplexes of varying conditions, including PEG-PBAE molecular weight, mass ratios of ePBAE to PEG-PBAE, and total polymer to DNA mass ratios, were further evaluated for nanoparticle size, stability, cytotoxicity and transfection efficacy. Optimal PEG-PBAE formulation maintained its size under 300 nm over 24 h in physiological PBS or over 5 h in artificial cerebrospinal fluid and transfected cancer cells at the level comparable to ePBAE formulation. When human lung cancer cells were transfected with HSV-tk using the optimized PEG-PBAE polyplex and subsequently treated with ganciclovir, 35% of the cells were killed in contrast to 15% cell death to healthy human lung fibroblasts (IMR-90). The present study used a novel method to synthesize PEG-PBAE polymer and to formulate stable polyplexes that do not exhibit biomaterial-based cytotoxicity, can successfully transfect cancer cells, and can induce their death via HSV-tk/ganciclovir prodrug gene therapy.

2.6 References

(1) Rodriguez, E.; Lilenbaum, R. C., Small cell lung cancer: Past, present, and future. *Curr Oncol Rep* **2010,** 12, (5), 327-34.

(2) Paumier, A.; Le Pechoux, C., Radiotherapy in small-cell lung cancer: Where should it go? *Lung Cancer* **2010,** 69, (2), 133-40.

(3) Guerrero-Cazares, H.; Tzeng, S. Y.; Young, N. P.; Abutaleb, A. O.; Quinones-Hinojosa, A.; Green, J. J., Biodegradable polymeric nanoparticles show high efficacy and specificity at DNA delivery to human glioblastoma in vitro and in vivo. *ACS Nano* **2014,** 8, (5), 5141-53.

(4) Mangraviti, A.; Tzeng, S. Y.; Kozielski, K. L.; Wang, Y.; Jin, Y.; Gullotti, D.; Pedone, M.; Buaron, N.; Liu, A.; Wilson, D. R.; Hansen, S. K.; Rodriguez, F. J.; Gao, G. D.; DiMeco, F.; Brem, H.; Olivi, A.; Tyler, B.; Green, J. J., Polymeric nanoparticles for nonviral gene therapy extend brain tumor survival in vivo. *ACS Nano* **2015,** 9, (2), 1236-49.

(5) Jackson, M.; Hassiotou, F.; Nowak, A., Glioblastoma stem-like cells: At the root of tumor recurrence and a therapeutic target. *Carcinogenesis* **2015,** 36, (2), 177-85.

(6) Brade, A. M.; Tannock, I. F., Scheduling of radiation and chemotherapy for limited-stage small-cell lung cancer: Repopulation as a cause of treatment failure? *J Clin Oncol* **2006,** 24, (7), 1020-2.

(7) Siegel, R.; Naishadham, D.; Jemal, A., Cancer statistics, 2012. *CA Cancer J Clin* **2012,** 62, (1), 10-29.

(8) Lang, F. F.; Bruner, J. M.; Fuller, G. N.; Aldape, K.; Prados, M. D.; Chang, S.; Berger, M. S.; McDermott, M. W.; Kunwar, S. M.; Junck, L. R.; Chandler, W.; Zwiebel, J. A.; Kaplan, R. S.; Yung, W. K., Phase i trial of adenovirus-mediated p53 gene therapy for recurrent glioma: Biological and clinical results. *J Clin Oncol* **2003,** 21, (13), 2508-18.

(9) Wang, S.; El-Deiry, W. S., Trail and apoptosis induction by tnf-family death receptors. *Oncogene* **2003,** 22, (53), 8628-33.

(10) Moolten, F. L., Tumor chemosensitivity conferred by inserted herpes thymidine kinase genes: Paradigm for a prospective cancer control strategy. *Cancer Res* **1986,** 46, (10), 5276-81.

(11) Hollon, T., Researchers and regulators reflect on first gene therapy death. *Am J Ophthalmol* **2000,** 129, (5), 701.

(12) Pack, D. W.; Hoffman, A. S.; Pun, S.; Stayton, P. S., Design and development of polymers for gene delivery. *Nat Rev Drug Discov* **2005,** 4, (7), 581-93.

(13) Anderson, D. G.; Akinc, A.; Hossain, N.; Langer, R., Structure/property studies of polymeric gene delivery using a library of poly(beta-amino esters). *Mol Ther* **2005,** 11, (3), 426-34.

(14) Bhise, N. S.; Wahlin, K. J.; Zack, D. J.; Green, J. J., Evaluating the potential of poly(beta-amino ester) nanoparticles for reprogramming human fibroblasts to become induced pluripotent stem cells. *Int J Nanomedicine* **2013,** 8, 4641-58.

(15) Cho, S. W.; Yang, F.; Son, S. M.; Park, H. J.; Green, J. J.; Bogatyrev, S.; Mei, Y.; Park, S.; Langer, R.; Anderson, D. G., Therapeutic angiogenesis using genetically engineered human endothelial cells. *J Control Release* **2012,** 160, (3), 515-24.

(16) Tzeng, S. Y.; Green, J. J., Subtle changes to polymer structure and degradation mechanism enable highly effective nanoparticles for sirna and DNA delivery to human brain cancer. *Adv Healthc Mater* **2013,** 2, (3), 468-80.

(17) Vandenbroucke, R. E.; De Geest, B. G.; Bonne, S.; Vinken, M.; Van Haecke, T.; Heimberg, H.; Wagner, E.; Rogiers, V.; De Smedt, S. C.; Demeester, J.; Sanders, N. N., Prolonged gene silencing in hepatoma cells and primary hepatocytes after small

interfering rna delivery with biodegradable poly(beta-amino esters). *J Gene Med* **2008,** 10, (7), 783-94.

(18) Kim, J.; Sunshine, J. C.; Green, J. J., Differential polymer structure tunes mechanism of cellular uptake and transfection routes of poly(beta-amino ester) polyplexes in human breast cancer cells. *Bioconjug Chem* **2014,** 25, (1), 43-51.

(19) Sunshine, J. C.; Peng, D. Y.; Green, J. J., Uptake and transfection with polymeric nanoparticles are dependent on polymer end-group structure, but largely independent of nanoparticle physical and chemical properties. *Mol Pharm* **2012,** 9, (11), 3375-83.

(20) Harris, T. J.; Green, J. J.; Fung, P. W.; Langer, R.; Anderson, D. G.; Bhatia, S. N., Tissue-specific gene delivery via nanoparticle coating. *Biomaterials* **2010,** 31, (5), 998-1006.

(21) Shen, Y.; Tang, H.; Zhan, Y.; Van Kirk, E. A.; Murdoch, W. J., Degradable poly(beta-amino ester) nanoparticles for cancer cytoplasmic drug delivery. *Nanomedicine* **2009,** 5, (2), 192-201.

(22) Shenoy, D.; Little, S.; Langer, R.; Amiji, M., Poly(ethylene oxide)-modified poly(beta-amino ester) nanoparticles as a ph-sensitive system for tumor-targeted delivery of hydrophobic drugs. 1. In vitro evaluations. *Mol Pharm* **2005,** 2, (5), 357-66.

(23) Harris, J. M.; Chess, R. B., Effect of pegylation on pharmaceuticals. *Nat Rev Drug Discov* **2003,** 2, (3), 214-21.

(24) Owens, D. E., 3rd; Peppas, N. A., Opsonization, biodistribution, and pharmacokinetics of polymeric nanoparticles. *Int J Pharm* **2006,** 307, (1), 93-102.

(25) Hatakeyama, H.; Akita, H.; Harashima, H., A multifunctional envelope type nano device (mend) for gene delivery to tumours based on the epr effect: A strategy for overcoming the peg dilemma. *Adv Drug Deliv Rev* **2011,** 63, (3), 152-60.

(26) Ge, Z.; Chen, Q.; Osada, K.; Liu, X.; Tockary, T. A.; Uchida, S.; Dirisala, A.; Ishii, T.; Nomoto, T.; Toh, K.; Matsumoto, Y.; Oba, M.; Kano, M. R.; Itaka, K.; Kataoka, K., Targeted gene delivery by polyplex micelles with crowded peg palisade and crgd moiety for systemic treatment of pancreatic tumors. *Biomaterials* **2014,** 35, (10), 3416-26.

(27) Williford, J. M.; Archang, M. M.; Minn, I.; Ren, Y.; Wo, M.; Vandermark, J.; Fisher, P. B.; Pomper, M. G.; Mao, H. Q., Critical length of peg grafts on lpei/DNA nanoparticles for efficient in vivo delivery. *ACS Biomater Sci Eng* **2016,** 2, (4), 567-578.

(28) Vandenbergh, J. R., K.; Junkers, T., Synthesis of (bio)-degradable poly(beta-thioester)s via amine catalyzed thiol-ene click polymerization. *Macromol Chem Phys* **2012,** 213, 2611-2617.

(29) Filipe, V.; Hawe, A.; Jiskoot, W., Critical evaluation of nanoparticle tracking analysis (nta) by nanosight for the measurement of nanoparticles and protein aggregates. *Pharm Res* **2010,** 27, (5), 796-810.

(30) Nobbmann, U. M., A., Light scattering and nanoparticles. *Mater Today* **2009,** 12, 52-54.

(31) Bhise, N. S.; Gray, R. S.; Sunshine, J. C.; Htet, S.; Ewald, A. J.; Green, J. J., The relationship between terminal functionalization and molecular weight of a gene delivery polymer and transfection efficacy in mammary epithelial 2-d cultures and 3-d organotypic cultures. *Biomaterials* **2010,** 31, (31), 8088-96.

(32) Boucher, P. D.; Ruch, R. J.; Shewach, D. S., Differential ganciclovir-mediated cytotoxicity and bystander killing in human colon carcinoma cell lines expressing herpes simplex virus thymidine kinase. *Hum Gene Ther* **1998,** 9, (6), 801-14.

(33) Shalev, M.; Kadmon, D.; Teh, B. S.; Butler, E. B.; Aguilar-Cordova, E.; Thompson, T. C.; Herman, J. R.; Adler, H. L.; Scardino, P. T.; Miles, B. J., Suicide gene therapy toxicity after multiple and repeat injections in patients with localized prostate cancer. *J Urol* **2000,** 163, (6), 1747-50.

(34) Rubsam, L. Z.; Boucher, P. D.; Murphy, P. J.; KuKuruga, M.; Shewach, D. S., Cytotoxicity and accumulation of ganciclovir triphosphate in bystander cells cocultured with herpes simplex virus type 1 thymidine kinase-expressing human glioblastoma cells. *Cancer Res* **1999,** 59, (3), 669-75.

(35) Tomicic, M. T.; Thust, R.; Kaina, B., Ganciclovir-induced apoptosis in hsv-1 thymidine kinase expressing cells: Critical role of DNA breaks, bcl-2 decline and caspase-9 activation. *Oncogene* **2002,** 21, (14), 2141-53.

(36) Steichen, S. D.; Caldorera-Moore, M.; Peppas, N. A., A review of current nanoparticle and targeting moieties for the delivery of cancer therapeutics. *Eur J Pharm Sci* **2013,** 48, (3), 416-27.

(37) Boeckle, S.; von Gersdorff, K.; van der Piepen, S.; Culmsee, C.; Wagner, E.; Ogris, M., Purification of polyethylenimine polyplexes highlights the role of free polycations in gene transfer. *J Gene Med* **2004,** 6, (10), 1102-11.

(38) Park, M. R.; Han, K. O.; Han, I. K.; Cho, M. H.; Nah, J. W.; Choi, Y. J.; Cho, C. S., Degradable polyethylenimine-alt-poly(ethylene glycol) copolymers as novel gene carriers. *J Control Release* **2005,** 105, (3), 367-80.

(39) Green, J. J.; Langer, R.; Anderson, D. G., A combinatorial polymer library approach yields insight into nonviral gene delivery. *Acc Chem Res* **2008,** 41, (6), 749-59.

(40) Mishra, S.; Webster, P.; Davis, M. E., Pegylation significantly affects cellular uptake and intracellular trafficking of non-viral gene delivery particles. *Eur J Cell Biol* **2004,** 83, (3), 97-111.

(41) Kamat, C. D.; Shmueli, R. B.; Connis, N.; Rudin, C. M.; Green, J. J.; Hann, C. L., Poly(beta-amino ester) nanoparticle delivery of tp53 has activity against small cell lung cancer in vitro and in vivo. *Mol Cancer Ther* **2013,** 12, (4), 405-15.

(42) Tzeng, S. Y.; Higgins, L. J.; Pomper, M. G.; Green, J. J., Student award winner in the ph.D. Category for the 2013 society for biomaterials annual meeting and exposition, april 10-13, 2013, boston, massachusetts : Biomaterial-mediated cancer-specific DNA delivery to liver cell cultures using synthetic poly(beta-amino ester)s. *J Biomed Mater Res A* **2013,** 101, (7), 1837-45.

(43) Kim, J.; Wilson, D. R.; Zamboni, C. G.; Green, J. J., Targeted polymeric nanoparticles for cancer gene therapy. *J Drug Target* **2015,** 23, (7-8), 627-41.

2.7 Figures & Tables

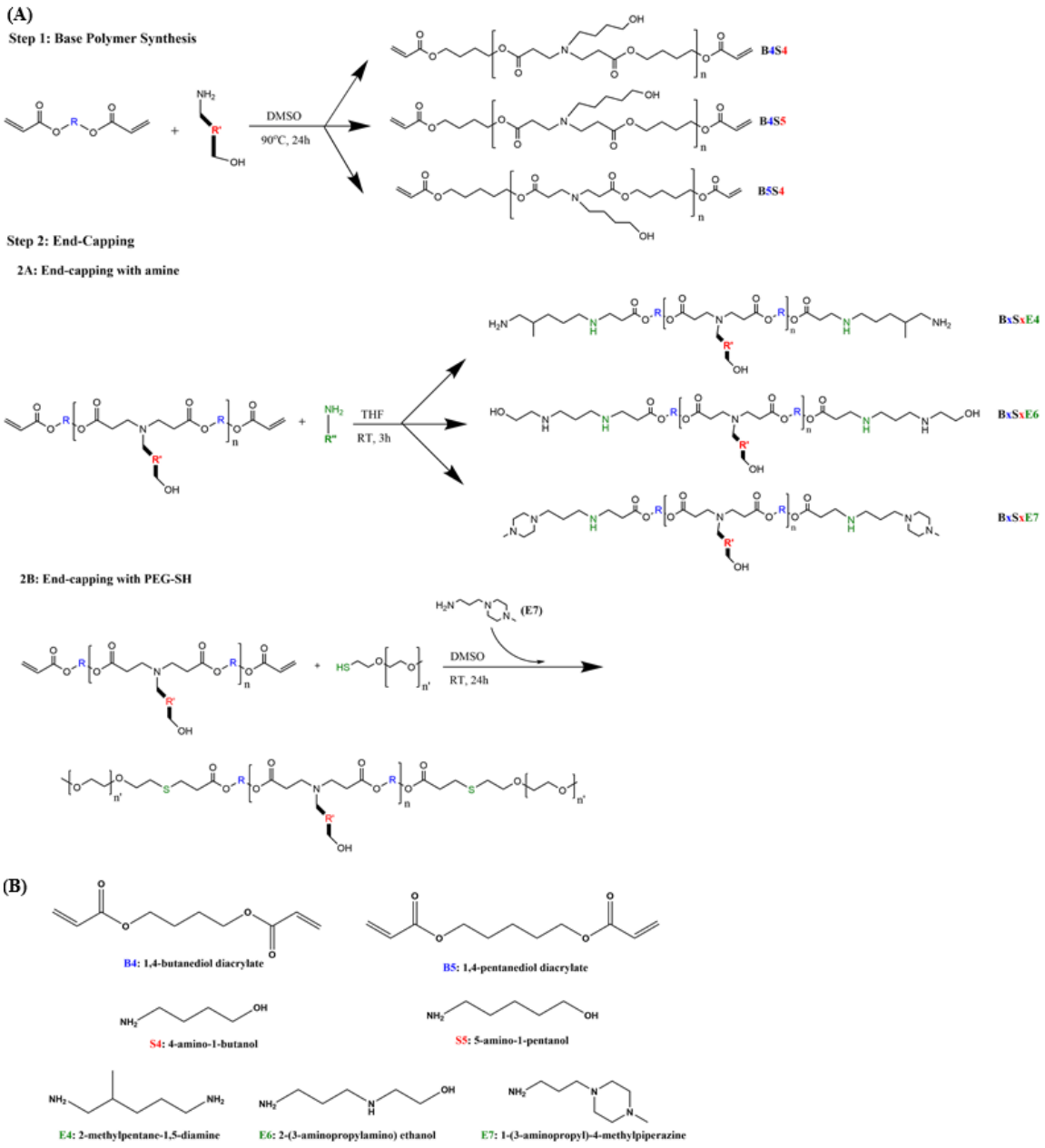

Figure 2.1. Polymer synthesis. (A) Synthesis scheme of conventionally end-capped poly(β-amino ester)s (ePBAEs) and poly(ethylene glycol)-co-poly(β-amino ester)s (PEG-PBAEs). (B) Chemical structures of monomers used.

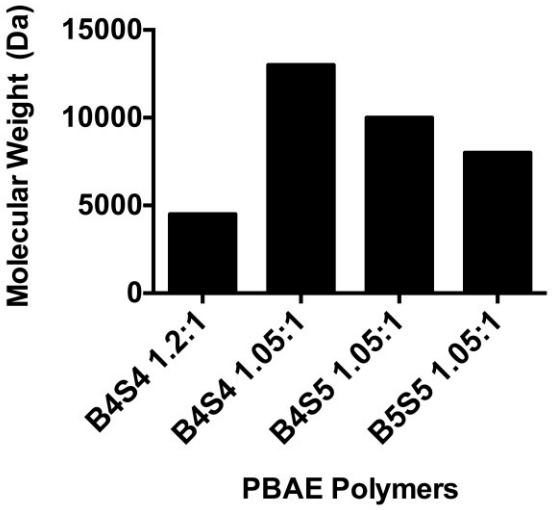

Figure 2.2. Polymer molecular weight. The molecular weights of four PBAE backbone polymers used to PEGylate or end-cap. Ratios are molar ratios of (B) to (S) monomers used during polymer synthesis. Molecular weights are determined using ^{1}H NMR spectrum by taking ratios of area under peaks.

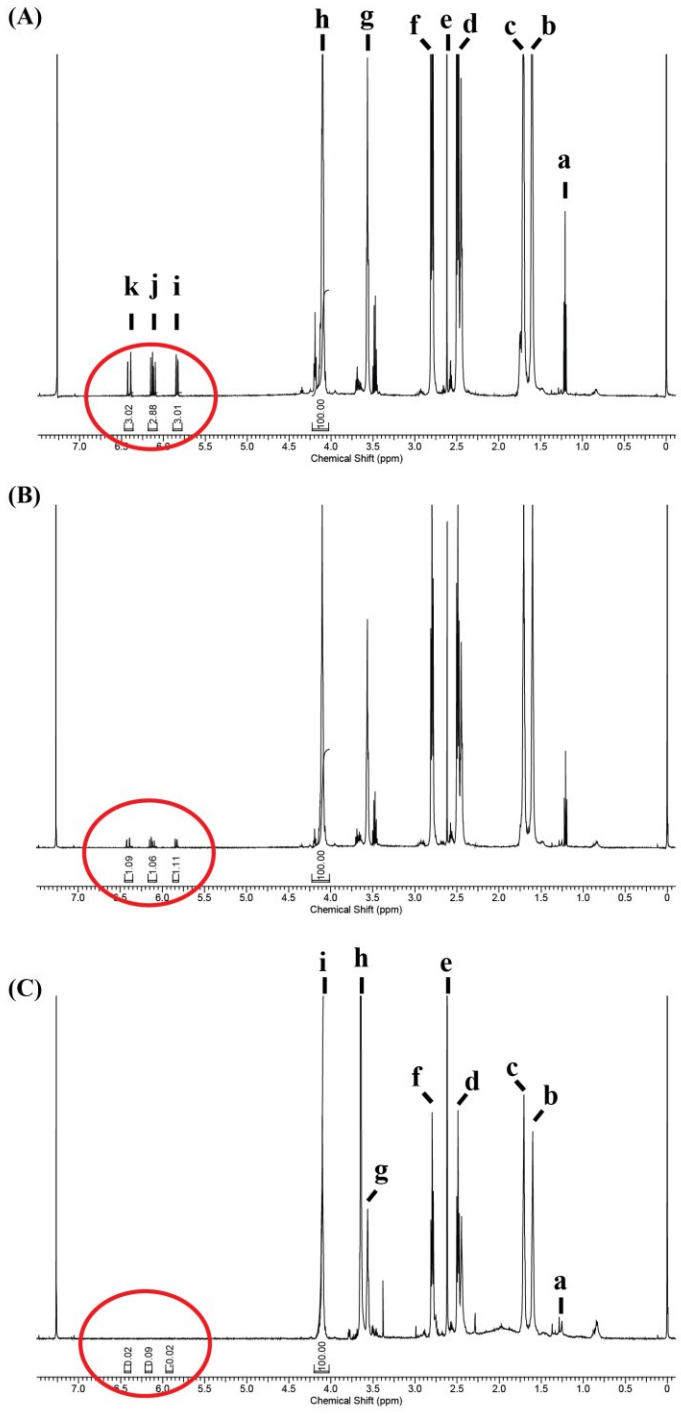
(A)
h
g
f
e
d
c
b
a
k
j
i
3.02
2.88
3.01
00.00
Chemical Shift (ppm)
(B)
0.09
1.06
1.11
00.00
Chemical Shift (ppm)
(C)
i
h
e
f
d
c
b
g
a
0.02
0.09
0.02
00.00
Chemical Shift (ppm)

Figure 2.3. ^{1}H NMR spectra of PBAE polymers. (A) B4S4 1.2:1, (B) B4S4 1.05:1, (C) B4S4 1.2:1 end-capped with PEG_{5k} to synthesize 5k-4k. The removal of acrylate peaks (shown by red circles) confirms the complete conjugation of PEG-SH molecule.

(A) and (B) B4S4

a: 1.2–1.35 (m, $NCH_2C\boldsymbol{H_2}CH_2CH_2OH$)
b: 1. 5-1.6 (m, $NCH_2CH_2C\boldsymbol{H_2}CH_2OH$)
c: 1.6-1.75 (t, $COOCH_2C\boldsymbol{H_2}C\boldsymbol{H_2}CH_2OOC$)
d: 2.35-2.6 (t, $NC\boldsymbol{H_2}CH_2CH_2CH_2OH$)
e: DMSO solvent
f: 2.7-2.85 (t, $COOC\boldsymbol{H_2}C\boldsymbol{H_2}NC\boldsymbol{H_2}C\boldsymbol{H_2}OOC$)
g: 3.55-3.7 (t, $NCH_2CH_2CH_2C\boldsymbol{H_2}OH$)
h: 4.0-4.2 (t, $COOC\boldsymbol{H_2}CH_2CH_2C\boldsymbol{H_2}OOC$)
i: 5.6-5.85 (dd, $COOCCHC\boldsymbol{H_2}$)
j: 6.0-6.25 (dd, $COOCC\boldsymbol{H}CH_2$)
k: 6.3-6.5 (dd, $COOCCHC\boldsymbol{H_2}$)

(C) PEG-B4S4-PEG

a: 1.2–1.35 (m, $NCH_2C\boldsymbol{H_2}CH_2CH_2OH$)
b: 1. 5-1.6 (m, $NCH_2CH_2C\boldsymbol{H_2}CH_2OH$)
c: 1.6-1.75 (t, $COOCH_2C\boldsymbol{H_2}C\boldsymbol{H_2}CH_2OOC$)
d: 2.35-2.6 (t, $NC\boldsymbol{H_2}CH_2CH_2CH_2OH$ and t, $COOC\boldsymbol{H_2}CH_2SC\boldsymbol{H_2}CH_2O$)
e: DMSO solvent
f: 2.7-2.85 (t, $COOCH_2C\boldsymbol{H_2}SCH_2CH_2O$ and t, $COOC\boldsymbol{H_2}C\boldsymbol{H_2}NC\boldsymbol{H_2}C\boldsymbol{H_2}OOC$)
g, h: 3.55-3.7 (t, $NCH_2CH_2CH_2C\boldsymbol{H_2}OH$ and s, $SCH_2C\boldsymbol{H_2}OC\boldsymbol{H_2}C\boldsymbol{H_2}OC\boldsymbol{H_3}$)
i: 4.0-4.2 (t, $COOC\boldsymbol{H_2}CH_2CH_2C\boldsymbol{H_2}OOC$)

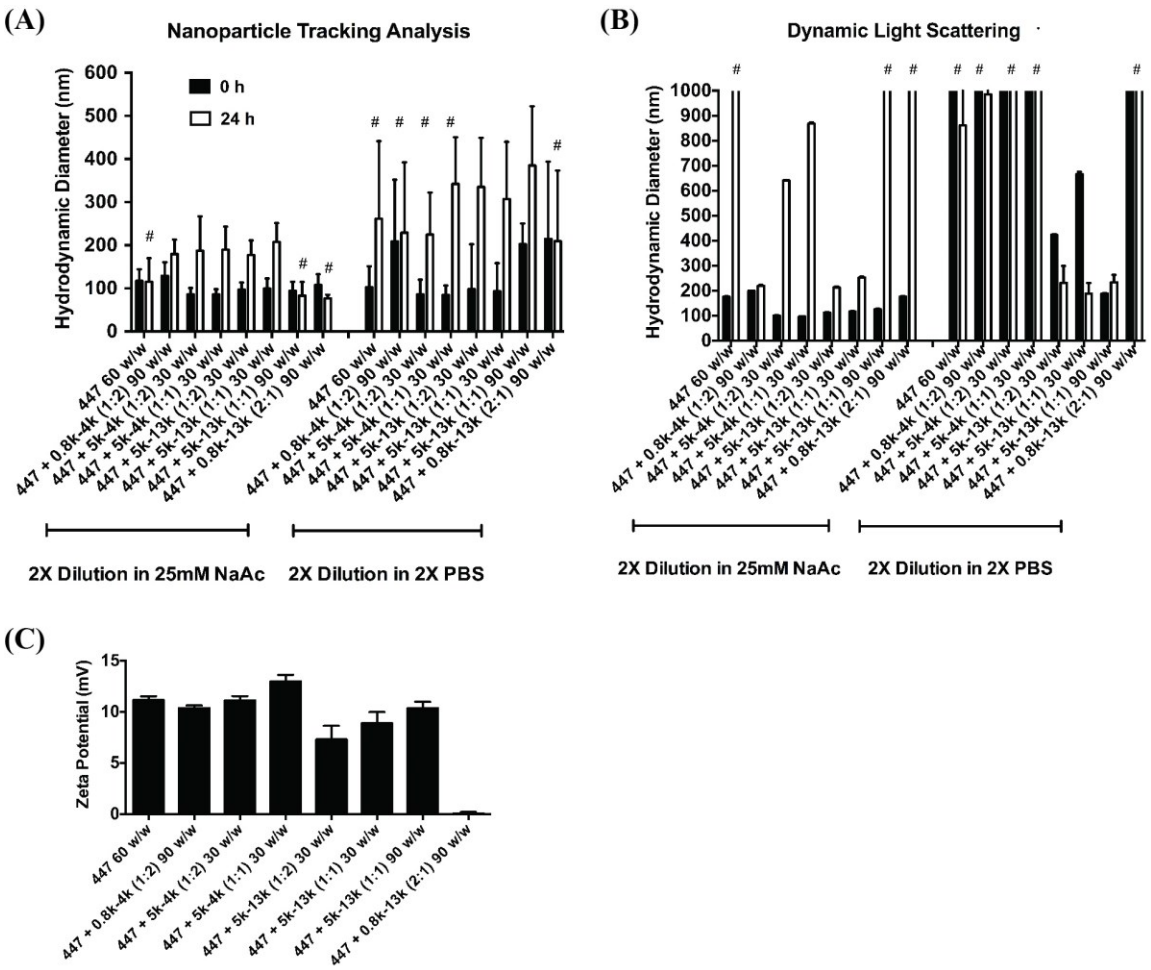

Figure 2.4. 447 ePBAE polyplex size stability and surface charge. (A) The size of polyplexes formed by self-assembly of enhanced green fluorescent protein (pEGFP) DNA with 447 alone or in combination with PEG-PBAE at various polymer:DNA and 447:PEG-PBAE w/w ratios. The stability of the polyplexes was tested by sizing them after a 24-h incubation in either sodium acetate or PBS at room temperature. #: Indicates formulation conditions where polyplex aggregation is occurring, leading to unreliable size measurements (low particle concentration by NTA or greater than a micron in size by DLS). (B) The zeta potential of polyplexes. Data are mean ± SD of particle population for NTA and mean ± SD of 3 independent measurements for DLS.

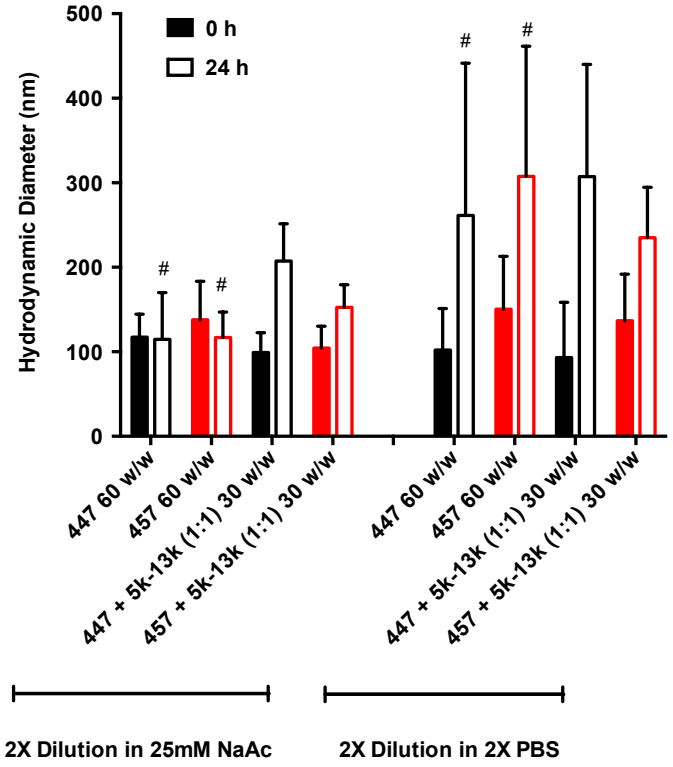

Figure 2.5. 457 vs. 447 ePBAE polyplex size stability. The NTA size measurement of polyplexes formed by self-assembly of enhanced green fluorescent protein (pEGFP) DNA with ePBAE 457 alone at 60 w/w or in combination with 5k-13k at 1:1 30 w/w, compared with polyplexes formed with ePBAE 447. The stability of the polyplexes was tested by sizing them after a 24-h incubation in either sodium acetate or PBS at room temperature. #: Indicates formulation conditions where polyplex aggregation is occurring, leading to unreliable size measurements (low particle concentration by NTA).

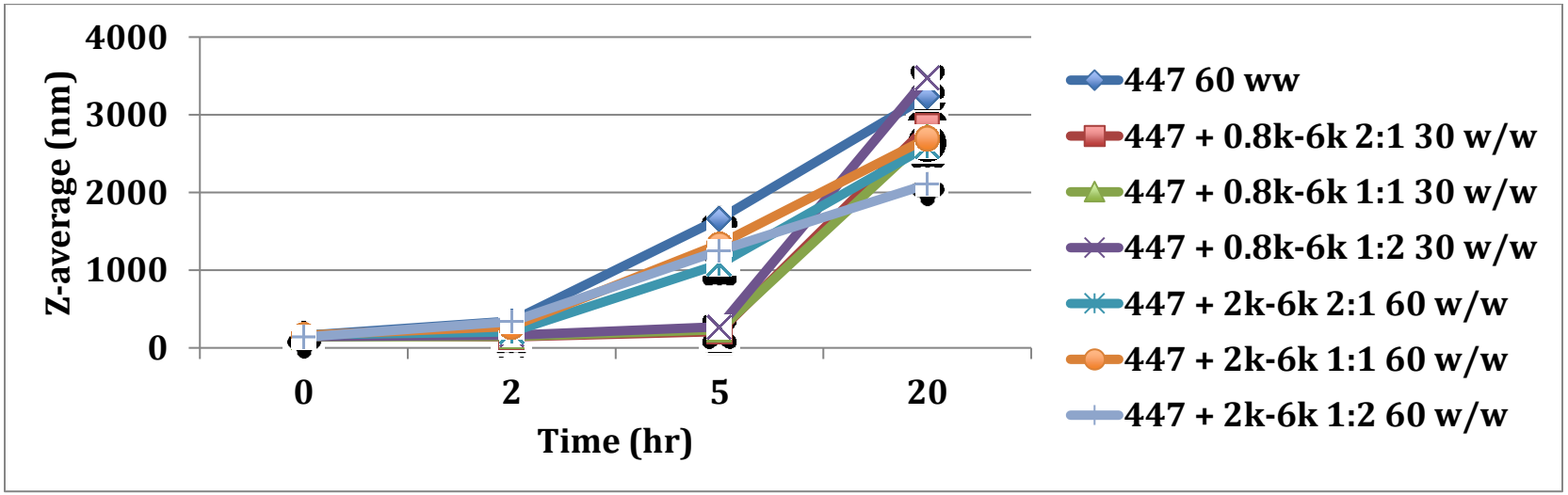

Figure 2.6. ePBAE and PEG-PBAE polyplex size stability in artificial cerebrospinal fluid. The size of polyplexes formed by self-assembly of enhanced green fluorescent protein (pEGFP) DNA with 447 alone or in combination with PEG-PBAE at various polymer:DNA and 447:PEG-PBAE w/w ratios. The stability of the polyplexes was tested by sizing them at 0, 2, 5, and 20 h time points following incubation in artificial cerebrospinal fluid.

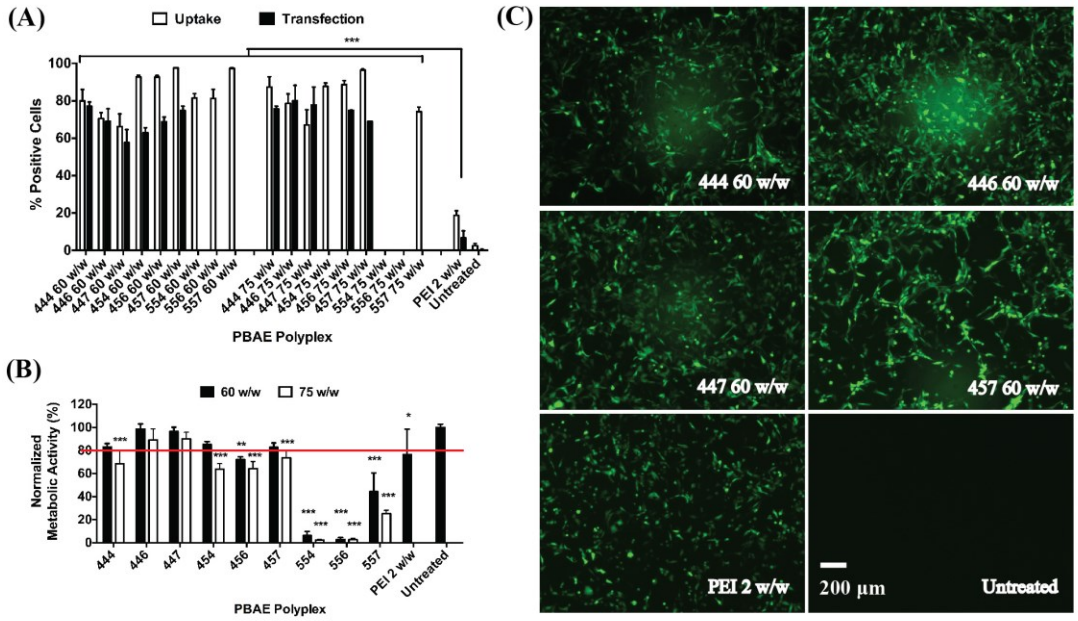

Figure 2.7. ePBAE polyplex uptake, transfection, and cytotoxicity screening on H446. (A) Flow cytometry data showing the uptake and transfection efficacy of nine PBAE polyplexes in H446 cells at 4 hrs and 2 days post-transfection, respectively. The efficiency is in terms of percentage of live H446 cells positive for Cy3 (uptake) or EGFP (transfection). Efficacy of ePBAEs is compared to that of polyethylenimine (PEI) 2 w/w. Data are mean ± SD (n=4) (*** $p < 0.001$ compared to untreated). (B) Cytotoxicity of PBAE polyplexes, quantified by normalizing metabolic activity to untreated cells. Data are mean ± SD (n=3) (*** $p < 0.001$, ** $p < 0.01$, * $P < 0.05$ compared to untreated). (C) Representative fluorescence microscope images (10x) of H446 cells transfected with 4 different PBAE polyplexes at 60 w/w and controls. Scale bar is 200 μm for all panels.

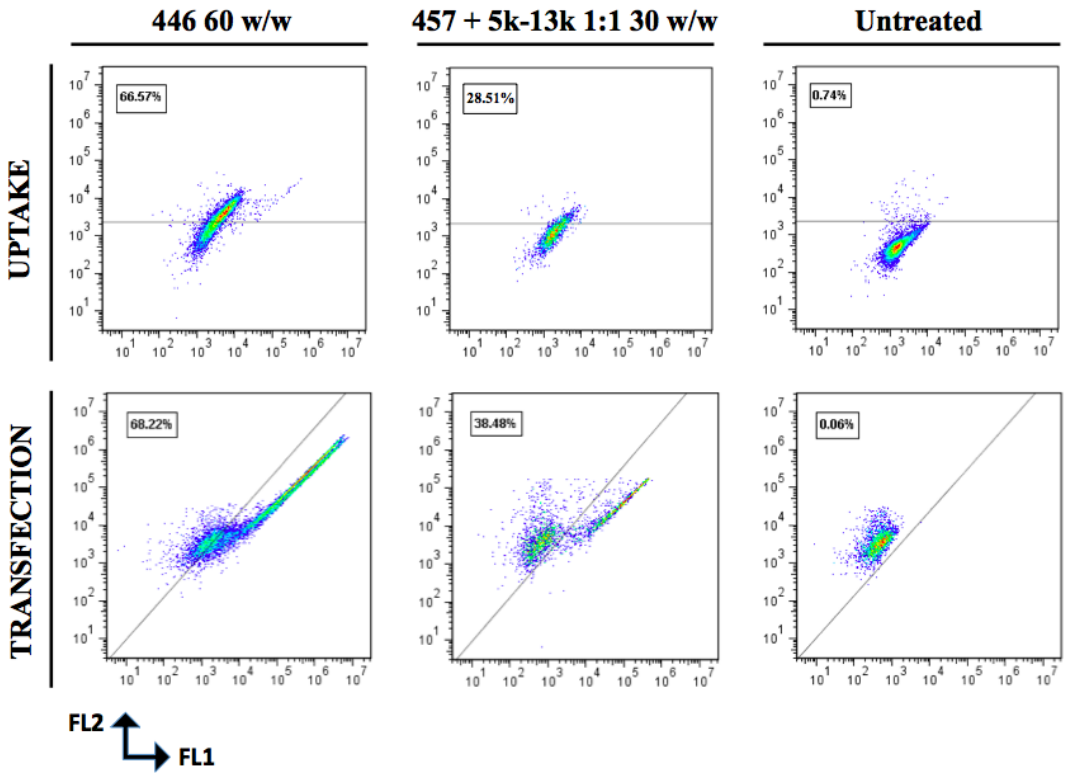

Figure 2.8. FACS plot for H446 cellular uptake and transfection. Flow cytometry plot showing the uptake and transfection efficacy of 446 60 w/w PBAE polyplexes, 457 + 5k-13k 1:1 30 w/w PEG-PBAE polyplexes, and untreated control in H446 cells.

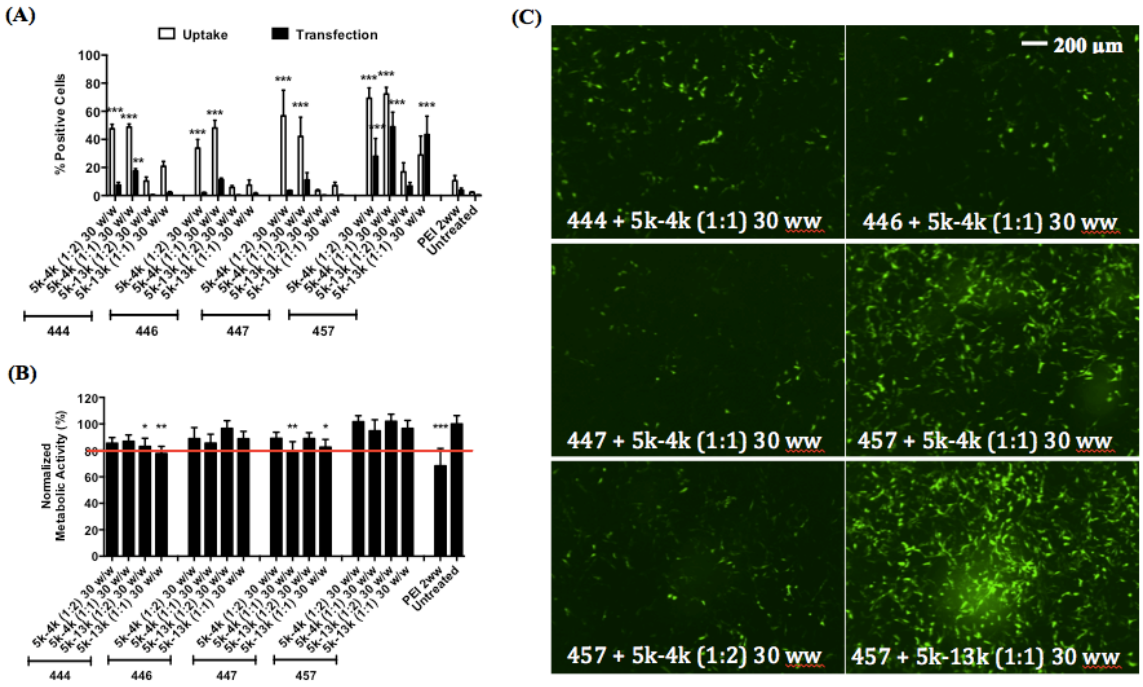

Figure 2.9. PEG-PBAE polyplex uptake, transfection, and cytotoxicity screening on H446. (A) Flow cytometry data showing the uptake and transfection efficacy of 16 different formulations of PEG-PBAE polyplexes in H446 cells 4 hrs and 2 days post-transfection, respectively. The efficiency is in terms of percentage of live H446 cells positive for Cy3 (uptake) or EGFP (transfection). Data are mean ± SD (n=4) (*** $p < 0.001$, ** $p < 0.01$ compared to untreated). (B) Cytotoxicity of PEG-PBAE polyplexes, quantified by normalizing metabolic activity to untreated cells. Data are mean ± SD (n=3) (*** $p < 0.001$, ** $p < 0.01$, * $P < 0.05$ compared to untreated). (C) Representative fluorescence microscope images (10x) of H446 cells transfected with 6 different PEG-PBAE polyplex formulations.

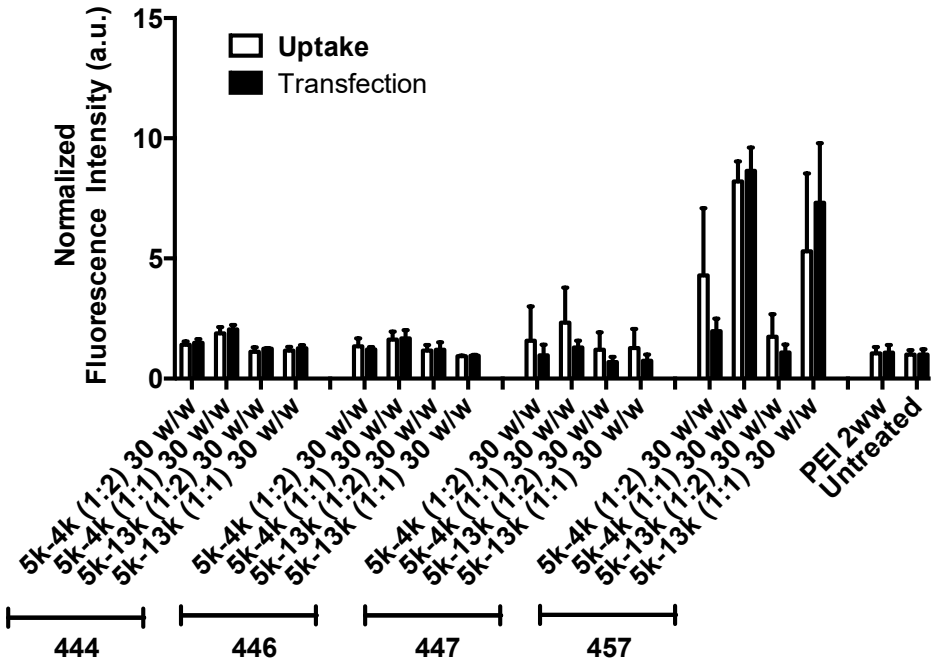

Figure 2.10. Geometric mean fluorescence following PEG-PBAE polyplex transfection of H446. Flow cytometry data showing the uptake and transfection efficacy of 16 different formulations of PEG-PBAE polyplexes in H446 cells, in terms of the normalized geometric mean fluorescence intensity of Cy3 (uptake) or EGFP (transfection). Data are mean ± SD (n=4).

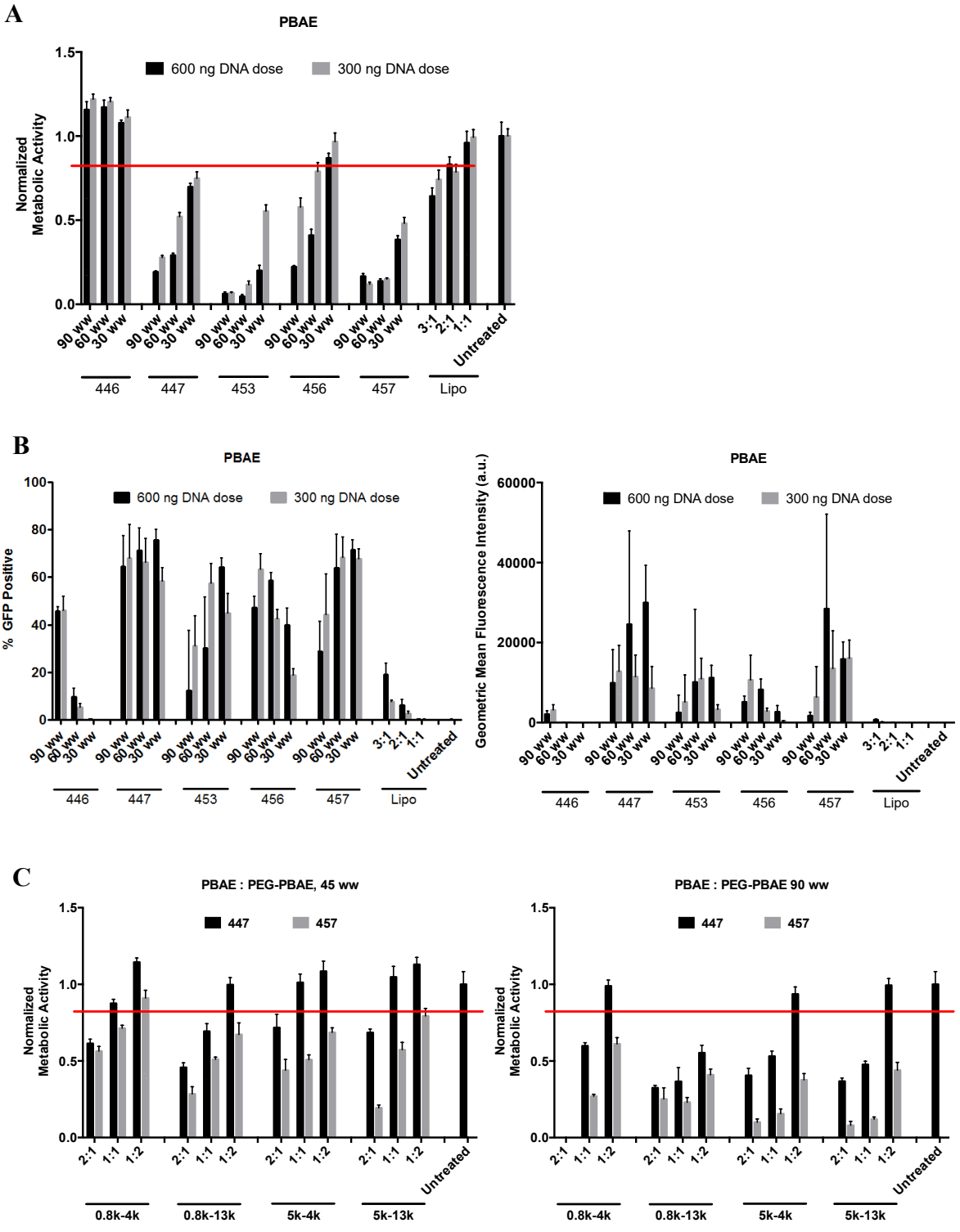
A
PBAE
600 ng DNA dose
300 ng DNA dose
Normalized Metabolic Activity
1.5
1.0
0.5
0.0
90 ww
60 ww
30 ww
3:1
2:1
1:1
Untreated
446
447
453
456
457
Lipo
B
PBAE
600 ng DNA dose
300 ng DNA dose
% GFP Positive
100
80
60
40
20
0
PBAE
600 ng DNA dose
300 ng DNA dose
Geometric Mean Fluorescence Intensity (a.u.)
60000
40000
20000
0
C
PBAE : PEG-PBAE, 45 ww
447
457
Normalized Metabolic Activity
2:1
1:1
1:2
Untreated
0.8k-4k
0.8k-13k
5k-4k
5k-13k
PBAE : PEG-PBAE 90 ww
447
457

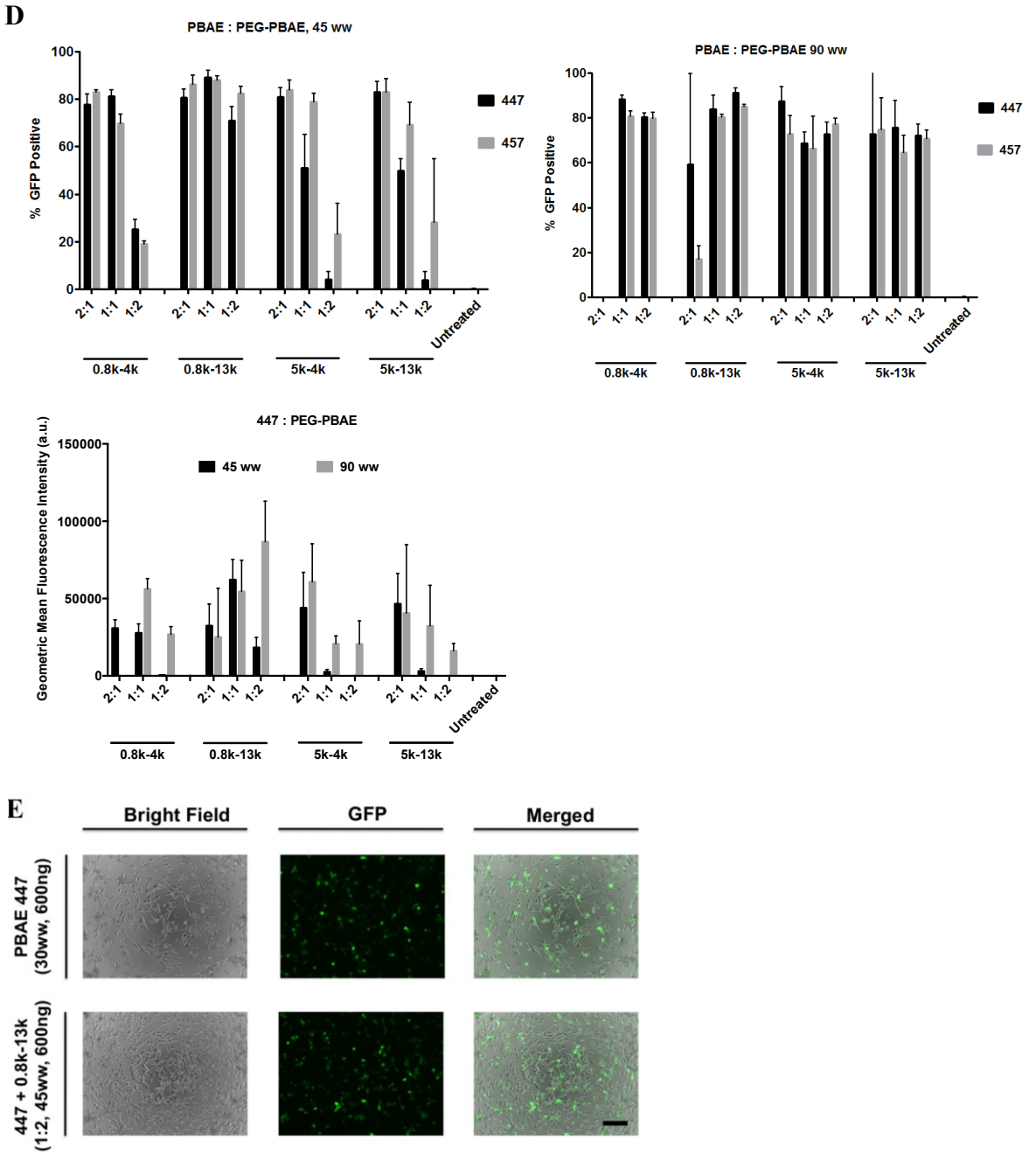

Figure 2.11. ePBAE polyplex transfection, and cytotoxicity screening on BTIC375. Cytotoxicity of (A) ePBAE and (C) PEG-PBAE polyplexes, quantified by normalizing metabolic activity to untreated cells. Data are mean ± SD (n=3). Flow cytometry data showing the transfection efficacy of (B) 30 ePBAE polyplexes and (D) 48 PEG-PBAE polyplexes in BTIC375 cells at 48 h post-transfection. The efficiency is in terms of percentage of BTIC375 cells positive and geometric mean fluorescence for EGFP (transfection). Data are mean ± SD (n=4) (E) Representative fluorescence microscope images of BTIC375 cells transfected with 447 ePBAE 30 w/w and PEG-PBAE (447 + 0.8k-13k 1:2 45 w/w) polyplexes (scale bar = 200 μm).

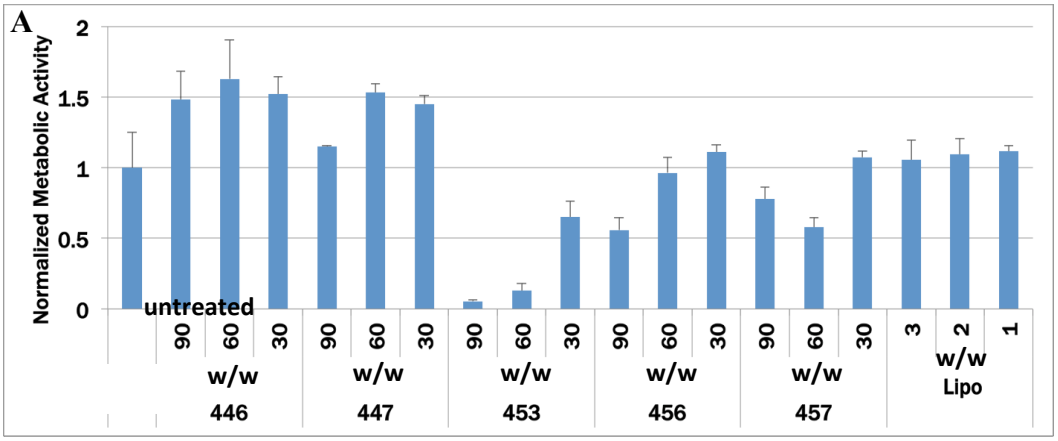
A
Normalized Metabolic Activity
2
1.5
1
0.5
0
untreated
90
60
30
w/w
446
447
453
456
457
3
2
1
Lipo

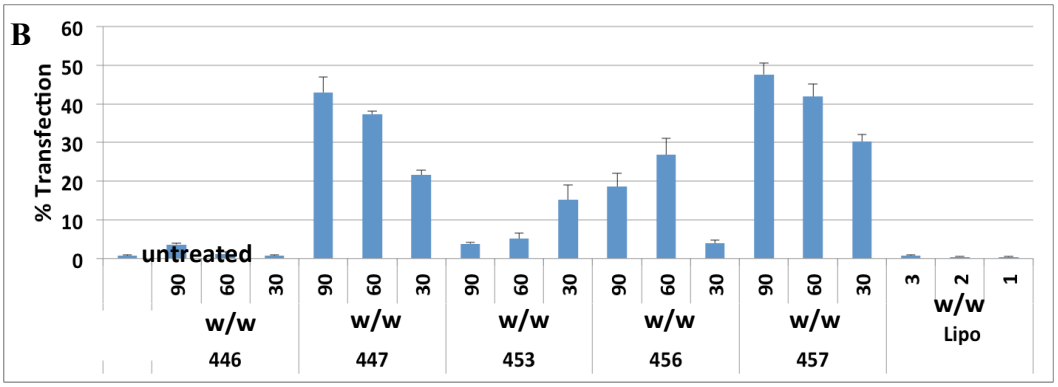
B
% Transfection
60
50
40
30
20
10
0
untreated
90
60
30
w/w
446
447
453
456
457
3
2
1
Lipo

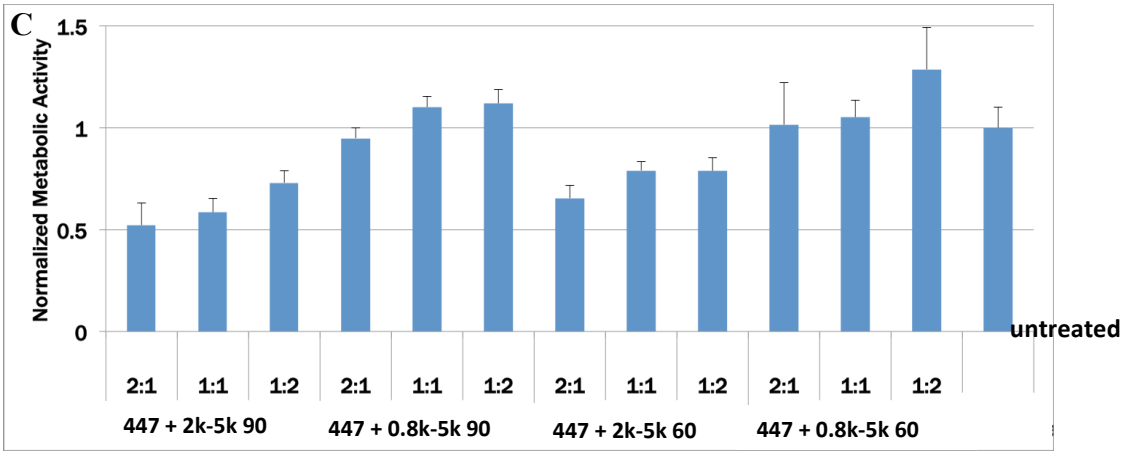
C
Normalized Metabolic Activity
1.5
1
0.5
0
2:1
1:1
1:2
447 + 2k-5k 90
447 + 0.8k-5k 90
447 + 2k-5k 60
447 + 0.8k-5k 60
untreated

D

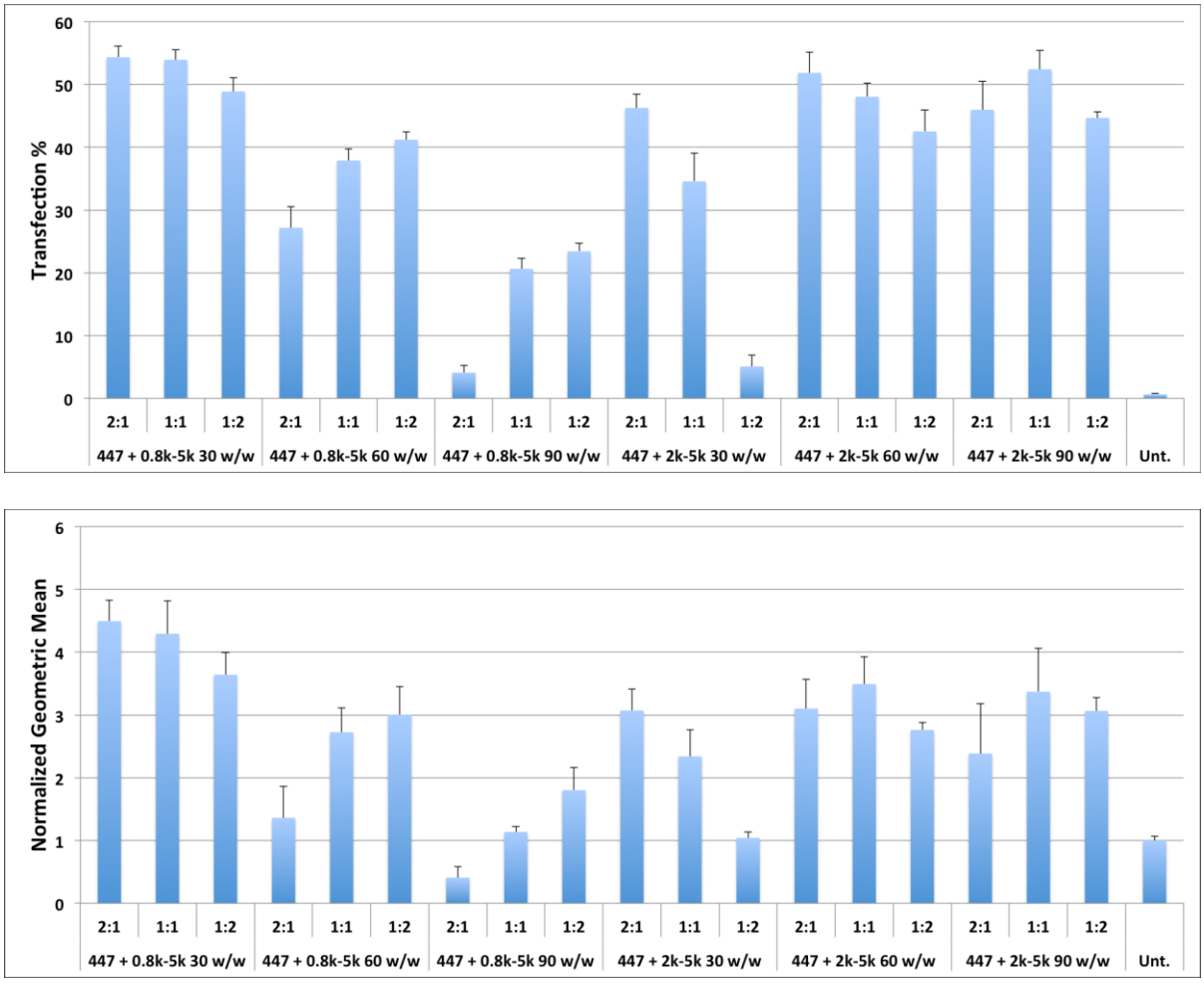

Figure 2.12. ePBAE polyplex transfection, and cytotoxicity screening on GBM1A. Cytotoxicity of (A) ePBAE and (C) PEG-PBAE polyplexes, quantified by normalizing metabolic activity to untreated cells. Data are mean ± SD (n=3). Flow cytometry data showing the transfection efficacy of (B) 15 ePBAE polyplexes and (D) 18 PEG-PBAE polyplexes in GBM1A cells at 48 h post-transfection. The efficiency is in terms of percentage of GBM1A cells positive and geometric mean fluorescence for EGFP (transfection). Data are mean ± SD (n=4).

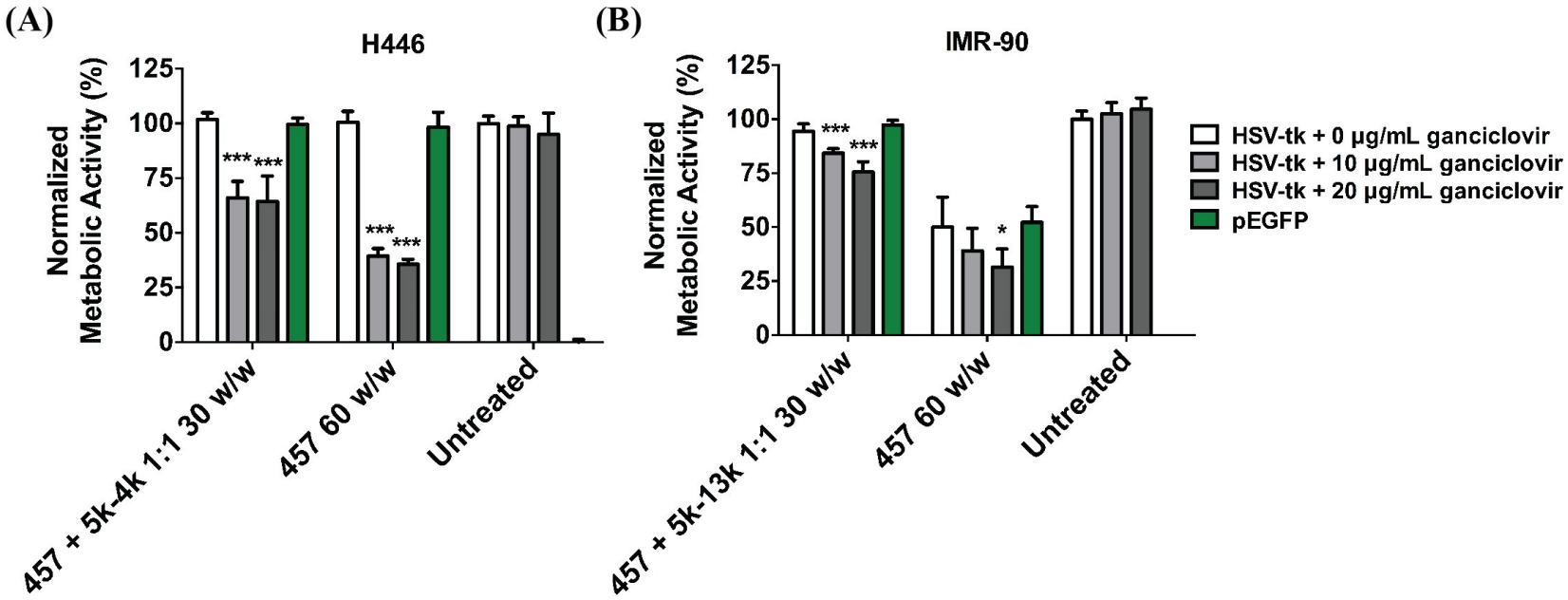

Figure 2.13. pHSV-tk and GCV-mediated H446 and IMR-90 cell killing by ePBAE and PEG-PBAE polyplexes. Percent killing of (A) H446 and (B) IMR-90 cells transfected with the optimized PEG-PBAE polyplex formulation (457 + 5k-13k 1:1 30 w/w) and PBAE polyplexes (457 60 w/w) delivering pHSV-tk, followed by two sequential ganciclovir treatments at either 10 or 20 g/mL dosage. Cell death is measured by MTS assay and normalized to metabolic activity of untreated cells. Data are mean ± SD (n=4) (* $p < 0.05$, *** $p < 0.001$ compared to pEGFP control of each group).

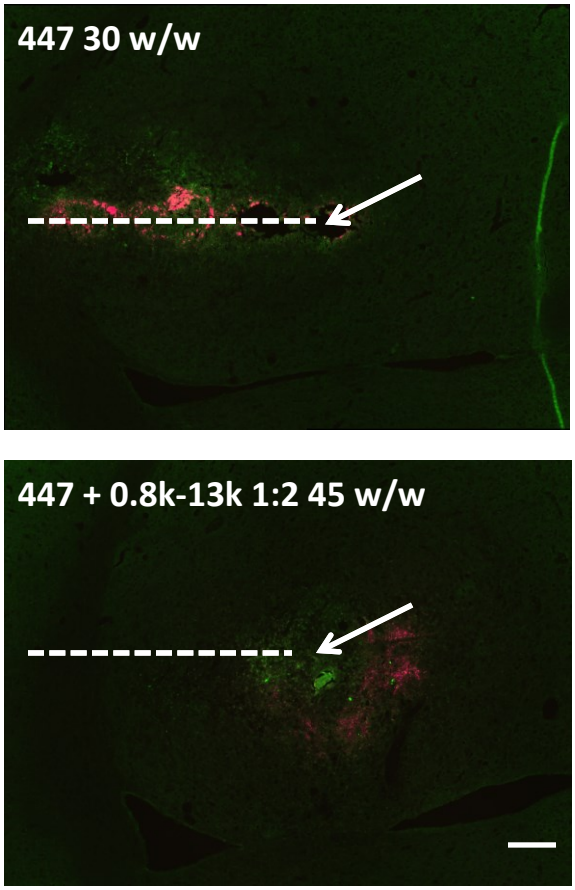

Figure 2.14. Polyplex spreading *in vivo* in orthotopic BTIC375 xenograft. Diffusion of Cy5-labeled (red) ePBAE (top, 447 30 w/w) and PEG-PBAE (bottom, 447 + 0.8k-13k 1:2 45 w/w) polyplexes in BTIC375 tumor mass (green). Arrow: point of injection. Dotted line: needle track. Scale bar: 200 μm

PEG-PBAE	Name
$PEG_{0.8k}$-B4S4$_{4k}$-$PEG_{0.8k}$	0.8k-4k
$PEG_{0.8k}$-B4S4$_{13k}$-$PEG_{0.8k}$	0.8k-13k
PEG_{5k}-B4S4$_{4k}$-PEG_{5k}	5k-4k
PEG_{5k}-B4S4$_{13k}$-PEG_{5k}	5k-13k

Table 2.1. Nomenclature of different PEG-PBAE polymers. The PBAE used was 1-4-butanediol diacrylate-co-1,4-aminobutanol (B4S4).

Polymers	ePBAE:PEG-PBAE w/w	Polymer:DNA w/w	Converted PBAE:DNA w/w	Converted N/P
447_{13k} + 0.8k - 4k	**1:2**	30 60 90	24.3 48.6 72.9	29.7 59.5 89.2
447_{13k} + 0.8k - 4k	**1:1**	30 60 90	25.7 51.4 77.1	31.5 63.0 94.5
447_{13k} + 0.8k - 4k	**2:1**	30 60 90	27.1 54.3 81.4	33.2 66.5 99.7
447_{13k} + 0.8k - 13k	**1:2**	30 60 90	27.8 55.6 83.4	33.2 66.3 99.5
447_{13k} + 0.8k - 13k	**1:1**	30 60 90	28.4 56.7 85.1	33.8 67.6 101.4
447_{13k} + 0.8k - 13k	**2:1**	30 60 90	28.9 57.8 86.7	34.5 68.9 103.4
447_{13k} + 5k - 4k	**1:2**	30 60 90	15.7 31.4 47.1	19.2 38.5 57.7
447_{13k} + 5k - 4k	**1:1**	30 60 90	19.3 38.6 57.9	23.6 47.2 70.9
447_{13k} + 5k - 4k	**2:1**	30 60 90	22.9 45.7 68.6	28.0 56.0 84.0
447_{13k} + 5k - 13k	**1:2**	30 60 90	21.3 42.6 63.9	25.4 50.8 76.2
447_{13k} + 5k - 13k	**1:1**	30 60 90	23.5 47.0 70.4	28.0 56.0 84.0
447_{13k} + 5k - 13k	**2:1**	30 60 90	25.7 51.3 77.0	30.6 61.2 91.8
447_{13k}	**No PEG-PBAE**	30 60 70	30 60 90	37.6 75.2 112.8

Table 2.2. Chart for w/w to N/P conversion. (447_{13k} = 13 kDa MW ePBAE 447)

Chapter 3

Verteporfin-loaded poly(ethylene glycol)-poly(beta-amino ester)-poly(ethylene glycol) triblock micelles for cancer therapy

3.1 Introduction

Polymeric nano-vehicles have been investigated as gene and drug delivery systems due to their small size and high loading capacity.[1,2] Specifically, amphiphilic block copolymers self-assemble into nano-sized structures due to the hydrophobic effect when exposed to an aqueous environment. This process produces micelles with a hydrophobic core and hydrophilic shell. As the majority of small molecule drugs have low solubility in aqueous medium, there is a significant need to engineer delivery vehicles capable of encapsulating poorly water-soluble drugs and enabling administration of these drugs at physiologically relevant dosages.[3] In addition, when designing a nanomedicine, it has been demonstrated that a hydrophilic corona, often consisting of poly(ethylene glycol) (PEG), can promote colloidal stability and neutralize surface charge, and consequently reduce clearance by the reticuloendothelial (RES) system, increase passive accumulation at neovasculature around a tumor, and improve diffusion through the interstitial space.[4,5]

Poly(beta-amino ester)s (PBAE) compose a class of cationic biodegradable polymers, that due to their positive charge, have been used by researchers to form polyplexes for the

Parts of this chapter were completed based on research in collaboration with Shamul JG, Shah SR, Shin A, Lee BJ, Quinones-Hinojosa A, and Green JJ.

delivery of hydrophilic anionic nucleic acid cargo, but have not been well-investigated for the potential to carry non-genetic cargo.[6,7] The capacity to synthesize libraries of PBAEs with distinct chemical properties through the use of monomers with differential structures has been an asset to explore structure/function relationships for gene delivery.[6,8] PBAE copolymers can be further developed through the synthesis of hydrophobic PBAE blocks combined with hydrophilic blocks to create an amphiphilic copolymer capable of forming micellar structures.[9] Tuning hydrophobicity of the PBAE segment of PBAE-based amphiphilic copolymers can affect the packing parameter thermodynamic equilibrium of the polymers in solution, and change the shape of the resulting micelles, such as spheres, filaments, and multilamellar vesicles.[10] Different shapes of particles have been previously shown to exhibit varying pharmacokinetics and biodistribution.[11] Also, one of the critical properties of gene delivery cationic polymers is their tertiary amines along the backbone that provide the pH buffering capacity to facilitate endosomal escape.[12] For PBAE-based micelles, the many tertiary amines can enable similar endosomal escape. In addition, the pH-sensitive ester linkages of PBAEs can allow environmentally-triggered release as pH-sensitive cargo release has been demonstrated in the more acidic tumor microenvironment with this class of materials.[5]

Verteporfin (VP) is a small molecule also known as benzoporphyrin derivative monoacid ring A, which belongs to the porphyrin family of photosensitizers in photodynamic therapy (PDT). Due to VP's low solubility of 13.6 μg/mL in aqueous medium, liposomal VP formulations were developed to as a PDT agent in neovascular age-related macular degeneration (NVAMD) and tumor.[13,14] Although Visudyne® remains the only FDA-approved liposomal VP for PDT against NVAMD, other nanoparticle VP formulations has

been tested in PDT against subcutaneous cancer *in vivo*, such as Meth-A sarcoma and rhabdomyosarcoma.[15,16]

It was recently demonstrated that VP leads to inhibition of growth and proliferation of human retinoblastoma cells and a number of central nervous system-derived cancer cells in the absence of light activation.[17,18] VP has been associated with down-regulation of the yes-associated protein-transcriptional enhancer factor domain (YAP-TEAD) complex, which is involved in the Hippo pathway in cancer cells to induce uncontrolled proliferation, but is inactive in healthy tissues.[18,19] This mechanism facilitates specific anti-cancer treatment of cancer cells without harming healthy cells.[20] YAP signaling is also known to be hyperactivated in epithelial-derived carcinomas. As liposomal VP formulations can readily destabilize in the presence of blood plasma[21] and can be quickly cleared by the reticuloendothelial system, there is a need to develop safe and effective alternative delivery vehicles to administer VP locally or systemically for specific treatment against cancer.

In this study, stable polymeric micelles encapsulating VP were formulated with a novel PEG-PBAE-PEG triblock copolymer and evaluated for non-photodynamic chemotherapy *in vitro* in two epithelial cancer cells, human small cell lung cancer (H446) and human triple-negative breast cancer (MDA-MB 231) cells. Furthermore, two different types of the triblock copolymers were synthesized to generate spherical and anisotropic micelles that showed shape-dependent differential uptake by macrophages. Anisotropic micelles exhibited longer blood half-life and greater tumor accumulation than spherical micelles in human glioblastoma (GBM1A) xenograft flank model in mice.

3.2 Methods

Materials

1,4-butanediol diacrylate (B4), octylamine (S8m), decylamine (S10m), pyrene (Sigma-Aldrich), 1,6-hexanediol diacrylate (B6), 1-(3-aminopropyl)-4-methylpiperazine (E7) (Alfa Aesar), dimethyl sulfoxide (DMSO), dimethyl formamide (DMF), hexane, methoxy poly(ethylene glycol) thiol (2 kDa and 800 Da) (Laysan Bio, Inc), and Verteporfin (VP) (U.S. Pharmacopeial Convention, Inc.) were purchased and used as received. CellTiter 96 AQueous One MTS assay (Promega, Fitchburg, WI) was used per manufacturer's instructions.

Synthesis of PEG-PBAE-PEG triblock copolymer

A PBAE-based triblock amphiphilic copolymer was synthesized by a two-step polymer synthesis. First, 1,4-butanediol diacrylate (B4) was reacted with octylamine (S8m) by Michael addition reaction at molar ratio of 1.15:1 at 90ºC for 72 h to yield acrylate-terminated hydrophobic PBAE base polymer (B4S8m) as shown in **Figure 3.1A/B.** The B4S8m base polymer was subsequently precipitated in hexane twice and then dried under vacuum with desiccant overnight. The structure and molecular weight of the base polymer was confirmed using Bruker Avance III 500 MHz ^{1}H NMR spectrometer in $CDCl_3$. Following the procedure described by Kim *et al.*, the base polymer reacted with 2 kDa mPEG-thiol in DMSO with trace amounts of 1-(3-aminopropyl)-4-methyl-piperazine (E7) as a primary amine-containing catalyst by thiol-ene Michael addition reaction at molar ratio of 1:6:0.25 (B4S8m : PEG : catalyst) while stirring at 50°C for 24 h.[22] The B4S8m triblock

copolymer with PEG 2 kDa, named PP1, was purified by first removing DMSO with a rotary evaporator and then precipitating with hexane twice. The structure of the PEG-PBAE-PEG triblock copolymer was confirmed using ^{1}H NMR in $CDCl_3$. The identical procedure was used for synthesis of B6S10m triblock copolymer with PEG 800 Da, named PP2. The partition coefficient of each copolymer was determined using ChemBioDraw software.

Formulation of micelles

Spherical VP-loaded micelles (sVPM) and filamentous VP-loaded micelles (fVPM) were prepared using nanoprecipitation method. First, PEG-PBAE-PEG triblock copolymer was dissolved in DMF at 20 mg/mL. Next, an equivalent volume of 1 mg/mL VP solution in DMSO was added to the polymer solution and vortexed. Each nanoprecipitation reaction was limited to 5 mg of the 10 mg/mL VP-polymer solution. 500 µL (5 mg) of the VP-polymer solution was added slowly using an insulin syringe into 3x volume of ultrapure water, while stirring at 500 rpm. Spherical blank micelle (sBM) and filamentous blank micelles (fBM) batches were identically synthesized excluding the presence of VP. Immediately after adding the solution, the reaction vial was placed in a water bath sonicator for 1 min and then placed back on stir plate for 4 h. The solution was then added to a 10 kDA MWCO filter (EMD Millipore, Burlington, MA) and spun for 15 minutes. Next, the remaining solution was added to a Sephadex column with Sephadex S-500 High Resolution. After spinning for 3 minutes at 800 g, the filtrate was spun at 17,000 g for 15 min. The supernatant was collected and then filtered through a 0.22 µm PTFE syringe filter. The micelle solution was lyophilized with

10% final sucrose solution as a cryoprotectant. Several aliquots were lyophilized without sucrose to measure loading and release of VP.

Characterization of micelles

Critical micelle concentration (CMC) of sVPM was measured by spectrofluorophotometry using pyrene as the indicator of micelle formation. Pyrene emission peaks shift depending on the polarity of the local environment. Briefly, 185.8 ng of pyrene in acetone was left to dry and 1.5 mL of water was added. Organic phase with a range of polymer concentrations in DMSO: DMF (1:1 v/v) was added to the aqueous solution as described above and sonicated for 1 min. Following the 4 h stirring step, excitation spectrum of the samples was recorded with a constant emission value of 390 nm. The intensity ratios of the excitation peaks at 339 and 335 nm were calculated and then plotted as a function of log[PEG-PBAE-PEG]. The inflection point of the fitted sigmoidal graph was determined as the CMC.

Micelle size and morphology was determined by transmission electron microscopy (TEM). 0.5% uranyl acetate was used as a negative stain for TEM. ImageJ was used to determine aspect ratio distribution of fVPM. Dynamic light scattering (DLS) with Malvern Zetasizer Nano ZS (Malvern Instruments, Malvern, U.K.) was used to determine initial size and particle stability at 0, 1, 3, 5, 12 and 31 h time points of micelle formulations. To determine particle stability, sVPM and sBM micelles were reconstituted with deionized water to reach isotonic concentration of 10% w/v sucrose and then further with four different mediums to reach a polymer concentration of 1 mg/mL: 1) 10% sucrose solution, 2) 1x PBS,

and 3) human serum plasma. Zeta potential was determined with Malvern Zetasizer by preparing micelle sample in 10 mM NaCl at 1 mg/mL.

Loading and release kinetics of VP

Dilution series of lyophilized VPM were made by dissolving in DMSO at the highest polymer concentration of 1.0 mg/mL. Fluorescence intensity was measured with excitation wavelength of 420 nm and emission wavelength of 680 nm using Synergy 2 plate reader (Biotek). Each concentration was tested as triplicates, and fluorescence intensity was translated to VP mass by using a standard curve. The DLC (drug loading content) and the DLE (drug loading efficiency) were then calculated according to the following formulas:

DLC (%) = (mass of loaded drug / mass of polymer) x 100%

DLE (%) = (final mass of loaded drug in lyophilized batch / initial mass of drug added during formulation) x 100%

Micelles were dissolved in a mixed buffer of citric acid monohydrate and sodium phosphate dibasic at three different pH's (5.0, 6.5, 7.4) at 0.1 mg/mL and 1 mL of each was transferred into separate scintillation vials. The vials were incubated on a shaker at 37°C. At time points of 1, 3, 5, and 12 h entire volume was spun down at 500k g for 20 min at 4°C to pellet remaining micelles. Released VP in the supernatant was stored in a separate tube for fluorescence measurement. Pelleted micelles were resuspended in 1mL of fresh buffer and

transferred to a new scintillation vial for incubation at 37℃ oven until the next time point. The release samples (supernatant solutions) were read under plate reader (Biotek) and concentration of VP was calculated based on the VP standard curve.

Cell culture

Human triple-negative breast cancer cells MDA-MB231 and murine macrophages RAW 264.7 (ATCC) were grown in high-glucose Dulbecco's modified Eagle medium (Invitrogen, Carlsbad, CA) with 10% FBS and 1% penicillin/streptomycin at 37°C and 5% CO_2.

Human small cell lung cancer cells H446 (ATCC) were grown with ATCC-modified RPMI 1640 media (Life Technologies, Carlsbad, CA), supplemented with 10% FBS and 1% penicillin/streptomycin, at 37°C and 5% CO_2.

Cellular uptake of VPM, BM, and free VP

MDA-MB 231, H446, and RAW 264.7 cells were seeded in 96 well plates at 15,000 cells per well in 100 µL of media, and incubated for 24 h at 37°C with 5% CO_2. Cells were then treated with free VP in 0.4% DMSO solution, sVPM and sBM in 10% sucrose solution, and fVPM and fBM in 1X PBS at 2-fold increasing final concentrations from 1.25 µM - 20 µM for 1.5 h. VPM and BM were sonicated for 10 s at 20% amplitude just prior to being added to cells. MDA-MB 231 and H446 cells were then washed twice with heparin-containing PBS (50 µg/mL) to remove VP adhered to cells' surface, trypsinized, resuspended

with 170 μL of FACS buffer (PBS with 2% FBS), transferred to a round-bottom 96-well plate, centrifuged at 800 rpm for 5 min, resuspended in 30 μL FACS buffer, and analyzed by flow cytometry (BD Accuri C6 with HyperCyt adaptor). The same procedure was followed for RAW 264.7 except vigorous trituration was performed to detach cells from the plate rather than trypsinization. The results were analyzed by FlowJo 7.6.5 software using FSC-H vs. SSC-H gating for singlet cells and FL3 vs. FSC-H gating for VP-positive cells. Wells with more than 500 singlet events were counted in analysis. All conditions were tested in quadruplicates.

Cell killing with VPM

MDA-MB 231, H446, and RAW 264.7 cells were seeded in 96-well plates at 15,000 cells per well and incubated for 24 h. Free VP, VPM, and BM were added to each well at 2-fold increasing final VP concentrations from 2.5 μM – 20 μM. VPM and BM were sonicated for 10s at 20% amplitude just prior to being added to cells. Following 2 h incubation, cells were washed with 1X PBS and replenished with fresh media. Cells were observed under bright-field microscope for viability at 2, 6, 24, and 48 h post-treatment. At each time-point, cell killing was measured by CellTiter 96AqueousOne MTS assay. Cells were incubated with 100 μL of media and cell titer reagent solution (6:1 v/v) at 37°C for 2 h, and absorbance at 490 nm was measured using Synergy 2 plate reader. All conditions were tested in quadruplicates.

In vivo *pharmacokinetics and biodistribution*

Athymic nude mice 5-7 weeks of age were inoculated with 2 x 10^6 human glioblastoma (GBM1A) cells in matrigel solution in the flank. Once tumors reached 150 mm^3, they were randomized into 4 different groups (n=4 each) for blood half-life and tissue distribution studies. For each study, one group was injected in tail-vein with spherical micelles while the other group was injected with filamentous micelles. These micelles were formulated following the protocol above with IR-dye (Lumiprobe) encapsulated in place of verteporfin for fluorescence imaging, lyophilized, and reconstituted to 1.75 mg/mL of IR-dye prior to injection. To study pharmacokinetics, blood was collected from saphenous vein at 5, 10, 30 min, 1, 2, 4, and 8 hr time points post injection into heparinized capillary tubes. Fluorescnece in capillary tubes was imaged using IVIS. To study biodistribution, whole animal live image was acquired using IVIS at 0, 0.5, 1, 2, 4, 8, and 24 hr post injection. Then, animals were sacrificed at 24 hr and organs (liver, spleen, kidneys, bladder, lungs, and heart) were harvested for imaging individually with IVIS. All IVIS fluorescence images were quantified with Living Image 3.2 software.

Statistics

GraphPad Prism 6 software package was used to perform statistical analysis. One-way ANOVA with Dunnett post-hoc test was performed to compare multiple conditions against the control group, Tukey post-hoc test to compare all pairs, or Student's t-test to compare two conditions. (* = $p < 0.05$)

3.3 Results

Synthesis and characterization of PBAE and PEG-PBAE-PEG triblock copolymer

Both hydrophobic PBAE backbone polymers, B4S8m and B6S10m, were synthesized with a 1.15:1 ratio of diacrylate to alkylamine monomer. Resulting molecular weights of each PBAE polymer were 5100 and 4300 Da for B4S8m and B6S10m, respectively, as determined by ^{1}H NMR (**Figure 3.2A-C**). The partition coefficients determined from the chemical structure of B4S8m and B6S10m matched the predicted hydrophobicity of both polymers (**Figure 3.2C**). B4S8m and B6S10m were then endcapped with 2000 Da and 800 Da mPEG-thiol to create PP1 and PP2 triblock copolymers, respectively (**Figure 3.1C**). PP2 exhibits greater hydrophobic proportion in the amphiphilic polymer chain in comparison to PP1. The thiol-ene Michael addition of PEG to both ends of PBAE was confirmed using ^{1}H NMR by the disappearance of the peaks from the acrylates (**Figure 3.2A/B**).

Formulation and characterization of micelles

To measure the critical micelle concentration (CMC), pyrene was loaded into the micelles at increasing concentrations of PP1 polymer, while keeping the organic solvent to water ratio and the final volume constant. The log of the polymer concentration is plotted against the ratio of the intensity values at two wavelengths. In **Figure 3.3A,** the resulting sigmoidal plot of log[PP1] vs. I_{339}/I_{336}, has an inflection point at an exact concentration of 0.056 mg/mL. The increase in the intensity ratio as polymer concentration is increased corresponds to the shift of pyrene excitation peak. This demonstrates micelle formation and

pyrene encapsulation. To further corroborate micelle formation and to confirm the morphology, resulting micelle structures pre- and post- lyophilization were visualized under TEM (**Figure 3.3B**). Micelles were spherical in shape, and there was no significant difference in shape or size between loaded micelles with VP (sVPM) and unloaded micelles (sBM), and between pre-lyophilized and post-lyophilized samples.

The size, polydispersity index (PDI), and zeta potential of micelles were measured with DLS. In order to be an effective vehicle for VP delivery via passive targeting, the size of our micelles should be below 200 nm to enter into the small pores on tumor tissue.[23] Before lyophilization and after filtration and removal of unloaded VP, spherical micelles sVPM and sBM were both sized at 50 nm in water (**Figure 3.3C**), which is similar to the size visualized under TEM**.** sVPM showed a lower PDI and standard deviation between multiple batch measurements, which can possibly be explained by more stable micellar structure with the presence of VP which increases the hydrophobic force the micelle formation. The surface charge of sVPM and sBM in 10 mM NaCl were approximately neutral at -3 ± 4 mV and 3 ± 5 mV, respectively, demonstrating that the PEG is effective at shielding the particle (**Figure 3.3D**).

Particle stability was determined by time-course DLS size measurement of lyophilized micelles that are reconstituted in different medium (**Figure 3.3E**). sVPM showed excellent size stability in 55:45 v/v human serum:1x PBS over 31 hr, with no aggregation occurring over time. The control solution of human serum and PBS solution contained particulates with a size of approximately 50 nm, which likely represents the various serum protein aggregates and extracellular vesicles present in the serum. In 1x PBS, sVPM was approximately stable at a moderately larger size of 160 nm. Both blank sBM samples were

initially smaller than their respective loaded samples, which is attributed to particle size needing to be larger to accommodate the VP cargo. While particle size is stable with time for sVPM samples in human serum and PBS, size increased over time for the empty sBPM particles, which signifies that the VP helped to improve the stability and minimize the aggregation of sVPM over time, likely due to the interactions between the hydrophobic VP in the hydrophobic core of the sVPMs. The amount of VP molecule encapsulated in VPM was measured by dissolving VPM with DMSO to release the VP and measuring the intrinsic fluorescence of VP molecule. Loading capacity is the amount of VP loaded per mass of particles, while loading efficiency is the amount of VP loaded per starting mass of VP. The loading capacity and efficiency of sVPM were 5.36% and 43.7%, respectively.

pH-sensitive release of VP from sVPM

PBAE-based polymers consist of tertiary amines along the backbone, enabling pH buffering at acidic conditions.[24] The release kinetics of VP from sVPM at pH 7.4, 6.5, and 5.0 at 37 °C in citrate-phosphate buffer was evaluated to simulate the intravenous, tumoral, and lysosomal environments, respectively. The release plot in **Figure 3.4** shows that pH 5.0 has the fastest release rate, 6.5 the slowest, and 7.4 has intermediate release. All three pH conditions followed similar kinetic trends, only varying in the absolute mass of VP released. Interestingly, the micelles showed the least total release of VP at pH 6.5 and an intermediate release at pH 7.4.

Filamentous micelle characterization and shape dependence of macrophage uptake

We next investigated micelle shape as a parameter by tuning the hydrophobicity of the amphiphilic triblock copolymer to create high-aspect ratio anisotropic micelles. The morphology of VP-loaded micelles formulated with PP2 was determined with TEM (**Figure 3.5A**). Analysis using ImageJ confirmed that the filamentous VP-loaded micelles (fVPM) had an average length of 651 nm, width of 31 nm, and resulting average aspect ratio (AR) of 20±10 (**Figure 3.5B**). The size of lyophilized fVPM determined using DLS was 69 nm with greater PDI than sVPM (**Figure 3.5C**). This is expected because DLS estimates the hydrodynamic diameter assuming that the sample being measured is spherical so filamentous micelles with variation to aspect ratio would be instead detected as spheres of varying sizes. There was no difference in particle size following lyophilization and re-suspension (**Figure 3.5C**).

After this filamentous morphology was confirmed, the cellular uptake to RAW 264.7 macrophages was compared between sVPM and fVPM to evaluate the potential advantage of anisotropic PEG-PBAE-PEG micelles at reducing non-specific uptake, which could be useful to better evade the immune system. As shown in **Figure 3.5D**, fVPM treatment resulted in a significantly lower percentage of macrophages that internalized the fVPM compared with sVPM at equivalent VP concentrations evaluated. Similarly, the normalized geometric mean values for internalized VP using fVPM as the vehicle were 15 – 20% of that for sVPM at all concentrations evaluated, demonstrating that there is significantly less VP uptake per cell in fVPM-treated cells (**Figure 3.5D**). Interestingly, as the concentration of VP decreased from 0.08 to 0.04 μM, the uptake percentage for fVPM shows a sharp decrease from 55% to 6% in

comparison to little decrease for sVPM. There was no cytotoxicity of macrophages resulting from delivered VP at the concentrations tested by either type of particle (**Figure 3.6**).

Cellular uptake by MDA-MB 231 and H446 cells

In order to investigate the level of internalized VP in MDA-MB 231 triple-negative human breast cancer cells and H446 human small cell lung cancer cells, the cellular uptake was measured by incubating the cells with equivalent concentrations of VP in the forms of free VP drug, sVPM, and fVPM for 1.5 hr. **Figure 3.7A/C** shows that there was near 100% cellular uptake for free VP, and sVPM in both cancer cells. At the concentrations tested, fVPM showed a slight decrease in the cellular uptake percentage. However, on a per cell basis, a much greater decrease in cellular uptake of fVPM occurred compared to free VP and sVPM in MDA-MB 231 cells as demonstrated by the normalized geometric mean fluorescence, which measures the level of VP uptake on a per cell basis in relative fluorescence units (RFU), (**Figure 3.7B**). This is in concert with the observation with macrophages. In the H446 cells, there is a similar significant decrease for fVPM as compared to sVPM and free VP in cellular uptake measured by geometric mean fluorescence, and also there is higher per cell uptake as compared to MDA-MB 231 for all VP formulations in general. This may be explained by differential cellular uptake pathways as well as varying degree of exocytosis between different cells.[25] The difference in cellular uptake is in part demonstrated by the difference in the level of total signal between the two cell types, as indicated by the scale on y-axes (**Figure 3.7B/D**).

VP-induced death of MDA-MB-231 and H446 cells

To determine cancer cell death induced by VP-loaded micelles, both cancer cells were incubated with free VP, sVPM and fVPM for 2 hr, and cell viability was measured at 2, 6, 24, and 48 hr post treatment. For MDA-MB 231 cells, free VP and sVPM showed similar cell killing of approximately 85% and 40% at 20 μM and 10 μM VP concentrations at 48 hr, respectively, which corresponds to similar cellular uptake level (**Figure 3.8A / 3.9A**). This suggests that once endocytosed, free VP and sVPM have similar efficiencies of VP ultimately reaching the nucleus. For fVPM, as expected from the lowest cellular uptake, cell killing was either equivalent to or was the the lowest of the formulations at all VP concentrations and time points tested, with 20 μM VP concentration measured at 48 hr showing the maximum cell killing of fVPM at 44% of MDA-MB 231 cells. All negative controls, including 0.4% DMSO 99.6% PBS solution for free VP vehicle and blank micelles (sBM and fBM), did not show any toxicity, demonstrating the therapeutic effect is from the VP drug payload (**Figure 3.9**).

For H446 cells, there was an overall greater sensitivity towards VP as compared with MDA-MB 231 cells, which follows the cellular uptake findings (**Figure 7D**). All three VP treatments fully killed the human small cell lung cancer cells at the two highest concentrations of 10 μM and 20 μM at the 24 and 48 time points (**Figure 3.8C / 3.9A**). Cell killing by sVPM was very effective at even lower concentrations, showing 100% and 69% cell death at 5 and 2.5 μM, respectively. These efficiencies are significantly greater than both free VP and fVPM. sVPM may therefore improve the transport of VP intracellularly to the nucleus compared to free VP. For fVPM, its low cellular uptake can also lead to lower cell

killing efficiency compared with sVPM. It is important to also note the difference in cell death kinetics between MDA-MB 231 and H446 cells (**Figure 3.8B/D**), which can be due to a combination of downstream steps following cellular uptake and perhaps greater drug resistance to VP by the human triple negative breast cancer cells compared to the human small cell lung cancer cells, or different level of YAP activity between the two cell types. This observation highlights that the same drug and delivery vehicle may require different optimization across different tumors to be most effective.

In vivo *pharmacokinetics and biodistribution*

Based on the efficient cancer cell killing and shape-dependent macrophage uptake of the micelles *in vitro*, we compared *in vivo* blood half-life and biodistribution between spherical and filamentous micelles in tumor-bearing mice. Micelles loaded with a near-infrared dye were injected through tail-vein in nude mice with human glioblastoma implanted in the flank, and the fluorescence signal was monitored in the blood and in various organs over time through imaging. **Figure 3.10A** shows the IR fluorescence signal in blood collected at different time points, with exponential decay curves fitted to calculate the half-life. As expected, filamentous micelles showed approximately five-fold increase in the half-life of systemic circulation time, potentially by evading reticuloendothelial system-mediated clearance. Moreover, there was a corresponding two-fold increase in the tumor accumulation of 7.4% for the filamentous micelles in comparison to spherical micelles (**Figure 3.10B/C**). This can be partially explained through enhanced passive targeting to the tumor microenvironment from prolonged blood circulation.

3.4 Discussion

While polymeric drug delivery systems can provide clear advantages and opportunities for cancer therapy, there is a need to safely optimize these systems with biodegradable materials to minimize delivery to off-target cells and tissues while maximizing delivery to cancer cells.[26] We wished to i) evaluate a new putative anti-cancer drug, verteporfin, for efficacy to human triple negative breast cancer cells and human small cell lung cancer cells; ii) evaluate a new biodegradable micelle system for drug delivery based on poly(ethylene glycol)-poly(beta-amino ester)- poly(ethylene glycol) triblock copolymers; and iii) explore the role of shape of PEG-PBAE-PEG micelles in varying cellular uptake and drug delivery. Our proof-of-concept spherical drug delivery system was further optimized by inducing a high aspect ratio morphological shift through chemical modifications to the triblock copolymer backbone. Our group has shown that hard polymeric particles can be produced via a "top-down" stretching platform after synthesis, however chemical tuning of soft nanoparticles via a "bottom-up" approach does not require post-synthesis steps and can also confer greater scalability and manufacturability for this nanomedicine system.[27]

Two new PEG-PBAE-PEG triblock copolymers were synthesized, each with a varying number of carbons in the diacrylate monomer and the primary amine monomer, and a different PEG molecular weight. This chemical tuning shifts the packing parameter value, which can be used to predict the shape of the resulting self-assembled micelles[11]. This parameter value is defined by the effective hydrocarbon volume of the polymer chain V, divided by the product of the area of the hydrophilic headgroup α_0 and the fully extended chain length l_c.[10] PP2 consists of longer hydrocarbon chain monomers for the PBAE

backbone as well as smaller molecular weight PEG at both ends, leading to increased packing parameter and more anisotropic structures. This prediction corroborates the observed morphological shift with the PEG-PBAE-PEG micelles.

Interestingly, the novel PEG-PBAE-PEG micelles show biphasic release trends with varying pH. This is consistent with a previous finding from Zhang *et al.* that a VP-analog molecule has shown to dimerize at pH 6.5, which could affect the drug release from the micelles.[28] Also, it has been shown previously that PBAE nanoparticles can release more slowly at weakly acidic conditions.[29] Non-protonated amines in the backbone of PBAEs at pH 7.4 can act as weak bases, sequestering protons from water molecules, leaving free hydroxyl groups to act as nucleophiles and degrade ester bonds, and releasing the cargo faster than at weakly acidic pH. However, tertiary amines along the backbone of PBAE become protonated at pH 5 to allow disintegration of micelles and release of VP. This balance between VP dimerization, base-catalyzed hydrolysis, and micelle disassembly cause the pH-sensitive release kinetics. The slower release of VP at pH 6.5 compared to 7.4 and the fastest release at pH 5.0 have an advantage with intracellular VP delivery to cancer cells. The tumor microenvironment can have a pH range from 6.5-7.2, therefore it can be favorable for an intracellular drug, such as VP, to be released less in the extracellular space. Intracellularly following endocytosis as the pH is reduced below 6.5 in the endosomes/lysosomes, VP can be released following demicellization to target the nucleus.

The cellular uptake of spherical and filamentous micelles by macrophages shows that at moderate doses, fVPM cellular uptake by macrophages is a bottleneck that is sensitive to fVPM concentration whereas for sVPM it is not a bottleneck and cellular uptake to macrophages is high even at reduced dosages. This difference is likely due to the high aspect

ratio filamentous structures limiting the number of nanoparticles entering macrophages, via physically resisting macrophage engulfment.[30]

For cellular uptake by cancer cells, there is a significantly higher amount of sVPM entering cancer cells than fVPM as expected from the morphology-dependent cellular uptake effect, according to the normalized geometric mean fluorescence of cellular uptake. This observation translates into greater cell killing efficacy by sVPM compared with fVPM at several concentrations. Therefore, at the cellular level, spherical shape of VP-loaded micelles is shown to be more advantageous than filamentous shape. However, the capability of fVPM to avoid macrophage uptake is an advantageous feature at the systemic level, as shown by prolonged circulation and greater accumulation of the drug at the tumor site. This can improve anti-cancer efficacy as well as reduce off-target effects in macrophages and other phagocytic cells. Since we were able to tune the triblock copolymer chemistry to observe a morphological shift from spherical micelles to filamentous micelles, a similar approach could be used to fabricate PEG-PBAE-PEG micelles with alternative aspect ratios and cargos depending on the application. We found dramatic efficacy of VP in killing human triple negative breast cancer cells and human small cell lung cancer cells without the need of a photodynamic trigger. This non-photodynamic approach to using VP therapeutically could obviate the many of the detrimental side effects of using a photodynamic therapy, such as skin photosensitivity or systemic toxicity.[31] Moreover, VP acts on the Hippo pathway of tumor cells, hence would have minimal toxicity against normal cells. Alternatively, PEG-PBAE-PEG micelles for the delivery of VP could open up the possibility of combination therapies where the micelles could preferentially accumulate in the tumor compared to standard VP due to their shape properties and then a photodynamic trigger could further

potentiate their efficacy. This work represents an important advancement in the design of anisotropic pH-sensitive PBAE delivery systems and the utility of VP as a chemotherapeutic agent.

3.5 Conclusion

PBAE polymers are excellent candidates for polymeric drug delivery systems due to their intrinsic biodegradability and pH-sensitivity, but their use for non-nucleic acid delivery has been limited. Through novel PBAE polymer design and modification, we synthesized a PEG-PBAE-PEG micellar system of two different morphologies capable of encapsulating and delivering a water-insoluble, newly emerging anti-cancer therapeutic drug, verteporfin. The spherical micelles displayed excellent stability in both human serum and PBS buffers, with size measuring sub-150 nm. The creation of PBAE-based filamentous micelles with an average aspect ratio of 20 enabled avoidance of off-target macrophage uptake. Filamentous micelles were able to persist in systemic circulation longer and localize at flank glioblastoma tumor in comparison to spherical micelles *in vivo*. When treated to both human triple negative breast cancer cells and human small cell lung cancer cells *in vitro*, the micelles showed a larger therapeutic range when compared with free VP, being more effective at lower concentrations. This work demonstrates the first anisotropic PBAE-based self-assembled drug delivery system, and in addition, one of the first validations of VP nanomedicine as a direct anti-cancer approach without the need of external photodynamic therapy.

3.6 References

(1) Kataoka, K.; Harada, A.; Nagasaki, Y., Block copolymer micelles for drug delivery: Design, characterization and biological significance. *Adv Drug Deliv Rev* **2001,** 47, (1), 113-31.

(2) Xu, W.; Ling, P.; Zhang, T., Polymeric micelles, a promising drug delivery system to enhance bioavailability of poorly water-soluble drugs. *J Drug Deliv* **2013,** 2013, 340315.

(3) Williams, H. D.; Trevaskis, N. L.; Charman, S. A.; Shanker, R. M.; Charman, W. N.; Pouton, C. W.; Porter, C. J., Strategies to address low drug solubility in discovery and development. *Pharmacol Rev* **2013,** 65, (1), 315-499.

(4) Kim, J.; Wilson, D. R.; Zamboni, C. G.; Green, J. J., Targeted polymeric nanoparticles for cancer gene therapy. *J Drug Target* **2015,** 23, (7-8), 627-41.

(5) Ko, J.; Park, K.; Kim, Y. S.; Kim, M. S.; Han, J. K.; Kim, K.; Park, R. W.; Kim, I. S.; Song, H. K.; Lee, D. S.; Kwon, I. C., Tumoral acidic extracellular ph targeting of ph-responsive mpeg-poly(beta-amino ester) block copolymer micelles for cancer therapy. *J Control Release* **2007,** 123, (2), 109-15.

(6) Green, J. J.; Langer, R.; Anderson, D. G., A combinatorial polymer library approach yields insight into nonviral gene delivery. *Acc Chem Res* **2008,** 41, (6), 749-59.

(7) Nguyen, D. N.; Green, J. J.; Chan, J. M.; Longer, R.; Anderson, D. G., Polymeric materials for gene delivery and DNA vaccination. *Adv Mater* **2009,** 21, (8), 847-867.

(8) Kim, J.; Sunshine, J. C.; Green, J. J., Differential polymer structure tunes mechanism of cellular uptake and transfection routes of poly(beta-amino ester) polyplexes in human breast cancer cells. *Bioconjug Chem* **2014,** 25, (1), 43-51.

(9) Eltoukhy, A. A.; Chen, D.; Alabi, C. A.; Langer, R.; Anderson, D. G., Degradable terpolymers with alkyl side chains demonstrate enhanced gene delivery potency and nanoparticle stability. *Adv Mater* **2013,** 25, (10), 1487-93.

(10) Lombardo, D.; Kiselev, M. A.; Magazu, S.; Calandra, P., Amphiphiles self-assembly: Basic concepts and future perspectives of supramolecular approaches. *Adv. Cond. Matter Phys.* **2015**.

(11) Geng, Y.; Dalhaimer, P.; Cai, S.; Tsai, R.; Tewari, M.; Minko, T.; Discher, D. E., Shape effects of filaments versus spherical particles in flow and drug delivery. *Nat Nanotechnol* **2007,** 2, (4), 249-55.

(12) Lachelt, U.; Kos, P.; Mickler, F. M.; Herrmann, A.; Salcher, E. E.; Rodl, W.; Badgujar, N.; Brauchle, C.; Wagner, E., Fine-tuning of proton sponges by precise diaminoethanes and histidines in pdna polyplexes. *Nanomedicine* **2014,** 10, (1), 35-44.

(13) Holzer, M. P.; Solomon, K. D.; Vroman, D. T.; Sandoval, H. P.; Margaron, P.; Kasper, T. J.; Crosson, C. E., Photodynamic therapy with verteporfin in a rabbit model of corneal neovascularization. *Invest Ophthalmol Vis Sci* **2003,** 44, (7), 2954-8.

(14) Wilson, B. C.; Patterson, M. S., The physics, biophysics and technology of photodynamic therapy. *Phys Med Biol* **2008,** 53, (9), R61-109.

(15) Ichikawa, K.; Takeuchi, Y.; Yonezawa, S.; Hikita, T.; Kurohane, K.; Namba, Y.; Oku, N., Antiangiogenic photodynamic therapy (pdt) using visudyne causes effective suppression of tumor growth. *Cancer Lett* **2004,** 205, (1), 39-48.

(16) Konan-Kouakou, Y. N.; Boch, R.; Gurny, R.; Allemann, E., In vitro and in vivo activities of verteporfin-loaded nanoparticles. *J Control Release* **2005,** 103, (1), 83-91.

(17) Brodowska, K.; Al-Moujahed, A.; Marmalidou, A.; Horste, M. M. Z.; Cichy, J.; Miller, J. W.; Gragoudas, E.; Vavvas, D. G., The clinically used photosensitizer verteporfin (vp) inhibits yap-tead and human retinoblastoma cell growth in vitro without light activation. *Exp Eye Res* **2014,** 124, 67-73.

(18) Martinez-Gutierrez, J. C. R.-V., A.; Shah, S. R.; Riggins, G. J.; Quinones-Hinojosa, A., Meningioma growth inhibition and radiosensitization by the small molecule yap inhibitor verteporfin. *Neuro-Oncology* **2015,** 17, (suppl_5), v131.

(19) Shah, S. R.; David, J. M.; Tippens, N. D.; Mohyeldin, A.; Martinez-Gutierrez, J. C.; Ganaha, S.; Schiapparelli, P.; Hamilton, D. H.; Palena, C.; Levchenko, A.; Quinones-Hinojosa, A., Brachyury-yap regulatory axis drives stemness and growth in cancer. *Cell Rep* **2017,** 21, (2), 495-507.

(20) Liu-Chittenden, Y.; Huang, B.; Shim, J. S.; Chen, Q.; Lee, S. J.; Anders, R. A.; Liu, J. O.; Pan, D., Genetic and pharmacological disruption of the tead-yap complex suppresses the oncogenic activity of yap. *Genes Dev* **2012,** 26, (12), 1300-5.

(21) Chang, H. I.; Yeh, M. K., Clinical development of liposome-based drugs: Formulation, characterization, and therapeutic efficacy. *Int J Nanomedicine* **2012,** 7, 49-60.

(22) Kim, J.; Kang, Y.; Tzeng, S. Y.; Green, J. J., Synthesis and application of poly(ethylene glycol)-co-poly(beta-amino ester) copolymers for small cell lung cancer gene therapy. *Acta Biomater* **2016,** 41, 293-301.

(23) Kobayashi, H.; Watanabe, R.; Choyke, P. L., Improving conventional enhanced permeability and retention (epr) effects; what is the appropriate target? *Theranostics* **2013,** 4, (1), 81-9.

(24) Sunshine, J. C.; Peng, D. Y.; Green, J. J., Uptake and transfection with polymeric nanoparticles are dependent on polymer end-group structure, but largely independent of nanoparticle physical and chemical properties. *Mol Pharm* **2012,** 9, (11), 3375-83.

(25) Oh, N.; Park, J. H., Endocytosis and exocytosis of nanoparticles in mammalian cells. *Int J Nanomedicine* **2014,** 9 Suppl 1, 51-63.

(26) Hassan, S.; Prakash, G.; Ozturk, A.; Saghazadeh, S.; Sohail, M. F.; Seo, J.; Dockmeci, M.; Zhang, Y. S.; Khademhosseini, A., Evolution and clinical translation of drug delivery nanomaterials. *Nano Today* **2017,** 15, 91-106.

(27) Meyer, R. A.; Sunshine, J. C.; Perica, K.; Kosmides, A. K.; Aje, K.; Schneck, J. P.; Green, J. J., Biodegradable nanoellipsoidal artificial antigen presenting cells for antigen specific t-cell activation. *Small* **2015,** 11, (13), 1519-25.

(28) Zhang, J. X.; Hansen, C. B.; Allen, T. M.; Boey, A.; Boch, R., Lipid-derivatized poly(ethylene glycol) micellar formulations of benzoporphyrin derivatives. *J. Control. Release* **2003,** 86, (2-3), 323-38.

(29) Tzeng, S. Y.; Green, J. J., Subtle changes to polymer structure and degradation mechanism enable highly effective nanoparticles for sirna and DNA delivery to human brain cancer. *Adv. Healthc. Mater.* **2013,** 2, (3), 468-80.

(30) Champion, J. A.; Mitragotri, S., Role of target geometry in phagocytosis. *Proc Natl Acad Sci U S A* **2006,** 103, (13), 4930-4.

(31) Lucky, S. S.; Soo, K. C.; Zhang, Y., Nanoparticles in photodynamic therapy. *Chem. Rev.* **2015,** 115, (4), 1990-2042.

3.7 Figures & Tables

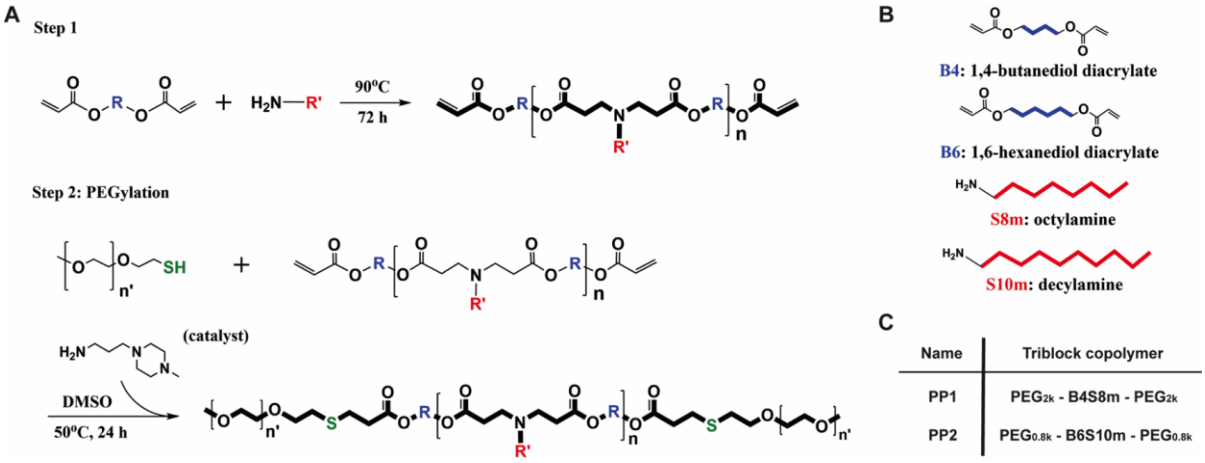

Figure 3.1. Schematic diagram of polymer synthesis. (A) Two-step Michael addition reaction for PEG-PBAE-PEG synthesis, (B) chemical structures of diacrylate and primary amine monomers used in the synthesis, and (C) nomenclature of final polymers.

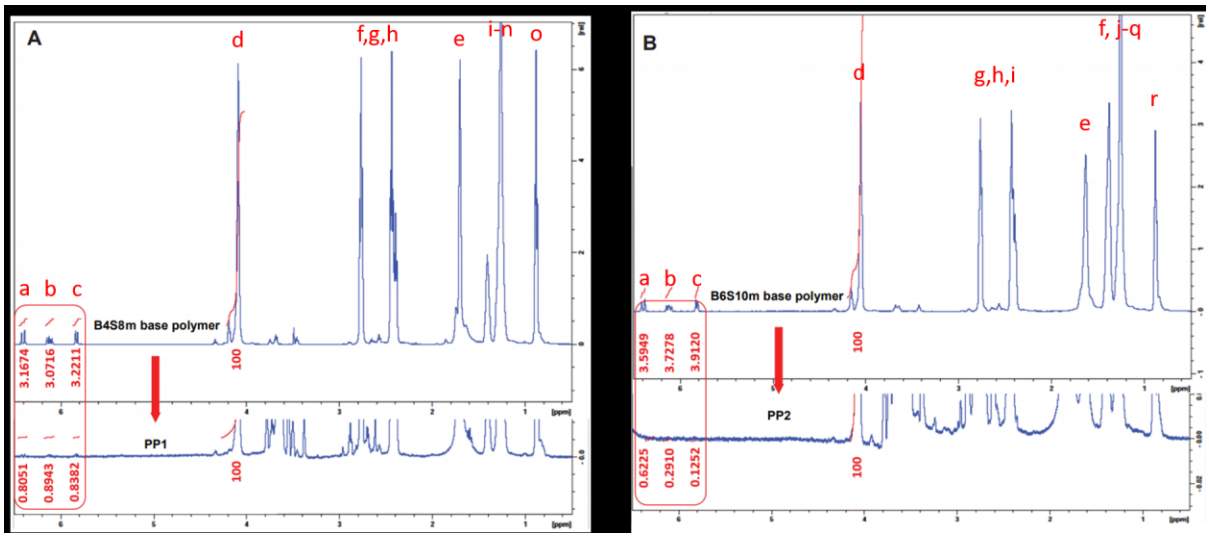

C

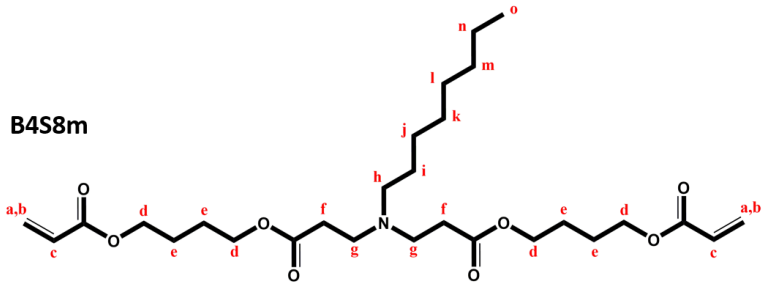

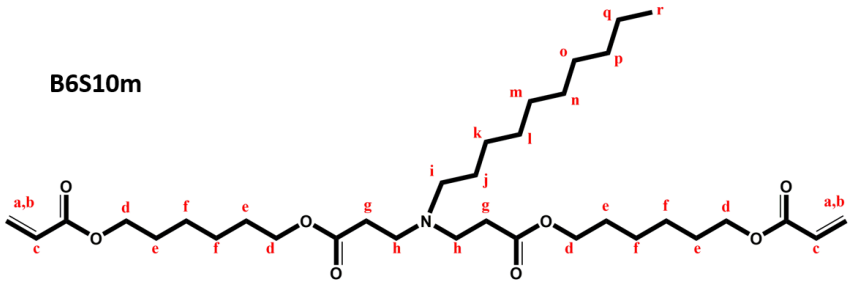

B4S8m:

0.85-1.00 (o, 3H, t, NCH2CH2CH2CH2CH2CH2CH2C***H3)***

1.2-1.35 (j/k/l/m/n, 10H, br, NCH2CH2C***H2***C***H2***C***H2***C***H2***C***H2***CH3),

1.35-1.45 (I, 2H, br, NCH2C***H2***CH2CH2CH2CH2CH2CH3),

1.65-1.8 (e, 4H, br, CH2CH2NCH2CH2(COO)CH2C***H2***C***H2***CH2(COO)),

2.3-2.4 (f/h, 6H, br, C***H2***CH2NCH2C***H2***(COO)CH2CH2CH2CH2(COO) and

NC***H2***CH2CH2CH2CH2OH),

2.6-2.7 (g, 4H, br, CH2C***H2***NC***H2***CH2(COO)CH2CH2CH2CH2(COO)),

3.9-4.05 (d, 4H, br, CH2CH2NCH2CH2(COO)C***H2***CH2CH2C***H2***(COO)),

5.9-6 (b, 1H, d, COOCH=C***H2***),

6.1-6.2 (c, 1H, dd, COOC***H***=CH2),

6.3-6.4 (a, 1H, d, COOCH=C***H2***)

B6S10m:

0.85-1.00 (r, 3H, t, NCH2CH2CH2CH2CH2CH2CH2CH2CH2C***H3)***

1.2-1.35 (k/l/m/n/o/p/q, 14H, br, NCH2CH2C***H2***C***H2***C***H2***C***H2***C***H2***C***H2***C***H2***CH3),

1.35-1.45 (j/f, 6H, br, NCH2C***H2***CH2CH2CH2CH2CH2CH2CH2CH3 and

CH2CH2NCH2CH2(COO)CH2CH2C***H2***C***H2***CH2CH2(COO)),

1.65-1.8 (e, 4H, br, CH2CH2NCH2CH2(COO)CH2C***H2***CH2CH2C***H2***CH2(COO)),

2.3-2.4 (g/I, 6H, m, C***H2***CH2NCH2C***H2***(COO)CH2CH2CH2CH2(COO) and

NC***H2***CH2CH2CH2CH2OH),

2.6-2.7 (h, 4H, t, CH2C***H2***NC***H2***CH2(COO)CH2CH2CH2CH2(COO)),

3.9-4.05 (d, 4H, br t, CH2CH2NCH2CH2(COO)C***H2***CH2CH2CH2CH2C***H2***(COO)),

5.9-6 (b, 1H, d, COOCH=C***H2***),

6.1-6.2 (c, 1H, dd, COOC***H***=CH2),

6.3-6.4 (a, 1H, d, COOCH=C***H2***)

PBAE base polymer	Molecular Weight (Da)	Partition Coefficient (logP)
B4S8m	5100	4.71
B6S10m	4305	6.63

Figure 3.2. Polymer characterization. ^{1}H NMR spectra for the backbone PBAE (top) and the PEG-thiol endcapped PBAE (bottom) for (A) PP1 and (B) PP2 polymers. The absence of the acrylate peaks (red box) in the copolymer plot confirms that methoxy-PEG-thiol has successfully conjugated to the diacrylate ends of the PBAE base polymer. (C) Polymer structure of B4S8m and B6S10m PBAE base polymers with letters to indicate corresponding hydrogen peaks in NMR spectra. (D) Molecular weight and partition coefficient of two base PBAE polymers used to synthesize PEGylated triblock copolymer.

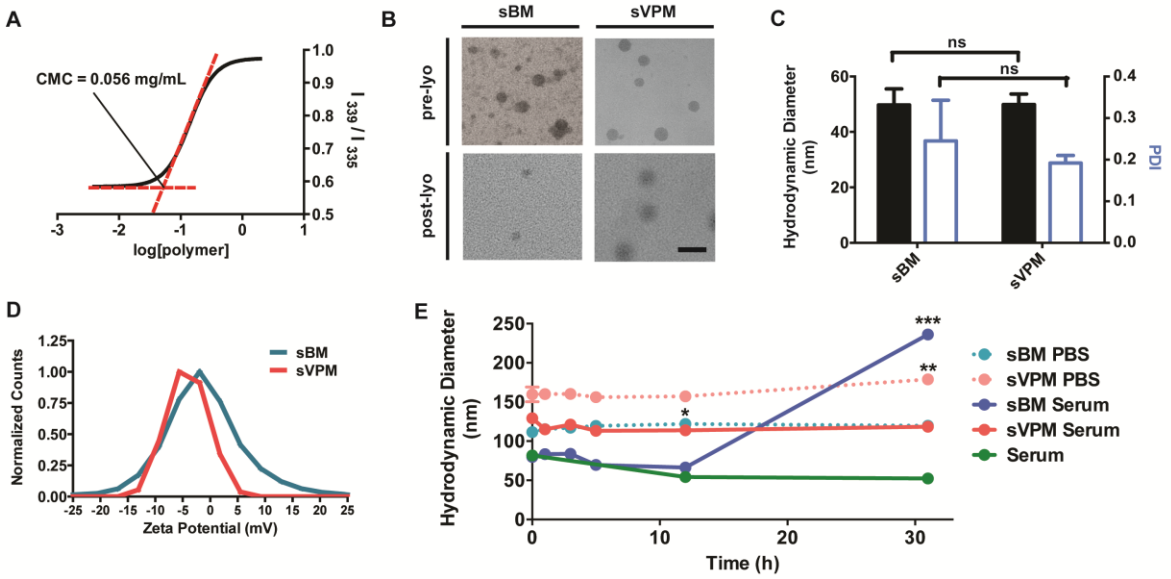

Figure 3.3. Spherical PP1 micelle characterization. (A) Critical micelle concentration (CMC) measured by pyrene sensitivity assay, (B) TEM images of both sBM and sVPM pre- and post-lyophilization (scale bar = 100 nm), (C) DLS mean size and PDI of both (sBM) and (sVPM) (n=3, mean ± SD, Student's t-test), (D) zeta potential of sBM and sVPM measured with Zetasizer, and (E) stability of sBM and sVPM in 1x PBS and human serum (45% serum, 55% 1X PBS) at room temperature for 31 hours (n=3, mean ± SD, One-way ANOVA with Dunnett post-hoc test compared to the initial size).

A

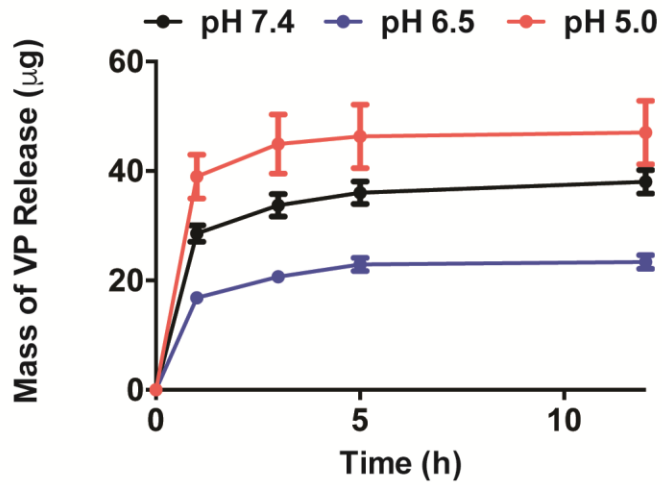

B

	Time (hr)			
	1	3	5	12
pH 5.0 vs pH 6.5	****	****	****	****
pH 5.0 vs pH 7.4	**	**	**	*
pH 6.5 vs pH 7.4	**	**	**	***

Figure 3.4. pH-sensitive VP release kinetics. Release of VP from sVPM at 37°C at 1, 3, 5, and 12 hour time points in buffers prepared to pH 7.4, 6.5, and 5.0 (n=3, mean ± SD).

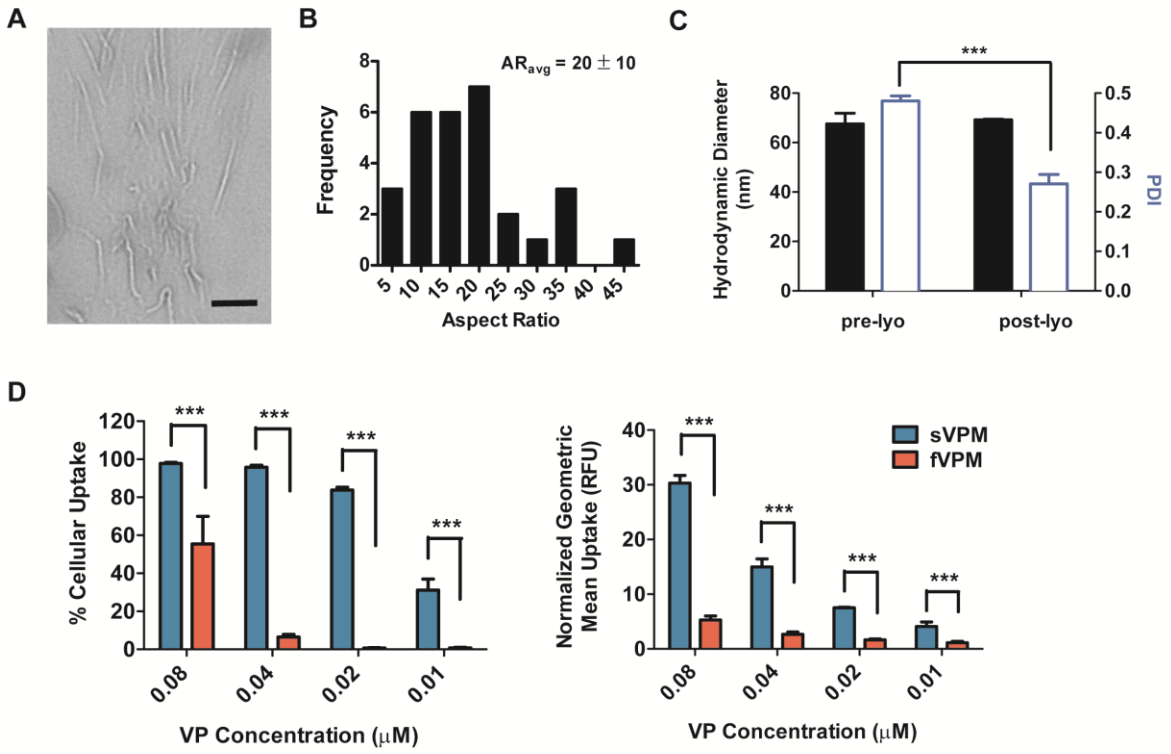

Figure 3.5. Filamentous PP2 micelle (fVPM) characterization. (A) TEM image (scale bar = 100 nm), (B) aspect ratio (AR) distribution of fVPM post-lyophilization reconstituted in water, (C) DLS mean size and PDI of fVPM following reconstitution with 1x PBS (n=3, mean ± SD), and (D) sVPM and fVPM uptake efficiency in RAW 264.7 cells and geometric mean of uptake normalized to untreated cells measured by flow cytometry after treatment for 1 hr at equivalent VP concentrations (n=4, mean ± SD, One-way ANOVA with Bonferroni post-hoc test).

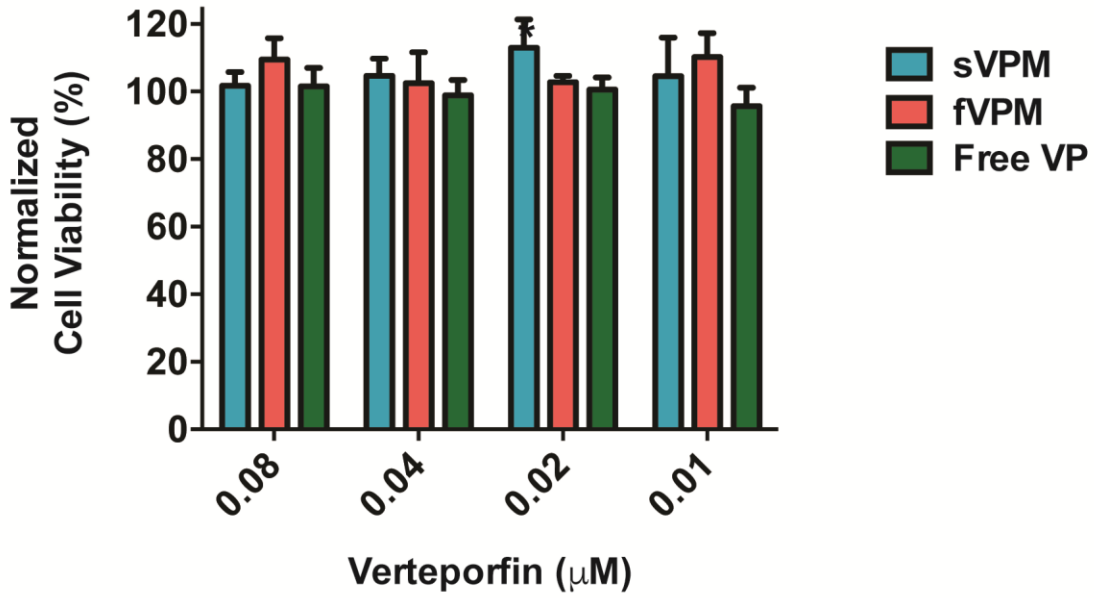

Figure 3.6. RAW 264.7 cell viability. Metabolic activity measured by MTS assay of macrophages 24 h post-treatment with free VP, sVPM, and fVPM at concentrations ranging from 0.01 – 0.08 μM (n=4, mean ± SD, One-way ANOVA with Tukey post-hoc test).

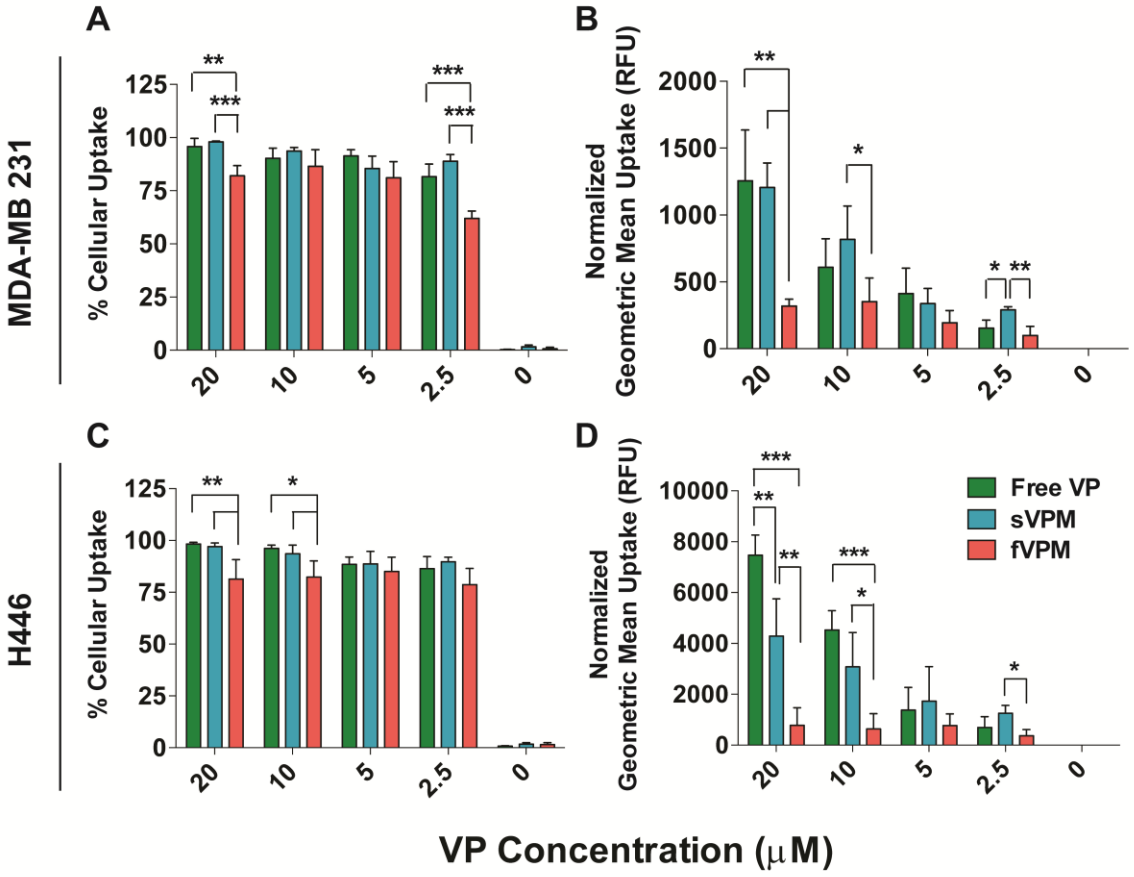

Figure 3.7. Cancer cell uptake. (A/C) Percentage of cells that internalize VP in human triple-negative breast cancer (MDA-MB 231) and human small cell lung cancer (H446) cells incubated with free VP, sVPM, and fVPM at equivalent VP concentrations from 2.5-20 μM for 1.5 hr and (B/D) the corresponding geometric mean fluorescence of cellular uptake normalized to the untreated condition (RFU) (n=4, mean ± SD, One-way ANOVA with Tukey post-hoc test).

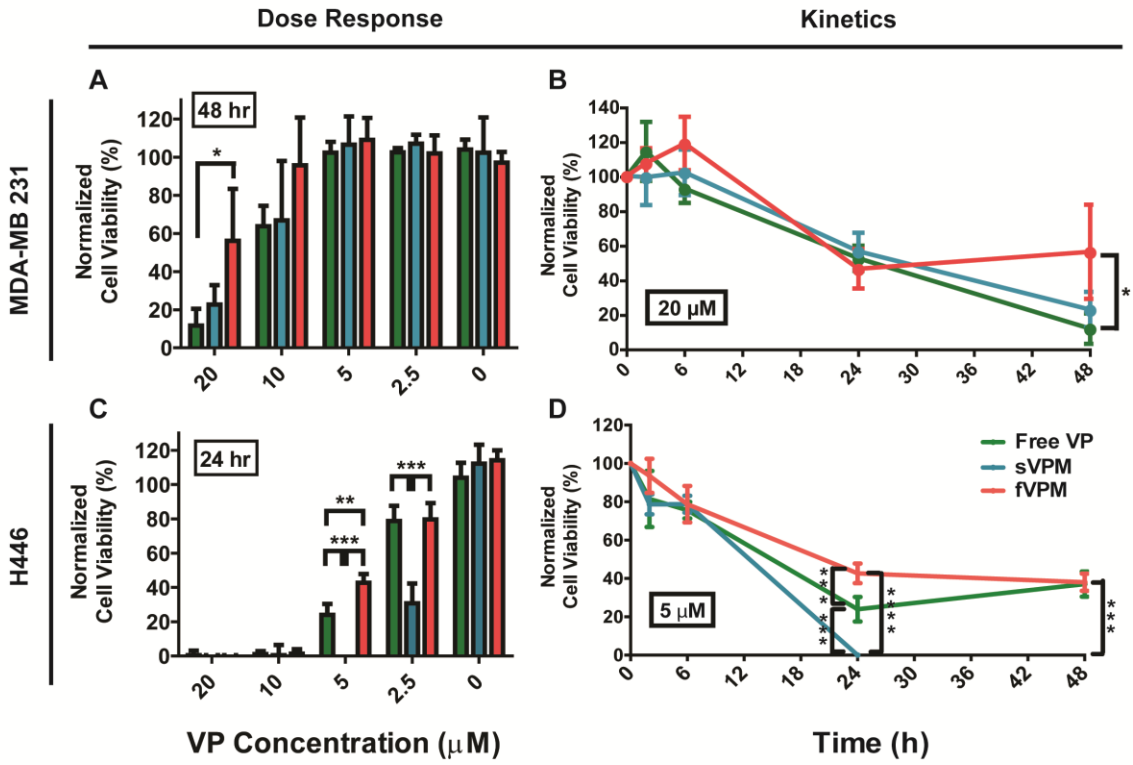

Figure 3.8. VP-induced cell death. (A/C) VP delivery dose-response to cell viability in MDA-MB 231 and H446 cells incubated with free VP, sVPM, and fVPM at equivalent VP concentrations from 2.5- 20 µM for 2 hrs and measured over time, and (B/D) cell killing kinetics measured at 2, 6, 24, and 48 hr time points at stated VP concentrations (n=4, mean ± SD, One-way ANOVA with Tukey post-hoc test).

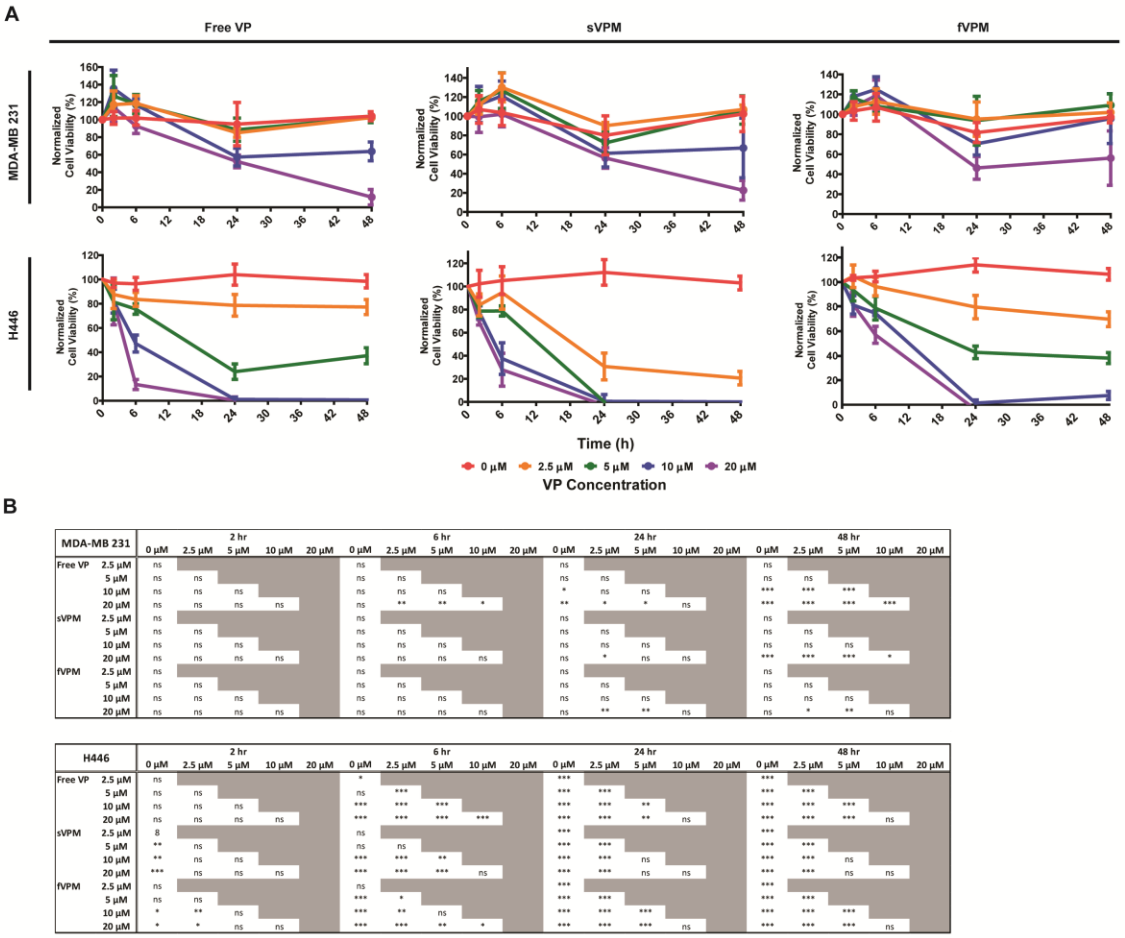

Figure 3.9. VP-induced cell death. (A) Cell killing kinetics with free VP, sVPM, and fVPM measured at 2, 6, 24, and 48 hr time points at equivalent VP concentrations from 2.5 - 20 µM (n=4, mean ± SD, One-way ANOVA with Tukey post-hoc test), (B) statistical analysis summary, and (C) representative bright-field image of MDA-MB 231 and H446 cells at stated VP concentration at 24 hr.

A

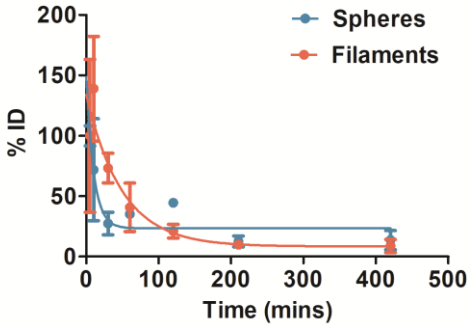

	Spheres	Filaments
Half-life (mins)	7.144	34.36
R square	0.7540	0.7729

B

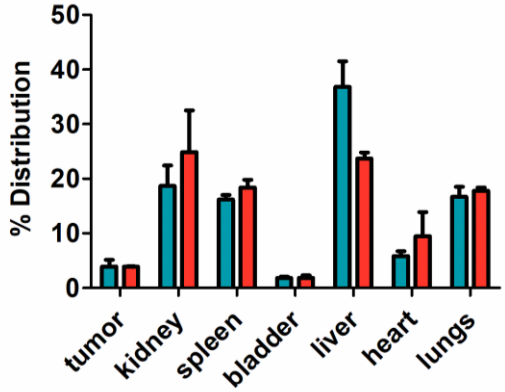

8 hr

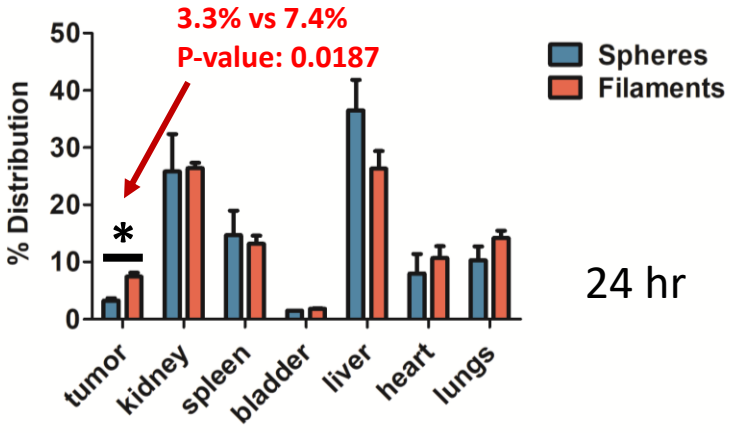

24 hr

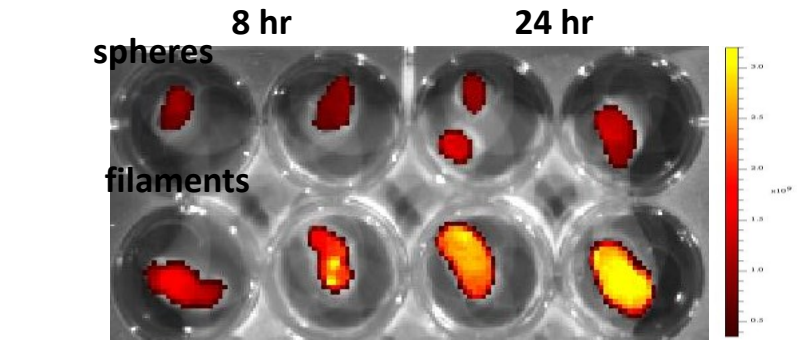

Figure 3.10. Pharmacokinetics and biodistribution of spherical and filamentous micelles. IRD-loaded micelles are injected via tail-vein into nude mice bearing human glioblastoma in the flank. (A) Fluorescence signal from IRD-loaded micelles in blood collected at different time points normalized to time = 0 min. Exponential decay function is fitted to calculate the half-life. (B) Fluorescence signal from different organs harvested at 8 hr and 24 hr time points, normalized to the total fluorescence from all organs (n=4, mean ± SD, two-tailed Student t-test for tumor comparison).

Chapter 4

High-throughput *in vivo* screening of biomaterial-mediated tissue targeting of PBAE nanoparticles using DNA barcodes

4.1 Introduction

Gene therapy as a modality to treat disorders with genetic origin has gained much research and clinical attention. Replacing or eliminating genetic defects with exogenous DNA or RNAi, respectively, has the advantage of potentially curing diseases and not just treating symptoms.[1,2] More recently, using genetic engineering to reprogram cells *ex vivo* for applications in cell therapy has shown some success, such as the recent FDA approval for CAR T-cell therapy.[3] However, there remains the need for improvement in the design of a safe and effective vector that can deliver the nucleic acids to the target site. While modified viruses are widely investigated for their high transduction efficiency, their safety concerns and design limitations have triggered parallel effort to engineering biocompatible synthetic polymers as gene delivery vectors.[4-6]

Poly(beta-amino ester) (PBAE) is a class of biodegradable polymer that becomes positively charged at low pH and complexes with negatively charged nucleic acids to form nanoparticles.[7] PBAE nanoparticles have been shown to effectively transfect multiple types of cells, including stem cells and various cancer cells.[8-11] An important property that

Parts of this chapter were completed based on research in collaboration with Vaughan H, Zamboni CG, Wilson DR, Shin A, and Green JJ.

strengthens the utility of PBAEs as gene delivery vectors is their tunability of chemical structure via synthesis design, which can lead to a library of polymers with differential structures.[12] Our group has also shown previously that individual PBAEs or group of PBAEs with similar structures can have specific structure-function relationships that can improve aspects of intracellular delivery such as the cellular uptake, endosomal escape, transfection, and cell-type specificity.[11,13-15]

This chapter expands on PBAE's structure-function relationships beyond the cellular level to systemic circulation and tissue targeting. Nanoparticle optimization for passive and active targeting modalities based on particle size and specific ligand-receptor binding, respectively, has been an active area of research, but less attention has been given to a biomaterial's potential inherent property to control tissue targeting.[16] Previous literature has shown that different forms (linear or branched) and molecular weights of polyethylenimine (PEI) can result in differential tissue targeting.[17] Another group used a layer-by-layer technique to expose different biomaterials on the surface to also show unique biodistribution of each nanoparticle type.[18] Here, we demonstrate that specific structures of PBAEs can determine the final destination of the resulting nanoparticles in an organism once injected into the blood stream. Such an *in vivo* biodistribution study with many possible variant structures of the PBAE polymer could quickly become cost- and time-ineffective, as well as prone to variability between animals. Hence, we also validate a novel high-throughput method using circular plasmid DNA as a barcode to investigate biomaterial-mediated tissue targeting and subsequent transfection from a library of PBAE polymers.

4.2 Methods

Materials

1,4-butanediol diacrylate (B4), 4-amino-1-pentanol (S4), 5-amino-1-pentanol (S5), 1-(3-aminopropyl)-4-methylpiperazine (E7) (Alfa Aesar), 1,5-pentanediol diacrylate (B5) (Monomer Polymer & Dajac Labs), 2-methylpentane-1,5-diamine (E4) (TCI America), and 2-(3-aminopropylamino)ethanol (E6) (Fluka) were purchased and used as received. pEGFP-N1 DNA was purchased from Elim Biopharmaceuticals and amplified by Aldevron, Fargo, ND. Purelink Genomic DNA Extraction kit (Thermo Fisher Scientific), PowerUp SYBR Green Master Mix (Applied Biosystems, Foster City, CA), Label IT®-Tracker™ Cy™3 and Cy™5 kit (Mirus Bio LLC, Madison, WI) were obtained from commercial vendors and used per manufacturer's instructions.

Polymer synthesis and characterization

Linear PBAE polymer is synthesized via a two-step Michael addition reaction as shown in **Figure 4.1**. First, acrylate-terminated base polymer is created by reacting a diacrylate monomer with a primary amine-containing side chain monomer at a stoichiometric molar ratio of 1.2:1 for 24 h at 90^{o}C. Then, the base polymer is reacted with 20-fold excess molar amount of primary amine-containing end-capping molecule in THF for 3 h at room temperature. The final polymer was ether-precipitated and stored in DMSO at 100 mg/mL in -20^{o}C. A total of 9 PBAE polymers were synthesized using 2 different diacrylate monomers, 1,4-butanediol-diacrylate (B4) and 1,5-pentanediol-diacrylate (B5), 3 side chain monomers, 3-amino-1-propanol (S3), 4-amino-1-butanol (S4), and 5-amino-1-pentanol (S5), and 3 end-

capping molecules. Nomenclature for the final polymer follows the label of each monomer used. For example, a polymer synthesized with B4, S5, and E7 is named B4S5E7 or 457 in short. The molecular weights of three base polymers were determined with Bruker Avance III 500 MHz ^{1}H NMR spectrometer and Bruker TopSpin software by analyzing the AUC ratio between hydrogen peaks in repeating and non-repeating unit (**Table 1**).

Nanoparticle formulation and characterization

Nanoparticles were formed by bulk mixing of PBAE polymer and plasmid DNA to allow electrostatic interaction. PBAE polymer in DMSO at 100 mg/mL and plasmid DNA in water at 1 mg/mL were diluted to 15 mg/mL and 0.5 mg/mL, respectively, using 25 mM sodium acetate (NaAc) buffer at pH 5.0. Equal volume of polymer and DNA solutions were mixed and incubated for 10 min to form nanoparticles. This ensures the mass ratio of polymer to DNA to be consistent at 30 w/w across different nanoparticles.

Hydrodynamic diameter and zeta potential were measured by dynamic light scattering using Zetasizer Nano ZS (Malvern Instruments, detection angle 173°, 633 nm laser). Nanoparticles were diluted to polymer concentration of 1 mg/mL with 25 mM NaAc buffer to a final volume of 100 μL and 750 μL prior to size and surface charge measurements, respectively. The mean and standard deviation were calculated.

Plasmid preparation

A total of five plasmids were used, three encoding for fluorescent proteins and two encoding random nucleotide sequences. In order to ensure that all plasmids were similar in size and had the same backbone, pEGFP-N1 was used as the base plasmid and genes encoding other fluorescent proteins, mOrange and iRFP, or two random sequences were cloned in to replace EGFP gene.

For two plasmids with random sequences, two random 1500–b.p. sequences were first generated using an online software with 25% fraction each of A, C, G, and T nucleotides (URL - http://users-birc.au.dk/biopv/php/fabox/random_sequence_generator.php). The double-stranded linear DNAs were custom ordered using gBlock Gene Fragments (IDT, Inc, Skokie, IL). All plasmids were stored at 1 mg/mL in sterile water at 4°C.

Primer optimization

In order to generate forward and reverse primers specific to each plasmid DNA and avoid non-specific amplification of other plasmids or murine genomic DNA, Basic Local Alignment Search Tool (BLAST) from National Institute of Health's National Center for Biotechnology Information was used to extensively check for homology. First, Primer-BLAST was used to generate 50 primer candidates for each plasmid that match the conditions listed in **Figure 4.2A**. Then, the primer candidates for each plasmid were used as query sequence in BLASTn to check for homology against other plasmids as well as mouse genome. Primer candidates that showed undesired homology (matching sequence) in the last 6 base pairs or in more than 10 base pairs total were excluded (**Figure 4.2B**). Lastly, the top-scoring candidate for each plasmid was checked for hairpin, self-dimerization and hetero-

dimerization using IDT OligoAnalyzer 3.1. The final primer sequences were custom ordered (IDT, Inc, Skokie, IL), and stored as 3 μM aliquots in -20ºC.

Primer sequences were experimentally checked for their specificity toward the corresponding plasmids by quantitative real time polymerase chain reaction (qRT-PCR) and gel electrophoresis. Briefly, 100 ng of each plasmid was amplified against each of the five primer pairs to determine C_T values and generate the melt curve. 2 μL of plasmid DNA, 2 μL of 3 μM forward primer, 2 μL of 3 μM reverse primer, and 14 μL of PowerUp SYBR Green Master Mix solutions were mixed for qRT-PCR amplification. PCR reaction consisted of initial polymerase activation stage at 95ºC for 2 min, followed by 40 cycles of denaturation at 95ºC for 15 sec, annealing at 55ºC for 15 sec, and elongation at 72ºC for 1 min. After PCR amplification, the 25 amplified products along with DNA ladder were also run through gel electrophoresis in 1% agarose gel.

Föster resonance energy transfer (FRET) between Cy3- and Cy5-labeled nanoparticles

Förster resonance energy transfer (FRET) analysis was conducted to investigate any intermixing between different nanoparticles co-dispersed in a single solution. One batch of nanoparticles was formulated using PBAE polymer 447 with Cy3-labeled pDNA, and another batch was formulated using a different PBAE polymer 457 with Cy5-labeled pDNA. The two nanoparticle batches were incubated together with gentle pipette mixing, and the emission spectrum was read with Cy3 excitation wavelength (550 nm) to measure peak Cy3 (570 nm) and Cy5 (670 nm) emission intensities using spectrofluorophotometry (Shimadzu

RF-5301). A mixed plasmid positive control batch of nanoparticles was formulated by complexing PBAE polymer 447 with a 1:1 mixture of Cy3-labeled and Cy5-labeled DNAs.

Generating standard curves of the amount of plasmid vs. C_T values for each organ

Standard curves were generated to be able to determine the absolute amount of plasmid present in PCR samples based on C_T values from the amplification plot. The plot of overall workflow is shown in **Figure 4.3**. 5-7 week old female balb/c mouse was euthanized and major organs – liver, kidneys, spleen, lungs, heart, bladder – were harvested. Organs were washed with 1X PBS three times, cut into small pieces with a razor blade, and minced between the frosted ends of two microscope slides. Then, 10 mg of liver sample and 5 mg of samples from all other organs were separately placed into eppendorf tubes. Tissues were digested using digestion solution provided in the Purelink Genomic DNA Extraction kit. Following the digestion and prior to the subsequent steps instructed in the manual, 10X dilutions of each plasmid DNA, from 100 ng to 100 pg, were spiked into digested tissue. Once DNA was purified through the extraction column, it was diluted with water 10-fold for liver samples and 2-fold for all other organ samples. 2 μL of extracted DNA, 2 μL of 3 μM forward primer, 2 μL of 3 μM reverse primer, and 14 μL of PowerUp SYBR Green Master Mix solutions were mixed for qRT-PCR amplification. The same PCR reaction protocol was used as described above.

High-throughput in vivo screening

Biodistribution of 13 different PBAE polymers was tested *in vivo* in high-throughput manner in 5-7 week old female balb/c mice. The workflow is again shown in **Figure 4.4**, however, this chapter only discusses the results from qRT-PCR, and not from flow cytometry. For each mouse, 200 μL of a cocktail solution with five different PBAE nanoparticles was prepared for tail-vein injection. Each of the five nanoparticles was paired with one of the five plasmid DNAs to serve as the identifier barcode (**Table 4.2**). Each nanoparticle formulation had 10 μg pDNA for a total of 50 μg pDNA in the cocktail solution. Five additional mice were injected with 447 30 w/w nanoparticles alone with 50 μg DNA dose as controls to compare biodistribution with high-throughput samples. All nanoparticle-injected mice were sacrificed 30 min post injection for DNA extraction. Major organs – liver, kidneys, spleen, lungs, heart, bladder – were harvested, washed with 1X PBS three times, cut into small pieces with a razor blade, and minced between the frosted ends of two microscope slides. Then, 10 mg of liver sample and 5 mg of samples from all other organs were separately placed into eppendorf tubes. Plasmid DNA was extracted from minced tissues using the Purelink Genomic DNA Extraction kit and following the manual instruction. Once DNA was purified through the extraction column, it was diluted with water 10-fold for liver samples and 2-fold for all other organ samples. 2 μL of extracted DNA, 2 μL of 3 μM forward primer, 2 μL of 3 μM reverse primer, and 14 μL of PowerUp SYBR Green Master Mix solutions were mixed for qRT-PCR amplification. The same PCR reaction protocol was used as described above.

4.3 Results & Discussion

Nanoparticle characterization

Nanoparticles formulated with 9 different PBAE polymers were characterized based on particle size and surface charge. These physicochemical properties of these nanoparticles were determined to hold as potential confounding variables for affecting biodistribution. As shown in **Figure 4.5**, the hydrodynamic diameter measured by dynamic light scattering ranged from 150 – 200 nm for most nanoparticle formulations. 446 polymer / DNA particles resulted in aggregation, yielding particles greater than a micron in diameter. 200 – 250 nm nanoparticles were made with PBAEs 444 and 536, while sub-200 nm nanoparticles were made with 537 PBAE polymers. All nanoparticles formed from these linear PBAE polymers showed positive zeta potential between +30 to +40 mV, due to exposure of positively charged polymer on the particle surfaces.

Melt curve and gel electrophoresis showing primer specificity

Primers were selected using BLAST using the most conservative conditions to ensure the greatest specificity to each plasmid used in the study. The forward and reverse primer pairs for each plasmid were designed to produce an approximately 100-basepair long amplicon. Each of the primer pairs specific to the corresponding plasmid was mixed with all five plasmids individually for qRT-PCR reaction to confirm the specificity. As shown in **Figure 4.6A**, only conditions with correctly matched primers and plasmid resulted in amplification. Also, each set of primers was run alone or mixed with other primer sets, and did not yield any false positive result from self- or hetero-dimerization. In addition, the melt curve also showed a clean single peak only for correctly matched conditions, which indicates

that there is no non-specific amplification occurring in the PCR reaction (**Figure 4.6B**). PCR-amplified products were run on gel electrophoresis to confirm that the amplicons had the expected length, based on our primer design. Gel image shows bands appearing for primer-plasmid matching conditions only at the height level of approximately 100-basepair mark on the DNA ladder (**Figure 4.6C**). When the primers were mixed with fresh animal tissue lysates from all major organs listed above for PCR reaction as the final quality control test for the designed primers, they did not show any amplification (data not shown). All of these observations strongly confirmed the specificity of each primer set to its corresponding plasmid.

FRET analysis showing the absence of nanoparticle intermixing

The high-throughput screening method requires different nanoparticles be injected as a cocktail solution into a single animal and be individually identified in tissue lysates by the plasmid DNA barcodes. Therefore, it is critical to ensure that a nanoparticle formulation maintains the same plasmid DNA from the original synthesis step until the detection step from tissue lysates. We employed a FRET tool to validate that there is no intermixing of nanoparticles in the cocktail solution that would void plasmid DNA's role as the barcode for each PBAE nanoparticle. Plasmid DNA was either labeled with Cy3 or Cy5 fluorophores, which act as FRET pair dyes when in close proximity to each other. **Figure 4.7A** shows fluorescence intensity measured at Cy3's emission wavelength when samples are excited at Cy3's excitation wavelength. A positive control sample, where Cy3-labeled and Cy5-labeled plasmid DNAs are used together to form a single nanoparticle batch, demonstrated a

reduction in Cy3 emission intensity, as some energy is absorbed by neighboring Cy5 fluorophores. In contrast, FRET does not occur in the condition where two separate nanoparticles each formulated first with Cy3-labeled or Cy5-labeled DNA are then co-incubated together in a cocktail solution, demonstrating that there is no exchange of plasmid DNAs between two PBAE nanoparticle types that would allow both fluorophores to be positioned close enough to transfer energy. This is further supported by an increase in Cy5 emission intensity for the positive control sample and a drop to baseline level for the cocktail solution condition (**Figure 4.7B**). The absence of FRET signal in a cocktail solution verifies that different nanoparticles are able to retain their own specific plasmid DNAs.

Standard curve of plasmid DNA concentration vs. C_T values

qRT-PCR is often used to produce results in terms of relative expression level of the target gene with respect to a housekeeping gene, such as GAPDH. However, as Ho *et al*. have shown, standard curves can be made for each plasmid DNA in each organ / tissue lysate in terms of DNA concentration vs. amplification C_T values for absolute quantification of the amount of DNA.[19] We produced 30 different standard curves with $R^2 > 0.96$ for all possible combinations from 5 plasmids and 6 major organs. Each panel in **Figure 4.8A** shows the standard curves for each plasmid in 6 different organs. Plasmid amplification was not affected by the type of tissue lysates, as demonstrated by the overlapping standard curves in each panel. The same data was used to plot **Figure 4.8B**, where each panel now shows standard curves for 5 plasmids in each organ. As expected, distinct standard curves were

created for different plasmids in the same organ / tissue lysate, indicating that PCR was dependent on the amplification efficiency of specific primers-plasmid pair.

High-throughput screening of biomaterial-mediated tissue targeting

With the generated standard curves, the absolute amount of each plasmid DNA accumulated in different organs 30 min after injection was calculated by qRT-PCR. The accumulation of each plasmid DNA can be translated to that of each nanoparticle type due to the specific PBAE structure used in the formulation. **Figure 4.9** shows the biodistribution of each PBAE nanoparticle formulation in all organs, while **Figure 4.10** shows the accumulation of all PBAE nanoparticles in each organ. As expected, there was the greatest proportion of accumulation in the liver for all PBAE nanoparticle types, as it is one of the main organs responsible for reticuloendothelial system (RES)-mediated clearance. There was near zero signal detected from the bladder. As such, there was no statistically significant difference between PBAE nanoparticles in the liver, spleen, and bladder. However, we observed significantly higher amount of 446 and 536 PBAE nanoparticles in the kidneys, lungs, and heart. In the case of 446 nanoparticle, accumulation in the lungs may be explained by its large particle size rather than the polymer structure. But particle size may be insufficient to explain its buildup in the kidneys and heart. 536 nanoparticle's high accumulation in these three organs is more likely to be independent of particle's physicochemical properties since another formulation (444) with similar physicochemical properties showed a different biodistribution profile.

qRT-PCR shows the accumulation of nanoparticles in an organ over time, however its efficacy does not necessarily translate to the final function of these nanoparticles, gene transfection. As shown by previous studies, there are unique structure-function relationships at the cellular level affecting the cellular uptake, endosomal escape, and transfection. Therefore, it is critical to conduct a follow-up study to investigate level of transfection by these nanoparticles (flow cytometry for fluorescence read-out or qRT-PCR of mRNA read-out) in parallel to qRT-PCR from the same tissue sample. This would allow a more holistic perspective to selecting the PBAE nanoparticle formulation most optimal for specific target and application. This is one of the advantages of our DNA barcode system, in comparison to other previously reported system, such as using a short linear DNA sequence as the barcode.[20] A short linear DNA barcode may be a confounding variable since it is an extra material added to a nanoparticle formulation, may be more susceptible to inter-nanoparticle mixing, and is unable to provide a functional output to determine transfection efficacy.

Finally, in order to further validate our novel high-throughput tissue targeting screening method, we compared the biodistribution of 447 nanoparticles when injected alone in mice to that when injected as a cocktail solution along with four other nanoparticle formulations. There was no statistical difference in the proportion of nanoparticle accumulation in the major organs between the two conditions (**Figure 4.11**). This further validates that using a high-throughput approach does not interfere with the pharmacokinetic behavior of the individual nanoparticle formulations.

4.4 Conclusion

With gene therapy emerging as one of the major clinical options to cure various diseases, optimizing the delivery vectors for nucleic acids has become an active area of research. Particularly, different targeting modalities have been investigated to achieve specific biodistribution with gene delivery vehicles. We explored the capability of a polymer's chemical structure to direct specific tissue targeting. A novel high-throughput method using DNA as barcodes was successfully validated by comparing biodistribution profile of a nanoparticle formulation from independently tested animals against that from high-throughput animals. We then showed that 446 and 536 PBAE structures accumulate to the kidneys and lungs significantly more than other polymer structures, making them ideal candidates for gene delivery vectors targeting disease in those organs. Future study of assessing tissue targeting by PCR and transfection efficacy by functional output simultaneously would allow more holistic approach to optimizing polymeric vectors from injection to end-point transfection.

4.5 References

(1) Jafari, M.; Soltani, M.; Naahidi, S.; Karunaratne, D. N.; Chen, P., Nonviral approach for targeted nucleic acid delivery. *Curr Med Chem* **2012,** 19, (2), 197-208.

(2) Viola, J. R.; El-Andaloussi, S.; Oprea, II; Smith, C. I., Non-viral nanovectors for gene delivery: Factors that govern successful therapeutics. *Expert Opin Drug Deliv* **2010,** 7, (6), 721-35.

(3) Prasad, V., Immunotherapy: Tisagenlecleucel - the first approved car-t-cell therapy: Implications for payers and policy makers. *Nat Rev Clin Oncol* **2018,** 15, (1), 11-12.

(4) Sharon, D.; Kamen, A., Advancements in the design and scalable production of viral gene transfer vectors. *Biotechnol Bioeng* **2018,** 115, (1), 25-40.

(5) Thomas, C. E.; Ehrhardt, A.; Kay, M. A., Progress and problems with the use of viral vectors for gene therapy. *Nat Rev Genet* **2003,** 4, (5), 346-58.

(6) Yin, H.; Kanasty, R. L.; Eltoukhy, A. A.; Vegas, A. J.; Dorkin, J. R.; Anderson, D. G., Non-viral vectors for gene-based therapy. *Nat Rev Genet* **2014,** 15, (8), 541-55.

(7) Kim, J.; Kang, Y.; Tzeng, S. Y.; Green, J. J., Synthesis and application of poly(ethylene glycol)-co-poly(beta-amino ester) copolymers for small cell lung cancer gene therapy. *Acta Biomater* **2016,** 41, 293-301.

(8) Shmueli, R. B.; Sunshine, J. C.; Xu, Z.; Duh, E. J.; Green, J. J., Gene delivery nanoparticles specific for human microvasculature and macrovasculature. *Nanomedicine* **2012,** 8, (7), 1200-7.

(9) Tzeng, S. Y.; Green, J. J., Subtle changes to polymer structure and degradation mechanism enable highly effective nanoparticles for sirna and DNA delivery to human brain cancer. *Adv Healthc Mater* **2013,** 2, (3), 468-80.

(10) Tzeng, S. Y.; Hung, B. P.; Grayson, W. L.; Green, J. J., Cystamine-terminated poly(beta-amino ester)s for sirna delivery to human mesenchymal stem cells and enhancement of osteogenic differentiation. *Biomaterials* **2012,** 33, (32), 8142-51.

(11) Zamboni, C. G.; Kozielski, K. L.; Vaughan, H. J.; Nakata, M. M.; Kim, J.; Higgins, L. J.; Pomper, M. G.; Green, J. J., Polymeric nanoparticles as cancer-specific DNA delivery vectors to human hepatocellular carcinoma. *J Control Release* **2017,** 263, 18-28.

(12) Green, J. J.; Langer, R.; Anderson, D. G., A combinatorial polymer library approach yields insight into nonviral gene delivery. *Acc Chem Res* **2008,** 41, (6), 749-59.

(13) Bishop, C. J.; Abubaker-Sharif, B.; Guiriba, T.; Tzeng, S. Y.; Green, J. J., Gene delivery polymer structure-function relationships elucidated via principal component analysis. *Chem Commun (Camb)* **2015,** 51, (60), 12134-7.

(14) Kim, J.; Sunshine, J. C.; Green, J. J., Differential polymer structure tunes mechanism of cellular uptake and transfection routes of poly(beta-amino ester) polyplexes in human breast cancer cells. *Bioconjug Chem* **2014,** 25, (1), 43-51.

(15) Sunshine, J. C.; Peng, D. Y.; Green, J. J., Uptake and transfection with polymeric nanoparticles are dependent on polymer end-group structure, but largely independent of nanoparticle physical and chemical properties. *Mol Pharm* **2012,** 9, (11), 3375-83.

(16) Kim, J.; Wilson, D. R.; Zamboni, C. G.; Green, J. J., Targeted polymeric nanoparticles for cancer gene therapy. *J Drug Target* **2015,** 23, (7-8), 627-41.

(17) Jeong, G. J.; Byun, H. M.; Kim, J. M.; Yoon, H.; Choi, H. G.; Kim, W. K.; Kim, S. J.; Oh, Y. K., Biodistribution and tissue expression kinetics of plasmid DNA complexed with polyethylenimines of different molecular weight and structure. *J Control Release* **2007,** 118, (1), 118-25.

(18) Poon, Z.; Lee, J. B.; Morton, S. W.; Hammond, P. T., Controlling in vivo stability and biodistribution in electrostatically assembled nanoparticles for systemic delivery. *Nano Lett* **2011,** 11, (5), 2096-103.

(19) Ho, J. K.; White, P. J.; Pouton, C. W., Tissue-specific calibration of real-time pcr facilitates absolute quantification of plasmid DNA in biodistribution studies. *Mol Ther Nucleic Acids* **2016,** 5, (10), e371.

(20) Dahlman, J. E.; Kauffman, K. J.; Xing, Y.; Shaw, T. E.; Mir, F. F.; Dlott, C. C.; Langer, R.; Anderson, D. G.; Wang, E. T., Barcoded nanoparticles for high throughput in vivo discovery of targeted therapeutics. *Proc Natl Acad Sci U S A* **2017,** 114, (8), 2060-2065.

4.6 Figures & Tables

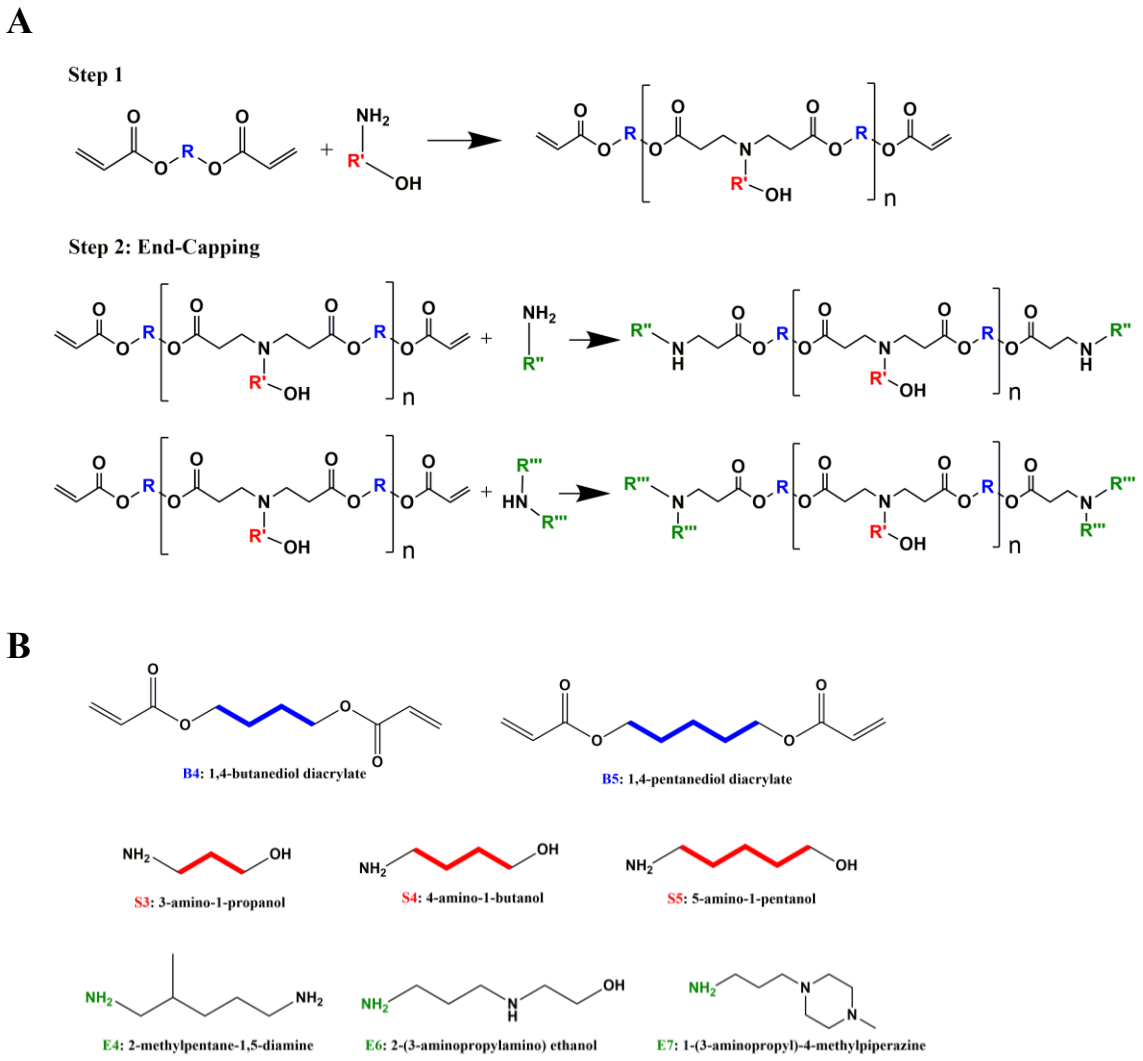

Figure 4.1. Polymer synthesis scheme. A library of biodegradable, cationic polymer is created by synthesizing PBAE polymers via (A) two-step Michael addition reaction with (B) base (B), side-chain (S), and end-capping (E) monomers.

A

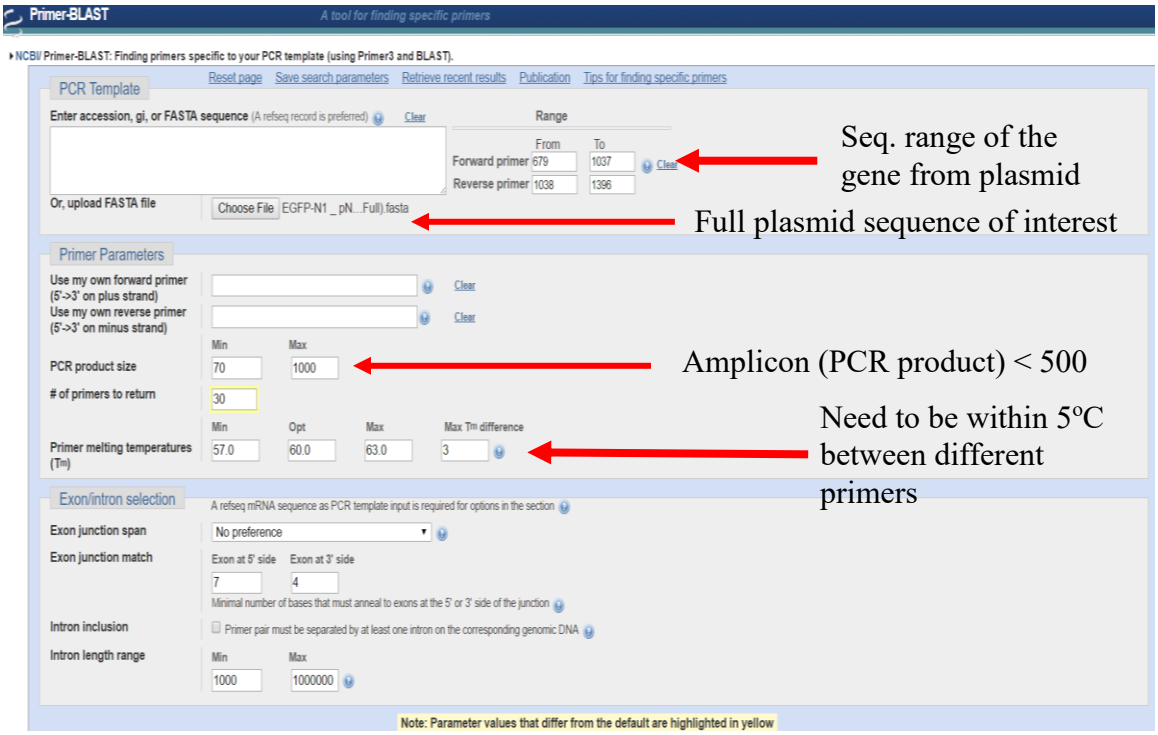
Primer-BLAST
A tool for finding specific primers
NCBI Primer-BLAST: Finding primers specific to your PCR template (using Primer3 and BLAST).
Reset page
Save search parameters
Retrieve recent results
Publication
Tips for finding specific primers
PCR Template
Enter accession, gi, or FASTA sequence (A refseq record is preferred)
Clear
Range
From
To
Forward primer 679 1037
Reverse primer 1038 1396
Clear
Or, upload FASTA file
Choose File
EGFP-N1 _ pN...Full).fasta
Primer Parameters
Use my own forward primer (5'->3' on plus strand)
Use my own reverse primer (5'->3' on minus strand)
Min
Max
PCR product size 70 1000
# of primers to return 30
Min
Opt
Max
Max Tm difference
Primer melting temperatures (Tm) 57.0 60.0 63.0 3
Exon/intron selection
A refseq mRNA sequence as PCR template input is required for options in the section
Exon junction span
No preference
Exon junction match
Exon at 5' side
Exon at 3' side
7
4
Minimal number of bases that must anneal to exons at the 5' or 3' side of the junction
Intron inclusion
Primer pair must be separated by at least one intron on the corresponding genomic DNA
Intron length range
Min
Max
1000
1000000
Note: Parameter values that differ from the default are highlighted in yellow
Seq. range of the gene from plasmid
Full plasmid sequence of interest
Amplicon (PCR product) < 500
Need to be within 5ºC between different primers

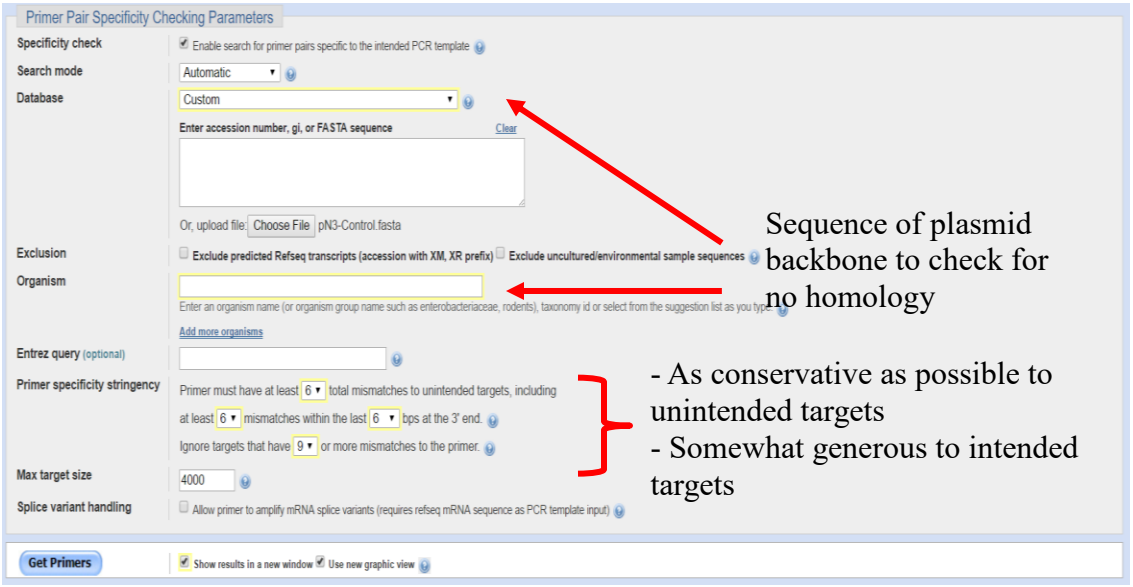
Primer Pair Specificity Checking Parameters
Specificity check
Enable search for primer pairs specific to the intended PCR template
Search mode
Automatic
Database
Custom
Enter accession number, gi, or FASTA sequence
Clear
Or, upload file:
Choose File
pN3-Control.fasta
Exclusion
Exclude predicted Refseq transcripts (accession with XM, XR prefix)
Exclude uncultured/environmental sample sequences
Organism
Enter an organism name (or organism group name such as enterobacteriaceae, rodents), taxonomy id or select from the suggestion list as you type
Add more organisms
Entrez query (optional)
Primer specificity stringency
Primer must have at least 6 total mismatches to unintended targets, including
at least 6 mismatches within the last 6 bps at the 3' end.
Ignore targets that have 9 or more mismatches to the primer.
Max target size
4000
Splice variant handling
Allow primer to amplify mRNA splice variants (requires refseq mRNA sequence as PCR template input)
Get Primers
Show results in a new window
Use new graphic view
Sequence of plasmid backbone to check for no homology
- As conservative as possible to unintended targets
- Somewhat generous to intended targets

B

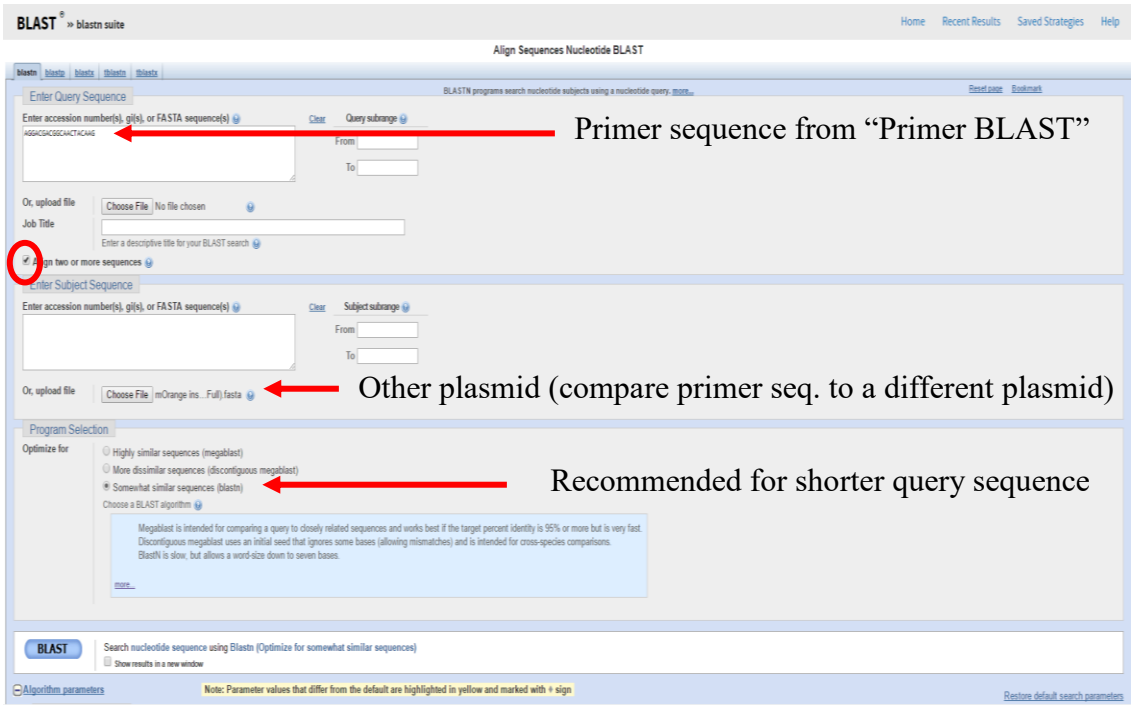
BLAST » blastn suite
Home
Recent Results
Saved Strategies
Help
Align Sequences Nucleotide BLAST
Enter Query Sequence
Primer sequence from "Primer BLAST"
Enter Subject Sequence
Other plasmid (compare primer seq. to a different plasmid)
Program Selection
Recommended for shorter query sequence
BLAST

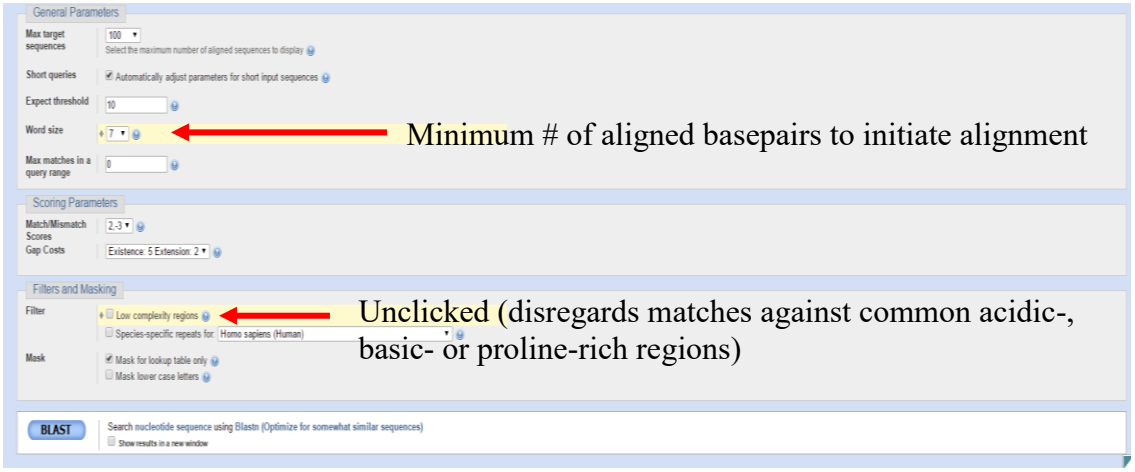
General Parameters
Minimum # of aligned basepairs to initiate alignment
Scoring Parameters
Filters and Masking
Unclicked (disregards matches against common acidic-, basic- or proline-rich regions)
BLAST

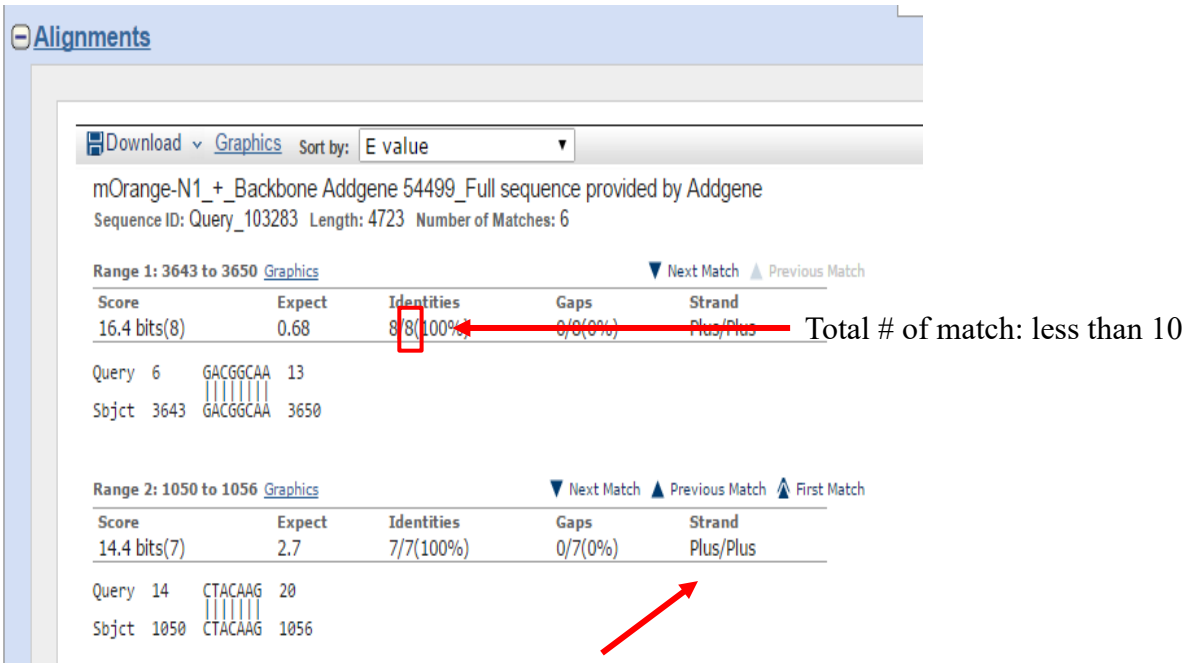

Figure 4.2. Primer design with BLAST. (A) Generating forward and reverse primer candidates through Primer-BLAST based on minimizing homology against the plasmid backbone, restricting amplicon size, and ensuring a window of melting temperature, and (B) checking specificity of primer candidate for a plasmid through BLASTn by comparing its homology against sequence of plasmids other than the one it was generated for.

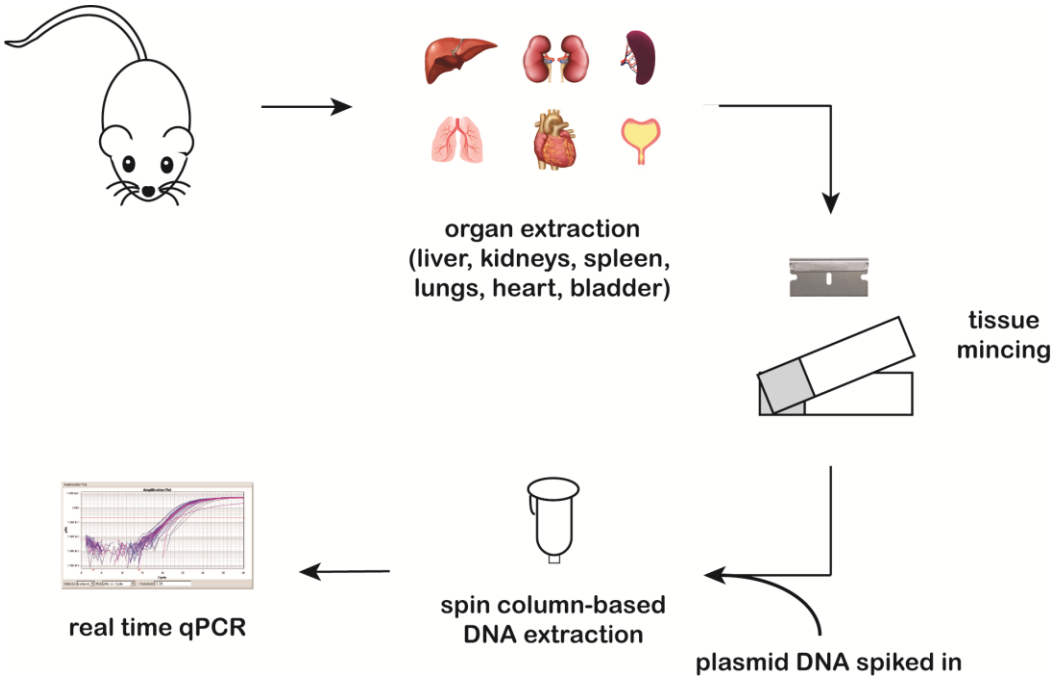

Figure 4.3. Workflow for generating standard curves. Schematic diagram showing the procedure for preparing samples to make standard curves of plasmid DNA concentration vs. C_T values in qRT-PCR.

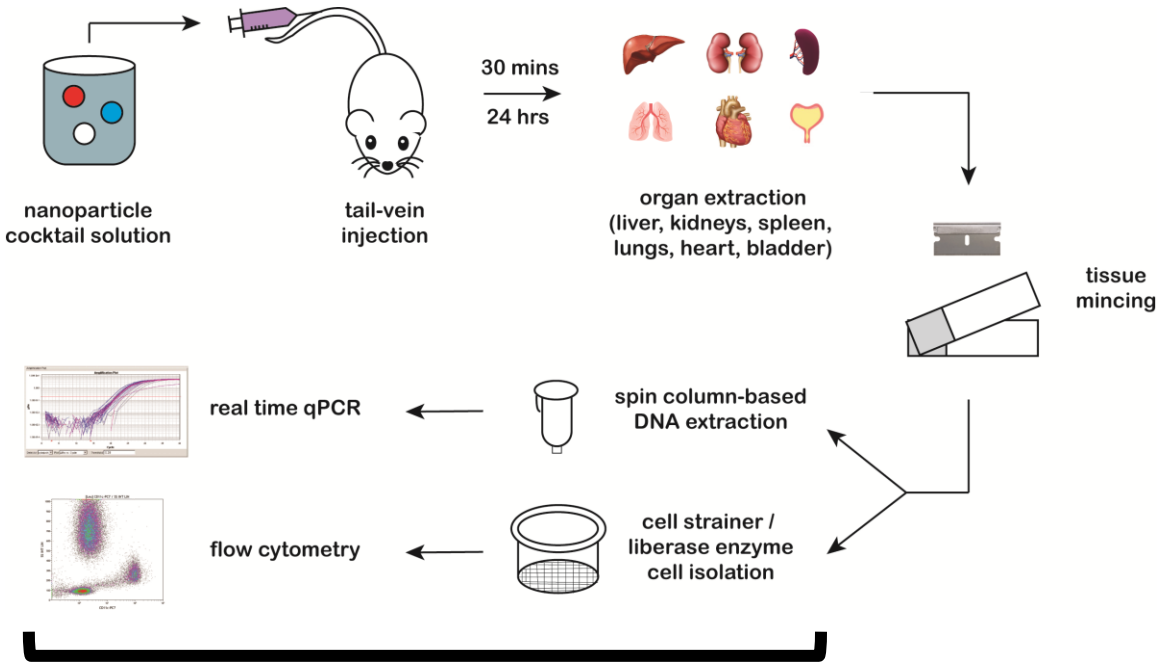

Simultaneous evaluation of biodistribution and transfection

Figure 4.4. Workflow for high-throughput screening. Schematic diagram showing the high-throughput procedure for preparing samples to investigate tissue targeting (qRT-PCR) and cellular transfection (flow cytometry) simultaneously using DNA barcode.

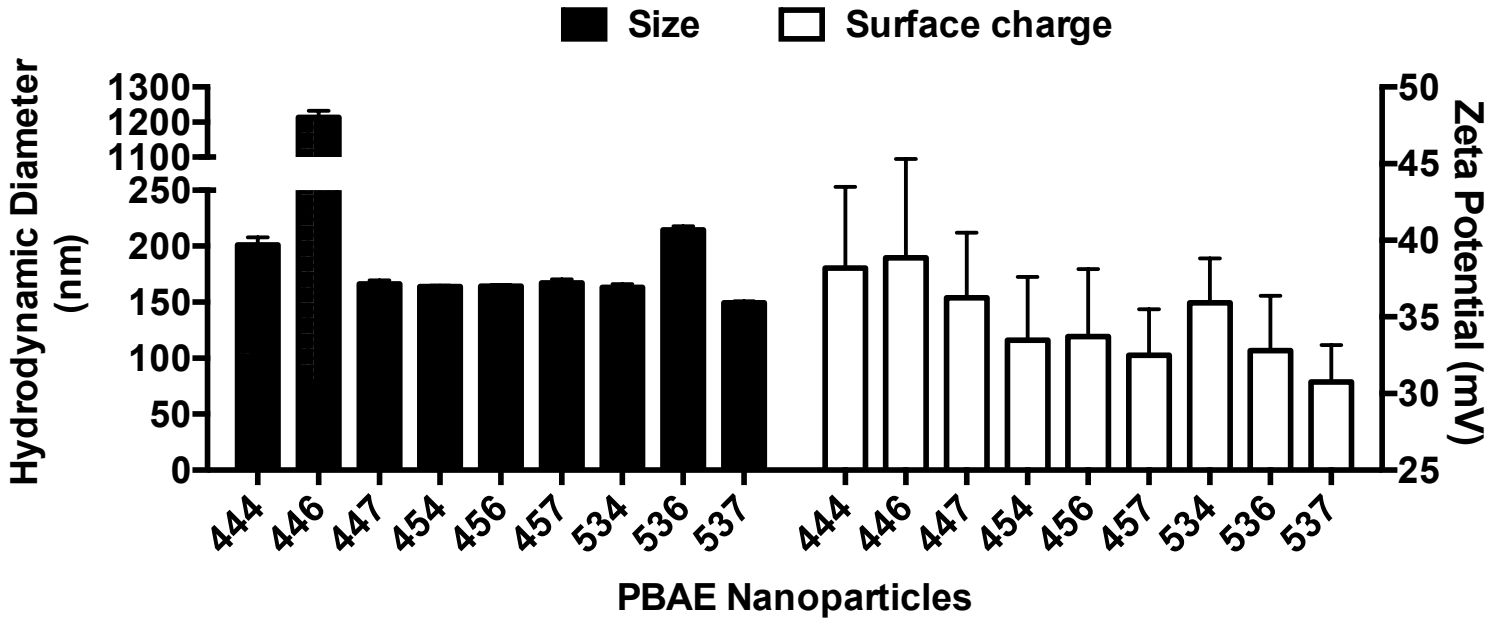

Figure 4.5. PBAE nanoparticle characterization. Hydrodynamic diameter and zeta potential of 12 different PBAE nanoparticles measured by dynamic light scattering using Zetasizer Nano ZS. Samples are diluted in 25 mM NaAc pH 5.0 to approximately 1 mg/mL polymer concentration for measurement (n=3, mean ± SD).

A

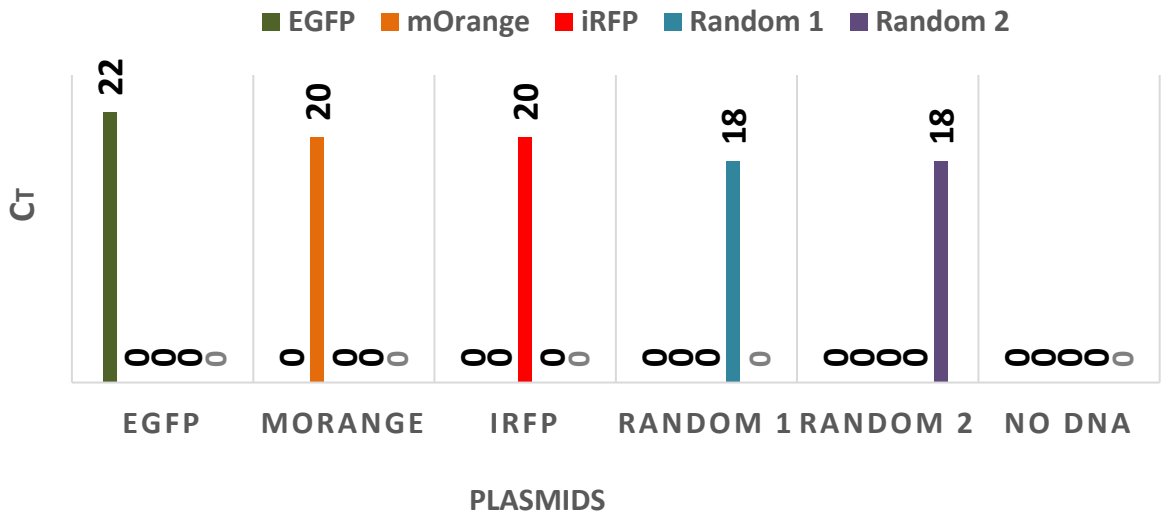
EGFP
mOrange
iRFP
Random 1
Random 2
CT
22
20
20
18
18
EGFP
MORANGE
IRFP
RANDOM 1
RANDOM 2
NO DNA
PLASMIDS

B

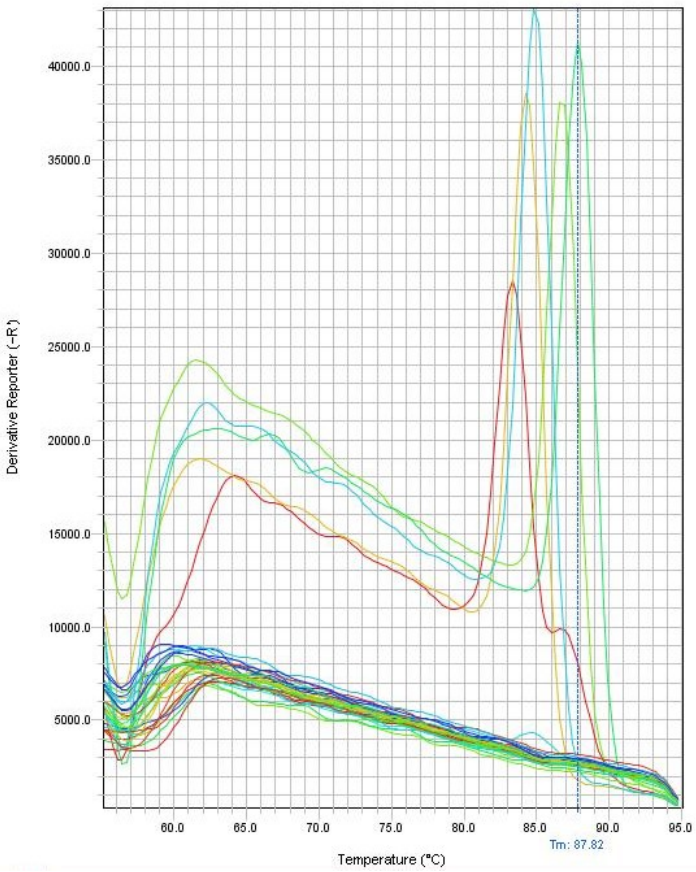
Derivative Reporter (-R')
40000.0
35000.0
30000.0
25000.0
20000.0
15000.0
10000.0
5000.0
60.0
65.0
70.0
75.0
80.0
85.0
90.0
95.0
Tm: 87.82
Temperature (°C)

C

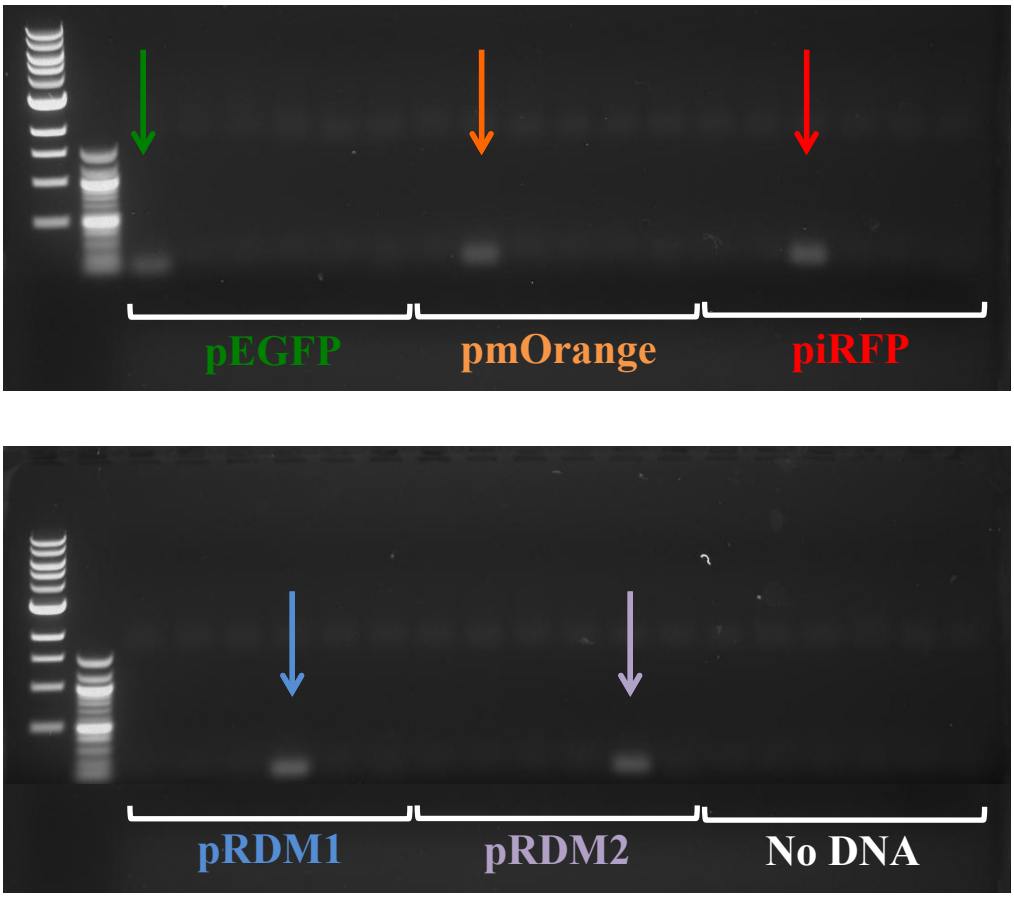

Figure 4.6. Primer specificity confirmation. (A) C_T values from qRT-PCR reaction of all possible combinations of 5 plasmids and 5 corresponding primer sets, showing only specific amplification occurred and (B) melt curve from qRT-PCR reaction, showing that there was no non-specific amplification. (C) Gel electrophoresis of PCR-amplified product, showing specific amplicons' size of approximately 100 base-pairs. For each plasmid, there are 6 wells with primers' order of EGFP, mOrange, iRFP, RDM1, and RDM2 going from left to right. DNA ladder: 1 kbp left and 100 bp right.

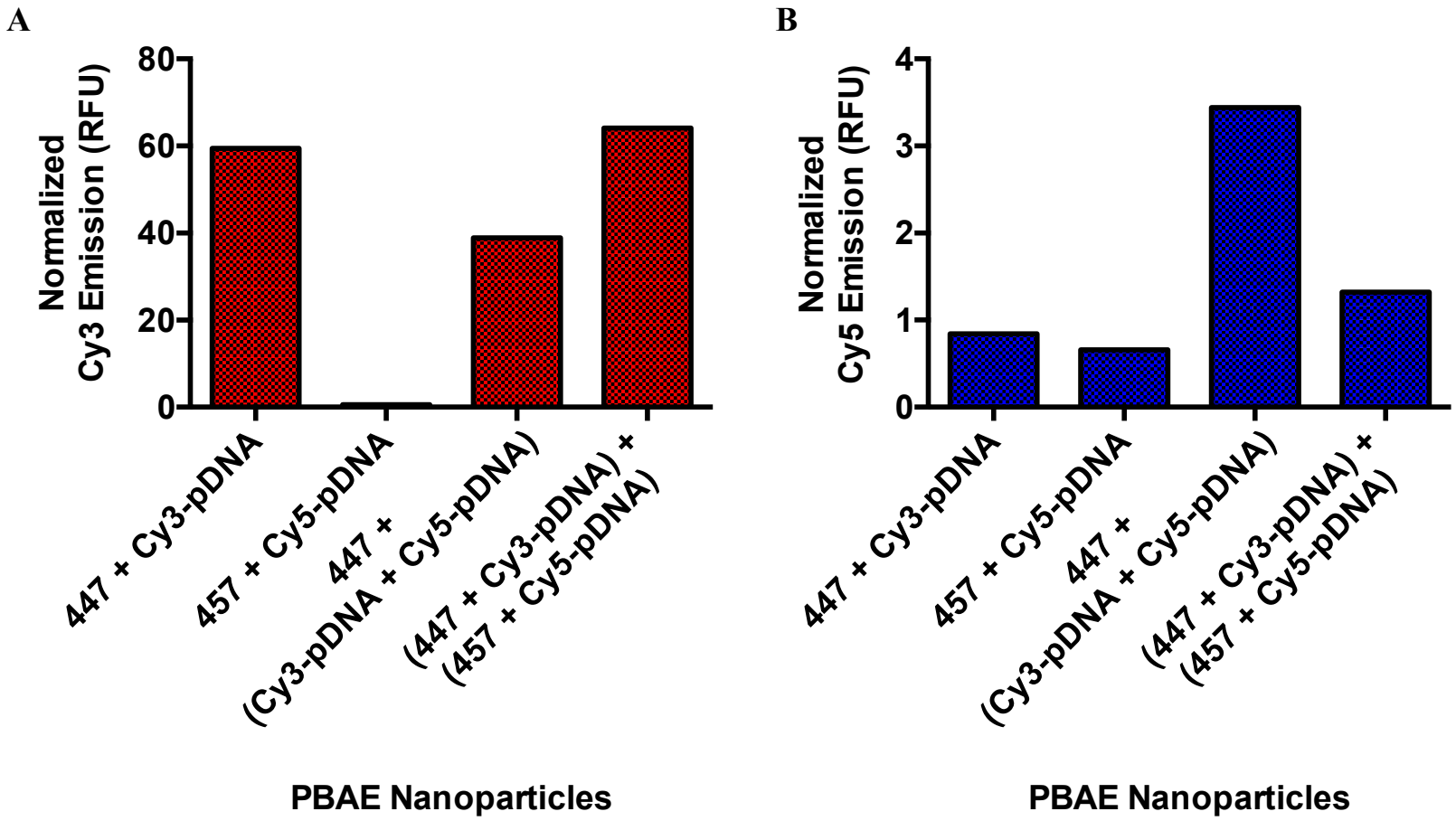

Figure 4.7. Absence of inter-nanoparticle DNA mixing. FRET analysis using Cy3-labeled and Cy5-labeled DNA. Cy3 emission (570 nm) and Cy5 emission (670 nm) was recorded following Cy3 excitation (550 nm) of nanoparticles individually made with Cy3- or Cy5-labeled DNA, nanoparticles made with both Cy3- and Cy5-labeled DNA together, and two nanoparticles made separately with either Cy3- or Cy5-labeled DNA then co-incubated together in a single solution. All values are normalized to the fluorescence signal measured from 25 mM NaAc only control.

A

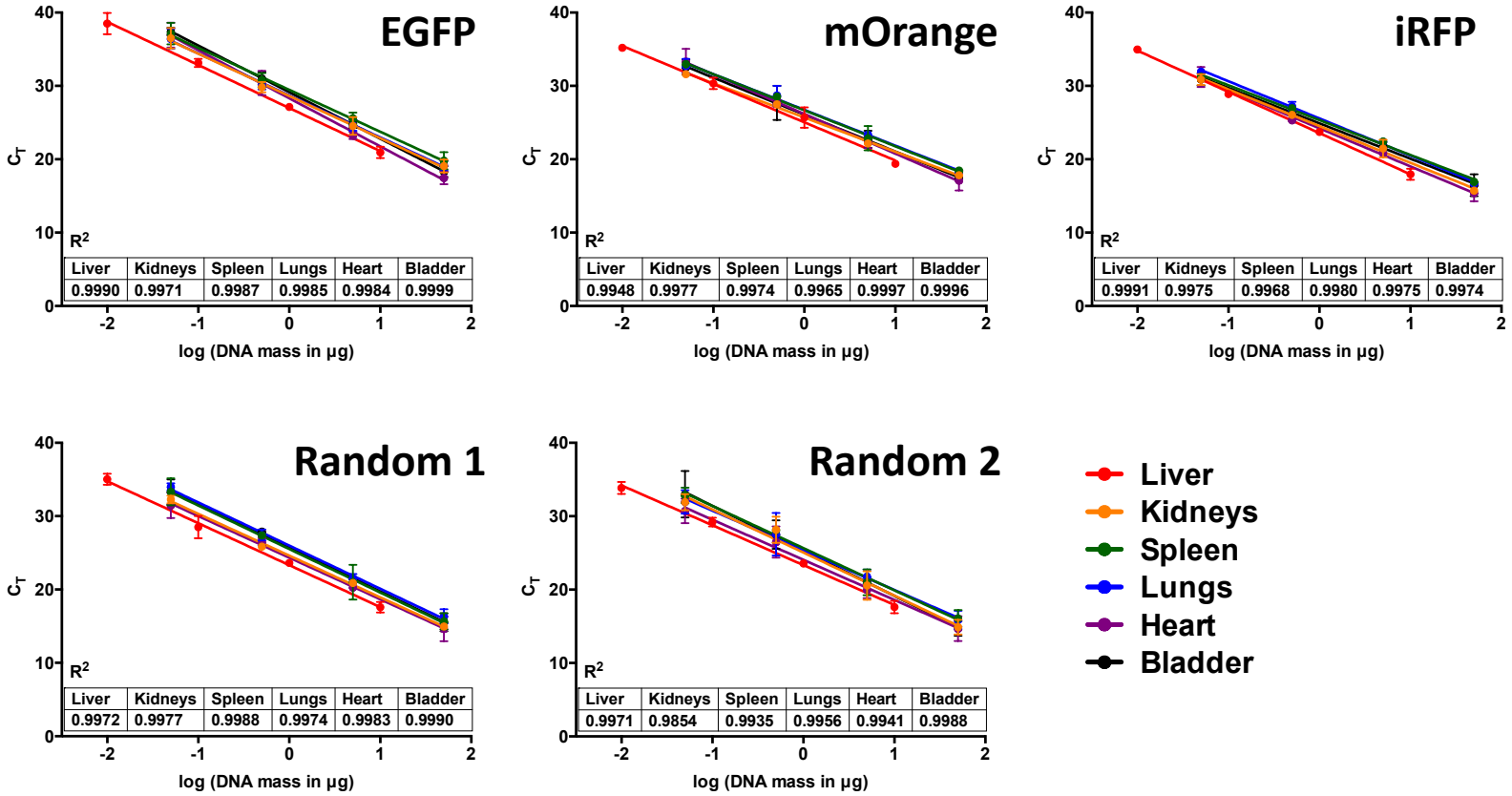
EGFP
C_T
R^2
Liver Kidneys Spleen Lungs Heart Bladder
0.9990 0.9971 0.9987 0.9985 0.9984 0.9999
log (DNA mass in µg)
mOrange
C_T
R^2
Liver Kidneys Spleen Lungs Heart Bladder
0.9948 0.9977 0.9974 0.9965 0.9997 0.9996
log (DNA mass in µg)
iRFP
C_T
R^2
Liver Kidneys Spleen Lungs Heart Bladder
0.9991 0.9975 0.9968 0.9980 0.9975 0.9974
log (DNA mass in µg)
Random 1
C_T
R^2
Liver Kidneys Spleen Lungs Heart Bladder
0.9972 0.9977 0.9988 0.9974 0.9983 0.9990
log (DNA mass in µg)
Random 2
C_T
R^2
Liver Kidneys Spleen Lungs Heart Bladder
0.9971 0.9854 0.9935 0.9956 0.9941 0.9988
log (DNA mass in µg)
Liver
Kidneys
Spleen
Lungs
Heart
Bladder

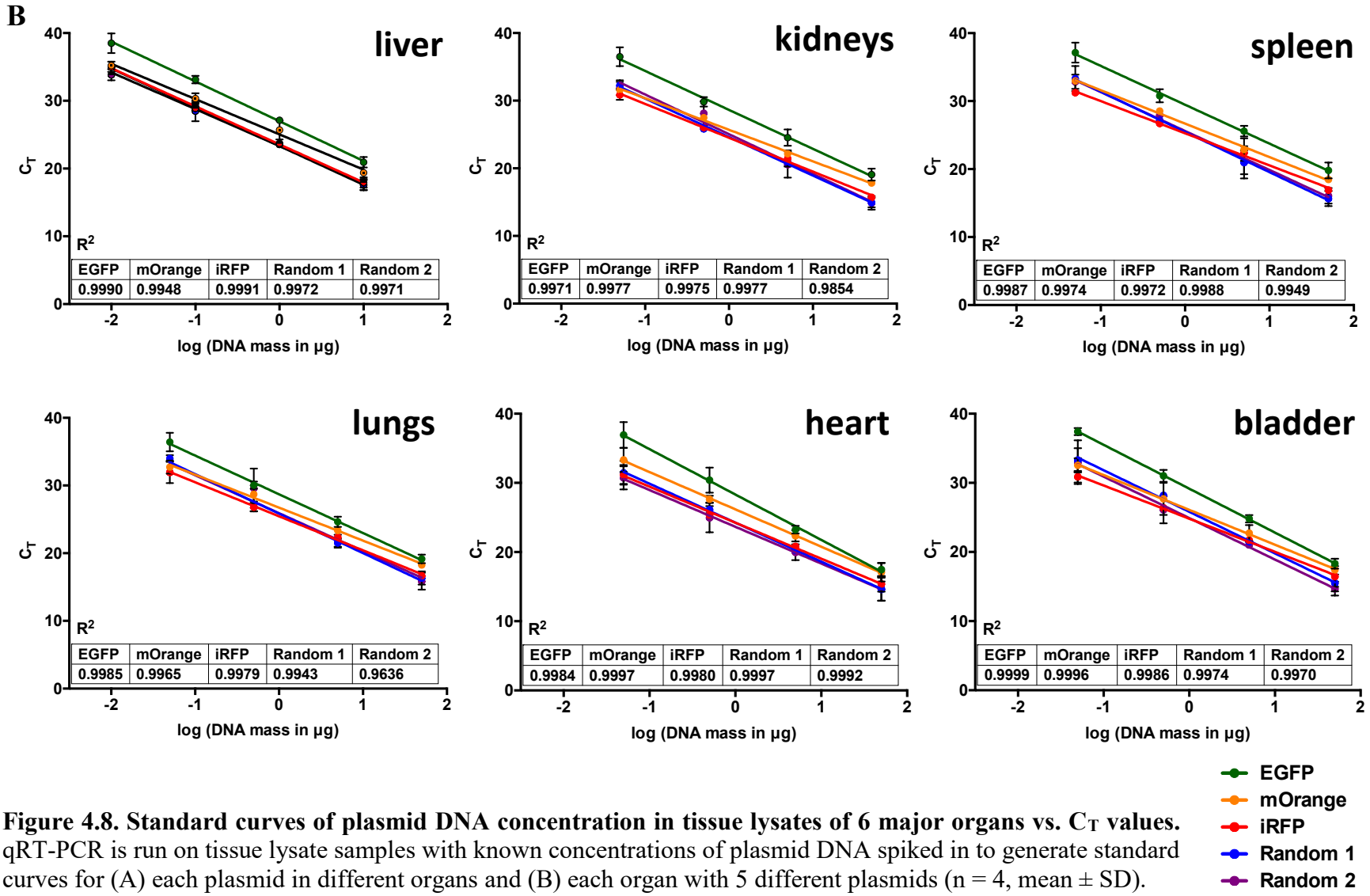

Figure 4.8. Standard curves of plasmid DNA concentration in tissue lysates of 6 major organs vs. C_T values. qRT-PCR is run on tissue lysate samples with known concentrations of plasmid DNA spiked in to generate standard curves for (A) each plasmid in different organs and (B) each organ with 5 different plasmids (n = 4, mean ± SD).

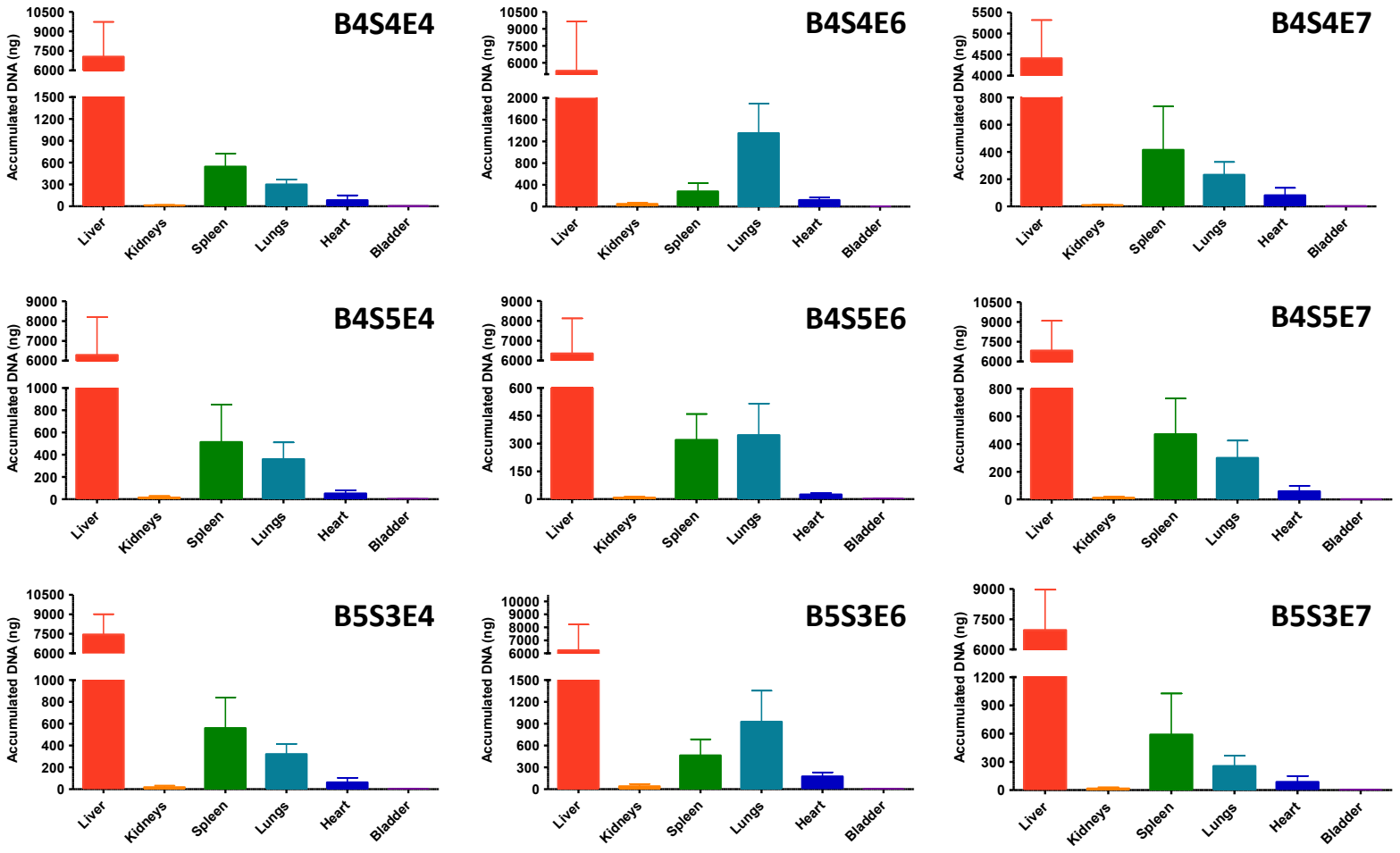

Figure 4.9. Biodistribution of each PBAE nanoparticle in 6 major organs. Each panel shows pooled biodistribution data of a PBAE nanoparticle formulation with 5 distinct DNA barcodes from 5 different mice. The amount of DNA accumulated was measured by the amplification of DNA barcodes in the organs 30 min after injection. (n=5, mean ± SD)

liver

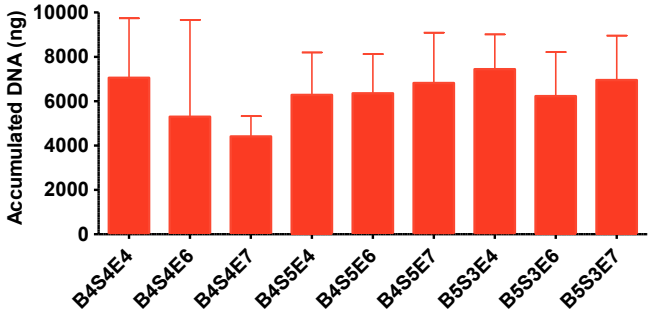

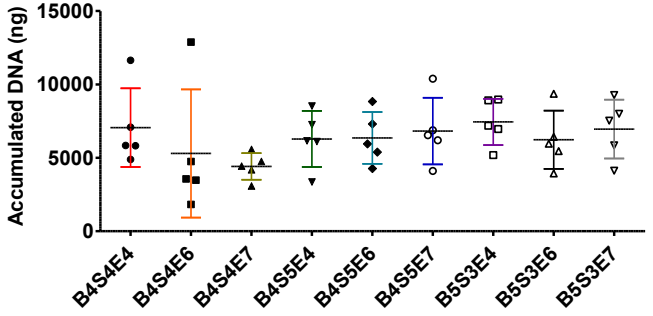

spleen

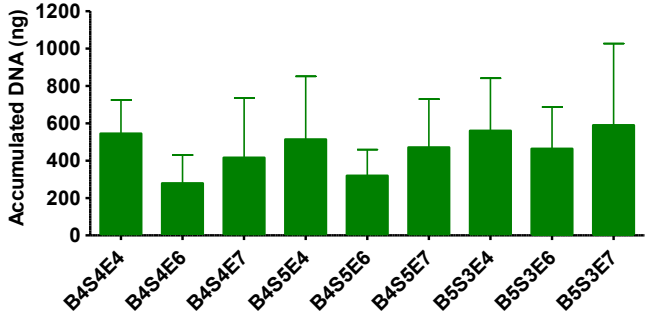

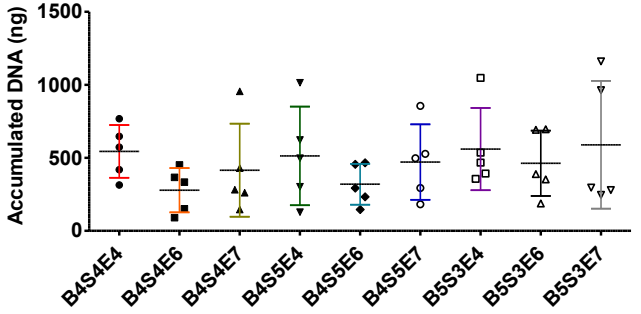

bladder

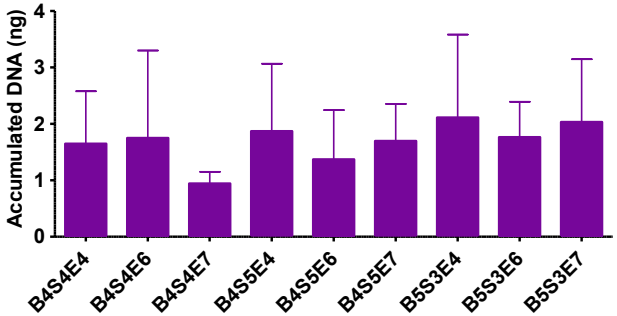

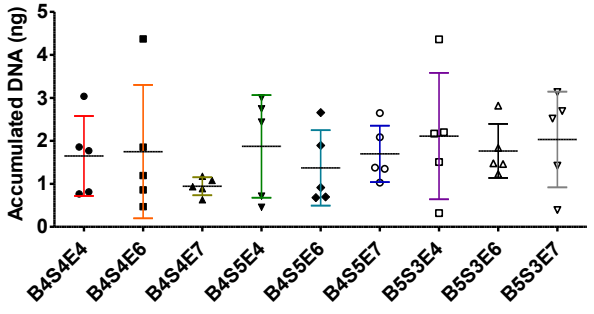

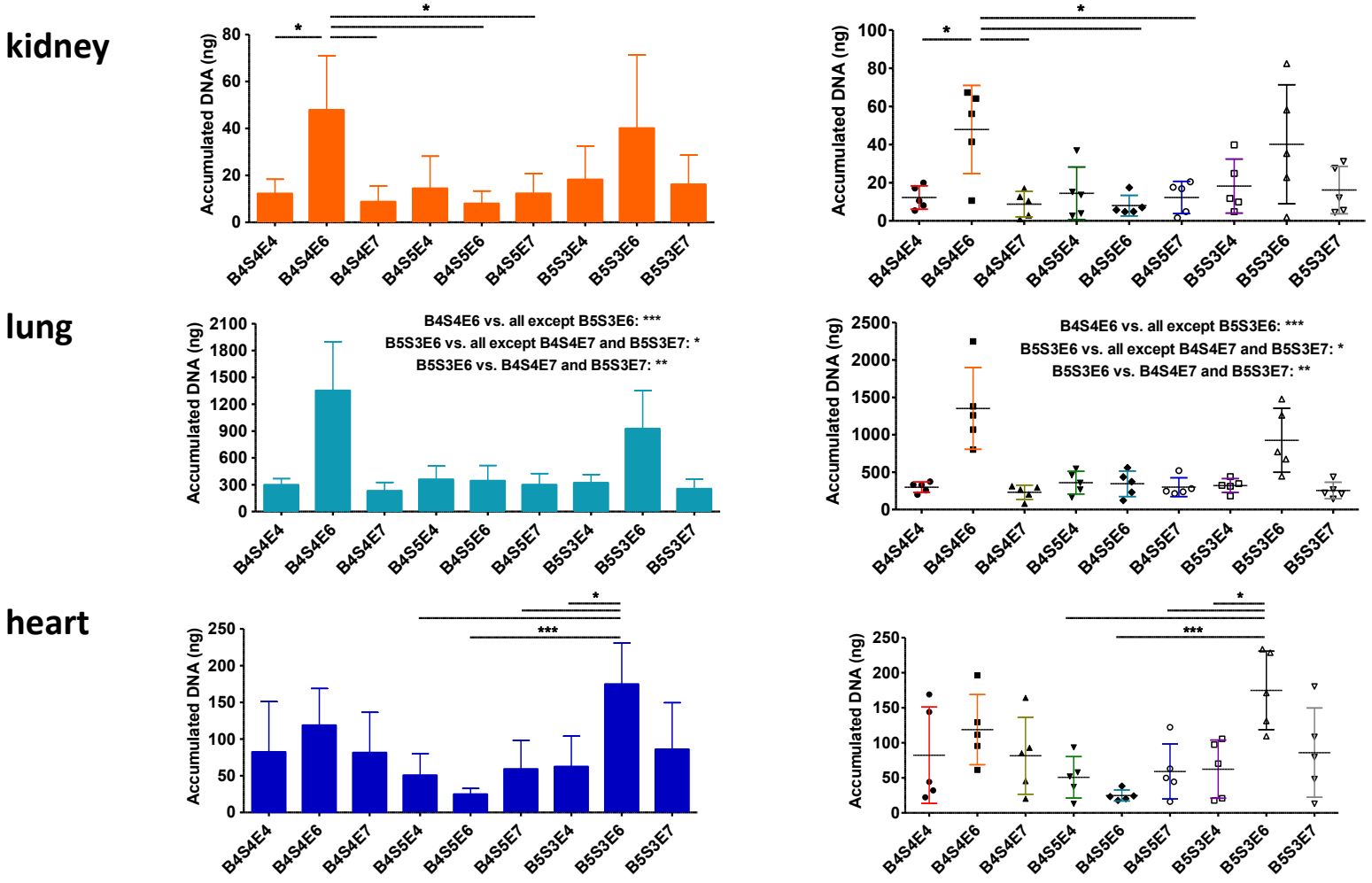

Figure 4.10. Organ accumulation of 9 PBAE nanoparticles in each organ. Each panel shows pooled data of 9 PBAE nanoparticle formulations with 5 distinct DNA barcodes from 5 different mice. Left: bar graph, Right: scatter dot plot (n=5, mean ± SD, One-way ANOVA with Bonferroni post-hoc test; α=0.05).

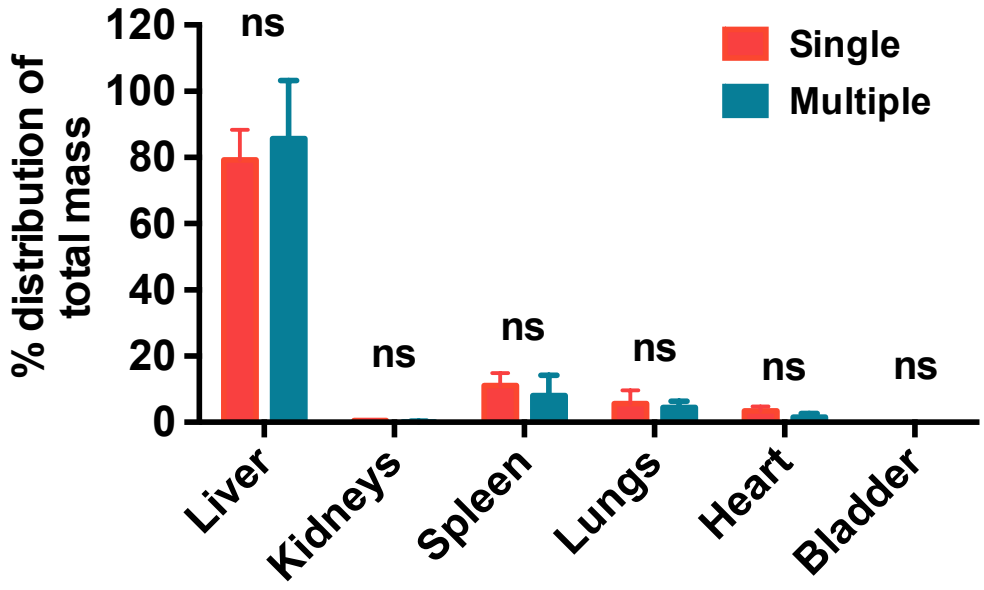

Figure 4.11. Comparison of single- vs. high-throughput screening of tissue targeting. Biodistribution profile of 447 nanoparticles injected alone (n=4) was compared against that of 447 nanoparticles from high-throughput screening (n=5), shown as % distribution normalized to total DNA mass detected in all measured organs (mean ± SD, Two-way ANOVA with Sidak's multiple comparison test α=0.05).

	Ac-B4S4-Ac	Ac-B4S5-Ac	Ac-B5S3-Ac
Molecular weight (Da)	5354	5085	4869

Table 4.1. Molecular weight of 3 PBAE base polymers. Molecular weight of acrylate-terminated PBAE base polymers were calculated based on the ratio of AUC for hydrogen peaks in non-repeating and repeating units, as measured by ^{1}H NMR.

PBAE Polymer

Mouse Group	1	2	3	4	5	6	7	8	9
1	a	b	c	d	e				
2		a	b	c	d	e			
3			a	b	c	d	e		
4				a	b	c	d	e	
5					a	b	c	d	e
6	e					a	b	c	d
7	d	e					a	b	c
8	c	d	e					a	b
9	b	c	d	e					a

a: pEGFP
b: pmOrange
c: piRFP
d: pRDM1
e: pRDM2

Table 4.2. Matrix of 9 different cocktail solutions for injection in 9 mice. For each mouse, 5 PBAE polymers are paired individually with each of the 5 plasmids listed on the right (a-e) for injection as a cocktail solution. A total of 9 mice results in n=5 for each of the 9 PBAE nanoparticles via the high-throughput screening method.

Chapter 5

Targeted poly(lactic-co-glycolic acid)-co-poly(ethylene glycol) (PLGA-PEG) nanoparticles using a biomimetic peptide as both targeting and therapeutic agent

5.1 Introduction

Drug delivery of chemotherapeutic compounds to breast cancer and other solid tumors is often limited by short half-lives and systemic toxicity stemming from an inability to specifically target the tumor site.[1-3] A commonly proposed solution to this problem is encapsulation of drugs within a biodegradable polymer nanoparticle (NP) with specifically altered surface chemistry to aid in targeting of the tumor tissue.[4,5] For example, PEGylated poly(lactic-co-glycolic acid) (PLGA-PEG) NPs have been used to improve the blood circulation time and accumulation in tumors, thereby enhancing efficacy of doxorubicin,[6] platinum prodrugs,[5,7] docetaxel,[8,9] paclitaxel,[10,11] and other common chemotherapeutics in animal models. However, compared to the number of preclinical studies reported, these PLGA-PEG NPs have had relatively little success achieving FDA approval due to insufficient drug efficacy in the tumor and potential accumulation in off-target tissue such as the liver.[12] Protein and peptide-loaded NPs have been explored as well, but are often limited

Parts of this chapter were originally published in and modified from Bressler EM*, Kim J*, Shmueli RB*, Mirando AC, Bazzazi H, Lee E, Popel AS, Pandey NB, Green JJ. "Biomimetic peptide display from a polymeric nanoparticle surface for targeting and antitumor activity to human triple-negative breast cancer cells." *J Biomed Mater Res Part A,* 106(6): 1753-1764, 2018.

by packing density within the polymer matrix of the NPs and challenges with encapsulation.[13]

Early strategies for targeting PLGA-PEG and other NPs to tumors relied in large part on the passive enhanced permeability and retention (EPR) effect, which hypothesized that NPs can extravasate through leaky neovasculature near the tumor and are not easily drained by irregularly formed lymph vessels.[14] Though this effect has been shown to contribute to NP accumulation in solid tumors, further targeting is needed to reduce nonspecific accumulation and buildup in other healthy tissues. Growing effort has focused on developing active targeting methods using ligands that target receptors known to be upregulated on the surface of neovasculature and tumor cells, such as integrin $\alpha_v\beta_3$ [5,15,16] and folate receptors.[11,17,18] A common ligand used in conjunction with PLGA-PEG NPs to target integrin $\alpha_v\beta_3$ is the peptide sequence RGD, including cyclic-RGD peptide. The RGD motif is present in the extracellular matrix components such as fibronectin and vitronectin, aiding in the binding of these components to the cell surface. The use of cyclic-RGD ligands has been shown to increase tumor localization and improve efficacy of a number of chemotherapeutic drugs in preclinical models.[19] However, despite promising preclinical studies, integrin facilitated drug delivery has not been validated in clinical applications to date. In addition, aside from cyclic-RGD ligands and RGD mimics, non-RGD-based $\alpha_v\beta_3$ integrin targeting systems for NPs have not yet been developed.[19] Alternative nanomedicine targeting strategies utilize other biological molecules to reach different cellular targets, such as ribonucleic acid aptamer ligands to prostate-specific membrane antigen, to better target PLGA-PEG NPs to prostate cancer cells.[20]

The roles of particle physical properties, such as size and shape, are increasingly

being investigated in polymeric and inorganic NP drug delivery systems.[21-23] The size of particles can be controlled such that following systemic administration, particles are large enough to avoid filtration by the kidneys (particle diameter designed to be greater than ~10 nm) and small enough to enable enhanced diffusion to reach a target tissue (particle diameter designed to be less than ~100 nm). Discoidal and ellipsoidal particles can marginate to the side of the blood vessel, enhancing their possibility of extravasation at the tumor site. While the delivery of drugs by polymeric NPs can also be improved by targeting, encapsulation capacity of drugs in PLGA-PEG NPs is generally limited to a small percentage of the total weight of the particle.[4] Targeted NP systems are canonically limited to drug loading within the particle while the targeting ligand decorates the outside. The hydrophobic nature of polymeric NPs makes them ideal delivery systems for hydrophobic drugs, but limits the ability to load many drugs into this system with high efficiency.[24] This poses a problem when a relatively larger dose of drug is required for therapeutic efficacy or enhanced durability. If a drug, such as a peptide, were covalently coupled to the NP surface, the total loading could potentially be increased by an order of magnitude compared to loading by physical encapsulation alone. A surface tethered drug can target a receptor of interest, facilitate avidity, and potentiate a therapeutic effect. If the surface tethered drug contains degradable linkages, it could also be designed to enable controlled release from the NP. Further, the amount of the targeting ligand on the surface of NPs can be optimized to increase accumulation in the tumor and minimize off target delivery, avoid interaction and clearance through the reticuloendothelial system, and enhance targeted cellular uptake.[25,26]

Anti-angiogenesis is one of many key methods of cancer therapy, as tumor growth requires robust neovascularization in its microenvironment for increased oxygen and nutrient

supply.[27] Popel *et al.* showed that a collagen-IV derived 20-mer peptide, that we refer to here as AXT050, inhibit tumor growth in a number of models, including a metastatic tumor model, through its potent anti-angiogenic, anti-lymphangiogenic, and anti-tumorigenic activities.[28-31] The naked peptide is also shown to bind to integrin $\alpha_v\beta_3$ and disrupt integrin-dependent protein signaling pathways, thereby expanding the arsenal of vascular endothelial growth factor (VEGF)-independent, anti-angiogenesis based cancer therapies. By surface-functionalization and encapsulation of the AXT050 peptide in PLGA-PEG NPs, we hypothesize that targeted NPs with high loading capacity can be fabricated. As naked AXT050 biomimetic peptide can therapeutically modulate angiogenesis through extracellular interactions, we further hypothesize that presentation of AXT050 from the NP surface and soluble PEG-AXT050 conjugates released from the surface through hydrolysis can directly inhibit angiogenesis.

Herein, we design, characterize, and validate PLGA-PEG-AXT050 NPs, including in vitro adhesion and proliferation inhibition using both whole particles and the breakdown products of degraded particles. We also report the optimization of PLGA-PEG NPs functionalized with AXT050 peptide for in vivo biodistribution to tumors using an orthotopic human triple-negative breast cancer (MDA-MB-231) mouse model that is challenging to target through conventional approaches.

5.2 Methods

Materials

Poly(D,L-lactide-co-glycolide) (65/35), dimethyl formamide (DMF), dimethyl

sulfoxide (DMSO), di-isopropylethylamine (DIPEA), methanol, and ether were purchased from Sigma- Aldrich (St. Louis, MO). Poly(vinyl alcohol) [PVA; Mw 25,000] was purchased from Polysciences (Warrington, PA). Poly(D,L-lactide-co-glycolide) (50/50) with terminal methoxy groups (PLGA-mPEG) or terminal n-hydroxysuccinimide groups (PLGA-PEG-NHS) (each with Mw 20,000:5,000 Da, PLGA:PEG) were purchased from Akina (West Lafayette, IN). AXT050,[28,30] AXT051 (AXT050 analog where the last amino acid residue is swapped from a F to a W to enable stronger intrinsic fluorescence), biotinylated AXT050, and AXT050-IRD800 were custom synthesized and ordered from New England Peptide (Gardner, MA). Human recombinant integrin was purchased from R&D Systems (Minneapolis, MN). IRDye 800 CW was purchased from LI-COR (Lincoln, NE). Tissue culture reagents and cell lines were purchased from Lonza (Portsmouth, NH). Biological buffers were purchased from Fisher Scientific (Hampton, NH).

Binding kinetics between AXT050 and integrin $\alpha_v\beta_3$

The ForteBio Octet RED96, capable of an automated high-throughput assay using 96-well plates, was used to investigate the binding kinetic profile of AXT050 to integrin $\alpha_v\beta_3$. Twenty five micromolar stock of biotinylated AXT050 in 5% DMSO/95% water was diluted 100-fold using 0.05% Tween 20 in 1X phosphate buffered saline (PBS). The peptide was incubated with streptavidin biosensor probe from Pall ForteBio (Fremont, CA) for 300 s, flanked by 60 s of incubation in the same buffer without the peptide. Subsequently in the binding association step, the peptide-attached biosensor probe was incubated with various concentrations of integrin $\alpha_v\beta_3$ ranging from 10 to 300 nM in the same buffer solution for

600 s. The probe is further incubated in the buffer solution without integrin for 1800 s to observe the dissociation profile. Optical interference signal resulting from the binding of integrins to peptide-attached probe was exported for analysis in MATLAB (Mathworks 2015). A 1:1 binding model was implemented in MATLAB and the resulting differential equation describing the concentration changes in peptide and peptide-integrin binding complex was solved using ODE15s function. The fitting was performed using pattern-search algorithm as part of the MATLAB optimization toolbox to determine k_{on} and k_{off} of the reaction using the experimental time course data.

Formulation of spherical and ellipsoidal PLGA NPs

PLGA NPs was formulated using an emulsion method. First, PLGA (65/35) was first dissolved into dichloromethane (DCM) at 20 mg/mL in a test tube, vortexed to fully dissolve, and mixed with 20 mg/mL AXT050 stock in DMSO at the desired mass ratio of peptide to PLGA; a common formulation is 1:50 peptide:PLGA. The mixture was sonicated with the test tube on ice. Sonication (Misonix) was performed with an amplitude of 30A, which equals approximately 5–10 W, for 20 s. This primary emulsion was immediately poured into 50 mL of 1% PVA solution and sonicated at an amplitude of between 30 and 100A for 2 min on ice. The full volume was then transferred to 100 mL of 0.5% PVA solution and stirred in a chemical hood for 3.5 h. Then, NPs were washed three times by centrifuging at 48ºC, 17 krpm for 10 min, removing the supernatant, and resuspending NPs with 30 mL of refrigerated Milli-Q water. After the last wash, 5 mL of water was added to resuspend the sample, which was then snap-frozen with liquid nitrogen for lyophilization. NPs were stored

at -20ºC prior to use.

To generate ellipsoidal PLGA NPs, pre-made spherical PLGA NPs were stretched using a previously described method.[32] Briefly, lyophilized spherical PLGA NPs were suspended in water and mixed with 10% PVA/2% glycerol solution at 5 mg/mL NP concentration. The solution was added to a mold (5 x 7 cm rectangular petri dishes) and allowed to dry into a film. The film was heated above the Tg of PLGA and then stretched through a custom made stretching device, after which the film was dissolved, NPs washed as described above, and stored for future use.

Synthesis of peptide-functionalized PLGA-PEG

PLGA-PEG-NHS was dissolved at 170 mg/mL in DMF, and AXT050 or AXT051 in DMSO at 100 mg/mL was added at a 1.2:1 molar ratio in excess of the peptide. A 40-fold molar excess of DIPEA was added to the mixture and stirred overnight at room temperature. The mixture was then added drop-wise to a cold mixture of ether (50%) and methanol (50%) and spun down to produce a pellet. The supernatant was discarded and the pellet was disturbed and washed in 100% methanol, and spun down repeatedly to remove unreacted peptide. The pellet was left to dry under vacuum for several hours to yield solid PLGA-PEG-AXT050. Typical batches yield 10–100 mg, approximately 80% of the starting material. A similar protocol was used for the functionalization of PLGA-PEG-NHS polymer with IR-Dye 800 CW to prepare fluorescent NPs.

High performance liquid chromatography was used to confirm the conjugation. Five hundred microgram of the AXT051-functionalized PLGA-PEG reaction mixture (prior to

precipitation in methanol and ether) was diluted in acetonitrile and run through an Agilent Poroshell 300 column. AXT051 was utilized as an analog of AXT050 that allows improved quantification of intrinsic ultraviolet absorption/fluorescence through the tryptophan residue at the C-terminus of the peptide. The reaction mixture was compared to a control mixture using PLGA-mPEG in place of the reactive PLGA-PEG-NHS. Area under the curve (AUCs) of peaks from unreacted peptide were compared to determine the extent of the reaction, which was calculated according to signals at 220 nm (peptide backbone), 280 nm (trp absorption), and 295/348 excitation/emission (trp fluorescence).

Formulation of peptide-functionalized PLGA-PEG NPs

The functionalized PLGA-PEG NPs were formulated following a nanoprecipitation method. PLGA-PEG-AXT050 and PLGA-mPEG were each dissolved in DMF in any desired mass ratio (i.e., 10% NP: 1 to 9 mass ratio of PLGA-PEG AXT050 to PLGA-mPEG) at 10 mg/mL total polymer concentration. For encapsulation, this was then mixed with AXT050 in DMSO at 5% (w/w) and/or with a dye such as 5-carboxytetramethylrhodamine (TAMRA). The polymer/peptide mix was then added drop-wise to a volume of deionized water ten times larger than the DMF solution under magnetic stirring. After 4–6 h stirring in a chemical hood, the NPs were filtered and concentrated using ultracentrifugation columns (EMD Millipore, UFC810096) and GPC spin columns (Thermo Scientific) using S-400 HR media (Sephacryl) to ensure all free peptide was filtered. NPs were then either used immediately or stored overnight at 4^{o}C before use.

Quantification of peptide content on functionalized NPs

LavaPep peptide quantification kit (Gel Company, LP022010) was used to determine peptide content following NP formation. As per the LavaPep protocol, particles were incubated at 3 mg/mL in the dark in the Lava- Pep working solution for 1 h. The epicocconone dye interacts with the arg residues in the peptide to become highly fluorescent. Fluorescence was read at 530/590 nm on a Biotek HT Synergy plate reader. The signal from the NPs was compared to a standard dilution curve of known amounts of free peptide.

Characterization of NPs

The particle size distributions were generally measured through dynamic light scattering (Malvern Zetasizer Nano ZS90) at 25ºC at a scattering angle of 908 and at a concentration of approximately 1 mg/mL NP in water, PBS, or fetal bovine serum (FBS). NP tracking analysis (NTA) was performed using a Nanosight NS500 instrument and NP solutions were diluted so that the NP concentrations were appropriate for NTA analysis.[33] NTA videos were captured for 60 s and analyzed using Nanosight NTA software. For transmission electron microscopy (TEM) sizing, 10 μL of NP sample at 1 mg/mL was dropped onto carbon coated copper grids and left to dry in chemical hood for 2 h. Unstained TEM imaging was then performed using the Philips CM120 system. Zeta potential was measured on a Malvern Zetasizer Nano ZS90 at 1 mg/mL in 10 mM NaCl.

In vitro targeting activity assay

MDA-MB-231 cells and microvascular endothelial cell (MEC) cells were trypsinized and suspended in appropriate media at 2000 cells/mL. One hundred percent AXT050 peptide coated NPs and non-coated PEG-PLGA NPs that encapsulated TAMRA dye were added at 5 mg/mL to the cells in suspension, and the mixture was incubated while shaking at 37ºC for 1 h to allow binding between cells and particles. After 1 h, cells were spun down and supernatant was discarded. Cells were resuspended in PBS and spun down twice to wash away any non-bound particles or dye in solution. Cells were resuspended in 1 mL of PBS and 100 μL of that solution was assessed for TAMRA fluorescence using a Biotek Synergy Plate Reader at 530/590 nm excitation/emission.

Integrin $\alpha_v\beta_3$, $\alpha_5\beta_1$,and human serum albumin (HAS) were labeled with AlexaFluor 488 Protein Labeling Kit (Thermo Scientific) according to the manufacturer's instructions. Labeled proteins at 50 mg/mL were incubated with either peptide conjugated or non-conjugated NPs in PBS at concentrations of 5 mg/mL. After 1 h shaking at 37ºC, NPs were separated from free proteins in solution through GPC spin columns (Thermo Scientific) using S-400 HR media (Sephacryl) and the fluorescence of the filtrate was measured. For free peptide competition experiments, a similar protocol was followed, but a 100-fold excess of non-labeled AXT050 peptide or an inactive scrambled peptide control sequence known to have no activity in in vitro adhesion activity assays was added to the NP solution before the addition of labeled peptide.

In vitro antitumor functional activity assay

Prior to use in in vitro activity assays, particles were transferred from ultrapure water to appropriate media using the same ultracentrifugation columns used for purification after NP formation. To test activity in an adhesion assay, particles were concentrated to 20 mg/mL in media and added to 96 well plates. Regular media was used as a negative control and media supplemented with 100 and 25 μM of free AXT050 were used as positive controls. MDA-MB-231 triple-negative breast cancer cells or primary MECs were added at 20,000 cells/well on top of the particles. The plate was then incubated for 2 h at 37ºC and 5% CO2. Wells were next washed twice with dulbecco's phosphate buffered saline (DPBS) with Ca^{2+} and Mg^{2+} and then filled with media containing 4 μg/mL Calcein AM dye. Plates were then incubated for 30 min and washed again with DPBS with Ca^{2+} and Mg^{2+}. Fluorescence was read on a Biotek Synergy HT at 485/528 nm excitation/emission to quantify the number of cells adhered to the surface of the well.

Particle breakdown products were assessed for their efficacy relative to fully intact particles and free peptide by allowing hydrolysis of 10% functionalized particles in PBS at 37ºC for 5 days on a shaker. The resulting broken down particles were confirmed to have lost their structure through dynamic light scattering as described above, and were determined to be broken down when particles could no longer be detected at sufficient concentration to analyze particle size. The breakdown products were then added to MDA-MB-231 cells as above and compared to free peptide and to equal amounts of peptide included on intact particles at 10% functionalization.

To test activity on MEC cells in a proliferation assay, 2000 cells/well were plated in 96-well plates in phenol red-free ECM-2 MV media and allowed to adhere over 18–20 h. Media was replaced with particles suspended in media at 5 mg/mL or AXT050 peptide in

media or media alone. After four days, media was replaced with 100 μL 3-(4,5-dimethylthiazol- 2-yl)-2,5 diphenyltetrazolium bromide (MTT) reagent as per the manufacturer's recommendations. After 4 h, 100 μL of sodium dodecyl sulfate (SDS) solution was added to each well and incubated at 37^{o}C for another 4 h. Absorbance was read at 570 nm on a Biotek Synergy HT plate reader to capture the change from MTT to formazan by mitochondrial reductase in the living cells.

In vivo pharmacokinetics of functionalized PLGA-PEG NPs

Animals were housed and treated in accordance with NIH and IACUC guidelines for the care and use of laboratory animals (NIH Publication #85–23 Rev. 1985), and used protocols approved by the Johns Hopkins University Animal Care and Use Committees. 2 x 10^6 human triple-negative breast cancer cells (MDA-MB-231) mixed 1:1 with matrigel (Corning) were implanted orthotopically or on the flank of a 5-week old athymic nude mouse (Charles River Laboratories, Wilmington, MA). Tumors were then allowed to grow until they reached a volume of 100 mm^3. Mice received tail-vein injection of PBS, naked peptide, spherical or ellipsoidal PLGA NPs, or PLGA-PEG NPs with 0, 10, and 100% peptide functionalization. In the non-targeted biodistribution experiment, peptide was labeled with IRD-800 CW dye. In the functionalized NP experiment, 1% of the polymer used to form particles was bound to IRD-800 CW dye by NHS chemistry described above. All NPs contained 1% (w/w) IRD-800 CW. Blood samples were taken through saphenous vein in heparin-coated glass capillary tubes at 5, 15, 30, 60, 120, and 300 min as well as at 24 h. Fluorescence in capillary tubes were imaged with LI-COR Pearl Impulse NIR Imager and

quantified by assigning ROI. For biodistribution, whole live animals were imaged at 5 and 24 h, and then the animals were sacrificed at 24 h to harvest, weight, and image organs separately. For imaging, Xenogen IVIS Spectrum Imager (Living Image v4.1 software) was used for naked peptide and non-targeted NP studies, while LI-COR Pearl Impulse NIR Imager (Pearl Impulse v2.0 software) with higher resolution and sensitivity was used for targeted NP studies.

5.3 Results

Peptide AXT050 has high molecular binding affinity to integrin $\alpha_v\beta_3$

$\alpha_v\beta_3$ is one of the most overexpressed integrin isoforms in endothelial cells that compose the leaky vasculature around tumor tissue as well one of the most overexpressed integrin isoforms in tumor and tumor progenitor cells.[34,35] As our goal was surface engineering of NPs to target tumors and their vasculature, we evaluated the binding affinity between AXT050 and recombinant integrin $\alpha_v\beta_3$. The ForteBio Octet RED96, a label-free molecular binding assay that employs bio-layer interferometry to detect specific, native interaction of ligand and receptor, was used. The binding of AXT050 to $\alpha_v\beta_3$ revealed a kinetic binding curve typical of 1:1 association and dissociation (**Figure 5.1A**). The reaction rate constants k_{on} and k_{off} were determined to be 1 $\mu M^{-1}s^{-1}$ and 0.0032 s^{-1}, respectively, by fitting the raw binding data to simple single-binding site association model in MATLAB.

The resulting equilibrium dissociation constant K_D was determined to be 3.2 nM, which is a strong affinity with the same order of magnitude to that of antibodies and specific enzyme–substrate interactions. Strong binding affinity to integrin $\alpha_v\beta_3$ measured here corroborates a

recent report that the anti-angiogenic peptide's mechanism of action is through downstream signaling from its specific binding to integrin isoforms.[29]

AXT050 localizes to tumor tissue following systemic delivery

Based on the biding affinity to integrin $\alpha_v\beta_3$, a biodistribution experiment of near-infrared fluorescence-tagged AXT050, AXT050-IRD800, injected intravenously was performed. An orthotopic human xenograft triple-negative breast cancer (MDA-MB-231) mouse model was used for this experiment with liver, kidneys, spleen, lungs, heart and the tumor harvested at 24 h post-injection to detect fluorescence. Small biological molecules, such as a peptide composed of natural amino acids, are expected to degrade and clear from the blood quickly, and we find that AXT050 is cleared from the blood with a half-life of approximately 11 min. However, due to its binding affinity to integrin $\alpha_v\beta_3$, approximately 15% of AXT050 was able to reach the tumor based on the fluorescence signal from tumor relative to the other organs within each mouse. As expected, kidneys were the main route of clearance for the small peptide, as seen by the highest level of its detection in the kidneys compared to other organs. **Figure 5.1B–D** illustrates these biodistribution findings.

Formulation and characterization of non-targeted NPs

Three different NP systems were developed and investigated to enable improved delivery of the anti-angiogenic AXT050 peptide. For the first approach, PLGA NPs were fabricated using a double emulsion protocol to encapsulate peptide. The sonication settings

and surfactant concentration were varied to determine their effect on particle size measured by NTA as shown in **Figure 5.2A**. Increasing the sonication setting from 30 to 60 A decreased hydrodynamic particle size from a micron scale to a size of approximately 200 nm, but further increases to the sonication power did not affect particle size. Increasing the PVA concentration from 2 to 3% also did not affect the NP size. TEM images of the NPs are shown in **Figure 5.2A**. Loading efficiency of the peptide into these PLGA NPs was found to be approximately 20–30%.

To improve drug delivery, properties such as physical shape (higher aspect ratio) and chemical surface functionalization (PEGylation) have been previously shown to influence the biological response of drug delivery NPs and enhance blood circulation and passive targeting.[36,37] To explore the effect of shape on the NPs, a previously developed thin-film stretching particle method[32] was utilized on the approximately 200 nm spherical PLGA NPs to create ellipsoidal PLGA NPs with aspect ratio of 2.8 by stretching two-fold along one axis (**Figure 5.2B**). To explore the role of surface coating, PLGA-PEG NPs were also prepared to deliver the peptide. These NPs were made with PLGA-PEG block copolymers using a nanoprecipitation method. PLGA-PEG NPs had a stable hydrodynamic particle of approximately 70 nm in a range of media, including water, phosphate buffered saline (PBS), and 100% fetal bovine serum (FBS) (**Figure 5.2C**).

Biodistribution of non-targeted NPs

A biodistribution experiment with the same design as with the naked peptide was performed using the non-targeted NP systems. The injected groups were PBS only, spherical

PLGA NPs, ellipsoidal PLGA NPs, and PLGA-PEG NPs all loaded with AXT050-IRD800 labeled peptide. In all treated groups, the total amount of peptide injected was the same, at 20 mg per mouse. In **Figure 5.2D** and **Figure 5.3**, the relative distribution of the fluorescence across the different organs within each mouse is shown. By encapsulating AXT050 in NPs, the liver became the primary organ of biodistribution for all three conditions (spherical PLGA NP, ellipsoidal PLGA NP, and PEGylated PLGA NP). There were no statistically significant differences between the groups in terms of accumulation in the tumor after 24 h (7–15%).

Formation and characterization of targeted NPs

In order to enhance accumulation of NPs in the tumor, we engineered targeted PLGA-PEG NPs using AXT050 peptide as the targeting ligand. We synthesized surface-functionalized PLGA-PEG NPs by conjugating AXT050 to PLGA-PEG-NHS and then forming NPs through nanoprecipitation such that AXT050 ligands coat the outer surface of the particles as illustrated in **Figure 5.4A/B**. High performance liquid chromatography showed approximately 90% conjugation of PLGA PEG-NHS to free peptide (**Figure 5.5**). Formation of functionalized PLGA-PEG copolymers prior to NP formation allowed control over the amount of peptide exposed on the surface of the NPs and optimization of surface ligand density. As physicochemical properties, such as ligand density, surface charge, and particle size, have a large effect on stealth properties and thus half-life of the particle,[36] this synthesis method was important as it allowed us to mix functionalized and inert PLGA-PEG polymers in any ratio that we desired to tune the surface properties of the NPs.

NP size was found to be affected by functionalization, with a greater percentage of AXT050 peptide on the surface leading to greater particle size as seen in **Figure 5.6A/B**. The percentage (e.g., 100, 50%) represents the percentage of conjugated polymer (PLGA-PEG-AXT050) by mass relative to the total polymer (conjugated polymer and methoxy-terminated PLGA-PEG) used in NP formulation. NP size, as measured by z-average hydrodynamic diameter, ranged from approximately 65 nm for 0% NP to 80 nm for 100% NP. A similar effect of increased size has been seen in other studies, which show that PEG length can have a significant effect on size.[38] Increased peptide surface-functionalization also resulted in wider particle size distributions. Zeta potential was observed to be negative (approximately -20 mV) and not significantly affected by the surface peptide content, which may be explained by the overall neutral charge of the peptide (**Figure 5.6C**). LavaPep peptide quantification determined that approximately 80% of the theoretical peptide mass was exposed on the surface of the NP, regardless of the ratio of peptide-conjugated polymer to non-conjugated polymer used in the NP formulation.

AXT050 targeted NPs bind to cells and recombinant integrin in vitro

In order to confirm the preferential homing of the targeted NPs to integrin, which we found to have a high molecular binding affinity, the NP binding to vascular cells expressing integrins, cancer cells expressing integrins, and free recombinant integrin was evaluated. First, 100% AXT050 peptide-coated PLGA-PEG NPs, which refers to the mass percentage of PLGA-PEG-AXT050 compared to PLGA-mPEG, encapsulated with TAMRA-dye were incubated with MECs and triple-negative breast cancer cells, and then spun down to separate

free NPs from those bound to cells. As depicted in **Figure 5.7A**, cells incubated with surface-functionalized NPs consistently showed approximately four- and two-fold higher signals to indicate binding compared to control PLGA-PEG NPs without peptide (0%) in MEC and MDA-MB-231 cells, respectively.

When NPs were incubated with labeled $\alpha_v\beta_3$, $\alpha_5\beta_1$, and HSA, 100% AXT050-functionalized targeted NPs showed significantly higher binding compared to non-targeted 0% AXT050 NPs with both integrin isoforms (**Figure 5.7B**). Critically, NPs were found to have higher binding to the integrins compared to HSA, indicating that the targeted NPs bind preferentially to these integrins with low non-specific interactions. Finally, when 100% NPs were incubated with labeled $\alpha_v\beta_3$ and a 100-fold excess of AXT050 or an active fragment of AXT050 (AF_AXT050) (**Figure 5.7B**), competition from the excess peptide completely prohibited binding of the targeted PLGA-PEG-AXT050 NPs to integrin. In contrast, when an inactive scrambled variant of AXT050 peptide was used as the free competitor rather than active AXT050, signal from the PLGA-PEG-AXT050 NPs binding to labeled integrin persisted. Although interactions between functionalized NPs and additional biomolecules may also be present, the specificity and high-affinity of the binding between the peptide-coated NPs and $\alpha_v\beta_3$ integrin can enable cellular targeting of the NPs.

Efficacy of targeted NPs in vitro

Human triple-negative breast cancer cells (MDA-MB-231) and primary MEC were used to demonstrate anti-tumorigenic and anti-angiogenic activity of peptide-functionalized and peptide-loaded NPs *in vitro* with dose response related to both the density of targeting

ligand and the presence or absence of encapsulated peptides. Recently, we demonstrated that the naked form of an analog peptide could inhibit the proliferation and adhesion of MDA-MB-231 cells at concentrations of approximately 25–100 mM *in vitro*.[39] At NP concentration of 10 mg/mL, particles showed a peptide dose-dependent inhibition of adhesion on both cell types. NPs were analyzed at varying levels of functionalization and encapsulation as shown in **Figure 5.8A/B**. Relative to control wells, wells with 100% PLGA-PEG-AXT050 NPs encapsulating 1% (w/w) free AXT050 consistently showed the highest adhesion inhibition on all cell types. This is expected as this condition represents the greatest amount of peptide delivered to the target cells. Increased levels of surface conjugated AXT050 and encapsulated AXT050 increased efficacy in a dose dependent fashion. Whether AXT050 was encapsulated or not, as AXT050 conjugation and display from the NP surface increased (100%>50%>10%>0%), so did the biological activity of the NPs. When comparing surface conjugated AXT050 NPs to free bolus administration of AXT050, it was observed that unloaded 10% PLGA-PEGAXT050 NPs, which correspond to approximately 40 mM of surface conjugated peptide, showed significantly less ($p<0.001$) inhibition of adhesion on both cell types than 25 μM naked bolus AXT050 peptide, suggesting the availability and presentation of the peptide from the NP surface could affect its biological potency. Since the cells are plated in a monolayer, and the peptide is displayed from the NP's three-dimensional surface, it is likely that more than half of the displayed peptide could be inaccessible to the cellular integrins due to the peptide's orientation on the NPs *in vitro*. However, this effect may become less relevant *in vivo* as particle breakdown occurs over several days within a tumor microenvironment compared to several hours as measured in *in vitro* adhesion assays. Decorated particles with no encapsulated peptide that were subject to degradation in PBS

solution at 37ºC showed increased activity in *in vitro* adhesion assays using MDA-MB-231 cells compared to intact particles, but decreased activity compared to equal doses of free peptide (**Figure 5.9**). The increased efficacy after particle breakdown is likely due to PEG-peptide released from the surface as particles undergo hydrolysis. This is consistent with our findings that PEG-peptide shows adhesion activity against MDA-MB-231 cells, but with less activity as the length of the PEG increases (**Figure 5.10**). Degradation of particles in the days following initial administration could result in further efficacy when PEG-peptide fragments and peptide metabolites escape the NPs through hydrolysis and proteolysis, respectively. In MDA-MB-231 cells, 50–100% PLGAPEG- AXT050 NPs encapsulating 1% AXT050 reduced human cancer cell adhesion by 80–81%. In MECs, these two leading NP formulations reduced adhesion in these endothelial cells by 85–87% as well. These results demonstrate that these peptide-coated NPs have the biological capability to disrupt the endothelial cells that make up the leaky vasculature supplying oxygen and nutrients to tumors as well as disrupt the human breast cancer cells themselves.

We also evaluated NP activity against MEC proliferation over 4 days. In addition to adhesion, NPs also inhibit proliferation of MECs with dose dependence of the peptide at the NP concentration of 5 mg/mL. Unlike the adhesion assay, where the effective peptide concentration appeared lower than surface conjugated peptide, likely due to orientation of immobilized peptide, proliferation inhibition more clearly followed the total amount of peptide present in the NP. As shown in **Figure 5.8C**, unloaded 10 and 50% NPs, which have equivalent total peptide concentration of 20 and 100 mM, show comparable levels of proliferation inhibition as 25 and 100 mM bolus naked peptide groups. One possible explanation is particle degradation over the 4-day experiment. Free, soluble peptide becomes

available through release of encapsulated peptide, release of PEG-AXT050 through hydrolysis of PLGA,[4] or protease-mediated degradation of AXT050 into active fragments. For example, AXT050 conjugated with PEG of two different molecular weights still resulted in adhesion inhibition of MECs at 25 and 100 mM concentrations (**Figure 5.10**). This suggests that the combination of PEG-AXT050 and AXT050 metabolites have activity in addition to the activity generated by PLGA-PEG-AXT050 in an intact particle. This provides a mechanism for sustained release of active AXT050 in the tumor microenvironment following initial binding of the PLGA-PEG-AXT050 NPs to overexpressed $\alpha_v\beta_3$ integrin on tumors and tumor vasculature. In this manner, the surface-conjugated peptide functions as a NP targeting agent, a multivalent surface-bound drug agent, and a reservoir for controlled release of drug agent over time. This combined function, along with multimodality at affecting both tumors and tumor vasculature (endothelial cells), is promising for a cancer nanomedicine strategy.

Finally, we investigated the effect of AXT050 peptide surface coating to improve the targeting of PEG-PLGA NPs to mice inoculated with human triple-negative breast cancer (MDA-MB-231) (**Figure 5.11A-D**). We evaluated the pharmacokinetics of the PLGA-PEG-AXT050 NPs in the blood and the effect of increasing AXT050 conjugation. **Figure 5.11C** shows the half-life curves for targeted NPs over approximately 5 h, after which the signal reached baseline levels. We observed blood half-lives of approximately 110, 103, and 45 min for 0, 10, and 100% PLGA-PEG-AXT050 NPs, respectively. This extended half-life of nearly 2 h for 0–10% PLGA-PEG-AXT050 (100–90% PEG-PLGA) NPs clearly demonstrates the beneficial effect of PEGylation at slowing the clearance of these particular NPs from the blood. Half-life was found to decrease with increasing amount of peptide

conjugated to the surface of the NP. This decrease in half-life may be a result of increased peptide density obviating the stealth effect of PEG, leading to particle destabilization or increased opsonization and subsequent uptake by the immune system.[40] Alternatively, it is possible that a very high density of the peptide on the surface of the NPs could lead to increased avidity and potential off-target binding of the NPs. Thus, maximizing the amount of peptide on the NP surface does not lead to optimal pharmacokinetics.

Interestingly, biodistribution results showed a biphasic trend in tumor accumulation of targeted NPs (**Figure 5.11A/B**). Using labeled AXT050 peptide, the fluorescence signal in the tumor for 10% PLGA-PEG-AXT050 (90% PEG-PLGA) NP at 24 h post-injection was 14% of the total fluorescence measured in all harvested organs, a 2.2-fold increase compared to non-targeted 0% PLGA-PEG-AXT050 (100% PEG-PLGA) NP and a 3.5-fold increase from 100% PLGA-PEG-AXT050 in this head-to-head study. Moreover, 10% NP showed 14% lower signal in liver than both 0 and 100% NP. This finding highlights the utility of combining the AXT050 targeting peptide to the surface of the PEGylated NPs. This finding also demonstrates the double-edged sword of using a ligand such as AXT050 for targeting. Too little surface functionalization and the NPs circulate for a long time but without sufficient active targeting to the tissue of interest, and too much active targeting and the NPs are cleared to off-target sites too quickly (**Figure 5.11D**). The relatively high amount of the injected dose that reaches the tumor is quite promising when compared to the median 0.9% targeted NP accumulation of an injected dose to the tumor as has been reported by Wilhelm et al. by analyzing the literature from the past decade.[41] Faster clearance by the reticulo-endothelial system of the 100% NPs that has the least PEG shielding could explain both its short half-life and low tumor accumulation. Non-specific accumulation of the NPs occurred

in liver, kidneys, and spleen, which are the expected routes of clearance, but minimally in lungs and heart, organs that must be avoided for safety considerations. It is also important to note that no acute systemic toxicity was observed in the animals injected with any formulation of NPs at the doses given and the NPs were chosen so that they were composed of biodegradable and bio-eliminable materials.

5.4 Discussion

The half-life of PLGA-PEG NPs and factors affecting clearance time *in vivo* has been widely studied, with half-life increasing significantly, often several orders of magnitude, upon PEGylation of PLGA NP.[42] This is thought to decrease recruiting of opsonins on the surface of NPs that cue macrophages for clearance. Other means of elimination include off-target endocytosis, renal clearance, hepatic clearance, splenic filtration, and degradation of the polymer prior to arriving on target. While PEGylation allows longer circulation and potential passive accumulation in leaky vasculature, it does not enable specific binding to tumors or their vasculature.

Biomimetic peptide-PEG-PLGA NPs are a promising method of drug delivery addressing difficulties in both targeting and controlled release. Surface properties of NPs are incredibly important for facilitating successful transport from the site of injection to the tumor site,[43] thus targeting ligands used to increase uptake in the tumor must be optimized to prevent clearance prior to reaching the tumor site. Many targeting ligands have been used to target biomarkers to tumors and tumor vasculature, including integrin-targeted cyclic-RGD peptide, folate receptor-targeted folic acid, and prostate-specific membrane antigen-targeted small molecules.[44-46] However, since previously reported ligands generally only function as

targeting agents, cancer treatments with these particles rely on the delivery of additional therapeutic components such as chemotherapies like paclitaxel, doxorubicin, and docetaxel, that are physically encapsulated at low loading content within these particles. In the current study, we wanted to utilize and evaluate a novel biomimetic molecule on NP surfaces that could function as both a targeting agent and a multimodal therapeutic agent. By chemically conjugating the peptide to PEG-PLGA polymer, rather than relying on just physical encapsulation, we can increase the loading of the peptide in NPs, enable multivalent display from the surface of the particle to the surface of the cell, and consequently induce a greater therapeutic effect.

The slow off-rate constant and nanomolar K_D between the short AXT050 peptide and its cellular target suggests a strong interaction between the AXT050-coated NPs and the surfaces of cancer cells and angiogenic endothelial cells where $\alpha_v\beta_3$ is overexpressed. Multivalency and avidity between AXT050 presented from the NP surface to integrin $\alpha_v\beta_3$ clustered on the cellular surface could further enhance the strength of the interaction and duration of effect.[47] This could also explain the shorter half-life and reduced tumor accumulation of 100% NP compared to 10% NP, since greater surface exposure of the peptide could result in strong binding of the NPs with integrin receptors at sites with low expression of integrin $\alpha_v\beta_3$ in addition to the tumor microenvironment where there is high integrin $\alpha_v\beta_3$. Another explanation for faster clearance of 100% NP from the circulation could be the loss of stealth properties, as all surface PEG molecules are covered by the peptide.

In vitro targeting assays clearly showed affinity of the targeted NPs for integrin $\alpha_v\beta_3$, an important upregulated target in tumor neovasculature. In addition, the therapeutic

potential of the NPs was also validated through *in vitro* biological activity assays against human triple-negative breast cancer (anti-tumorigenic) and MEC (anti-angiogenic) cells. We observed activity of the functionalized particles against tumor cells and endothelial cells in short-term adhesion assays through their surface interactions despite the spatial restrictions that this places on the peptide. In addition, the surface peptide has further activity over time as it is released from the particle surface that is dependent on the hydrolytic breakdown of the particle, similar to release of encapsulated drug within the particle.

While this work has demonstrated that AXT050 peptide can be an effective targeting agent for nanomedicine by increasing the accumulation of NPs to human triple-negative breast cancer tumors significantly while also reducing liver accumulation, clearance and remaining accumulation in the liver and spleen still remain as issues. The non-specific accumulation in the liver and spleen is mostly due to clearance and elimination through the mononuclear phagocyte system (MPS). It is important to note that the peptide, unlike a traditional chemotherapy, is designed to only affect cells with upregulated integrin $\alpha_v\beta_3$, in particular tumor cells and their neovasculature, and will therefore trigger a minimal effect on the specific function of these off-target clearance cells. Nonetheless, the potential dose responsive systemic side effects of such a NP system should be further investigated in multiple preclinical animal models to ensure the safety of this approach.

5.5 Conclusion

We have found that AXT050, a multimodal peptide with anti-tumorigenic and anti-angiogenic properties, can function as both a targeting ligand and a therapeutic bioactive agent useful for NP-mediated delivery to human triple-negative breast cancer cells. We found

that these AXT050-targeted NPs were able to target integrin $\alpha_v\beta_3$ on the surface of cells in culture, which was confirmed through a series of binding experiments. The AXT050 NPs exhibit *in vitro* activity in adhesion and proliferation assays against human triple-negative breast cancer MB-MDA-231 cells and MEC endothelial cells, both through surface presentation of peptide and controlled release of the peptide from the NP. We also determined a biphasic response with peptide surface coating density and tumor targeting *in vivo*. Optimal 10% PLGA-PEG-AXT050/ 90% PEG PLGA NPs were found to exhibit an extended 103 min half-life and accumulate 14% of the peptide dose in human triple-negative breast cancer tumors in a xenograft mouse model. As the components of this NP system are each biodegradable and bio-eliminable, and as the AXT050 peptide NPs have the potential to target and disrupt both cancer cells and endothelial cells, this technology may be promising for applications in cancer nanomedicine.

5.6 References

(1) Corti, A.; Pastorino, F.; Curnis, F.; Arap, W.; Ponzoni, M.; Pasqualini, R., Targeted drug delivery and penetration into solid tumors. *Med Res Rev* **2012,** 32, (5), 1078-91.

(2) Khawar, I. A.; Kim, J. H.; Kuh, H. J., Improving drug delivery to solid tumors: Priming the tumor microenvironment. *J Control Release* **2015,** 201, 78-89.

(3) Sriraman, S. K.; Aryasomayajula, B.; Torchilin, V. P., Barriers to drug delivery in solid tumors. *Tissue Barriers* **2014,** 2, e29528.

(4) Danhier, F.; Ansorena, E.; Silva, J. M.; Coco, R.; Le Breton, A.; Preat, V., Plga-based nanoparticles: An overview of biomedical applications. *J Control Release* **2012,** 161, (2), 505-22.

(5) Graf, N.; Bielenberg, D. R.; Kolishetti, N.; Muus, C.; Banyard, J.; Farokhzad, O. C.; Lippard, S. J., Alpha(v)beta(3) integrin-targeted plga-peg nanoparticles for enhanced anti-tumor efficacy of a pt(iv) prodrug. *ACS Nano* **2012,** 6, (5), 4530-9.

(6) Alibolandi, M.; Ramezani, M.; Sadeghi, F.; Abnous, K.; Hadizadeh, F., Epithelial cell adhesion molecule aptamer conjugated peg-plga nanopolymersomes for targeted delivery of doxorubicin to human breast adenocarcinoma cell line in vitro. *Int J Pharm* **2015,** 479, (1), 241-51.

(7) Dhar, S.; Gu, F. X.; Langer, R.; Farokhzad, O. C.; Lippard, S. J., Targeted delivery of cisplatin to prostate cancer cells by aptamer functionalized pt(iv) prodrug-plga-peg nanoparticles. *Proc Natl Acad Sci U S A* **2008,** 105, (45), 17356-61.

(8) Cheng, J.; Teply, B. A.; Sherifi, I.; Sung, J.; Luther, G.; Gu, F. X.; Levy-Nissenbaum, E.; Radovic-Moreno, A. F.; Langer, R.; Farokhzad, O. C., Formulation of functionalized plga-peg nanoparticles for in vivo targeted drug delivery. *Biomaterials* **2007,** 28, (5), 869-76.

(9) Zhu, H.; Chen, H.; Zeng, X.; Wang, Z.; Zhang, X.; Wu, Y.; Gao, Y.; Zhang, J.; Liu, K.; Liu, R.; Cai, L.; Mei, L.; Feng, S. S., Co-delivery of chemotherapeutic drugs with vitamin e tpgs by porous plga nanoparticles for enhanced chemotherapy against multi-drug resistance. *Biomaterials* **2014,** 35, (7), 2391-400.

(10) Danhier, F.; Lecouturier, N.; Vroman, B.; Jerome, C.; Marchand-Brynaert, J.; Feron, O.; Preat, V., Paclitaxel-loaded pegylated plga-based nanoparticles: In vitro and in vivo evaluation. *J Control Release* **2009,** 133, (1), 11-7.

(11) Liang, C.; Yang, Y.; Ling, Y.; Huang, Y.; Li, T.; Li, X., Improved therapeutic effect of folate-decorated plga-peg nanoparticles for endometrial carcinoma. *Bioorg Med Chem* **2011,** 19, (13), 4057-66.

(12) Kamaly, N.; Xiao, Z.; Valencia, P. M.; Radovic-Moreno, A. F.; Farokhzad, O. C., Targeted polymeric therapeutic nanoparticles: Design, development and clinical translation. *Chem Soc Rev* **2012,** 41, (7), 2971-3010.

(13) Chopra, S. L., J.M.; Karnik, R.; Farokhzad, O. , Role of electrostatic interactions in protein loading in plga-peg nanoparticles. *40th Annual Northeast Bioengineering Conference (NEBEC)* **2014**, pp. 1-2.

(14) Prabhakar, U.; Maeda, H.; Jain, R. K.; Sevick-Muraca, E. M.; Zamboni, W.; Farokhzad, O. C.; Barry, S. T.; Gabizon, A.; Grodzinski, P.; Blakey, D. C., Challenges and key considerations of the enhanced permeability and retention effect for nanomedicine drug delivery in oncology. *Cancer Res* **2013,** 73, (8), 2412-7.

(15) Danhier, F.; Le Breton, A.; Preat, V., Rgd-based strategies to target alpha(v) beta(3) integrin in cancer therapy and diagnosis. *Mol Pharm* **2012,** 9, (11), 2961-73.

(16) Xie, J.; Shen, Z.; Li, K. C.; Danthi, N., Tumor angiogenic endothelial cell targeting by a novel integrin-targeted nanoparticle. *Int J Nanomedicine* **2007,** 2, (3), 479-85.

(17) Fasehee, H.; Dinarvand, R.; Ghavamzadeh, A.; Esfandyari-Manesh, M.; Moradian, H.; Faghihi, S.; Ghaffari, S. H., Delivery of disulfiram into breast cancer cells using folate-receptor-targeted plga-peg nanoparticles: In vitro and in vivo investigations. *J Nanobiotechnology* **2016,** 14, 32.

(18) Wang, Z.; Chui, W. K.; Ho, P. C., Design of a multifunctional plga nanoparticulate drug delivery system: Evaluation of its physicochemical properties and anticancer activity to malignant cancer cells. *Pharm Res* **2009,** 26, (5), 1162-71.

(19) Arosio, D.; Casagrande, C., Advancement in integrin facilitated drug delivery. *Adv Drug Deliv Rev* **2016,** 97, 111-43.

(20) Gu, F.; Zhang, L.; Teply, B. A.; Mann, N.; Wang, A.; Radovic-Moreno, A. F.; Langer, R.; Farokhzad, O. C., Precise engineering of targeted nanoparticles by using self-assembled biointegrated block copolymers. *Proc Natl Acad Sci U S A* **2008,** 105, (7), 2586-91.

(21) Alexis, F.; Pridgen, E.; Molnar, L. K.; Farokhzad, O. C., Factors affecting the clearance and biodistribution of polymeric nanoparticles. *Mol Pharm* **2008,** 5, (4), 505-15.

(22) Moghimi, S. M.; Hunter, A. C.; Andresen, T. L., Factors controlling nanoparticle pharmacokinetics: An integrated analysis and perspective. *Annu Rev Pharmacol Toxicol* **2012,** 52, 481-503.

(23) Xia, Q.; Li, H.; Xiao, K., Factors affecting the pharmacokinetics, biodistribution and toxicity of gold nanoparticles in drug delivery. *Curr Drug Metab* **2016,** 17, (9), 849-861.

(24) Zhang, L.; Chan, J. M.; Gu, F. X.; Rhee, J. W.; Wang, A. Z.; Radovic-Moreno, A. F.; Alexis, F.; Langer, R.; Farokhzad, O. C., Self-assembled lipid--polymer hybrid nanoparticles: A robust drug delivery platform. *ACS Nano* **2008,** 2, (8), 1696-702.

(25) Ernsting, M. J.; Murakami, M.; Roy, A.; Li, S. D., Factors controlling the pharmacokinetics, biodistribution and intratumoral penetration of nanoparticles. *J Control Release* **2013,** 172, (3), 782-94.

(26) Li, S. D.; Huang, L., Pharmacokinetics and biodistribution of nanoparticles. *Mol Pharm* **2008,** 5, (4), 496-504.

(27) Kim, J.; Mirando, A. C.; Popel, A. S.; Green, J. J., Gene delivery nanoparticles to modulate angiogenesis. *Adv Drug Deliv Rev* **2017,** 119, 20-43.

(28) Karagiannis, E. D.; Popel, A. S., A systematic methodology for proteome-wide identification of peptides inhibiting the proliferation and migration of endothelial cells. *Proc Natl Acad Sci U S A* **2008,** 105, (37), 13775-80.

(29) Lee, E.; Lee, S. J.; Koskimaki, J. E.; Han, Z.; Pandey, N. B.; Popel, A. S., Inhibition of breast cancer growth and metastasis by a biomimetic peptide. *Sci Rep* **2014,** 4, 7139.

(30) Rosca, E. V.; Koskimaki, J. E.; Pandey, N. B.; Tamiz, A. P.; Popel, A. S., Structure-activity relationship study of collagen-derived anti-angiogenic biomimetic peptides. *Chem Biol Drug Des* **2012,** 80, (1), 27-37.

(31) Rosca, E. V.; Penet, M. F.; Mori, N.; Koskimaki, J. E.; Lee, E.; Pandey, N. B.; Bhujwalla, Z. M.; Popel, A. S., A biomimetic collagen derived peptide exhibits anti-angiogenic activity in triple negative breast cancer. *PLoS One* **2014,** 9, (11), e111901.

(32) Meyer, R. A.; Sunshine, J. C.; Perica, K.; Kosmides, A. K.; Aje, K.; Schneck, J. P.; Green, J. J., Biodegradable nanoellipsoidal artificial antigen presenting cells for antigen specific t-cell activation. *Small* **2015,** 11, (13), 1519-25.

(33) Bhise, N. S.; Shmueli, R. B.; Gonzalez, J.; Green, J. J., A novel assay for quantifying the number of plasmids encapsulated by polymer nanoparticles. *Small* **2012,** 8, (3), 367-73.

(34) Desgrosellier, J. S.; Cheresh, D. A., Integrins in cancer: Biological implications and therapeutic opportunities. *Nat Rev Cancer* **2010,** 10, (1), 9-22.

(35) Haubner, R.; Wester, H. J.; Reuning, U.; Senekowitsch-Schmidtke, R.; Diefenbach, B.; Kessler, H.; Stocklin, G.; Schwaiger, M., Radiolabeled alpha(v)beta3 integrin antagonists: A new class of tracers for tumor targeting. *J Nucl Med* **1999,** 40, (6), 1061-71.

(36) Decuzzi, P.; Pasqualini, R.; Arap, W.; Ferrari, M., Intravascular delivery of particulate systems: Does geometry really matter? *Pharm Res* **2009,** 26, (1), 235-43.

(37) Farokhzad, O. C.; Langer, R., Impact of nanotechnology on drug delivery. *ACS Nano* **2009,** 3, (1), 16-20.

(38) Li, L.; Xiang, D.; Shigdar, S.; Yang, W.; Li, Q.; Lin, J.; Liu, K.; Duan, W., Epithelial cell adhesion molecule aptamer functionalized plga-lecithin-curcumin-peg nanoparticles for targeted drug delivery to human colorectal adenocarcinoma cells. *Int J Nanomedicine* **2014,** 9, 1083-96.

(39) Rosca, E. V.; Koskimaki, J. E.; Pandey, N. B.; Wolff, A. C.; Popel, A. S., Development of a biomimetic peptide derived from collagen iv with anti-angiogenic activity in breast cancer. *Cancer Biol Ther* **2011,** 12, (9), 808-17.

(40) Mosqueira, V. C.; Legrand, P.; Gulik, A.; Bourdon, O.; Gref, R.; Labarre, D.; Barratt, G., Relationship between complement activation, cellular uptake and surface physicochemical aspects of novel peg-modified nanocapsules. *Biomaterials* **2001,** 22, (22), 2967-79.

(41) Wilhelm, S. T., A.J.; Dai, Q.; Ohta, S.; Audet, J. Dvorak, H.F., Chan, W.C.W., Analysis of nanoparticle delivery to tumours. *Nat Rev Mater* **2016,** 16014.

(42) Avgoustakis, K.; Beletsi, A.; Panagi, Z.; Klepetsanis, P.; Livaniou, E.; Evangelatos, G.; Ithakissios, D. S., Effect of copolymer composition on the physicochemical characteristics, in vitro stability, and biodistribution of plga-mpeg nanoparticles. *Int J Pharm* **2003,** 259, (1-2), 115-27.

(43) Verma, A.; Stellacci, F., Effect of surface properties on nanoparticle-cell interactions. *Small* **2010,** 6, (1), 12-21.

(44) Danhier, F.; Vroman, B.; Lecouturier, N.; Crokart, N.; Pourcelle, V.; Freichels, H.; Jerome, C.; Marchand-Brynaert, J.; Feron, O.; Preat, V., Targeting of tumor endothelium by rgd-grafted plga-nanoparticles loaded with paclitaxel. *J Control Release* **2009,** 140, (2), 166-73.

(45) Esmaeili, F.; Ghahremani, M. H.; Ostad, S. N.; Atyabi, F.; Seyedabadi, M.; Malekshahi, M. R.; Amini, M.; Dinarvand, R., Folate-receptor-targeted delivery of docetaxel nanoparticles prepared by plga-peg-folate conjugate. *J Drug Target* **2008,** 16, (5), 415-23.

(46) Farokhzad, O. C.; Cheng, J.; Teply, B. A.; Sherifi, I.; Jon, S.; Kantoff, P. W.; Richie, J. P.; Langer, R., Targeted nanoparticle-aptamer bioconjugates for cancer chemotherapy in vivo. *Proc Natl Acad Sci U S A* **2006,** 103, (16), 6315-20.

(47) Tassa, C.; Duffner, J. L.; Lewis, T. A.; Weissleder, R.; Schreiber, S. L.; Koehler, A. N.; Shaw, S. Y., Binding affinity and kinetic analysis of targeted small molecule-modified nanoparticles. *Bioconjug Chem* **2010,** 21, (1), 14-9.

5.7 Figures & Tables

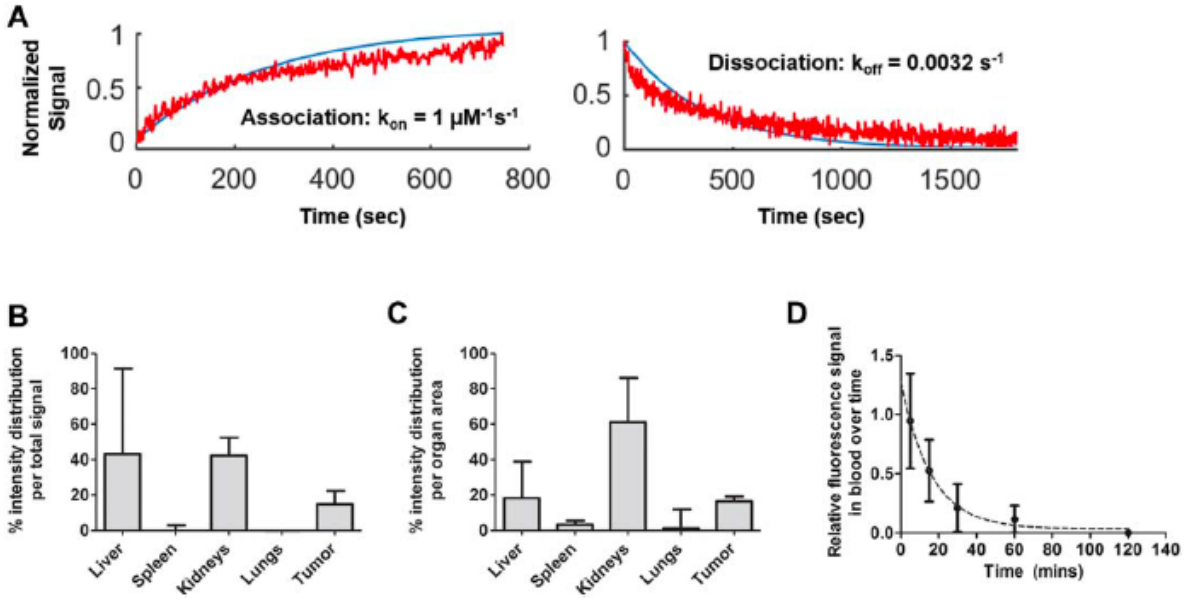

Figure 5.1. AXT050 binding and biodistribution. A: AXT050 binds to $\alpha_v\beta_3$ with a k_{on} of 1 $\mu M^{-1}s^{-1}$, k_{off} of 0.0032 s^{-1}, and K_D of 3.2 nM. B, C: AXT050 accumulated in MDA-MB-231 tumors and was cleared through the kidney with (D) a blood circulation half-life of approximately 11 min.

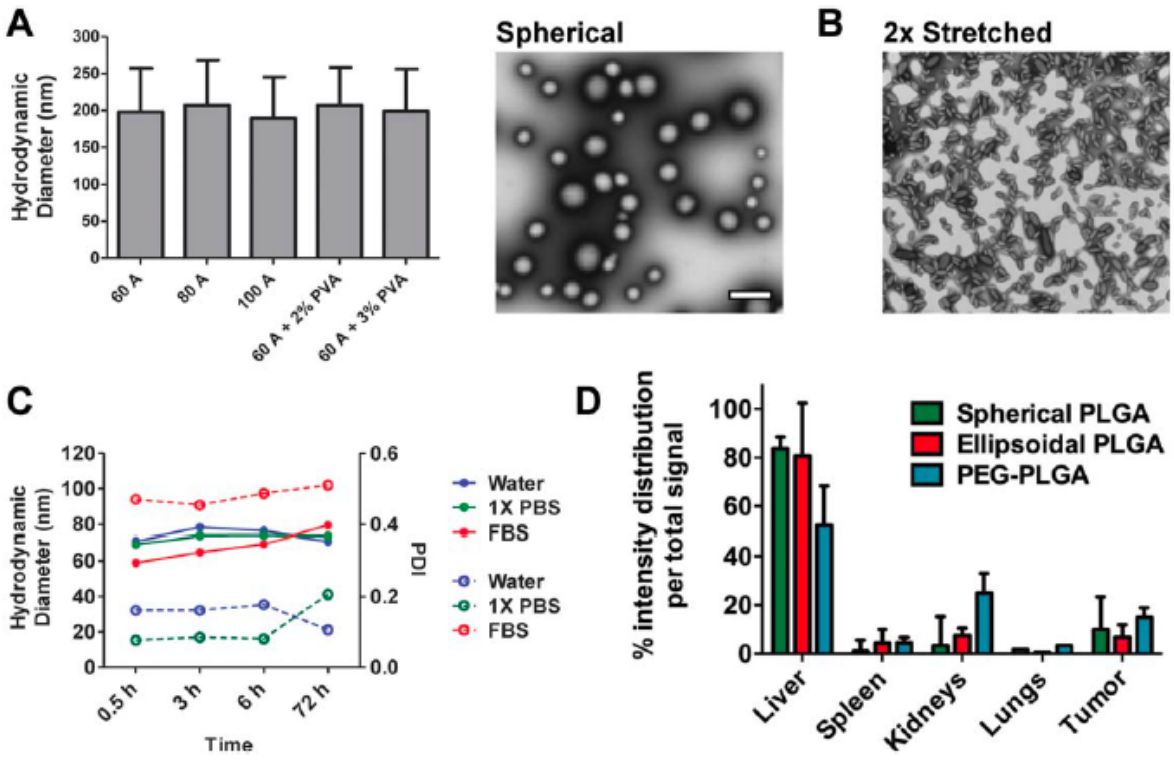

Figure 5.2. Biophysical characterization of non-targeted AXT050-containing PLGA NP. A: Hydrodynamic diameter (NTA) of non-modified PLGA NPs formulated with different conditions and a representative TEM image of PLGA NPs from "60A" condition, (B) TEM image of anisotropic PLGA NPs ("60A" PLGA NPs stretched twofold), (C) Stability of PLGA-PEG NPs over 3 days in different media by DLS (closed circle/solid line: size, open circle/dashed line: polydispersity index), and (D) Biodistribution of non-targeted NPs. NTA: mean ± SD (n>200 particles), TEM: scale bar = 1 μm.

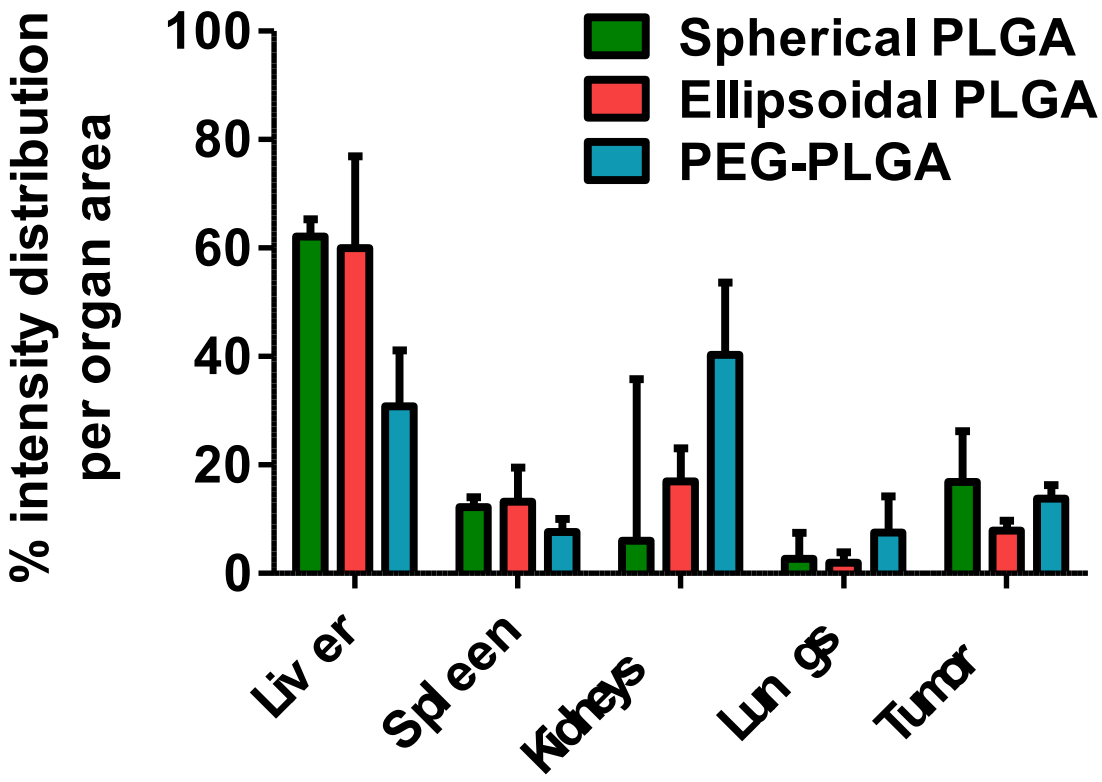

Figure 5.3. Biodistribution of non-targeted PLGA AXT050 NPs. Biodistribution quantified by fluorescence intensity normalized per organ area.

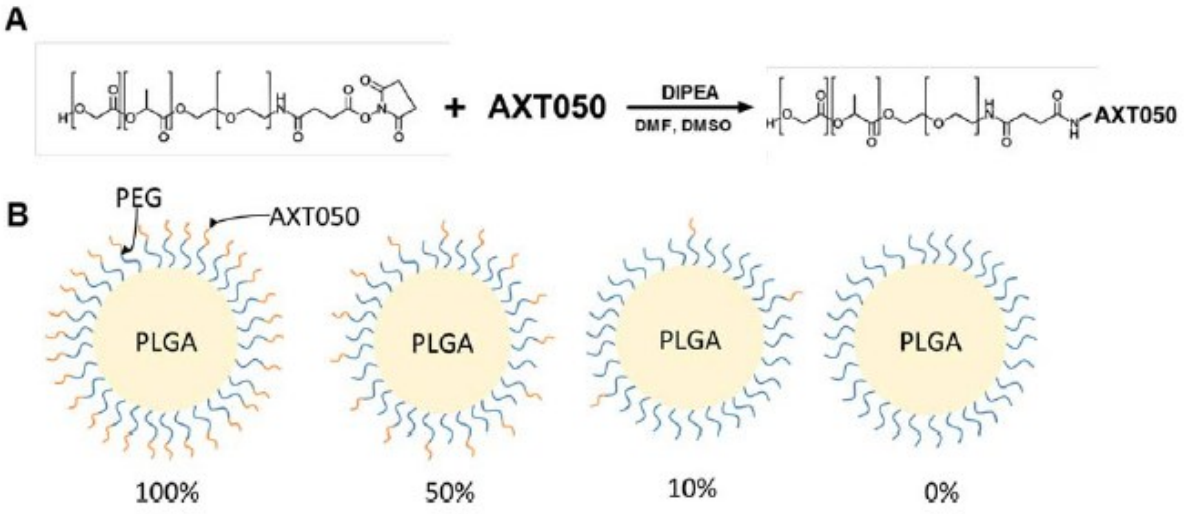

Figure 5.4. Fabrication of PLGA-PEG-AXT050 NPs. A: PLGA-PEG-NHS polymer is reacted with AXT050 to form PLGA-PEG-AXT050 conjugates. B: NPs are formed by nanoprecipitation utilizing PLGA-PEG-AXT050 and PLGA-mPEG at varied mass ratios including 100%:0%, 50%:50%,10%:90%, and 0%:100% PLGA-PEG-AXT050: PLGA-mPEG polymer.

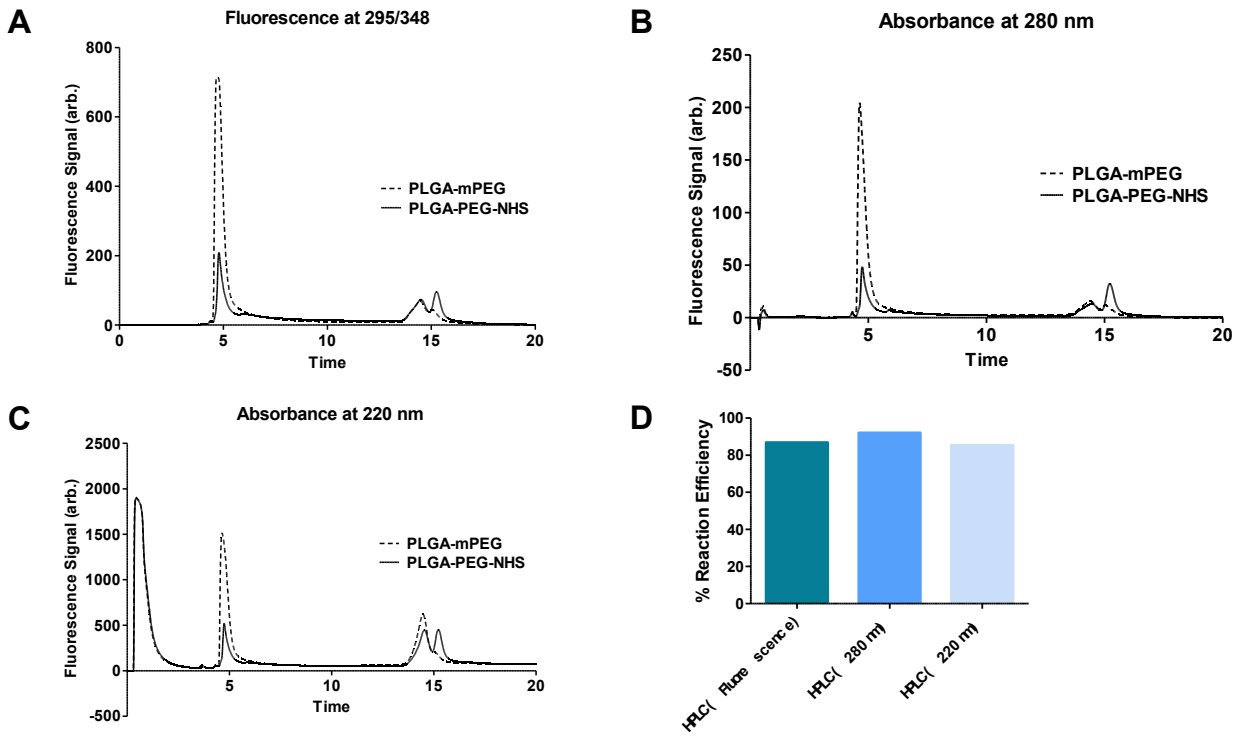

Figure 5.5. Characterization of PLGA-PEG-NHS coupling to AXT050 peptide. (A) HPLC spectrum showing absorbance at 280 nm, (B) 220 nm, (C) Fluorescence at 295/348 excitation/emission, and (D) Reaction efficiency calculated by the ratio of AUC for the peak at t = 5 mins.

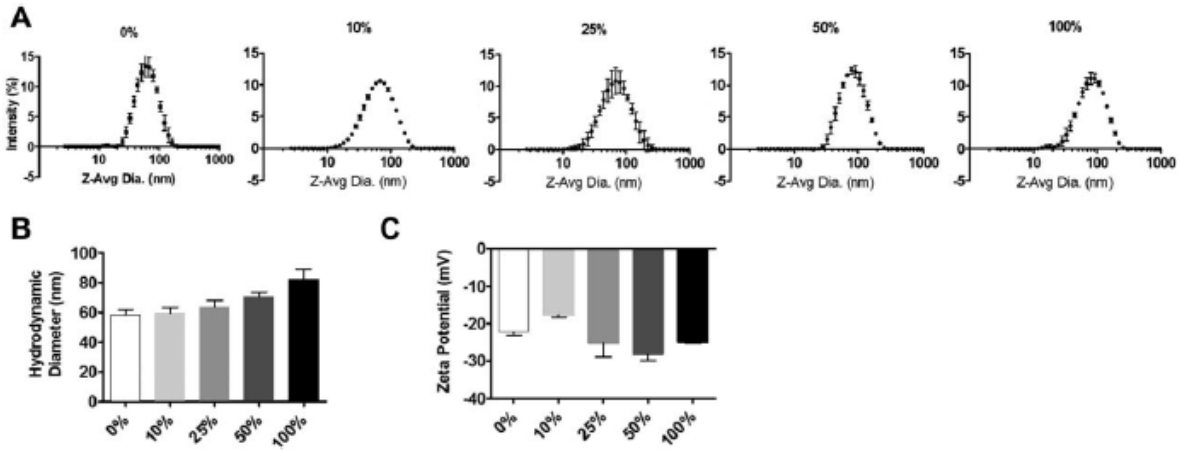

Figure 5.6. Biophysical characterization of PLGA-PEG-AXT050 NPs. A: The PLGA-PEG-AXT050 NPs have a hydrodynamic particle diameter of approximately 65–80 nm. B: Hydrodynamic particle diameter increased slightly as the percentage of AXT050 peptide conjugation increased. C: Particle zeta potential was determined to be approximately 220 mV, without AXT050 conjugation content significantly affecting the surface charge.

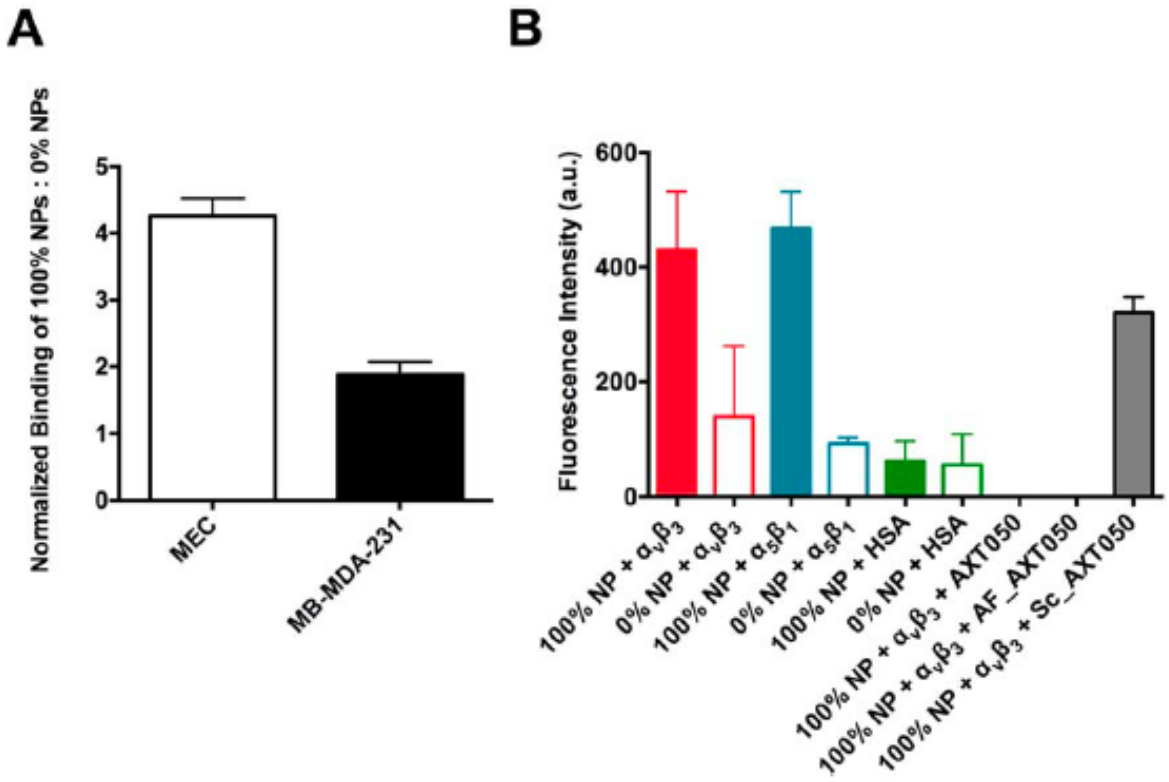

Figure 5.7. Targeted binding of NPs to cells and integrin molecules. A: Binding of targeted (PLGA-PEG-AXT050) 100% NPs to MEC cells and MDA-MB-231 cells in suspension normalized to the binding of untargeted (PLGA-mPEG) 0% NPs. B: Binding of targeted 100% NPs and non-targeted 0% NPs to integrin $\alpha_v\beta_3$, $\alpha_5\beta_1$, and to HSA as a negative control. Binding of targeted 100% NPs to integrin $\alpha_v\beta_3$ in the presence of a 100-fold excess of AXT050 peptide, an active fragment of AXT050 peptide, and scrambled AXT050 peptide.

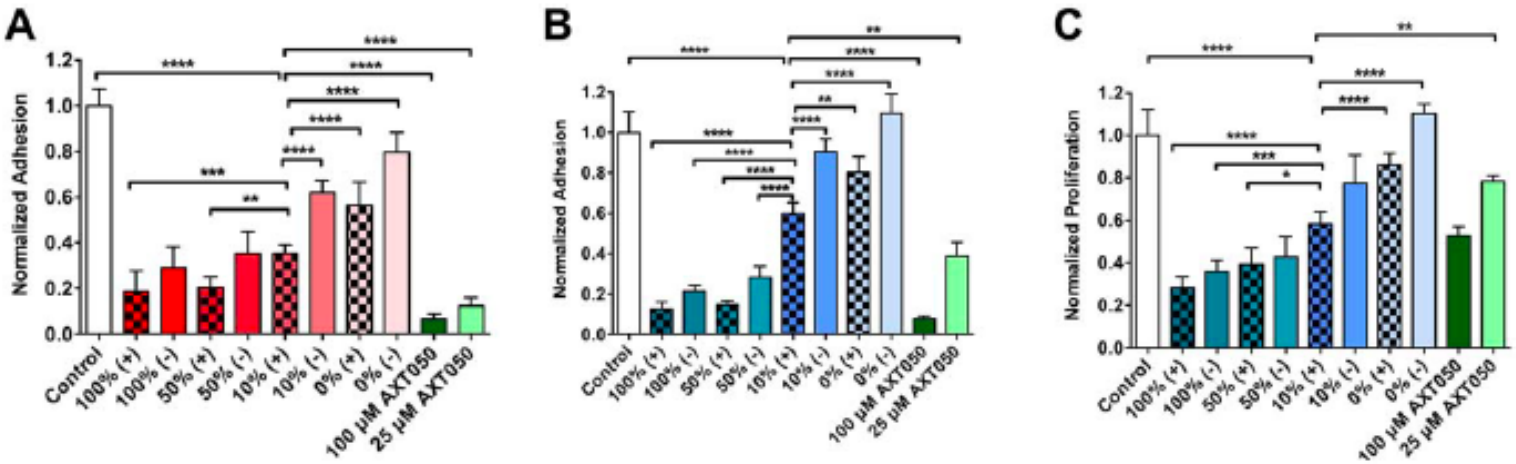

Figure 5.8. Functional biological activity of NPs composed of 0%-100% PLGA-PEG-AXT050 that contain (+) or do not contain (-) encapsulatedAXT050. NPs inhibit adhesion of (A) MDA-MB231 cells and (B) MECs. C: NPs also inhibit the proliferation of MECs normalized to untreated control. One-way ANOVA with Bonferroni post-tests comparing all pairs. Due to space limitations on the figures, representative comparisons with 10% PLGA-PEG-AXT050 encapsulating AXT050 found to be statistically significant are shown in the figures and all other comparisons are shown in the Supporting Information, (α=0.05; *p<0.05, **p<0.01, ***p<0.001, ****p<0.0001).

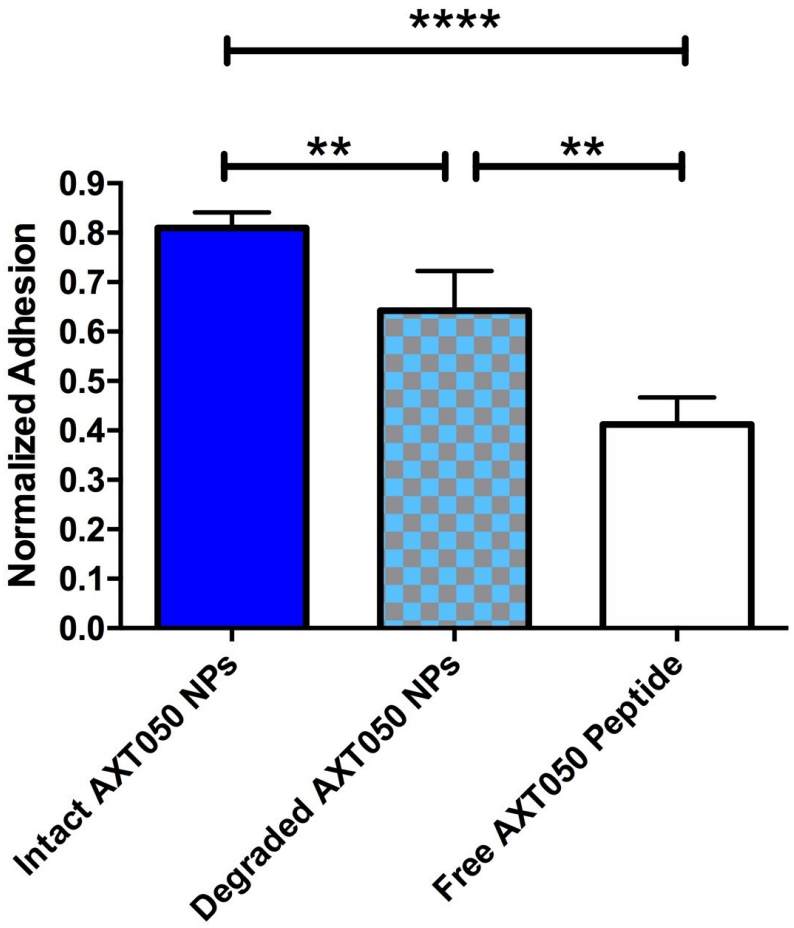

Figure 5.9. PLGA-PEG-AXT050 nanoparticle biodegradation increases biological activity at inhibiting the adhesion of MDA-MB-231 human breast cancer cells. A 30 μM peptide dose is used in each case, whether conjugated (10% AXT050) to the NPs and used directly (Intact AXT050 NPs), conjugated to the NPs (10% AXT050) and allowed to degrade in PBS at 37°C for 5 days (Degraded AXT050 NPs), or used as a bolus (Free AXT050 Peptide). One-way ANOVA and multiple comparisons were performed using Bonferroni post-tests to compare all pairs, (α=0.05; **: $p<0.01$, ****: $p < 0.0001$).

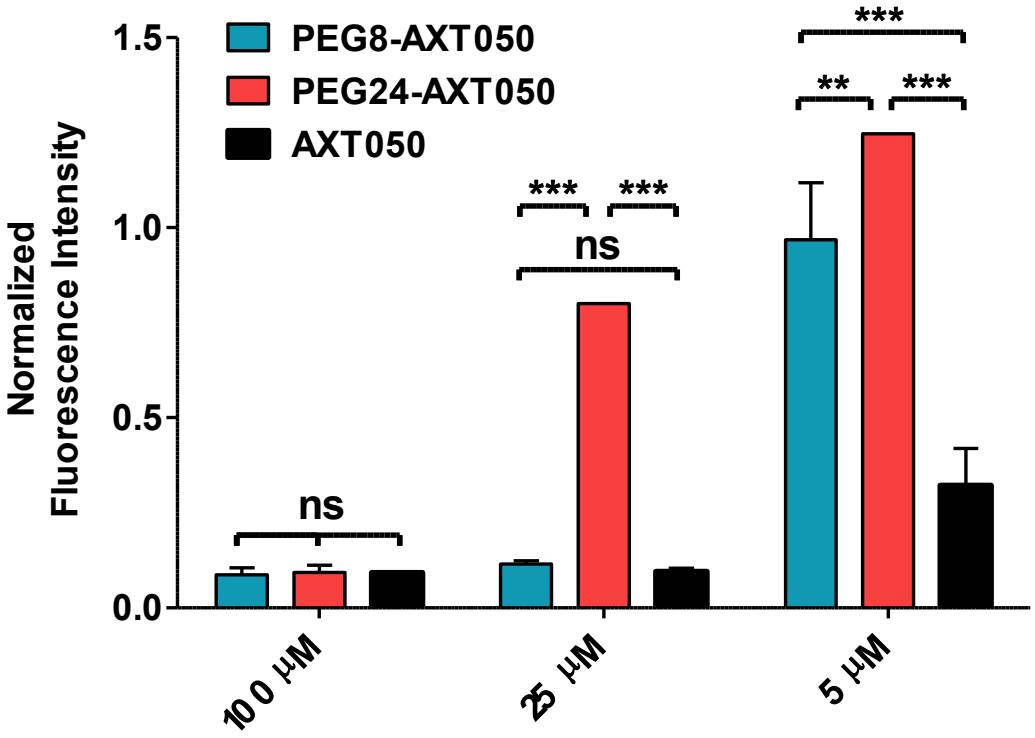

Figure 5.10. AXT050 peptide conjugated with PEG retains the ability to cause adhesion inhibition of MECs at 25 and 100 μM concentrations. Higher PEG-AXT050 doses and shorter length PEG conjugates improve efficacy. One-way ANOVA and multiple comparisons were performed using Bonferroni post-tests (α=0.05; **: $p<0.01$, ***: $p<0.001$).

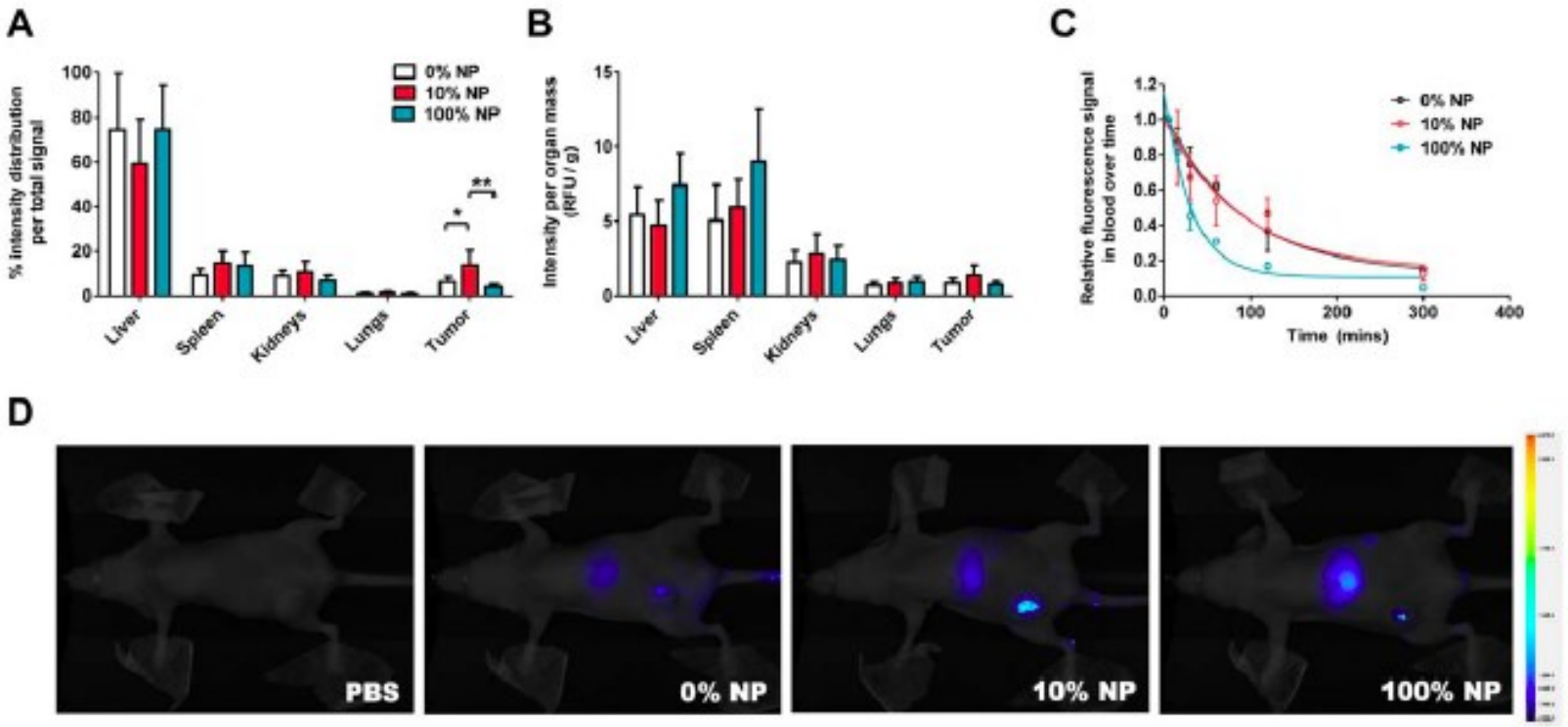

Figure 5.11. ***In vivo*** **tumor targeting of PLGA-PEG-AXT050 NPs to human triple-negative breast cancer tumors.** A, B: PLGA-PEG-AXT050 NPs accumulate in human TNBC tumors and exhibit a biphasic relationship between the level of AXT050 conjugation and TNBC tumor accumulation with 10% PLGA-PEG-AXT050/90% PLGA-mPEG NPs being optimal. C: The half-life of the 100% PLGA-PEG-AXT050 NPs was 45 min and longer half-lives were observed with 10% NPs (103 min) and 0% NPs (110 min), which were composed of increasing levels of PLGA-mPEG rather than PLGA-PEG-AXT050. D: Animal imaging demonstrates the whole body biodistribution of the peptide NPs, with the greatest tumor accumulation being with the 10% NPs.

Chapter 6

Suprachoroidal injection of PBAE nanoparticles for long-term retinal expression of exogenous DNA

6.1 Introduction

Neovascular age-related macular degeneration (NVAMD) is an ocular disease that affects more than 2 million people as the leading cause of blindness in the United States.[1] It involves macular damage from edema as fluid leaks out of choroidal neovasculature growing into subretinal space.[2] Therefore, anti-angiogenesis at the posterior of the eye in retinal and choroidal layer near the macula is the therapeutic target for NVAMD. The unique biological architecture of the eye allows targeted drug delivery to this region to be achieved by local injection using a few different administration routes.[3]

Topical delivery, including eye drops, has the advantage of being minimally invasive, but also has the disadvantages of difficulty in self-administration by elderly patients as well as low level of drug accumulation due to limited mucus penetration and fast clearance.[4] On the other hand, intravitreal injection is the method clinically used for delivering many anti-angiogenic compounds to localize the drug in confined space with better pharmacokinetics than topical administration.[5] However, it suffers from invasive procedure leading to low

Parts of this chapter were originally published in and modified from Kim J*, Mirando A*, Popel AS, Green JJ. "Gene delivery nanoparticles to modulate angiogenesis," *Advanced Drug Delivery Reviews*, 119:20-43, 2017. Other parts of this chapter were completed based on research in collaboration with Shen J, Ding K, Tzeng SY, Campochiaro P, and Green JJ.

patient compliance and potential complications with hemorrhage, endophthalmitis, and cataract. High concentration of drugs can be delivered to the retinal pigment epithelial (RPE) cells with subretinal injection, but it can lead to retinal detachment.[6] More recently, there has been increased effort in investigation of suprachoroidal space as the potential region for local drug delivery.[7] Suprachoroidal (SC) region is a space that is created only when a material is injected at the fine division between choroid and sclera layers. Due to high pressure generated, the injected fluid containing the drug can spread to all area surrounding the eye, including the posterior region.

Viral vectors have been widely investigated for gene therapy via intravitreal or subretinal delivery due to their efficiency and potential for long-term expression of transduced genes. Adeno-associated virus (AAV/AAV2)[8,9], lentivirus[10], and hybrid AAV with serotypes that targets specific cell populations (rAAV)[11] have all shown positive results against CNV in preclinical animal studies. These viruses have transferred genes encoding endogenous angiogenic inhibitors such as soluble VEGF receptor (sFlt-1)[8,9], pigment epithelium-derived factor (PEDF)[12,13], endostatin and angiostatin[10], and tissue inhibitor of metalloproteinases-3 (TIMP3)[14]. However, long-term expression of exogenous gene at distant sites due to viruses that made their way into the systemic circulation is a potential safety concern.[15]

Non-viral nanoparticles pose a safer alternative to gene therapy in comparison to viral complexes. There have been studies evaluating both *in vitro* and *in vivo* transfection of the RPE cell layer with non-viral gene delivery nanoparticles that have led to therapeutic efficacy against CNV.[16-18] In particular, Sunshine *et al.* demonstrated the utility of polymeric nanoparticle library approach for ocular gene therapy.[18] 180-nm nanoparticles formed from a

library of poly(beta-amino ester)s (PBAEs) with varying structures were screened and analyzed for transfection against RPE cells *in vitro*. When the best performing formulation was injected into the subretinal space, high expression was observed 72-h post injection by both reverse transcription polymerase chain reaction (RT-PCR) and fluorescence microscopy of a genetically-encoded reporter in both retina and RPE/choroid. The specificity and efficiency of PBAE nanoparticles were enhanced through the polymer library screening approach.

In this chapter, we aimed to transfect retinal cells *in vivo* by delivering plasmid DNA with PBAE nanoparticles via suprachoroidal injection. We hypothesized that injecting an exogenous DNA with PBAE polymer that is shown to be a safe and effective gene transfection vector into localized SC space would lead to a long-term expression in the retinal and choroidal layer.

6.2 Methods

Materials

1,4-butanediol diacrylate (B4), 5-amino-1-pentanol (S5), and 1-(3-aminopropyl)-4-methyl-piperazine (E7) (Alfar Aesar, Ward Hill, MA) were purchased and used as received. EGFP-N1 pDNA (Elim Biopharmaceuticals, Hayward, CA) was obtained and used per manufacturer's instructions.

Polymer synthesis

Poly(beta-amino ester) (PBAE) polymer was synthesized by a two-step reaction. First, acrylate-terminated base polymer (B4S5) was first synthesized by Michael addition reaction of 1,4-butanediol diacrylate (B4) with 5-amino-1-pentanol (S5) at 1.05:1 acrylate:amine monomer molar ratio in the dark under magnetic stirring for 24 h at 90°C (**Figure 6.1**). In the second step, the acrylate-terminated base polymer was end-capped through another Michael addition reaction in the presence of excess of primary amine-containing small molecule 1-(3-aminopropyl)-4-methyl-piperazine (E7). For example, 625 mg of polymer in 4 mL of THF was mixed with 4 mL of 0.5 M of end-capping amine solution in THF, and stirred at 500 rpm overnight at room temperature. The final polymer (B4S5E7, or 457) was ether purified and stored in DMSO at 100 mg/mL with desiccant at -20°C until use.

Nanoparticle formulation

pDNA-carrying nanoparticle was formulated by electrostatic binding of positively charged PBAE polymer and negatively charged pDNA (pEGFP or pVEGF). pVEGF construct was synthesized from pRho-VEGF and pEGFP-N1. VEGF fragment released from pRho-VEGF with BamHI was treated with Klowle I large fragment, and blunt end ligation was used to clone into EGFP-removed pEGFP-N1 vector. 457 PBAE polymer in DMSO at 100 mg/mL and pDNA in water or 1X TE buffer at 1 mg/mL were both diluted with 25 mM sodium acetate pH 5 (NaAc) to 5.55 and 0.28 mg/mL, respectively. Then, polymer and pDNA solutions were mixed at 3 to 2 v/v ratio for 30 w/w ratio of polymer to DNA, and incubated for 10 min to allow particle complexation. To lyophilize the nanoparticles, final

nanoparticle solution was mixed with sucrose as a cryoprotectant to a final 3% sucrose solution and then aliquoted such that each aliquot has 17.4 μg of pDNA and 5 mg sucrose. Aliquoted nanoparticles were lyophilized and stored with desiccant at -20°C until use. Particle size and zeta potential before and after lyophilization was measured by dynamic light scattering using Zetasizer Nano ZS (Malvern Instruments). Freshly prepared nanoparticles were diluted with 25 mM NaAc pH 5.0 and 10 mM NaCl for particle size and zeta potential measurements, respectively. Lyophilized particles were reconstituted with water first to 100 mg/mL sucrose, then diluted with 10% sucrose solution and 10 mM NaCl for particle size and zeta potential measurements, respectively.

Nanoparticle injection

7-8-week old Brown Norway rats were anesthesized with ketamine. First, using a 27G-needle, sclera was penetrated 2 mm from the limbus to make way to the suprachoroidal space. 33G Hamilton syringe with a blunt end was filled with 5 μL of nanoparticles that were reconstituted from lyophilized form with 45 μL of sterile water or 100 mM $MgCl_2$ solution. 5 μL of nanoparticle solution contained 1.74 μg of pDNA. Then, the Hamilton syringe was inserted into the path created by 27G needle using blunt dissection and advanced into the suprachoroidal space, where nanoparticle solution was injected. 10% sucrose solution was used as controls in the fellow eye in some experiments. Eyes were treated with antibiotic cream following the injection to prevent any infection. For multiple dosings, the injection procedure above was repeated three times at different locations in the eye with 4 days to

recover in between injections. The time points for ELISA on animals with multiple injections is the number of weeks after the last of the multiple injections.

Sample preparation for RT-PCR and enzyme-linked immunosorbent assay (ELISA)

At specified time points, rats were euthanized, and retinas and choroids were dissected and removed from each eye. For RT-PCR, retinal and choroidal RNAs were extracted using TRIzol reagent (Invitrogen, Carlsbad, CA) and treated with DNase (Ambion, Austin, TX), according to the manufacturer's instruction. cDNA was prepared using kit, which was then quantified with RT-PCR (StepOnePlus Real-time PCR system, Applied Biosystems) using PowerUp SYBR Green Master Mix (Thermo Fisher Scientific). Primer sequences for EGFP and GAPDH for normalization are shown in **Table 6.1**. For ELISA, specimens were incubated with 0.1% Triton X-100 in PBS with protease inhibitors (Roche, Mannheim, Germany) for 2 hr on ice, sonicated for ~ 10 sec, and centrifuged. Using the supernatant, Bradford protein assay was used to first measure the total amount of protein, then EGFP ELISA kit (Abcam) was used to quantify the amount of EGFP protein expressed from the transfection, according to the manufacturer's instruction.

Sample preparation for ocular section and immunostaining

At specified time points, rats were euthanized, then eyes were removed, frozen in OCT, and cut into 10 μm frozen ocular sections. Frozen ocular sections were post-fixed in 4% paraformaldehyde for 15 min for fluorescence imaging of EGFP expression directly.

Some frozen sections were incubated with FITC-labeled GSA-lectin for 2 hr at room temperature to visualize vasculature. Other sections were stained with rabbit polyclonal EGFP antibody and goat anti-rabbit secondary antibody conjugated with Alexa-594.

Fluorescein Angiography

At specified time points post injection with pVEGF-carrying nanoparticles, rats were anesthesized and pupils dilated with tropicamide drops. 10% sodium fluorescein (Akron, Inc) was injected intraperitoneally, and fundus images were taken using Micron III with appropriate filter set for fluorescence angiography.

6.3 Results & Discussion

Nanoparticle preparation and characterization

Poly(beta-amino ester) (PBAE) polymer has been widely used in formulating nanoparticles for gene delivery because it is biodegradable and is positively charged and titratable due to tertiary amines along the backbone and secondary amines at the end-caps.[19] Another important property of PBAE is its structural diversity. Because the polymer is synthesized through Michael addition reaction, any molecule with a nucleophile, such as primary amine, can be a potential monomer that is reacted with a diacrylate monomer. This can lead to a library of PBAE polymers, from which the most optimal PBAE polymer and nanoparticle formulation condition can be empirically determined through high-throughput *in*

vitro screening of cellular uptake, transfection and cytotoxicity in a target cell type.[20] In this work, 457 PBAE nanoparticles formulated at a 30 w/w polymer:DNA mass ratio was used based on a previously reported result from a high-throughout transfection screening with RPE cells and human retinal endothelial cells (HREC).[21] 457 PBAE polymer used in these studies had a molecular weight of 8100 Da based on ^{1}H NMR analysis.

Tzeng *et al.* had shown previously that PBAE nanoparticles can undergo lyophilization and long-term storage at -20ºC without losing the transfection efficacy.[22] From a clinical translation perspective, it is critical to be able to store PBAE nanoparticles frozen in the absence of water, as the polymer is hydrolytically cleavable and PBAE nanoparticles can become unstable. Comparison of the PBAE 457 / DNA nanoparticle physical properties before and after lyophilization showed that the nanoparticles aggregate post lyophilization potentially due to aggregation from the loss of positive surface charge (**Figure 6.2**). Since the nanoparticles are not injected into the systemic circulation but rather injected locally to prevent the need for extravasation to get to the target site, increase in size can be tolerated.

Short-term mRNA and protein transfection level detected with RT-PCR, ELISA, and fluorescence microscopy images

EGFP transfection with PBAE nanoparticles in retina and choroid was assessed at 2 and 4 weeks post-injection by three methods. First, qRT-PCR of isolated mRNA specimens showed transcription of pDNA in both retina and choroid (**Figure 6.3A**). Choroid consistently had significantly higher mRNA level of more than two-fold than retina at 2 and 4 weeks ($p<0.0001$). There was a small non-significant increase of mRNA expression in

retina between 2 and 4 weeks, whereas choroidal mRNA decreased by a small yet significant level ($p<0.05$).

Figure 6.3B shows the level of EGFP protein expression from ELISA. In retina, we saw a gradual increase in EGFP expression from 1 week to 4 weeks. Choroidal EGFP expression kinetic was bimodal, with significant decrease from 1 to 2 weeks, followed by significant increase from 2 to 4 weeks. With the exception of the 1-week time point, retinal and choroidal levels of EGFP were not significantly different. As it could be difficult for nanoparticles to diffuse to retina across choroid, the EGFP detected in retina could partly be due to EGFP initially expressed in choroid diffusing into retina. This follows the observation from RT-PCR that there is more mRNA transcription occurring in choroid due to transfection. Fellow control eyes that were injected with 10% sucrose showed EGFP concentration below the detection level for both retina and choroid, yielding negative mass of EGFP (data not shown).

Results from ELISA are further corroborated with fluorescence microscopy images of immune-stained ocular sections and whole mounts (**Figure 6.3C/D**). Ocular sections show high signal from choroid and RPE at 1 week and 4 weeks, whereas signal from retina increases with progressing time points. The overall EGFP signal from both retina and choroid is highest at 4 weeks. Whole mount fluorescent images also show that at 4 weeks, EGFP signal is strong and similar between retina and choroid. Interesting, fluorescence is mostly focused near the injection site and becomes faint and punctate on the opposite side of the eye from the injection site. This necessitates further optimization with nanoparticle formulation to aid with the longitudinal spread within the suprachoroidal space. As Kim *et al.* has shown

previously, a potential solution may be to use an excipient molecule, such as hyaluronic acid, that behaves as a non-Newtonian fluid to provide greater pressure once injected.[23]

Long-term EGFP expression level quantified with ELISA

Based on high transfection of pEGFP with PBAE nanoparticles at 4 weeks, we further investigated EGFP expression at longer time points (**Figure 6.4**). Surprisingly, similar level of EGFP concentration was measured across the time points and still detectable at 8 months, which was the last time point that was tested. No statistical difference was found in the amount of EGFP between retina and choroid at any long-term time points, similar to the 2- and 4-week results. Of note, considerable variability was measured even from a higher number of samples, potentially caused by a combination of different experiment batches, delicate injection procedure, and ELISA. However, the presence of expressed EGFP at 8 months is noteworthy for non-viral vectors that typically yield only transient expression of transfected gene(s) without further modified technologies, such as mini-circle plasmids or CRISPR/Cas-9 system.[24] One potential explanation for the long-term expression of exogenous plasmid DNA could be the successful transfection of non-dividing cells in retina. Sustained expression of protein or presence of expressed protein could be a significant benefit for clinical translation of non-viral gene delivery platforms.

Enhanced EGFP expression level from multiple dosing

Another limitation of non-viral vectors in gene delivery in comparison to viral counterparts is a lower magnitude of expression. In order to produce higher level of proteins, we evaluated two different approaches without altering the nanoparticle itself. One method was to include an excipient, such as $MgCl_2$, which has been reported to improve transfection efficacy in some applications.[25] The second approach was to inject nanoparticles multiple times. To minimize potential toxicity and side effects, we limited the dosing to three injections, with consecutive injections spaced out by 4 days. **Figure 6.5** shows that the addition of $MgCl_2$ only had marginal increase in EGFP production at 4 weeks post-injection compared to nanoparticle alone that was not statistically significant. However, triple injection significantly increased the level of EGFP protein in retina by approximately 5-fold in comparison to the single injection group. There was no side effect observed from multiple dosing of nanoparticles, such as inflammation or death from increased intraocular pressure. Higher expression level carries the potential benefit of inducing stronger as well as longer biological effect from functional proteins.

Neovascularization induced with pVEGF transfection

There are currently several rodent models of NVAMD and diabetic macular edema (DME), such as laser-induced CNV or transgenic mice models in which novel therapeutics can be evaluated.[26] A gold standard animal model for evaluating ocular drugs is the rabbit model, but rabbit models for CNV and DME are limited. One emerging method, induction of leakage with a bolus VEGF injection, lacks the tunability often necessary, especially the kinetics of the duration of the effect. Ocular disease models based on nanoparticle-mediated

VEGF transfection and expression can have controllable VEGF expression level and duration, and hence be useful to test novel therapeutics. A preliminary functional study was conducted to test the level of neovascularization achieved after a single suprachoroidal injection of PBAE nanoparticles carrying pVEGF into a rat eye. As shown by angiography and GSA-lectin-stained whole mount as well as ocular section images in **Figure 6.6A/B/C**, eyes injected with nanoparticles formed extensive neovascularization network at 8 and 12 weeks. Rats normally do not have much choroidal vasculature, hence GSA-lectin signal mostly translates to choroidal neovascularization as the effect of VEGF delivery. More quantitative assessment of the amount of VEGF expressed, area of neovascularization, and degree of fluid leakage would be necessary in future studies. There was no side effect associated with the injection in the animals. To our knowledge, this is the first reporting of inducing angiogenesis in rats using gene transfer technology with a non-viral vector.

6.4 Conclusion

Suprachoroidal injection, a relatively unexplored route of ocular drug administration, of polymeric nanoparticles carrying plasmid DNA was investigated for clinical application in ocular diseases, such as NVAMD and DME. As a proof of concept, we successfully showed long-term expression of fluorescent protein up to 8 months in retina and choroid of Brown Norway rat eyes through RT-PCR, ELISA, and ocular section images. We also demonstrated triple dosing of nanoparticles can enhance the expression level of the encoded proteins five-fold in the retina without causing adverse effect. Lastly, as a preliminary result to creating a NVAMD/DME animal model, we showed neovascularization in rat eye following the delivery of pVEGF with PBAE nanoparticles in SC space.

6.5 References

(1) Friedman, D. S.; O'Colmain, B. J.; Munoz, B.; Tomany, S. C.; McCarty, C.; de Jong, P. T.; Nemesure, B.; Mitchell, P.; Kempen, J.; Eye Diseases Prevalence Research, G., Prevalence of age-related macular degeneration in the united states. *Arch Ophthalmol* **2004,** 122, (4), 564-72.

(2) Ratner, M., Next-generation amd drugs to wed blockbusters. *Nat Biotechnol* **2014,** 32, (8), 701-2.

(3) Zulliger, R.; Conley, S. M.; Naash, M. I., Non-viral therapeutic approaches to ocular diseases: An overview and future directions. *J Control Release* **2015,** 219, 471-487.

(4) Schopf, L. R.; Popov, A. M.; Enlow, E. M.; Bourassa, J. L.; Ong, W. Z.; Nowak, P.; Chen, H., Topical ocular drug delivery to the back of the eye by mucus-penetrating particles. *Transl Vis Sci Technol* **2015,** 4, (3), 11.

(5) Geroski, D. H.; Edelhauser, H. F., Drug delivery for posterior segment eye disease. *Invest Ophthalmol Vis Sci* **2000,** 41, (5), 961-4.

(6) Qi, Y.; Dai, X.; Zhang, H.; He, Y.; Zhang, Y.; Han, J.; Zhu, P.; Zhang, Y.; Zheng, Q.; Li, X.; Zhao, C.; Pang, J., Trans-corneal subretinal injection in mice and its effect on the function and morphology of the retina. *PLoS One* **2015,** 10, (8), e0136523.

(7) Einmahl, S.; Savoldelli, M.; D'Hermies, F.; Tabatabay, C.; Gurny, R.; Behar-Cohen, F., Evaluation of a novel biomaterial in the suprachoroidal space of the rabbit eye. *Invest Ophthalmol Vis Sci* **2002,** 43, (5), 1533-9.

(8) Lukason, M.; DuFresne, E.; Rubin, H.; Pechan, P.; Li, Q.; Kim, I.; Kiss, S.; Flaxel, C.; Collins, M.; Miller, J.; Hauswirth, W.; Maclachlan, T.; Wadsworth, S.; Scaria, A., Inhibition

of choroidal neovascularization in a nonhuman primate model by intravitreal administration of an aav2 vector expressing a novel anti-vegf molecule. *Mol Ther* **2011,** 19, (2), 260-5.

(9) Pechan, P.; Rubin, H.; Lukason, M.; Ardinger, J.; DuFresne, E.; Hauswirth, W. W.; Wadsworth, S. C.; Scaria, A., Novel anti-vegf chimeric molecules delivered by aav vectors for inhibition of retinal neovascularization. *Gene Ther* **2009,** 16, (1), 10-6.

(10) Balaggan, K. S.; Binley, K.; Esapa, M.; MacLaren, R. E.; Iqball, S.; Duran, Y.; Pearson, R. A.; Kan, O.; Barker, S. E.; Smith, A. J.; Bainbridge, J. W.; Naylor, S.; Ali, R. R., Eiav vector-mediated delivery of endostatin or angiostatin inhibits angiogenesis and vascular hyperpermeability in experimental cnv. *Gene Ther* **2006,** 13, (15), 1153-65.

(11) Weber, M.; Rabinowitz, J.; Provost, N.; Conrath, H.; Folliot, S.; Briot, D.; Cherel, Y.; Chenuaud, P.; Samulski, J.; Moullier, P.; Rolling, F., Recombinant adeno-associated virus serotype 4 mediates unique and exclusive long-term transduction of retinal pigmented epithelium in rat, dog, and nonhuman primate after subretinal delivery. *Mol Ther* **2003,** 7, (6), 774-81.

(12) Campochiaro, P. A.; Nguyen, Q. D.; Shah, S. M.; Klein, M. L.; Holz, E.; Frank, R. N.; Saperstein, D. A.; Gupta, A.; Stout, J. T.; Macko, J.; DiBartolomeo, R.; Wei, L. L., Adenoviral vector-delivered pigment epithelium-derived factor for neovascular age-related macular degeneration: Results of a phase i clinical trial. *Hum Gene Ther* **2006,** 17, (2), 167-76.

(13) Raisler, B. J.; Berns, K. I.; Grant, M. B.; Beliaev, D.; Hauswirth, W. W., Adeno-associated virus type-2 expression of pigmented epithelium-derived factor or kringles 1-3 of angiostatin reduce retinal neovascularization. *Proc Natl Acad Sci U S A* **2002,** 99, (13), 8909-14.

(14) Takahashi, T.; Nakamura, T.; Hayashi, A.; Kamei, M.; Nakabayashi, M.; Okada, A. A.; Tomita, N.; Kaneda, Y.; Tano, Y., Inhibition of experimental choroidal neovascularization by overexpression of tissue inhibitor of metalloproteinases-3 in retinal pigment epithelium cells. *Am J Ophthalmol* **2000,** 130, (6), 774-81.

(15) Prea, S. M.; Chan, E. C.; Dusting, G. J.; Vingrys, A. J.; Bui, B. V.; Liu, G. S., Gene therapy with endogenous inhibitors of angiogenesis for neovascular age-related macular degeneration: Beyond anti-vegf therapy. *J Ophthalmol* **2015,** 2015, 201726.

(16) Farjo, R.; Skaggs, J.; Quiambao, A. B.; Cooper, M. J.; Naash, M. I., Efficient non-viral ocular gene transfer with compacted DNA nanoparticles. *PLoS One* **2006,** 1, e38.

(17) Kompella, U. B.; Amrite, A. C.; Pacha Ravi, R.; Durazo, S. A., Nanomedicines for back of the eye drug delivery, gene delivery, and imaging. *Prog Retin Eye Res* **2013,** 36, 172-98.

(18) Sunshine, J. C.; Sunshine, S. B.; Bhutto, I.; Handa, J. T.; Green, J. J., Poly(beta-amino ester)-nanoparticle mediated transfection of retinal pigment epithelial cells in vitro and in vivo. *PLoS One* **2012,** 7, (5), e37543.

(19) Green, J. J.; Langer, R.; Anderson, D. G., A combinatorial polymer library approach yields insight into nonviral gene delivery. *Acc Chem Res* **2008,** 41, (6), 749-59.

(20) Kim, J.; Kang, Y.; Tzeng, S. Y.; Green, J. J., Synthesis and application of poly(ethylene glycol)-co-poly(beta-amino ester) copolymers for small cell lung cancer gene therapy. *Acta Biomater* **2016,** 41, 293-301.

(21) Shmueli, R. B.; Sunshine, J. C.; Xu, Z.; Duh, E. J.; Green, J. J., Gene delivery nanoparticles specific for human microvasculature and macrovasculature. *Nanomedicine* **2012,** 8, (7), 1200-7.

(22) Guerrero-Cazares, H.; Tzeng, S. Y.; Young, N. P.; Abutaleb, A. O.; Quinones-Hinojosa, A.; Green, J. J., Biodegradable polymeric nanoparticles show high efficacy and specificity at DNA delivery to human glioblastoma in vitro and in vivo. *ACS Nano* **2014,** 8, (5), 5141-53.

(23) Kim, Y. C.; Oh, K. H.; Edelhauser, H. F.; Prausnitz, M. R., Formulation to target delivery to the ciliary body and choroid via the suprachoroidal space of the eye using microneedles. *Eur J Pharm Biopharm* **2015,** 95, (Pt B), 398-406.

(24) Conley, S. M.; Cai, X.; Naash, M. I., Nonviral ocular gene therapy: Assessment and future directions. *Curr Opin Mol Ther* **2008,** 10, (5), 456-63.

(25) Mercer, A. A.; Loutit, J. S., Transformation and transfection of pseudomonas aeruginosa: Effects of metal ions. *J Bacteriol* **1979,** 140, (1), 37-42.

(26) Silva, R. L. E.; Kanan, Y.; Mirando, A. C.; Kim, J.; Shmueli, R. B.; Lorenc, V. E.; Fortmann, S. D.; Sciamanna, J.; Pandey, N. B.; Green, J. J.; Popel, A. S.; Campochiaro, P. A., Tyrosine kinase blocking collagen iv-derived peptide suppresses ocular neovascularization and vascular leakage. *Sci Transl Med* **2017,** 9, (373).

6.6 Figures & Tables

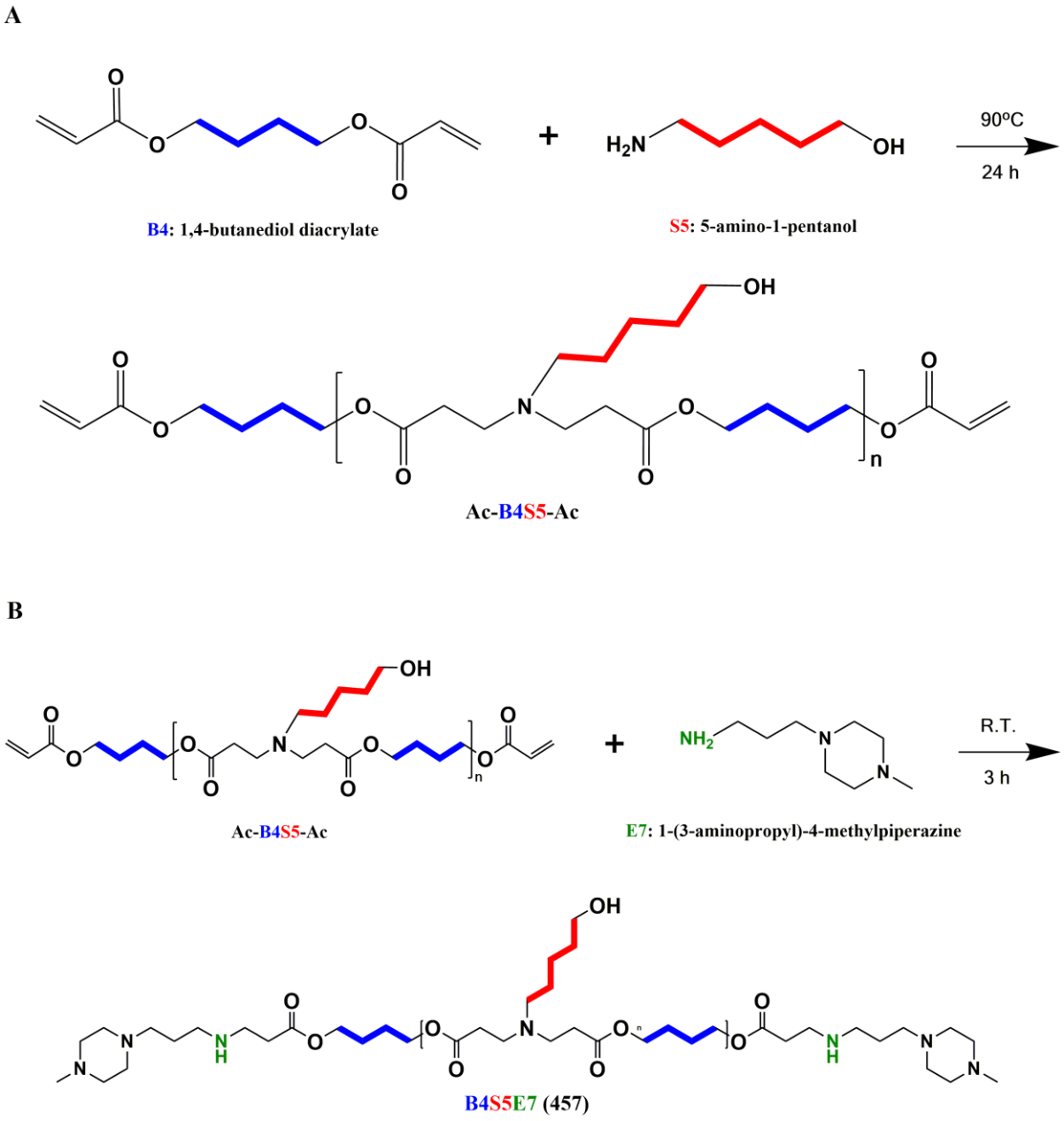

Figure 6.1. Polymer synthesis. (A) 1,4-butanediol-diacrylate (B4) is reacted with 5-amino-1-pentanol (S5) at 1.05:1 molar ratio in the first Michael addition reaction step, and (B) acrylate-terminated B4S5 base polymer was reacted with an excess of 1-(3-aminopropyl)-4-methyl-piperazine (E7) molecule to yield B4S5E7 (457) PBAE polymer.

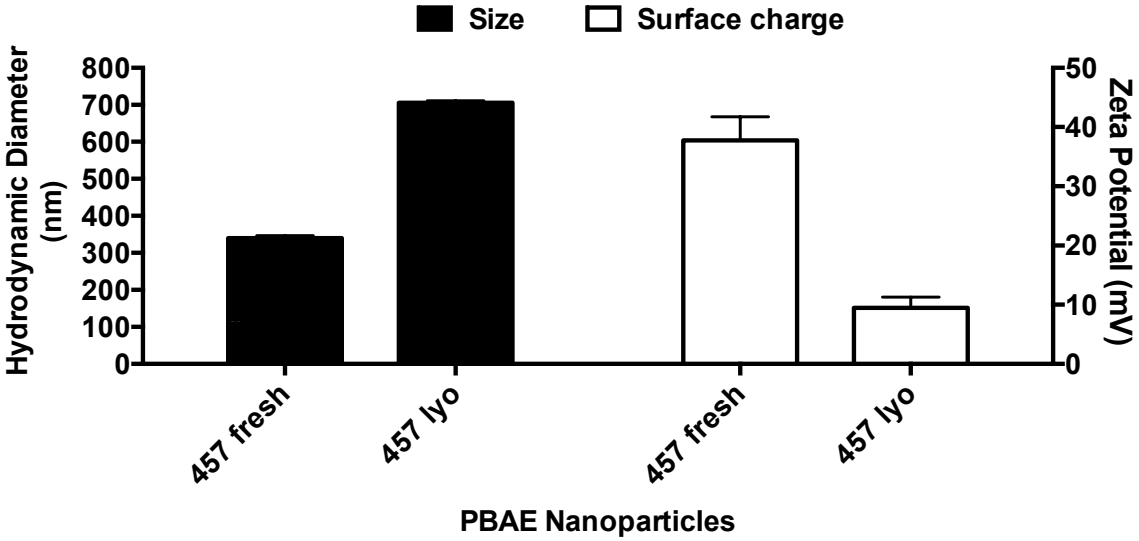

Figure 6.2. Nanoparticle characterization. (A) Hydrodynamic diameter and (B) zeta potential of 457 30 w/w nanoparticles pre- and post-lyophilization, measured by dynamic light scattering using Zetasizer Nano ZS.

A

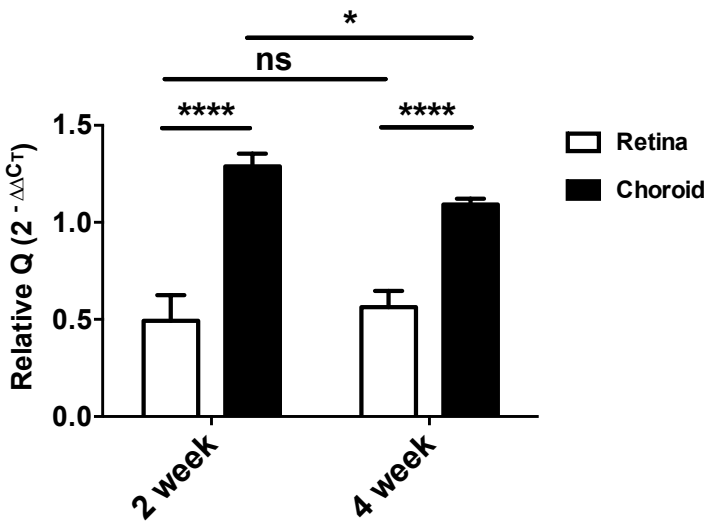
*
ns
****
****
1.5
1.0
0.5
0.0
Relative Q (2 - ΔΔCT)
Retina
Choroid
2 week
4 week

B

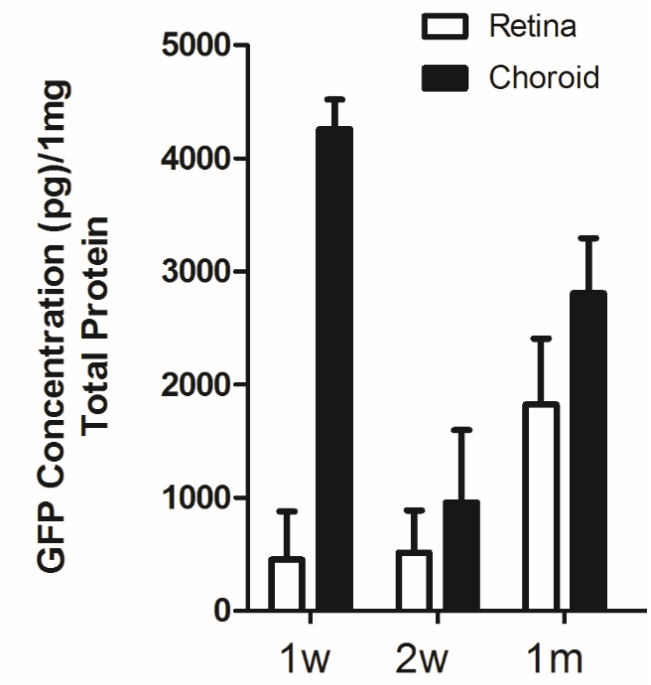
Retina
Choroid
5000
4000
3000
2000
1000
0
GFP Concentration (pg)/1mg
Total Protein
1w
2w
1m

C

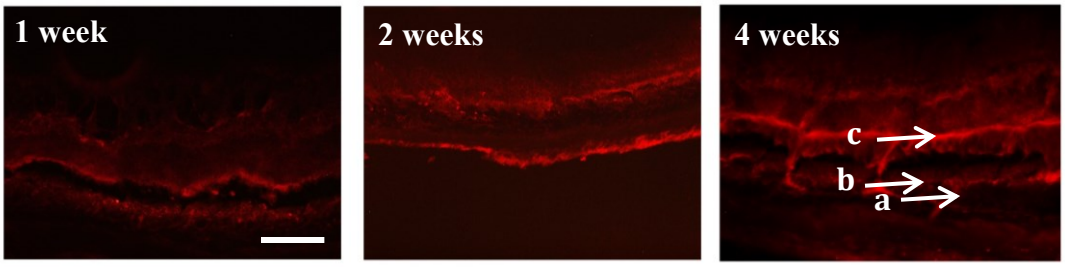

D

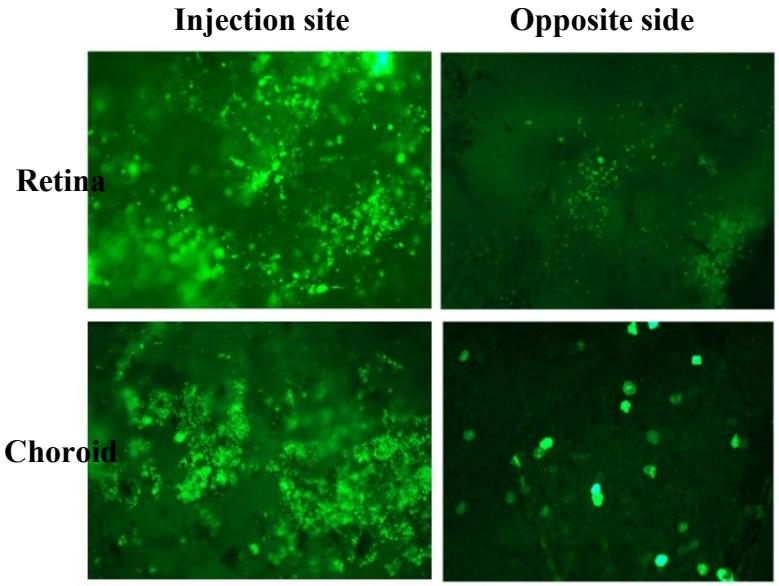

Figure 6.3. Short-term EGFP expression following suprachoroidal injection of PBAE-pEGFP nanoparticle. (A) qRT-PCR of EGFP mRNA level in retina and choroid at 2 and 4 weeks post injection (n=4, mean ± SD, One-way ANOVA with Tukey post-hoc test), (B) ELISA of EGFP protein level in retina and choroid at 1, 2, and 4 weeks post injection (n=3 for 1 week, n=7 for 2 weeks, n=8 for 4 weeks, mean ± SEM), (C) ocular sections immunostained with EGFP antibody (a: suprachoroidal space, b: RPE/choroid, c: inner segment, scale bar = 25 μm), and (D) whole mount images showing EGFP fluorescence (scale bar = 50μm)

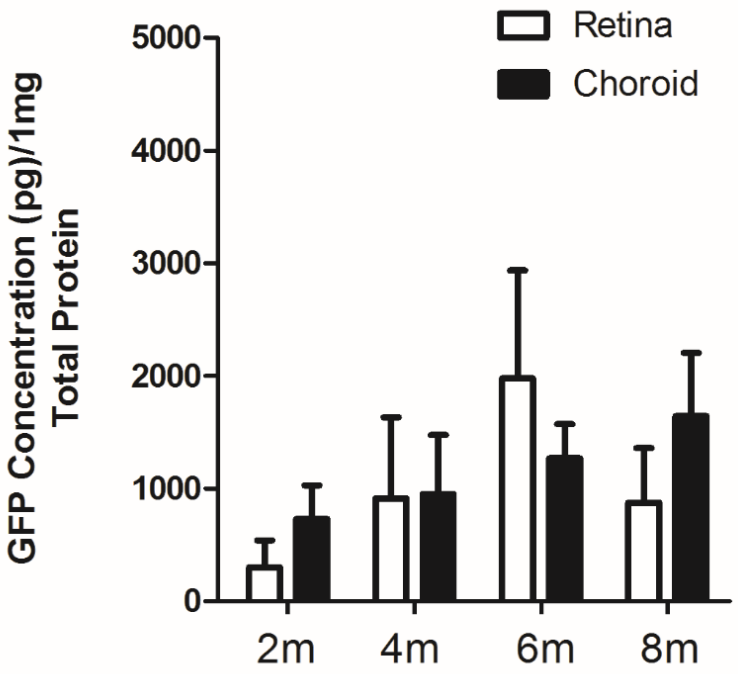

Figure 6.4. Long-term EGFP expression following suprachoroidal injection of PBAE-pEGFP nanoparticle. ELISA measurement of EGFP protein expression level at 2, 4, 6, and 8 months following suprachoroidal injection of PBAE-pEGFP nanoparticles ($n \geq 5$, mean ± SEM).

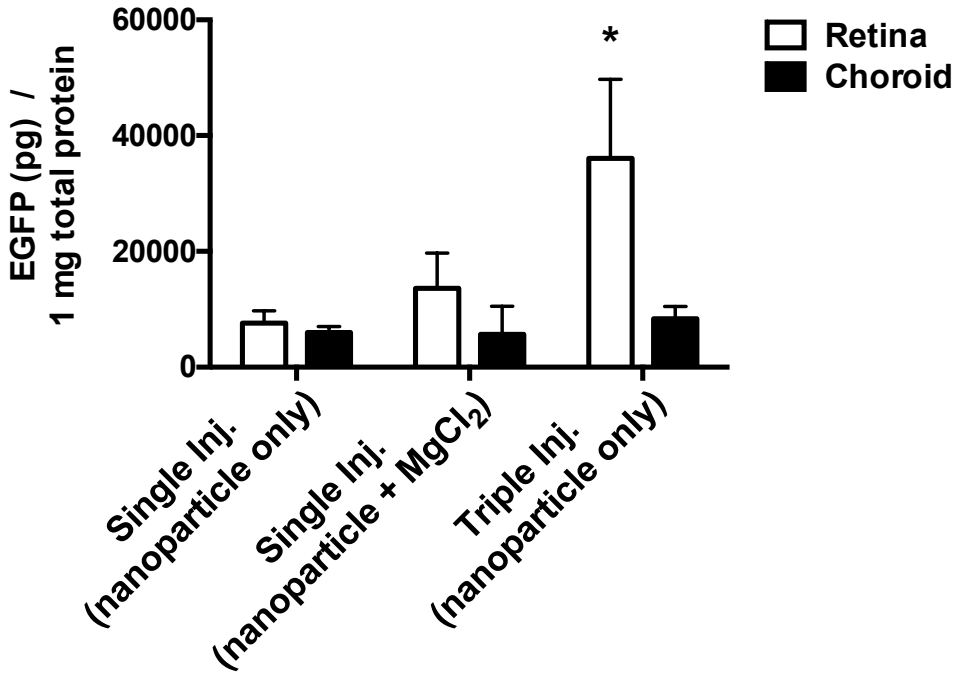

Figure 6.5. Comparison of EGFP expression level following modifications to nanoparticle injection conditions. ELISA measurement of EGFP protein expression level at 4 weeks following (the last) suprachoroidal injection of PBAE-pEGFP nanoparticles ($n = 10$ for single injections, $n \geq 7$ for triple injections, mean ± SEM, One-way ANOVA with Dunnett post-hoc test with comparison to single injection nanoparticle only control for retina and choroid).

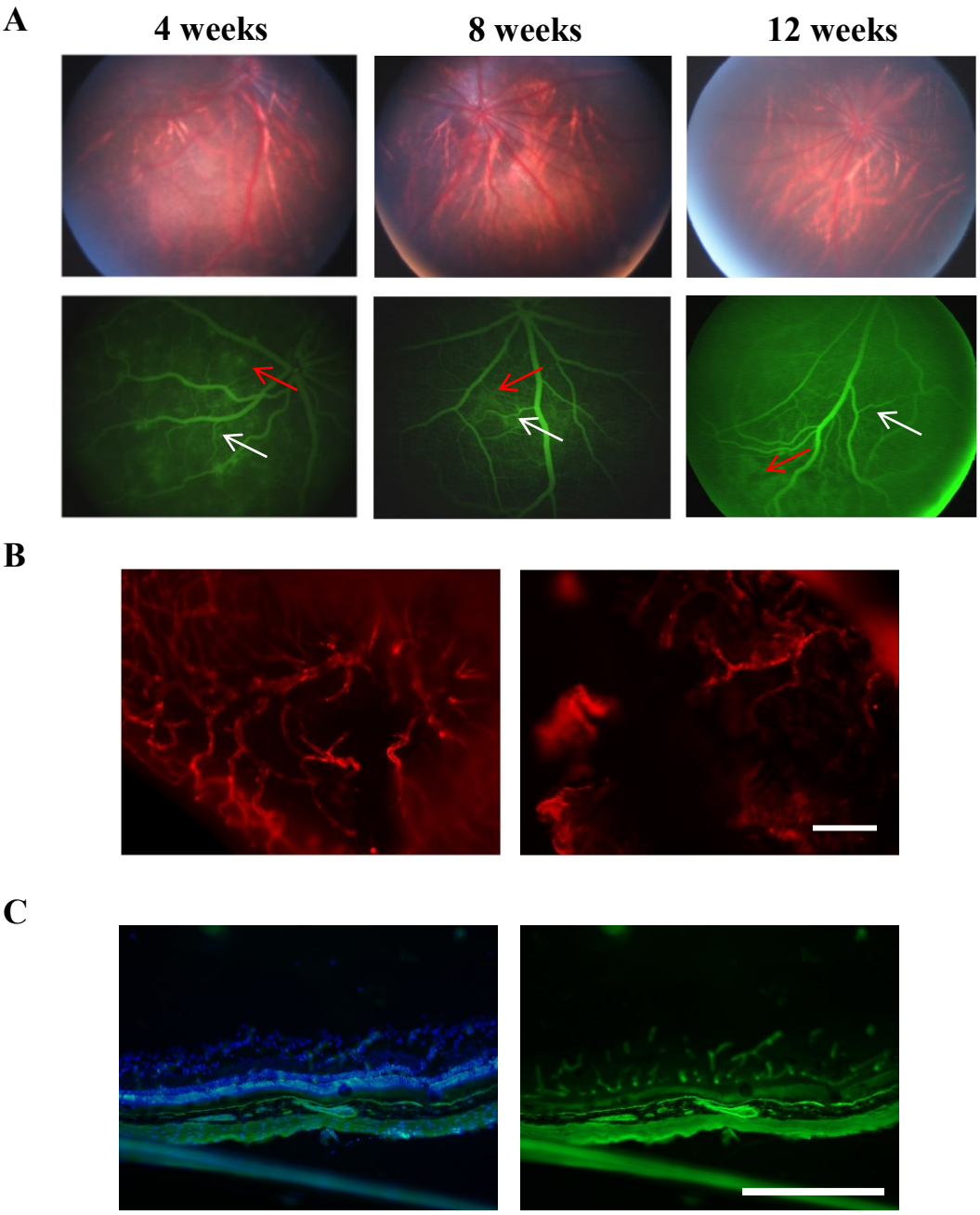

Figure 6.6. Retinal neovascularization following suprachoroidal injection of PBAE-pVEGF nanoparticles. (A) Fundus (top) and fluorescent angiography images visualizing IP-injected sodium fluorescein (bottom) at 4, 8, and 12 weeks post nanoparticle injection (white arrows: neovasculature, red arrows: leakage site), (B) fluorescent image of whole mount retinal (left) and choroidal (right) vasculature stained with GSA-lectin at 8 weeks post nanoparticle injection (scale bar = 100 μm), and (C) fluorescent image of ocular section stained with Hoescht and GSA-lectin (left) and GSA-lectin only (right) at 16 weeks post nanoparticle injection (scale bar = 100 μm).

	Forward primer (5’ → 3’)	Reverse primer (5’ → 3’)
EGFP	**CTACCCCGACCACATGAAGC**	**TGCTCAGGTAGTGGTTGTCG**
GAPDH	**GTCTACTGGCGTCTTCACCA**	**GTGGCAGTGATGGCATGG**

Table 6.1. Primer sequence used for qRT-PCR.

Chapter 7

Long-term efficacy against aberrant ocular neovascularization by sustained release of an anti-angiogenic peptide from intravitreal poly(lactic-co-glycolic acid) (PLGA) microparticles

7.1 Introduction

Vasculature has an important function to provide nutrients and oxygen to the surrounding tissue. The formation of new vessels from pre-existing vasculature, or angiogenesis, through a precise balance between pro- and anti-angiogenic factors plays an important role at sites of damaged vasculature, such as in wound repair.[1] On the other hand, an imbalance of these factors can lead to aberrant neovascularization and vascular leakage, which are often the pathologic trigger of a number of diseases, including neovascular age-related macular degeneration (NVAMD) and macular edema (ME) in the eye. In NVAMD and diabetic macular edema (DME), which are the leading causes of vision loss in patients over 60 years of age[2] and in working-age population[3], respectively, vascular endothelial growth factor (VEGF) has a significant role in inducing neovascularization and fluid leakage[4]; hence, anti-angiogenesis has been widely investigated as the approach for therapeutic intervention.

FDA-approved therapeutics currently used in clinic with anti-VEGF mechanism

This chapter was completed based on research in collaboration with Shmueli RB, Silva RL, Mirando AC, Pandey NB, Popel AS, Campochiaro PA, and Green JJ.

includes ranibizumab (Lucentis®) and aflibercept (Eylea). While these are a recombinant protein fragment or fusion protein, there are also a number of endogenous protein fragments, such as angiostatin and endostatin that have anti-angiogenic function.[5,6] Moreover, a computational strategy to find the domains from serpin and collagen IV protein fragments that are critical for their anti-angiogenic activity has led to the development of short biomimetic, non-canonical peptides.[7] Different variants of serpin- , somatotropin- , thrombospondin- , CXC chemokines- , and collagen IV-derived peptides have been shown to efficiently block neovascularization to inhibit tumor growth and metastasis.[7-11] More recently, AXT107, a collagen IV-derived 20-mer peptide has been studied more extensively for its anti-angiogenic activity in NVAMD *in vivo* model.[11] The peptide not only suppressed retinal neovascularization (NV) in three mouse models for NVAMD and ischemic retinopathy, but also showed prolonged significant reduction in VEGF-induced vascular leakage compared to aflibercept up to 2 months in rabbit eyes.

Despite the functional efficacy of these therapeutics, they still have sub-optimal pharmacokinetics, which can necessitate frequent intravitreal injections and lead to poor patient compliance as well as potential safety risks.[12] With the goal of providing long-term release and therapeutic effect of the drug from a single injection and reducing the number of injections required for continued therapy, our group has previously encapsulated one of the serpin-derived peptides (SP6001) in a biodegradable polymeric microparticle system.[13] A single dosing of microparticles loaded with the peptide demonstrated long-term efficacy up to 14 weeks a mouse choroidal NV (CNV) model.

In this chapter of the thesis, we developed and investigated a long-term release system for AXT107, the aforementioned collagen IV-derived peptide, with biodegradable

polymeric microparticles. Poly(lactic-co-glycolic acid) (PLGA) polymer, which has been approved by the FDA for certain drug delivery systems and is a generally regarded as safe (GRAS) material, was used to formulate slowly degrading microparticles using a double emulsion fabrication method. We also tested two PLGA polymers with different hydrophobicity to explore differential release kinetics of the encapsulated peptide. Moreover, we followed a previously described method to elongate and increase the aspect ratio of these microparticles in order to reduce potential immune detection and ensure enhanced biocompatibility.[14,15] Herein, we report an optimized safe, biodegradable polymeric microparticle (MP) delivery system that encapsulates and protects the biomimetic peptide from degradation, allows sustained release through polymer hydrolysis, and demonstrates prolonged anti-angiogenic effect *in vivo* in murine NVAMD models.

7.2 Methods

Materials

Poly(D,L-lactic-co-glycolic acid) (PLGA) of lactide:glycolide (65:35) Mw 40k–75k and lactide:glycolide (85:15) Mw 190k-240k], dimethylsulfoxide (DMSO), and dichloromethane (DCM) were purchased from Sigma Aldrich (St. Louis, MO). Poly(vinyl alcohol) (PVA) Mw 25,000 was purchased from Polysciences (Warrington, PA). Peptide (AXT107) was custom synthesized from New England Peptide (Gardner, MA).

PLGA microparticle formation

PLGA microparticles (MP) with AXT107 encapsulated were formed using the double emulsion method. Briefly, 100 – 200 mg of PLGA polymer with one of the two lactide:glycolide ratios was dissolved in DCM at 20 mg/mL, and the peptide was dissolved in DMSO at 20 mg/mL. The peptide solution (DMSO) was added into the polymer solution (DCM) at a v/v ratio of 1:20, which was determined by the desired theoretical peptide loading of 5% by mass of the total polymer. For blank microparticles without peptide encapsulation, pure DMSO was mixed with the polymer solution at 1:20 v/v ratio. After vortexing, the peptide/PLGA mixture was sonicated at an amplitude setting of '30A' for 20 sec with a tip sonicator (Misonix) for the first emulsion. This phase was then poured into 50 mL of water-phase 1% PVA solution, and immediately homogenized at 3.8 krpm for 1 min (Ika T25 digital Ultra-Turrax). The emulsion was transferred to 100 mL of 0.5% PVA solution and stirred for 4 h to allow solvent removal. The resulting microparticles were washed three times by centrifuging at 4 krpm for 5 min, removing the supernatant, adding 40 mL of fresh ddH_2O, and resuspending the pellet by vortexing. Following the last wash, the supernatant was removed and approximately 5 mL of ddH_2O was added to resuspend microparticles for lyophilization. All microparticles were stored in -20ºC after lyophilization until use.

To make elongated, ellipsoidal PLGA MP, the method previously described by Meyer *et al.* was used.[15] First, lyophilized PLGA MP was suspended in 0.5% PVA / 0.1% glycerol solution by trituration. 5 mL of particle solution was then cast onto a rectangular petri dish (5 x 7 cm, VWR International, Radnor, PA) and dried overnight. The dried film was mounted on to the automated stretching machine and placed inside a 60ºC oven to raise the temperature above the glass transition temperature of PLGA polymer. After the film was

stretched 2.5-fold in length, it was cooled, re-dissolved in ddH_2O, washed three times as described above, and lyophilized for storage in -20^oC.

Microparticle characterization

Scanning electron microscopy (SEM) images were used to characterize PLGA microparticles. A piece of carbon tape (Electron Microscopy Sciences, Hatfield, PA) was adhered on aluminum mounts. Then, lyophilized spherical and ellipsoidal PLGA MPs were placed on the tape using disposable plastic spatula. The samples were sputtered with 5 nm thick of gold/palladium, and imaged using LEO/Zeiss Field Emission SEM at the Johns Hopkins University School of Medicine Microscope Facility. ImageJ was used to analyze the size distribution and aspect ratio of PLGA MPs from SEM images. To visualize PLGA MPs that had been injected in the eye, the visible MP clump from dissected eye was removed and placed on the aluminum mount with carbon tape. Then, the entire aluminum mount was put into the lyophilizer overnight, and the samples were sputter-coated for imaging.

To quantify the amount of peptide loading in PLGA MP, either the BCA assay (Micro BCA Protein Assay Kit, Thermo Scientific) or gel electrophoresis (Bio-Rad Mini-PROTEAN system) followed by silver stain analysis (SilverQuest™, Invitrogen) was used. For the first method, pre-weighed lyophilized microparticles and peptide standards at 100, 50, 25, 12.5, 6.25, 3.125, and 1.5625 μg/mL dissolved in 5% DMSO / 95% 1X PBS solution were loaded to the BCA assay and analyzed as instructed by the manufacturer. Using a different approach, pre-weighed masses of both peptide-loaded and blank MPs were first dissolved with DMSO to 2 mg/mL, and then equal volume of sample buffer (24% glycerol in

1X PBS) was added to yield 1 mg/mL of dissolved MP solution. Two-fold dilution series of the MPs were prepared using 1:1 v/v of DMSO:sample buffer solution. Peptide standards of a known amount, including 0, 62.5, 125, 250, and 500 ng, as well as protein standard were also prepared at 1:1 v/v of DMSO to sample buffer. All samples were loaded into a 12-well 10-20% Mini-PROTEAN tris-tricine gel (Bio-Rad), along with 10X tris/tricine/SDS running buffer (Bio-Rad) diluted to 1X with ddH_2O. Gel electrophoresis was run at 110 mV for 45 min or until the 2.5 kDa band of the protein standard was down to the lower half of the gel. The gel was silver-stained using the protocol provided by the manufacturer. Digital photograph of the silver-stained gel was analyzed with ImageJ to quantify band intensity. Peptide loading values were calculated with the following equations:

$$\text{Loading efficiency (LE) \%} = \frac{final\ mass\ of\ loaded\ peptide}{starting\ mass\ of\ peptide} \times 100$$

$$\text{Loading capacity (LC) \%} = \frac{mass\ of\ loaded\ peptide}{mass\ of\ polymer} \times 100$$

Peptide release from PLGA MP

To determine release kinetics of encapsulated AXT107, PLGA MP was incubated in 1X PBS with 0.03% sodium azide at 20 mg/mL on a shaker at 37ºC. Every week for the first week and every month thereafter, samples were briefly vortexed and centrifuged at 4 krpm for 5 mins to collect the supernatant. Fresh 1X PBS with 0.03% sodium azide solution was added to the samples and placed on a shaker at 37ºC for the next time point. The collected supernatant was stored at -80ºC until analyzed by the BCA assay for peptide concentration.

The same peptide standards as above were used for the calibration curve, and hence the sample was brought to 5% DMSO prior to BCA analysis.

Inhibition and regression of choroidal neovascularization (CNV) in vivo

The experimental timeline for each *in vivo* study and animal model is outlined in **Figure 7.1**. Laser-induced CNV is a widely used mouse model to study a drug's effect on the inhibition and regression of CNV.[16] For an inhibition study, 1 μL of AXT107-loaded PLGA MP (spherical and ellipsoidal), blank PLGA MP, or 1X PBS as a control was first injected intravitreally in the eyes of 5 – 6 week old female C57BL/6 mice using the Harvard Pump Microinjection System (Harvard Apparatus, Holliston, MA) and pulled glass micropipettes as described previously.[17] Based on the peptide loading capacity, the required concentration of PLGA MP was determined in order to deliver 1 μg/μL of peptide. For blank PLGA MP, the equivalent MP concentration as the peptide-loaded MP group was injected. CNV was induced by laser photocoagulation in the treated eyes at various time points, but at 14 days prior to the final end-time point for measuring MP efficacy over time on NV area inhibition. NV area was measured by perfusing the mice with 1 mL of 50 mg/mL fluorescein-labeled dextran (2 x 10^6 Da, Sigma-Aldrich) in 1X PBS and imaging choroidal flat mounts using fluorescent microscopy. Image-Pro Plus software (Media Cybernetics, Silver Spring, MD) was used for image analysis to quantify NV area. For regression, CNV was first induced in C57BL/6 mice 14 days prior to the final end-time point for measuring NV area. Then, at day 7, a subset of mice was sacrificed to record the baseline area of NV, while other mice received a 1 μL intravitreal injection of AXT107-loaded PLGA MP, blank PLGA MP, or 1X

PBS as a control. At day 14, all eyes were harvested and NV area measured as described above.

Vascular leakage from retinal neovascularization in rhoVEGF transgenic mice

At postnatal day 20 (P20), hemizygous rhoVEGF transgenic mice received a 1μL intravitreal injection of AXT107-loaded PLGA MP (spherical only), blank PLGA MP, or 1X PBS control. At P21, vascular leakage was visualized by immunostaining of albumin. Briefly, mice were perfused with PBS, and retinas were dissected, flat-mounted, and fixed in 10% formalin for 4 h. After washing in PBS, retinas were incubated with normal donkey serum for 40 min at room temperature, followed by an overnight incubation in rabbit anti-mouse albumin (Abcam) in 1% Triton solution and in Cy3-labeled donkey anti-rabbit secondary antibody (Jackson Laboratories, Inc) for 50 min at room temperature. Flat mounts are also stained with GSA-lectin to visualize neovascularization.

Retinal detachment from tet/opsin/VEGF double transgenic mice as a model for macular edema

Tet/opsin/VEGF transgenic mice were intravitreally injected with 1μL intravitreal injection of AXT107-loaded PLGA MP (spherical only) or blank PLGA MP. At day 11 and 57 post injection, mice were given drinking water containing doxycycline at 2 mg/mL to induce VEGF expression and retinal detachment. Three days after the initiation of

doxycycline, eyes were observed by spectral domain ocular coherence tomography (OCT) using Bioptigen Envisu R2200 to evaluate the retinal detachment.

PLGA MP injection in the rabbit eye

Dutch belted rabbits were anesthetized with ketamine and xylazine and received intravitreal injection (inferior) of 100 µL of blank PLGA MP in 1X PBS at approximately 100 mg/mL particle concentration. At day 7, fundus (Micron III Retinal Imaging Microscope, Phoenix Research Laboratories, Inc) images were taken to observe MP deposition and eyes were harvested to cut 10-µm ocular sections, stain with hematoxylin and eosin-Y, and observe potential inflammatory response.

In vitro depot formation test with PLGA MP in rabbit vitreous humor

Rabbit vitreous was obtained from Biochemed Services (Winchester, VA), stored in 4ºC, and used within 3 days of receipt. 100 mg/mL of spherical PLGA MP was prepared in water with 5% PEG 300 as well as 0.25% mannitol. 2.5 mg/mL of naked AXT107 peptide (stock concentration at 100 mg/mL in DMSO) was mixed in to the MP solution. 20 µL of this final solution was injected slowly into 300 µL of rabbit vitreous in a 1.5 mL eppendorf tube using a 28G insulin syringe. The injection was recorded using a cell phone camera. Then, the vitreous with injected MP was incubated in a rotator at 37ºC for various time points, at which digital pictures of the tubes were taken.

7.3 Results & Discussion

AXT107 peptide as an anti-angiogenic therapeutic

Efficacy and biological mechanism of the biomimetic anti-angiogenic peptide, AXT107, in NVAMD and ME have been previously shown in a number of *in vivo* pre-clinical models through a collaborative effort with the laboratories of Dr. Popel and Dr. Campochiaro. In the laser-induced CNV mouse model, which is the same model that was used to predict efficacy of the currently used therapy aflibercept, an intravitreal injection of AXT107 was able to suppress and regress CNV.[12] The peptide also showed the ability to reduce vascular leakage from subretinal NV in rhoVEGF mice and prevent exudative retinal detachment in Tet/opsin/VEGF double transgenic mice. Additionally, in VEGF-induced leakage model in rabbits, AXT107 injected in the vitreous was able to significantly reduce the leakage long-term for at least 60 days, whereas aflibercept lost its efficacy between 30 and 60 days.

Translating a therapeutic to the clinic often carries more requirements than the functional efficacy. These factors include, but not limited to, the toxicity, pharmacokinetics, and side effects of the therapy or its administration route, which may affect overall patient compliance. Hence, in this chapter, polymeric microparticles were formulated with PLGA polymer to improve the delivery of AXT107, addressing these important criteria. PLGA MP releases the encapsulated drug slowly over time through polymer degradation, which allows for enhanced patient compliance due to prolonged effect from a single injection and prevents the potential of further vision loss from repeated dosing.[4,13] The release kinetics from PLGA MP can be tuned by using commercially available PLGA polymers of different lactide to

glycolide ratios, such as 65:35, 75:25, and 85:15. Greater proportion of lactide than glycolide leads to a more hydrophobic PLGA polymer that degrades more slowly and releases the drug more slowly. Therefore, PLGA MP can be optimized to provide a drug release profile in consideration of the biology of the target disease as well as the physical accessibility of the site of disease.

Spherical PLGA MP characterization and AXT107 release kinetics

PLGA MPs were formulated using a standard double emulsion technique with two different PLGA polymers (L to G ratio of 65:35 and 85:15). 65:35 and 85:15 PLGA MPs are termed LMP and HMP, respectively, in this chapter. **Figure 7.2A/B** shows SEM images of LMP and HMP with 0 or 5% initial peptide loading. Loading efficiency was determined to be approximately 20%, yielding final loading of 1% by mass. The shape and surface topography of the microparticles are not affected from the peptide encapsulation. The size as the number-average diameter of these microparticles analyzed using ImageJ was approximately 5 μm and showed no statistically significant difference between the microparticles of different PLGA polymers (**Figure 7.2C**). The error bar shows the standard deviation of particles within a batch.

As expected, PLGA MPs made with PLGA polymers of varying hydrophobicity showed differential rates of peptide release (**Figure 7.3**). The general trend between all MPs tested was an initial burst release, followed by a nearly zero-order kinetics with detectable release still occurring at 4 months. HMP resulted in a lower amount of burst release and slower rate afterwards than LMP, most likely due to the slower degradation of the PLGA

polymer and less effective diffusion of the hydrophobic peptide out from the particle. The continuous release of AXT107 for at least 4 months is an advantage of using such a polymeric delivery system, as it can lead to long-term efficacy from a single treatment.

Efficacy in the laser-induced choroidal neovascularization mouse model

In this animal model, CNV is induced from the rupture of Bruch's membrane by laser photocoagulation at the 9, 12, and 3 o'clock positions of the posterior pole.[18] A drug can be injected before or after the laser photocoagulation to study either inhibition or regression of induced CNV. Both AXT107-loaded LMP and HMP were tested to investigate the long-term inhibition and short-term regression of CNV. LMP demonstrated release of the peptide and inhibition of CNV *in vivo* over 8 weeks, and peptide-loaded HMP showed release and inhibition of CNV area at 12 weeks compared to empty particles and at 16 weeks compared to its no injection control (**Figure 7.4A/B**). LMP and HMP both demonstrated significant regression of CNV 1 week post injection and 2 weeks post laser photocoagulation (**Figure 7.4 C/D**). These results demonstrate that AXT107 released from the initial burst from the particles can immediately have anti-angiogenic activity. Long-term inhibition of CNV by AXT107-loaded HMP demonstrates one of the advantages of using a drug delivery system and could translate to a reduced needed frequency of injections in patients. Follow-up *in vivo* experiments in different animal models were conducted with HMP.

Efficacy in reducing vascular leakage in rhoVEGF transgenic mouse model

In *rho*VEGF transgenic mouse model, mice start to have rhodopsin promotor-driven overexpression of VEGF in photoreceptors at postnatal day 7 (P7), which leads to areas of subretinal NV and vascular leakage by P21.[19] At P14, microparticles were administered in order to study the effect of reducing vascular leakage. As shown in **Figure 7.5A/B**, AXT107-loaded HMP resulted in significant reduction in total area of vascular leakage compared to no treatment group. The greater level of subretinal NV that causes such vascular leakage in the untreated compared to AXT107-loaded HMP-treated group is shown by GSA-lectin staining of flat mounts (**Figure 7.5C**). This study further confirms the fast-acting, early effect of the peptide-loaded HMP, which can be explained by the design of the delivery system to have an initial burst release of peptide to have a therapeutic effect on current disease.

Efficacy in preventing retinal detachment in tet/opsin/VEGF double transgenic mouse model

While *rho*VEGF transgenic mice will express VEGF without any initiator, production of high level of VEGF in photoreceptors can be temporally controlled in tet/opsin/VEGF double transgenic mice. Treatment with doxycycline in drinking water will drive transient increased expression of VEGF that results in severe vascular leakage and exudative retinal detachment within 4 to 5 days.[20] Three-grade observation of retinal detachment (none, partial, or total) using optical coherence topography (OCT) was used as the functional read-out to treatment with AXT107-loaded HMP versus empty HMP. As shown in **Figure 7.6**, at an early time point of 2 weeks post HMP injection and 5 days post doxycycline treatment, the empty HMP group showed total retinal detachment in all 9 eyes, whereas the peptide-loaded HMP group prevented retinal detachment completely in 6 out of 7 eyes and partially

in the remaining 1 eye. The two-month time point in this aggressive leakage model showed a 20% / 80% divide between total / partial retinal detachment in peptide-loaded HMP, in comparison to a 57% / 43% total / partial detachment in empty HMP group.

Intravitreal injection of AXT107-encapsulated HMP in rabbit eye

To further investigate the PLGA HMP formulations, the delivery system was injected in Dutch belted rabbits. A 200-fold higher concentration of empty HMP as the concentration used in mouse models was introduced into the rabbit vitreous to investigate the tolerability of higher doses. As shown in **Figure 7.7A**, a high concentration of empty HMPs caused an immune response, evidenced by the infiltration of macrophages and neutrophils in H&E sections. Moreover, fundus images of the eye showed potential dispersion of the microparticles in the vitreous following intravitreal injection (**Figure 7.7B**), indicating the specific treatment could potentially cause interference with vision by not remaining as a local depot.

Efficacy of ellipsoidal PLGA HMP in the laser-induced choroidal neovascularization model

Previous literature has reported the effect of anisotropic particle shape in evading immune response and prolonging bioavailability in the systemic circulation.[14,21] In particular, Champion *et al.* has previously shown that when particles with higher aspect ratio and greater radius of curvature come into contact with macrophages on the surface with greater radius of curvature, there is a decreased rate of phagocytosis of the particles.[14] We

formulated ellipsoidal PLGA HMP by physically stretching spherical PLGA HMP at above the glass transition temperature of PLGA polymer, with the hypothesis that the resulting anisotropic microparticles will prevent immune response in rabbit eyes. SEM images of the ellipsoidal PLGA HMP was used to measure an average aspect ratio of 4 ± 1 (**Figure 7.8A**). Interestingly, the release of AXT107 peptide from ellipsoidal PLGA HMP occurred faster than both spherical LMP and HMP (**Figure 7.8B**), potentially due to the increased surface area that is prone to polymer degradation and release. When injected into mice with laser-induced CNV, ellipsoidal AXT107-loaded PLGA HMP showed significant inhibition of CNV area at 8, 12, and 16 weeks (**Figure 7.8C**). Improved efficacy at earlier time points compared to spherical PLGA HMP could be explained by the faster release of the peptide from ellipsoidal PLGA HMP. The results also indicate that the amount of peptide released at longer time points is still sufficient to have anti-angiogenic activity with ellipsoidal HMP for at least 4 months, and supports the evaluation of this system with larger animals in future studies.

Depot formation of spherical PLGA HMP with AXT107 as an excipient

To further facilitate depot formation, we introduced additional molecules to the microparticle formulation. Our previous study with the naked AXT107 peptide showed that the peptide forms a self-assembled gel when injected into the vitreous on its own. Based on this feature, we mixed free AXT107 peptide with AXT107-loaded PLGA HMP, with the hypothesis that the self-assembly of AXT107 will cause depot formation of the HMP within the AXT107 gel. We evaluated the injection of HMP with naked AXT107 peptide into rabbit

vitreous *in vitro*, and observed the formation of a gel-like depot that was still visible after a 24 h incubation on a rotator to imitate free animal movement (**Figure 7.9**). On the other hand, HMP alone in rabbit vitreous over time resulted in a cloudy solution, indicating free dispersion of the microparticles that may block the visual axis *in vivo*. Mixing AXT107 peptide with the microparticles can provide an additional benefit of providing increased free peptide and corresponding therapeutic activity at shorter time periods as well.

7.4 Conclusion

PLGA microparticles were formulated to encapsulate a biomimetic, anti-angiogenic peptide, AXT107, as a local delivery vehicle to the intraocular vitreous space. Peptide-loaded microparticles composed of PLGA polymer with 85:15 lactide to glycolide ratio showed long-term zero-order release kinetics, which translated to short and long-term therapeutic effects in various NVAMD animal models. In a laser-induced CNV mouse model, AXT107-loaded PLGA microparticles successfully inhibited NV for at least 16 weeks, while also regressing pre-formed NV. In VEGF-inducible rhoVEGF and tet/opsin/VEGF models, microparticles were able to significantly reduce vascular leakage as well as prevent retinal detachment. In order to further ensure safety in larger animal models including rabbits, the delivery system was further optimized using two approaches. The aspect ratio of microparticles was increased to evade immune response, and AXT107 peptide was added as an excipient to promote microparticle depot formation following injection. In summary, this therapy shows promise for the long-term treatment of NVAMD.

7.5 References

(1) Kim, J.; Mirando, A. C.; Popel, A. S.; Green, J. J., Gene delivery nanoparticles to modulate angiogenesis. *Adv Drug Deliv Rev* **2017,** 119, 20-43.

(2) Klein, R.; Klein, B. E.; Linton, K. L., Prevalence of age-related maculopathy. The beaver dam eye study. *Ophthalmology* **1992,** 99, (6), 933-43.

(3) Morello, C. M., Etiology and natural history of diabetic retinopathy: An overview. *Am J Health Syst Pharm* **2007,** 64, (17 Suppl 12), S3-7.

(4) Campochiaro, P. A., Gene transfer for ocular neovascularization and macular edema. *Gene Ther* **2012,** 19, (2), 121-6.

(5) O'Reilly, M. S.; Boehm, T.; Shing, Y.; Fukai, N.; Vasios, G.; Lane, W. S.; Flynn, E.; Birkhead, J. R.; Olsen, B. R.; Folkman, J., Endostatin: An endogenous inhibitor of angiogenesis and tumor growth. *Cell* **1997,** 88, (2), 277-85.

(6) O'Reilly, M. S.; Holmgren, L.; Shing, Y.; Chen, C.; Rosenthal, R. A.; Moses, M.; Lane, W. S.; Cao, Y.; Sage, E. H.; Folkman, J., Angiostatin: A novel angiogenesis inhibitor that mediates the suppression of metastases by a lewis lung carcinoma. *Cell* **1994,** 79, (2), 315-28.

(7) Karagiannis, E. D.; Popel, A. S., A systematic methodology for proteome-wide identification of peptides inhibiting the proliferation and migration of endothelial cells. *Proc Natl Acad Sci U S A* **2008,** 105, (37), 13775-80.

(8) Koskimaki, J. E.; Karagiannis, E. D.; Rosca, E. V.; Vesuna, F.; Winnard, P. T., Jr.; Raman, V.; Bhujwalla, Z. M.; Popel, A. S., Peptides derived from type iv collagen, cxc chemokines, and thrombospondin-1 domain-containing proteins inhibit neovascularization and suppress tumor growth in mda-mb-231 breast cancer xenografts. *Neoplasia* **2009,** 11, (12), 1285-91.

(9) Lee, E.; Lee, S. J.; Koskimaki, J. E.; Han, Z.; Pandey, N. B.; Popel, A. S., Inhibition of breast cancer growth and metastasis by a biomimetic peptide. *Sci Rep* **2014,** 4, 7139.

(10) Rosca, E. V.; Penet, M. F.; Mori, N.; Koskimaki, J. E.; Lee, E.; Pandey, N. B.; Bhujwalla, Z. M.; Popel, A. S., A biomimetic collagen derived peptide exhibits anti-angiogenic activity in triple negative breast cancer. *PLoS One* **2014,** 9, (11), e111901.

(11) Lee, E.; Rosca, E. V.; Pandey, N. B.; Popel, A. S., Small peptides derived from somatotropin domain-containing proteins inhibit blood and lymphatic endothelial cell proliferation, migration, adhesion and tube formation. *Int J Biochem Cell Biol* **2011,** 43, (12), 1812-21.

(12) Silva, R. L. E.; Kanan, Y.; Mirando, A. C.; Kim, J.; Shmueli, R. B.; Lorenc, V. E.; Fortmann, S. D.; Sciamanna, J.; Pandey, N. B.; Green, J. J.; Popel, A. S.; Campochiaro, P. A., Tyrosine kinase blocking collagen iv-derived peptide suppresses ocular neovascularization and vascular leakage. *Sci Transl Med* **2017,** 9, (373).

(13) Shikari, H.; Silva, P. S.; Sun, J. K., Complications of intravitreal injections in patients with diabetes. *Semin Ophthalmol* **2014,** 29, (5-6), 276-89.

(14) Shmueli, R. B.; Ohnaka, M.; Miki, A.; Pandey, N. B.; Lima e Silva, R.; Koskimaki, J. E.; Kim, J.; Popel, A. S.; Campochiaro, P. A.; Green, J. J., Long-term suppression of ocular neovascularization by intraocular injection of biodegradable polymeric particles containing a serpin-derived peptide. *Biomaterials* **2013,** 34, (30), 7544-51.

(15) Champion, J. A.; Mitragotri, S., Shape induced inhibition of phagocytosis of polymer particles. *Pharm Res* **2009,** 26, (1), 244-9.

(16) Meyer, R. A.; Meyer, R. S.; Green, J. J., An automated multidimensional thin film stretching device for the generation of anisotropic polymeric micro- and nanoparticles. *J Biomed Mater Res A* **2015,** 103, (8), 2747-57.

(17) Lambert, V.; Lecomte, J.; Hansen, S.; Blacher, S.; Gonzalez, M. L.; Struman, I.; Sounni, N. E.; Rozet, E.; de Tullio, P.; Foidart, J. M.; Rakic, J. M.; Noel, A., Laser-induced choroidal neovascularization model to study age-related macular degeneration in mice. *Nat Protoc* **2013,** 8, (11), 2197-211.

(18) Mori, K.; Duh, E.; Gehlbach, P.; Ando, A.; Takahashi, K.; Pearlman, J.; Mori, K.; Yang, H. S.; Zack, D. J.; Ettyreddy, D.; Brough, D. E.; Wei, L. L.; Campochiaro, P. A., Pigment epithelium-derived factor inhibits retinal and choroidal neovascularization. *J Cell Physiol* **2001,** 188, (2), 253-63.

(19) Tobe, T.; Ortega, S.; Luna, J. D.; Ozaki, H.; Okamoto, N.; Derevjanik, N. L.; Vinores, S. A.; Basilico, C.; Campochiaro, P. A., Targeted disruption of the fgf2 gene does not prevent choroidal neovascularization in a murine model. *Am J Pathol* **1998,** 153, (5), 1641-6.

(20) Tobe, T.; Okamoto, N.; Vinores, M. A.; Derevjanik, N. L.; Vinores, S. A.; Zack, D. J.; Campochiaro, P. A., Evolution of neovascularization in mice with overexpression of vascular endothelial growth factor in photoreceptors. *Invest Ophthalmol Vis Sci* **1998,** 39, (1), 180-8.

(21) Ohno-Matsui, K.; Hirose, A.; Yamamoto, S.; Saikia, J.; Okamoto, N.; Gehlbach, P.; Duh, E. J.; Hackett, S.; Chang, M.; Bok, D.; Zack, D. J.; Campochiaro, P. A., Inducible expression of vascular endothelial growth factor in adult mice causes severe proliferative retinopathy and retinal detachment. *Am J Pathol* **2002,** 160, (2), 711-9.

(22) Geng, Y.; Dalhaimer, P.; Cai, S.; Tsai, R.; Tewari, M.; Minko, T.; Discher, D. E., Shape effects of filaments versus spherical particles in flow and drug delivery. *Nat Nanotechnol* **2007,** 2, (4), 249-55.

7.6 Figures & Tables

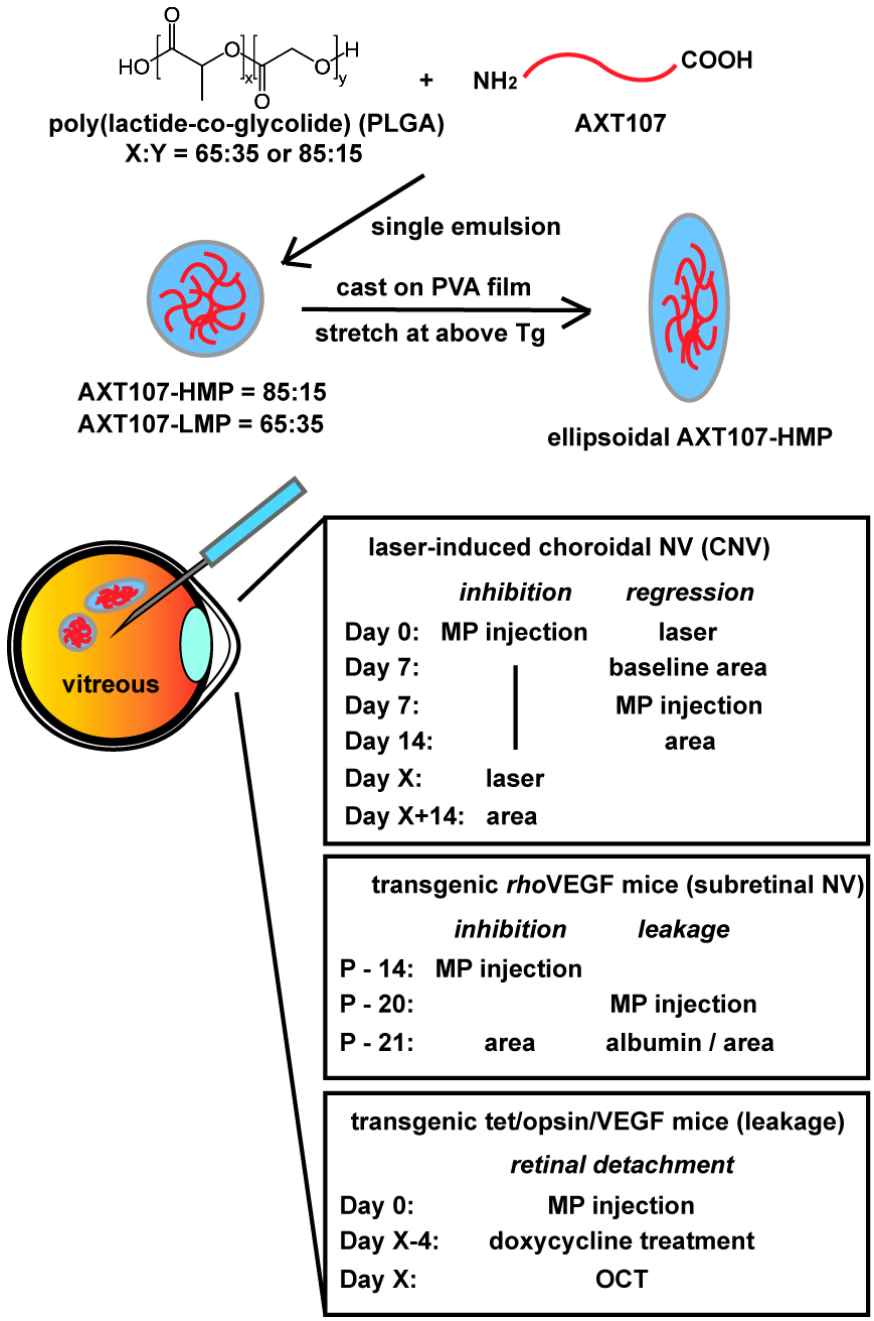

Figure 7.1. Schematic diagram of animal models and protocols. PLGA microparticles are formed with AXT107 peptide encapsulated to be treated to three different mouse models of NVAMD / ME. Laser-induced CNV can be used to test inhibition and regression of CNV, rhoVEGF transgenic mice for vascular leakage resulting from subretinal NV, and tet/opsin/VEGF double transgenic mice for vascular leakage and exudate retinal detachment.

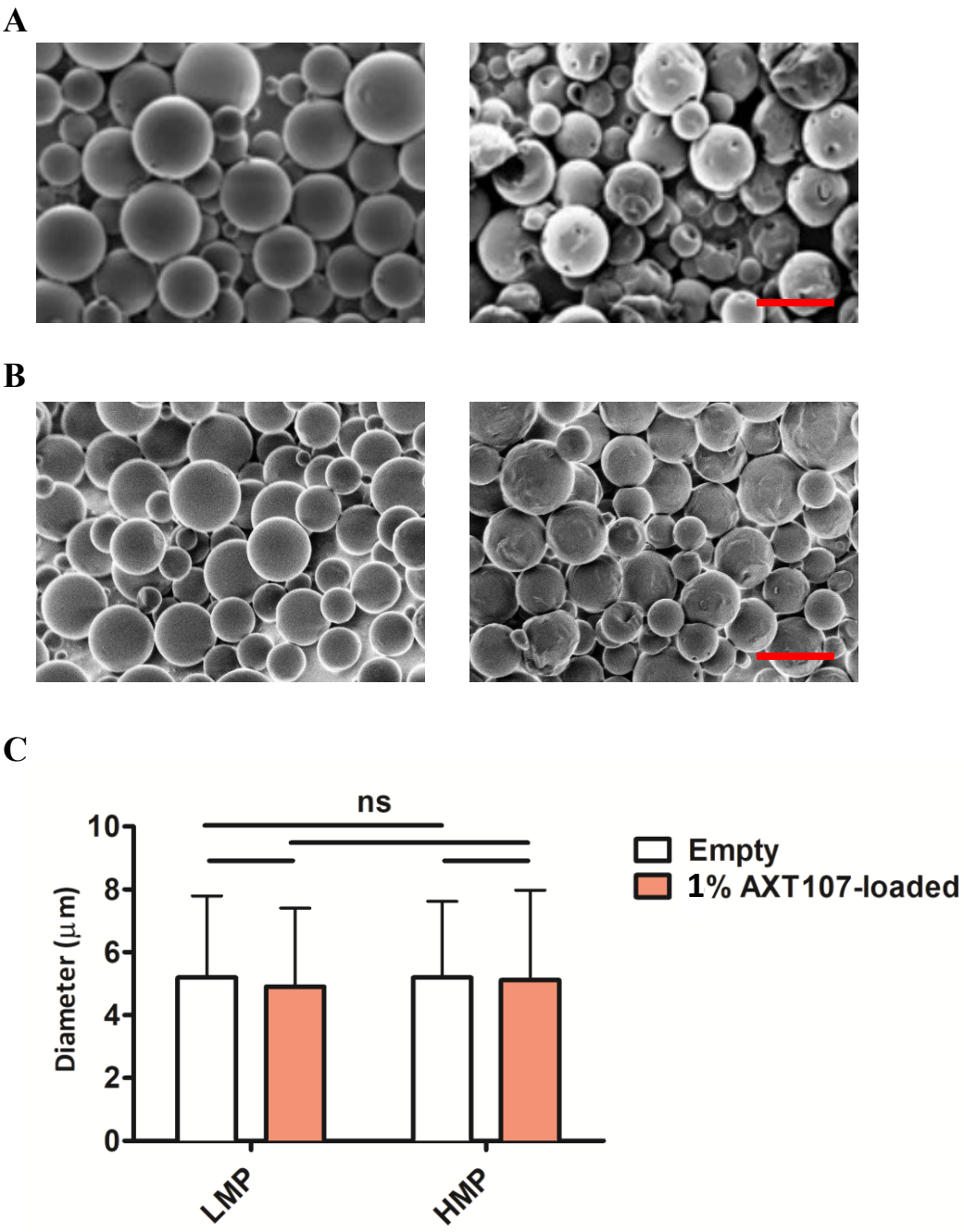

Figure 7.2. PLGA microparticle characterization. SEM images of empty and 1% AXT107-loaded PLGA microparticles formed with (A) 65:35 and (B) 85:15 PLGA polymers (scale bar = 10 μm). SEM images were analyzed by ImageJ to determine (C) number-averaged diameter of the microparticles (mean ± SD, n > 200, One-way ANOVA with Tukey post-hoc test α = 0.05).

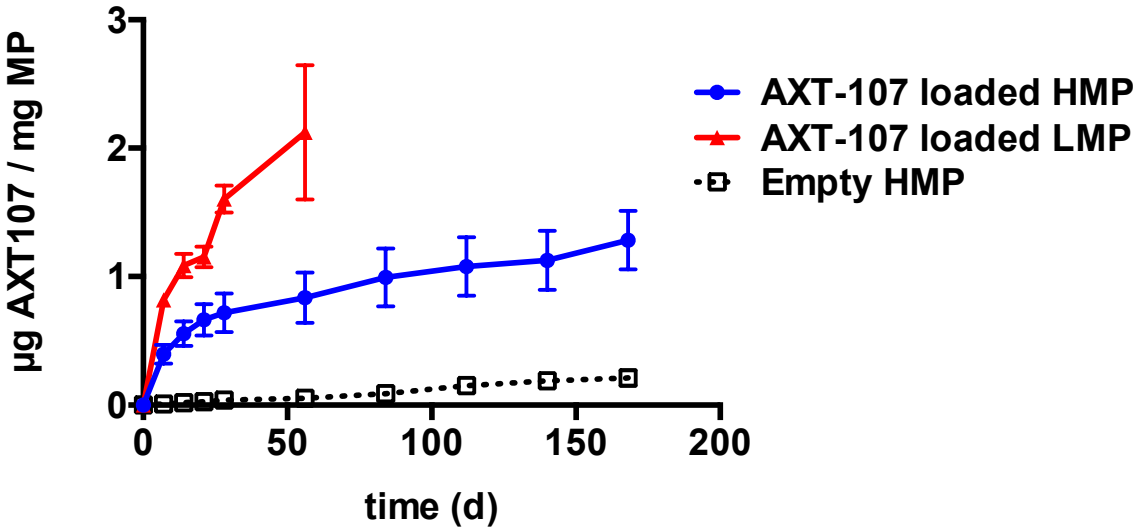

Figure 7.3. AXT107 peptide release from PLGA microparticles *in vitro*. Peptide release from PLGA LMP and HMP is determined by incubating microparticles in 1X PBS at 37ºC over time. Released peptide amount is detected and measured using micro BCA assay (n = 3, mean ± SD).

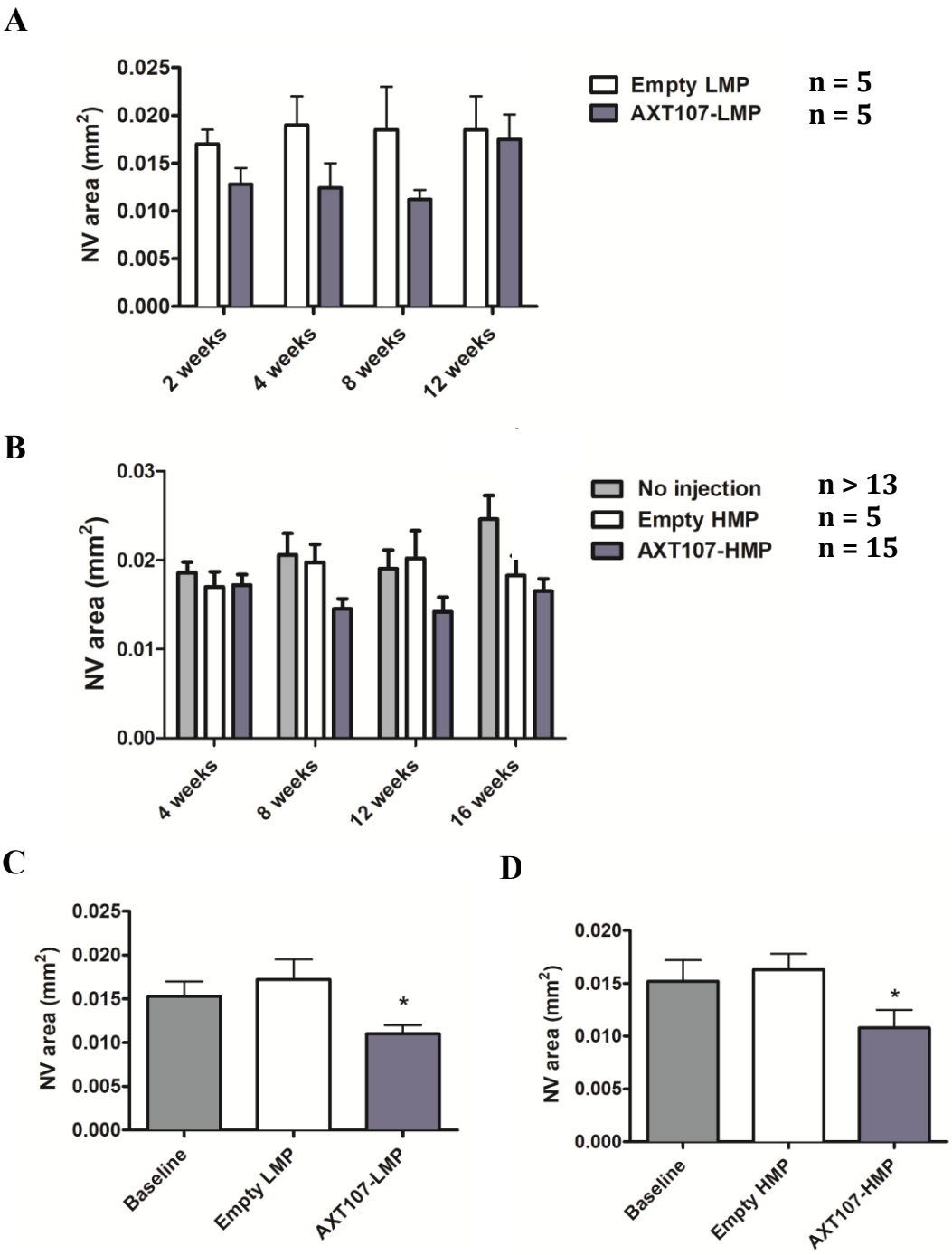

Figure 7.4. Efficacy in laser-induced choroidal neovascularization mouse model. Activity of AXT107 released from PLGA LMP and HMP in (A-B) inhibition and (C-D) regression of choroidal neovascularization area following laser photocoagulation. Neovascularization area is visualized by perfusing the animal with fluorescein-labeled dextran, and analyzed using Image-Pro Plus software ($n > 7$ for regression study, mean ± SEM, One-way ANOVA with Dunnett post-hoc test for regression to compare against baseline control, $\alpha = 0.05$).

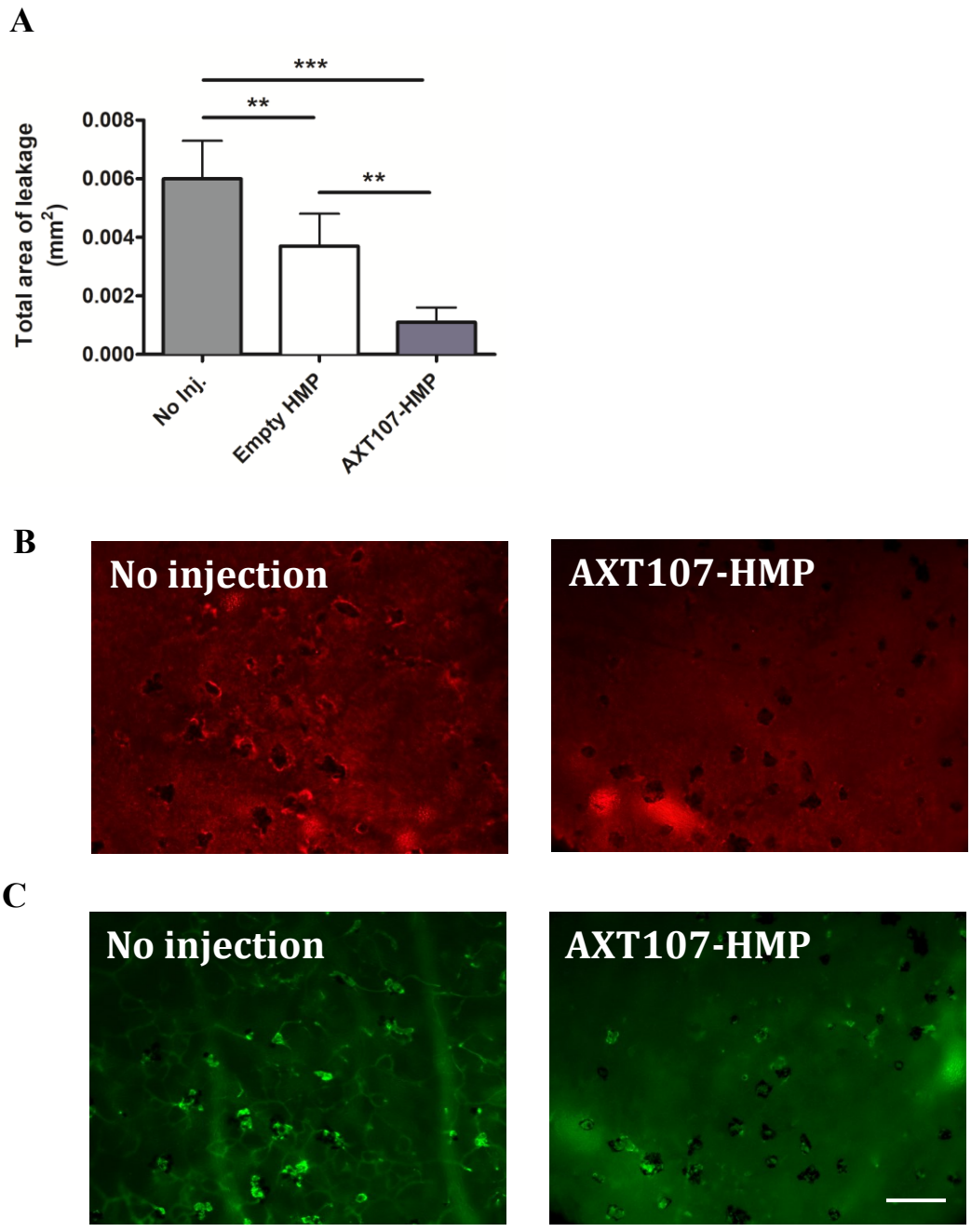

Figure 7.5. Efficacy in *rho*VEGF transgenic mouse model. (A) Activity of AXT107 released from PLGA HMP in reducing the area of vascular leakage from subretinal neovascularization (mean ± SEM, One-way ANOVA with Dunnett post-hoc test to compare against empty HMP control). Representative image of flat mounts stained with (B) albumin to calculate the area of vascular leakage and (C) GSA lectin to visualize neovascularization (scale bar = 100 μm)

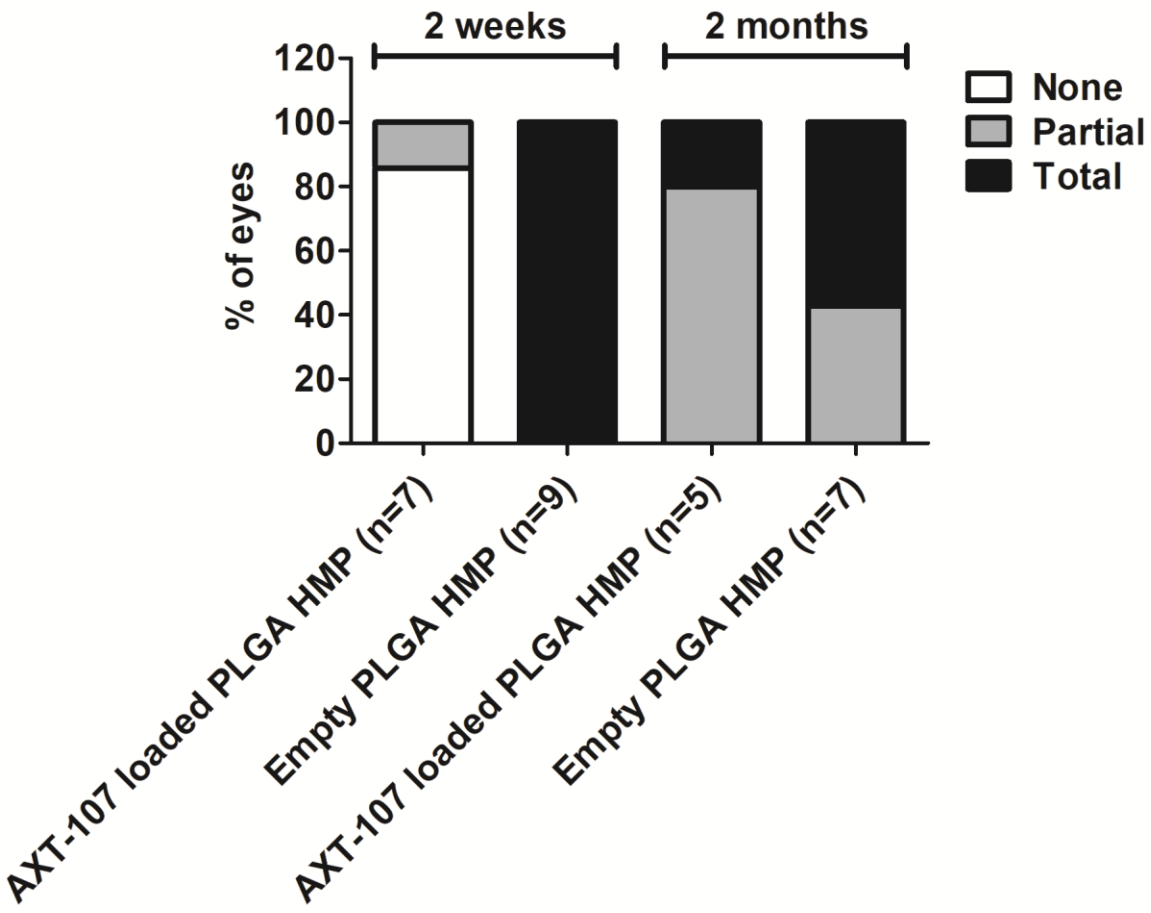

Figure 7.6. Efficacy in tet/opsin/VEGF transgenic mouse model. (A) Activity of AXT107 released from PLGA HMP in preventing exudative retinal detachment from vascular leakage following doxycycline-mediated VEGF overexpression. The degree of retinal detachment is evaluated in three grades: total, partial, and none.

A

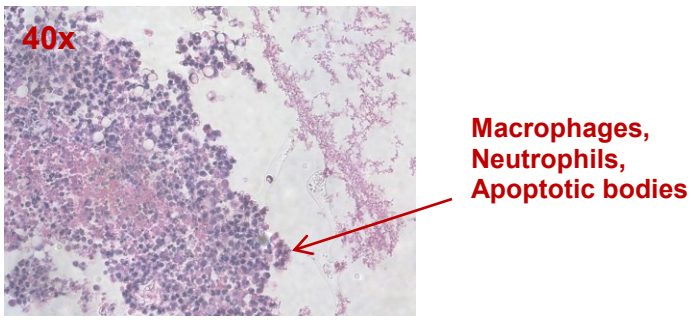

B

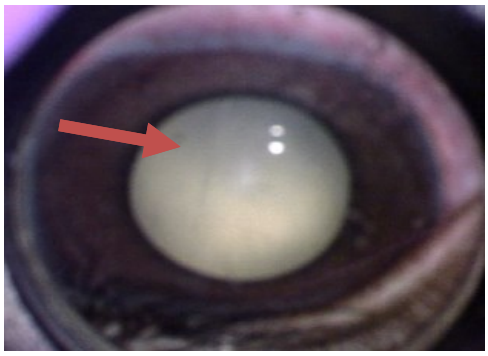

C

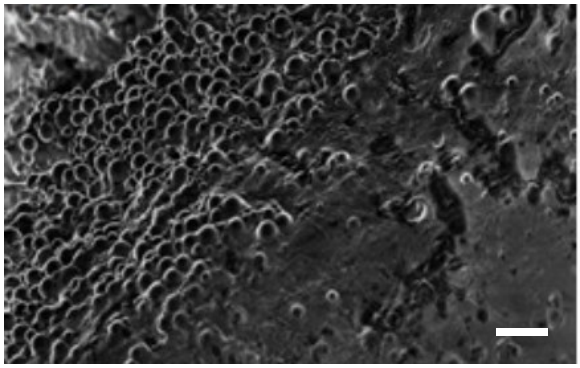

Figure 7.7. Intravitreal injection of PLGA HMP in Dutch belted rabbits. Safety investigated in rabbit eye following intravitreal injection of a high concentration PLGA HMP. (A) Potential immune response indicated by macrophage and neutrophil infiltration (red arrow) into rabbit vitreous shown in H&E-stained ocular section (scale bar = 10 μm), and (B) Potential vision occlusion resulting from microparticle dispersion (red arrow) in vitreous shown through fundus image. (C) Representative SEM image of PLGA HMP harvested from rabbit eyes after injection showed similar morphology as pre-injection PLGA HMP.

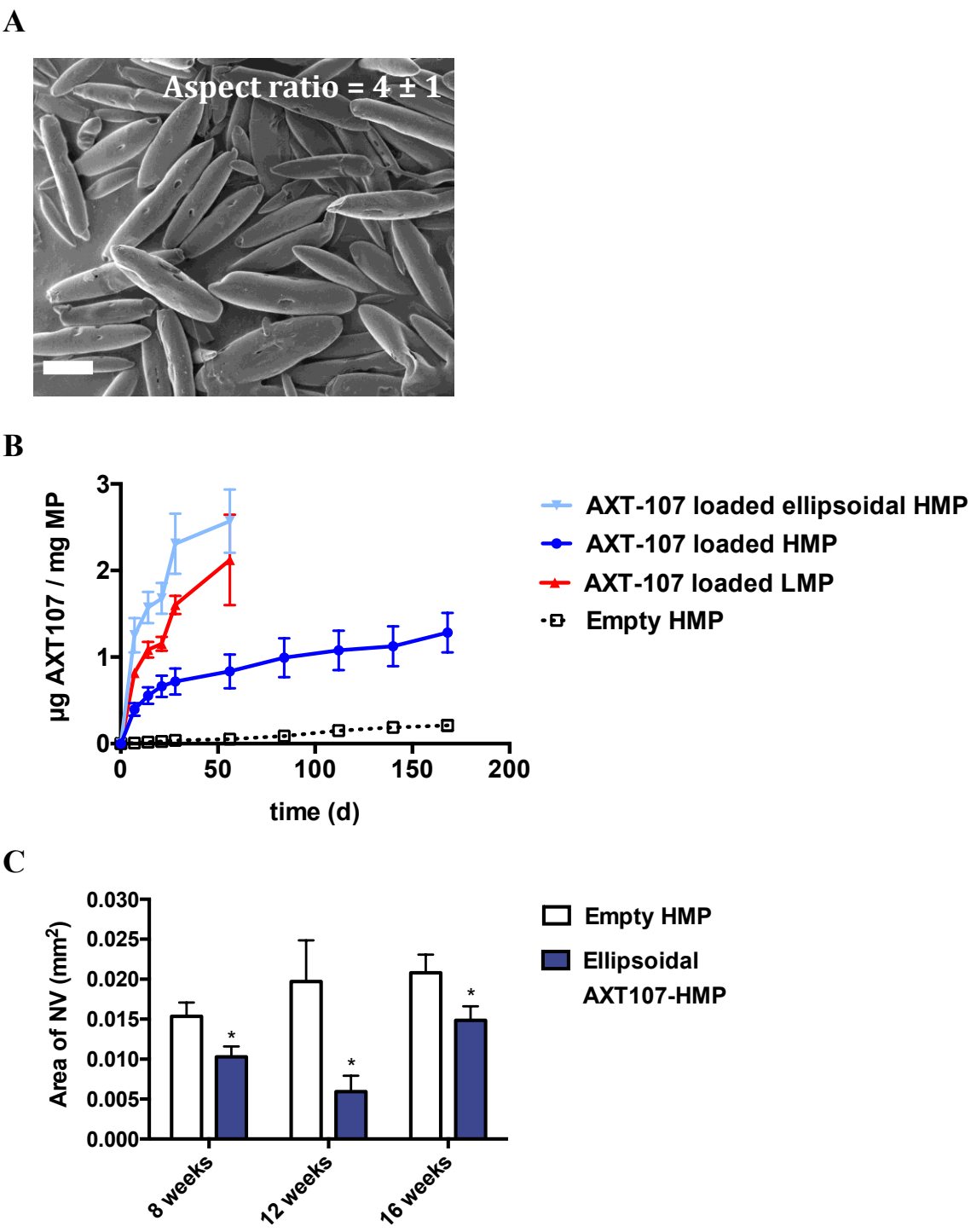

Figure 7.8. Characterization and efficacy of ellipsoidal PLGA HMP. (A) SEM image of stretched PLGA HMP (scale bar = 10 µm, n > 200), (B) Release kinetics of encapsulated AXT107 from ellipsoidal PLGA HMP (n = 3, mean ± SD), and (C) Its long-term effect in inhibiting choroidal neovascularization area induced by laser photocoagulation in mice (n > 6, mean ± SEM, One-way ANOVA with Tukey post-hoc test $\alpha = 0.05$).

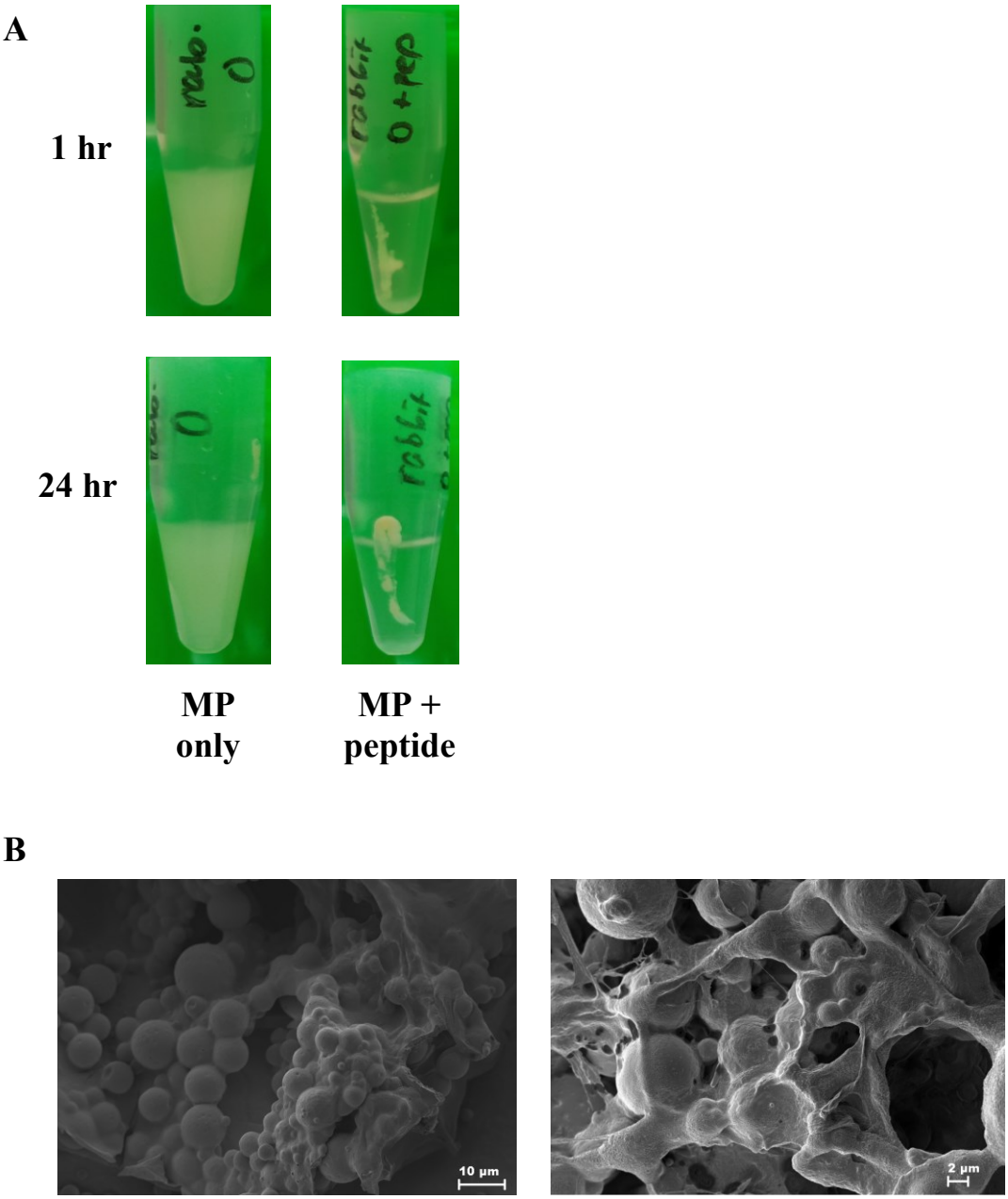

Figure 7.9. Characterization of depot formation of PLGA HMP with the addition of free AXT107. (A) Digital photograph of PLGA HMP or PLGA HMP and AXT107 injected into a tube of rabbit vitreous *in vitro* and rotated over 24 hrs, showing a dense persistent depot of PLGA HMP plus AXT107, and (B) SEM image of PLGA HMP plus AXT107 harvested from the rabbit eye following intravitreal injection.

Vita

Jayoung Kim was born in Seoul, Korea on October 19th, 1984. He had the opportunity to spend his childhood and youth in both the Republic of Korea and the United States due to his father's relocation as a (visiting) professor. He always had exceptional classmates and friends as he attended a number of schools from this relocation, Gadong Elementary School, Parkman Middle School, and Songpa Middle School. He was fortunate to have been exposed to both cultures and absorb the good aspects from them. After finishing up middle school education in Korea, he decided that he wanted to officially study abroad in the United States, and joined the Webb Schools in California for high school. He excelled especially in math and science, and eventually graduated as the valedictorian of his class.

He then went on to the University of California, Berkeley, where he graduated with a Bachelor of Science in Bioengineering and a minor in Industrial Engineering and Operations Research. While trying to take advantage of such well-rounded school and taking courses in all fields including economics and literature, he also had the opportunity to experience cutting-edge biomedical research, including in the field of tissue engineering.

As a Korean citizen, he had the complete compulsory military requirement in the home country, and came back to Korea to serve as an interpretation officer (Ret. 1st Lt.) in the Republic of Korea Air Force. There, he had the chance to attend and interpret at meetings with generals of both Korea and the United States in daily and strategic issues concerning North Korea. Towards the end of the service, he applied and was awarded the Samsung Scholarship, providing tuition and stipend support for graduate study.

After the military service, he had an 8-month gap until returning to the United States to continue his graduate study. As a preparation to become a better researcher, he joined a neuroscience laboratory at the Korea Institute of Science and Technology, a government-operated research organization, to participate in various *in vivo* studies, including animal surgery and behavioral study.

In order to further pursue his interests in the field of biomaterials, he joined the master's program at Johns Hopkins School University Department of Biomedical Engineering. Under the mentorship of Dr. Jordan Green, he participated in exciting research projects, both alone and together with members in and out of the lab. His graduate student mentor, Ron Shmueli, had a profound impact on his research career. His work as a master's student led him to apply for and stay as a PhD student in the same laboratory, with the renewal of the Samsung Scholarship. He has worked on a variety of projects investigating the tissue targeting capacity of polymeric drug delivery vehicles in both cancer and ocular disease applications. This work has resulted in a number of publications and patents that will hopefully have clinical use as therapeutics in the future.

Jayoung Kim

jkim397@jhu.edu (443) 956-3123

Education

8/ 2013 – 4/ 2018	**Johns Hopkins University**	Ph.D. in Biomedical Engineering
	Qualification exam: passed in April 2014	
	Thesis proposal: completed in May 2016	
	Thesis defense completed and dissertation submitted in April 2018	
8/ 2011 – 5/ 2013	**Johns Hopkins University (GPA: 3.87 / 4.0)**	M.S.E. in Biomedical Engineering
8/ 2011 – 5/ 2013	**University of California, Berkeley (GPA: 3.69 / 4.0)**	B.S. in Bioengineering

Honors / Awards / Affiliation

2013 - 2018	Samsung Scholarship recipient for PhD studies
2011 - 2013	Samsung Scholarship recipient for Master's studies
2010	US Army Commendation Medal
2007	Golden Key International Honour Society
2006	Bioengineering Honor Society
2006 - 2007	Undergraduate Scholarship

Research Experience

8/ 2011 – 4/ 2018 **The Green Group** Biomedical Engineering, Johns Hopkins School of Medicine

Thesis title: Engineering polymeric drug delivery vehicles for enhanced tissue targeting

*DNA / drug delivery with **poly(ethylene glycol)-co-poly(β-amino ester)** nanoparticles*

- Created a poly(ethylene glycol)-modified poly(β-amino ester) (PEG-PBAE) polymer
- Validated combinatorial approach to formulate PEG-PBAE/ DNA polyplexes and study enhanced diffusion and therapeutic efficacy in human glioblastoma model
- Investigated suprachoroidal delivery of PBAE polyplexes retinal transfection
- Engineered anisotropic PEG-PBAE micelles that deliver anti-cancer drug verteporfin

*Delivery of **anti-angiogenic peptide** with poly(lactide-co-glycolide) (PLGA) particles*

- Identified the molecular target and binding kinetics of the peptide
- Evaluated *in vivo* biodistribution and efficacy of peptide-coated targeted PLGA nanoparticles in breast cancer and glioblastoma model
- Investigated efficacy of peptide-loaded PLGA microparticles for ocular application in neovascular age-related macular degeneration model

High-throughput in vivo screening** of polyplex biodistribution using **DNA barcode

- Optimized the protocol for specific identification of multiple polyplexes in a mouse organ by using plasmid DNA as the barcode for each nanoparticle
- Identify structure-function relationship between polymer structure and *in vivo* tissue targeting of the resulting nanoparticles in high-throughput manner

***International Collaboration**: with Dr. Seung-woo Cho Lab at Yonsei University*

- Evaluated efficacy of PEG-PBAE nanoparticles on melanoma (manuscript submitted)

1/ 2011 – 7/ 2011 **Center for Functional Connectomics** Korea Institute of Science and Technology

Project. Functional study of hippocampal, astrocytic μ–opioid receptor (MOR) in addiction

- Conducted *in vivo* knock-down of MOR with lenti_shRNA and performed immunohistochemistry and confocal imaging to confirm gene knockdown
- Designed and conducted addiction behavior test with MOR-deficient mice

1/ 2005 – 5/ 2005 **Department of Cognitive Science** University of California, Berkeley

Project: Functional MRI imaging of nerve activation in dorso-lateral prefrontal lobe

- Assisted formulating the experiment and conducted screening of 20+ participants
- Analyzed anatomical and functional MRI data

Publications

2013 Shmueli RB, Ohnaka M, Miki A, Pandey NB, Lima e Silva R, Koskimaki JE, **Kim J**, Popel AS, Campochiaro PA, Green JJ. Long-term suppression of ocular neovascularization by intraocular injection of biodegradable polymeric particles containing a serpin-derived peptide. ***Biomaterials***, 34(30): 7544-7551, 2013.

Kim J, Sunshine JC, Green JJ. Differential polymer structure tunes mechanism of cellular uptake and transfection routes of poly(beta-amino ester) polyplexes in human breast cancer cells. ***Bioconjugate Chemistry***, 25(1): 43-51, 2013.

2014 Bishop CJ, **Kim J**, Green JJ. Biomolecule delivery to engineer the cellular microenvironment for regenerative medicine. ***Annals of Biomedical Engineering***, 42(7): 1557-1572, 2014.

2015 **Kim J**, Kozielski KL, Wilson DR, Green JJ. Biodegradable Polymeric Nanoparticles for Gene Delivery in Perspectives in Micro and Nanotechnology for Biomedical Applications. (**Imperial College Press, UK**) 2015.

Kim J, Wilson DR, Zamboni CG, Green JJ. Targeted polymeric nanoparticles for cancer gene therapy. ***Journal of Drug Targeting***, 23(7-8): 627-641, 2015.

2016 **Kim J,** Kang Y, Tzeng SY, Green JJ. Synthesis and application of poly(ethylene glycol)-co-poly(beta-amino ester) (PEG-PBAE) polymer in gene therapy against small cell lung cancer. ***Acta Biomaterialia***, 41: 293-301**,** 2016

2017 **Kim J**, Mirando A, Popel AS, Green JJ. Gene delivery nanoparticles to modulate angiogenesis. ***Advanced Drug Delivery Reviews***, 119: 20-43, 2017**.**

Lima e Silva R, Kanan Y, Mirando A, **Kim J**, Shmueli RB, Lorenc V, Fortmann S, Sciamanna J, Pandey NB, Green JJ, Popel AS, Campochiaro PA. Tyrosine kinase blocking collagen IV-derived peptide suppresses ocular neovascularization and vascular leakage. ***Science Translational Medicine***, 9(373): eaai8030, 2017**.**

Zamboni CG, Kozielski KL, Vaughan HJ, Nakata MM, **Kim J,** Higgins LJ, Pomper MG, Green JJ. Polymeric nanoparticles as cancer-specific DNA delivery vectors to human hepatocellular carcinoma. ***Journal of Controlled Release***, 263: 18-28, 2017**.**

2018 Bressler EM*, **Kim J***, Shmueli RB*, Mirando AC, Bazzazi H, Lee E, Pandey NB, Popel AS, Green JJ. Biomimetic peptide display from a polymeric nanoparticle surface targets and

shows anti-tumor activity against human triple-negative breast cancer cells. ***Journal of Biomedical Materials Research Part A,*** 106(6): 1753-1764, 2018

Min SJ, Jin YH, Hou CY, **Kim J**, Green JJ, Kang TJ, Cho SW. Bacterial tRNase-based gene therapy with poly(beta-amino esters) nanoparticles for suppressing tumor growth and relapse (**submitted to *Advanced Healthcare Materials***)

Kim J*, Shamul JG*, Shah SR*, Shin A, Lee B, Quiñones AH, Green JJ. An effective, non-photodynamic cancer therapy using verteporfin-loaded poly(ethylene glycol)-co-poly(beta-amino ester) micelle. (**Submitted to *Biomacromolecules***)

Shah SR*, **Kim J***, Carlos J, Ruiz A, Green JJ, Quiñones AH. Polymeric microparticles allow delivery of poorly water-soluble verteporfin for radiosensitization and attenuation of tumor growth. (**manuscript in preparation for *Biomaterials***)

Kim J*, Shmueli RB*, Lima e Silva R, Mirando AC, Pandey NB, Popel AS, Campochiaro PA, Green JJ. "Biodegradable polymeric microparticles carrying a biomimetic, anti-angiogenic peptide show therapeutic effect in murine models of neovascular age-related macular degeneration." (**manuscript in preparation for *Biomaterials***)

Patents

Oct. 7, 2016	Campochiaro, P.A., Green, J.J., **Kim, J.**, Shen, J. "Non-viral gene transfer to the suprachoroidal space." Provisional Patent Application. 2016. JHU Case #C14402
May 8, 2017	Green, J.J., Popel, A.S., Campochiaro, P.A., Pandey, N., **Kim, J.**, Lima e Silva, R., Shmueli, R., Mirando, A. "Biodegradable microparticles for sustained delivery of anti-angiogenic peptide." Provisional Patent Application. 2017. JHU Case #C14753_P14753-01
Sept. 26, 2017	Green, J.J., **Kim, J.**, Tzeng S. "Poly(beta-amino ester)-co-polyethylene glycol (PEG-PBAE-PEG) polymers for gene and drug delivery." US National Stage Application #15561869
April 18, 2018	Green, J.J., Quiñones-Hinojosa, A., **Kim, J.**, Shah, S.R., Shamul, J.G. "Poly(ethylene glycol)-poly(beta-amino ester)- poly(ethylene glycol) Triblock Micelles for Drug Delivery including Verteporfin Delivery to Cancer Cells." Provisional Patent Application. 2018. JHU Case #C15280

Presentations

May, 2012 Baltimore, MD	**Kim J**, Sunshine JC, Green JJ. Cellular uptake pathway of poly(β-amino esters) nanoparticles affects gene transfection in breast cancer cells. *Johns Hopkins INBT Symposium*. **(poster)**
May 22, 2014 Washington DC	**Kim J**, Sunshine JC, Green JJ. Subtle changes to polymer structure of poly(beta-amino ester) nanoparticles modulate cellular uptake pathway and transfection efficacy in human breast cancer cells. *American Society of Gene and Cell Therapy*. **(oral)**
Oct. 24, 2014 San Antonio, TX	**Kim J**, Mastorakos P, Park HW, Suk JS, Hanes JS, Green JJ. Optimizing poly(beta-amino ester) polyplexes for enhanced cellular uptake and particle stability. *Biomedical Engineering Society*. **(poster)**
Dec. 14, 2014 Washington DC	**Kim J**, Sunshine JC, Green JJ. Engineering poly(beta-amino ester) end-group and PEGylation to improve nanoparticle stability and cellular uptake. *TERMIS Americas*. **(poster)**
Oct. 9, 2015 Tampa, FL	**Kim J**, Kang Y, Green JJ. Engineering stable and efficient poly(ethylene glycol)-co-poly(beta-amino ester)polyplexes towards cancer gene therapy. *Biomedical Engineering Society*. **(poster)**
May 17, 2016 Montreal, QC	**Kim J**, Kang Y, Green JJ. High-throughput combinatorial approach to formulating stable and efficient poly(ethylene glycol)-poly(beta-amino ester) nanoparticles for gene delivery. *10th World Biomaterials Congress*, **(oral)**

Sept. 17, 2016 Baltimore, MD	**Kim J**, Bressler E, Shmueli RB, Mirando A, Pandey NB, Popel AS, Green JJ. Biomimetic peptide-conjugated polymeric nanoparticles to target human breast cancer. *Nano DDS*. (**poster**)
April 7, 2017 Minneapolis,MN	**Kim J**, Bressler E, Shmueli RB, Mirando A, Pandey NB, Popel AS, Green JJ. Biodegradable polymeric nanoparticles targeted by a novel biomimetic peptide to human breast cancer. *Society for Biomaterials*. (**poster**)
May 8, 2017 Baltimore, MD	**Kim J,** Lima e Silva R, Shmueli RB, Mirando A, Pandey NB, Popel AS, Campochiaro PA, Green JJ. Biodegradable polymeric microparticles allow sustained durability of a multimodal anti-angiogenic peptide to treat neovascular age-related macular degeneration. *Association for Research in Vision and Ophthalmology.* **(poster)**
Oct. 13, 2017 Phoenix, AZ	**Kim J**, Zamboni CG, Vaughan H, Wilson DR, Green JJ. High-throughput *In Vivo* Evaluation of Nanobiomaterial-mediated Tissue Targeting of Polymeric Gene Delivery Vectors Using DNABarcodes. *Biomedical Engineering Society.* **(oral)**

Leadership / Teaching Experience

10/ 2013 – 4/ 2018 — **Undergraduate Student Research Mentor** — Green Group, Johns Hopkins University

- Provided research mentorship to 5 undergraduate students in the lab
- Resulted in 2 publications, 1 oral presentation, and 3 poster presentations
- Mentee won awards, including Provost's Undergraduate Research Award (PURA), BMES Research Day, and Society for Biomaterials Student Drug Delivery Award

10/ 2017 – present — **Student Representative** — Biomedical Engineering Society

- International Affairs Committee

8/ 2016 – 12/ 2016 — **Course Instructor** — Johns Hopkins University

- Organized a course "Drug Shipments: How Medications Move Through the Body"
- Taught and advised 12 freshmen in BME on the topic of biomaterials and drug delivery
- Received interest to join the lab from 3 students (course evaluation: 4.18 / 5.0)

4/ 2014 – 4/ 2015 — **President, Korean Graduate Student Group** — Johns Hopkins University

- Fundraised over $1500
- Organized volunteer activity, academic forum, and music concert open to public
- Established network between current students and alumni
- Created mentor-mentee program with undergraduate students

8/ 2014 – 12/ 2014 — **Teaching Assistant (Evaluation: 3.97 / 5.0)** — Johns Hopkins University

- Assisted a core BME course: "Systems Bioengineering 1" (150+ students)
- Lectured during weekly sections and led weekly office hours

9/ 2007 – 12/ 2010 — **Military Officer (Ret. 1st Lieutenant)** — Republic of Korea, Air Force

- Non-compulsory service as 2nd and 1st lieutenant
- Official interpreter to the Director of Intelligence (Major General), United Nations Command in daily intelligence briefings and in formal meetings with US DIA / CIA / DoD / Joint Chief of Staff Intelligence / Secretary of State
- Participated in joint intelligence investigation with United Nations countries on North Korea's torpedo attack on Cheonan Ship and missile attack on Yeon-pyeong Island